FLUID-PARTICLE TRANSPORT DYNAMICS OF SANDWAVES

BY

ROLAND JAMES ONSLOW

A thesis submitted to the
Faculty of Engineering
of the
University of Birmingham
for the degree of
Doctor of Philosophy.

Fluid and Surface Transport Team,
School of Chemical Engineering,
University of Birmingham,
Birmingham B15 2TT.
England.

September 1993.

SYNOPSIS

The local dynamics of sandwaves and their crest-shedding turbulent flows has received little mechanistic attention, unlike recent advances in allied fields such as bubbly shear flows. One main purpose of the present project is to address these questions of particle engagement and transport by transient large eddies in the free shear layer over sandwaves. Experimental studies were conducted on the trajectories of model particles over suitably scaled fixed bedforms in a purpose built flume. Three important results emerged. Firstly, trajectories of particles jetted over the crest fell into seven primary modes from short paths beyond the crest to extended downstream transport. Secondly, the vertical profiles of particle concentration exhibited peaks at crest elevation over the trough, comparing with recent field observations by (Soulsby, 1989). Thirdly, flapping excursions of the shear layer were found to enhance lee slope scour and probably account for the sediment clouds observed in Soulsby's field study, here further conjectured to result in sandwave washout at high flow velocities. Favourable comparisons with previous studies are described.

Theoretical modelling of the shear layer eddies as Rankine vortices served to demonstrate the key role of pressure gradient/inertial forces as being primarily responsible for particle capture near the crest. A simple example is given to illustrate the striking distortion introduced by averaging out these fluctuating gradients, as is done in present engineering calculation methods. An idealised approximation to the eddies in the free shear layer is offered in terms of a translating-growing vortex core. Three behavioural regimes are identified: the first dominated by gravitational forces and characterised by particles falling from the layer; the second dominated by fluid forces and characterised by ejection trajectories; the third a transition regime characterised by trajectories looping within the core. Vortex flow drag determines the limits of gravity/looping behaviour whereas vortex pressure gradient/inertial force fixes the limits of looping/ejection behaviour. Escape trajectories were found to be confined to certain orientations which broadly accorded with trajectories obtained in the laboratory experiments.

As closing discussions, we focus on the need for improved practical calculation methods which properly represent the local dynamical features responsible for particle transport. Again taking our lead for developments in bubbly flow modelling (eg Thomas et al, 1983), we urge the adoption of discrete vortex modelling as a simplified Lagrangian scheme giving representation to large eddy structure.

ACKNOWLEDGEMENTS

I would like to express my gratitude to Dr Neale Thomas for his help, encouragement, insight, patient guidance on the preparation of this thesis and support with FAST Team facilities, without which this project would not have been possible. My thanks to Dr Richard Whitehouse of HR Wallingford Ltd. as external collaborating supervisor.

I would like to thank the members of the FAST Team, past and present, for their assistance. In particular, Mr X Yang for many hours of pleasurable discussion. Also, thankyou to Rachael for her many hours of patient assistance in the preparation of this thesis.

Finally, I would like to thank the technical staff of the School of Chemical Engineering for their support throughout the duration of this project, especially Mr Stan Ward for two years of back-breaking work constructing the experimental equipment.

This work was undertaken as a SERC-CASE project with HR Wallingford Ltd. Their sponsorship is gratefully acknowledged.

TABLE OF CONTENTS

CHAPTER 2: EXPERIMENTAL EQUIPMENT AND METHODS

CHAPTER 3: JETTING EXPERIMENTS

Figures

CHAPTER 4: LEE AND STOSS SUSPENSION EXPERIMENTS

CHAPTER 5: NUMERICAL SIMULATIONS WITH FIXED VORTEX CORES

CHAPTER 6: NUMERICAL SIMULATION OF PARTICLE TRAJECTORIES IN GROWING VORTICES

Figures

CHAPTER 7: RECAPITULATION AND RECOMMENDATIONS

Figures

Appendices

LIST OF FIGURES

Chapter 1

Figure 9. Muller & Gyr (1986). The diagram shows the spreading angle, size and distance between pairings of vortices in a mixing layer. The initial disturbance length causes the shear layer to roll up into discrete vortices of radius r, which subsequently doubles between generations due to entrainment and pairing.

Figure 10. Lasheras & Choi (1988). The series on the left shows the visualisation of the shear layer at 5, 7.5, 10, 12.5, 15, 17.5 and 20cm downstream from the splitter plate. The series on the right are stretched to account for the camera angle. Notice the streamwise vortices that have developed in the latter frames.

Figure 11. Muller & Gyr (1986). Schematic of the three dimensional distortion of a vortex tube downstream of the crest into the classical horseshoe structure.

Figure 12. Nezu & Nakagawa (1991). The kolk and boil features postulated by Nezu & Nakagawa in increasing and decreasing stages of the tide. Notice that they show a difference in reattachment point on the stoss slope. The kolk vortex is probably the remnants of shear layer vortices from an upstream crest.

Figure 13. Nezu & Nakagawa (1991). Schematic of the growing vortex tube impinging with the free surface. This picture, though rather simple, captures the main idea that the head structure of distorted vortex tubes could rise in the flow until constrained by the free surface.

Figure 14. Grass (1974). Sand suspended by ejection events in a flat plate turbulent boundary layer. The sand visualises the coherent flow structures.

Figure 15. Grass (1974). Streamwise and vertical velocity profiles recorded by sand particles suspended by ejection events in a flat plate turbulent boundary layer. y is the height and delta is 30mm at Re=2300. u_r=34.9mm/s and the sand grain quiescent fall speed w=12.7mm/s in the mean flow velocity

U=830mm/s.

Figure 16. Thomas et al (1983). Air entrainment by a plunging water jet. The white areas are bubbles entrained into and transported by large eddies in the free shear layer.

Figure 17. Lazaro & Lasheras (1992). Air-liquid flow visualised by stroboscopic lighting shows that the water droplets (white region) are densely packed in certain regions of the mixing layer but sparse in others. The sparse area circled is a vortex in the mixing layer.

Figure 18. Tsuji et al (1987). Particle concentration distribution for gas-solid flow in a horizontal channel at 7 and 15m/s. Notice that the integral equation gives a good fit at 7m/s, at which velocity the model was correlated, but a poor fit at the higher velocity.

Figure 19. Tsuji et al (1987). The air and particle velocities as computed for the two mean stream speeds in figure 18. The error at 15m/s in figure 18 would appear to be due either to the particle model or to the use of the integral method which ignores the fluctuations from the mean that are so important for two-phase modelling.

Figure 20. Johns et al (1990). Computed and experimentally determined distributions of mean and turbulent quantities over sandwaves. a) Velocity profiles b) TKE density c) Kinetic shear stress d) Kinematic bed shear stress. The failure of this model to predict separation (as shown by poor fit in graphs b) and c) was put down to the assumption of hydrostatic pressure. Nevertheless the model was used to predict sediment transport over a series of three bedforms. Any agreement with sediment transport data must therefore be fortuitous.

Figure 21. Johns et al (1991). Computed distributions of a) turbulent energy and b) kinematic stress profiles in steady state non-hydrostatic flow over sandwaves at H=3.8m, L=20m. Compare with figure 20. The inclusion of the

hydrodynamic component of the pressure gives the required separation at the crest. The model has yet to be applied to sediment suspension modelling.

Figure 22. Schematic depicting the theoretical discretisation of the vorticity generated at a boundary wall. The dark spots represent discrete vortex elements that sum to model the effect of the diffuse vorticity cloud (shaded area). Some problems for discrete vortex modelling of free shear layers are where to place the first vortices after the salient edge and how to set criteria for the free streamline.

Figure 23. Thomas et al (1983). Bubble trajectories computed near a line vortex. Notice that a narrow band of X starting points lead to bubble capture.

Figure 24. Thomas et al (1983). Dependence of the trapping width on the vortex strength parameter for discreta with various specific gravities.

Figure 25. Thomas et al (1983). Comparison between computed and experimental trapping width with vortex strength for bubbles in water.

Figure 26. Thomas et al (1983). Examples of the developing shear layer after a splitter plate at various times, as computed using the discrete vortex method.

Figure 27. Thomas et al (1983). Computational simulation of bubble trajectories in counter-buoyancy flow (buoyancy force is right to left, flow left to right in this figure). Notice that the model allows capture of bubbles (signified by the cycloid-like trajectories). In such flows this capture delays detrainment of the bubbles into the outer flows. Compare this with the regions of high bubble voidage in figure 16.

Chapter 1: Appendix 1

Figure 1. Utami & Ueno (1987). Conceptual model of the horseshoe vortices

in the boundary layer. a) The formation and development stages (lines represent vortex filaments). b-c) Fully developed stage (vortex tubes are multiple horseshoe filament structures in a).

Figure 2. Acarlar & Smith (1987). a-b) Side view comparison between hairpin vortex and turbulent boundary layer patterns visualised by hydrogen bubbles. a) Hairpin vortex x/R=20 b) turbulent boundary layer at Re=2200. c-d) Top view comparison.

Chapter 2

Figure 1. Table of design values for flume sizing. The maximum and minimum values are desirable only. Option 4 was chosen on the basis that the available electricity system would not cope with a higher flow-rate and such a large pump would be difficult to find gratis.

Figure 2. Layout of main flume components.

Figure 3a-b. The diagrams show the construction of the flume section of the equipment.

Figure 4a-b. Inlet and suction tanks showing weir and Raschig ring packing section (shaded area).

Figure 5&6. The suction tank, pump and valve and a schematic of the suction filter.

Figure 7. Dimensions of the pilot tube used for measuring the time-averaged flow velocity.

Figure 8. Cradle supporting Pitot tube allowing both lengthwise and widthwise traverse.

Figure 9. Velocity at various locations across the stream before and after

Chapter 2: Appendix 1

Chapter 3

Figure 1. After Allen (1984). Lee slope landing sites for sediment jetting over the crest of a sandwave. Sediment is deposited further along the lee slope with higher values of U/V.

Figure 2. After Allen (1984). Widthwise dispersion of sediment jetting over the lee slope of a sandwave.

Figure 3a-j. The plates show the development of a shear layer vortex over a steep-lee-faced dune at a crest velocity of about 0.1m/s. Had the camera been slightly further to the left we would see the vortex in plate a) move off downstream.

Figure 4. The cycloid-like trajectories of two particles entrained into the shear layer and transported downstream. The crest velocity is about 0.36m/s. The bedform angle is 30 degrees to the horizontal but appears larger due to graphical manipulation.

Figure 5. The view field, positioned after the second crest (the rightmost point of the bedform above) was divided into 24, 0.012m long categories for gathering of the trajectory data, giving a total view field length of 0.29m ie 44% of bedform wavelength). Subsequent analysis used groups of three landing sites denoted by the central value in the range, ie 2,5 etc.

Figure 6. Distribution of particle landing sites of U/V=6. Most of the particles land on the lee slope within two seconds of leaving the crest.

Figure 7a-g. The seven trajectory modes for jetted particles. a) M1 b)M2 c) M3 d) M4 e) M5 f) M6 g) M7.

Figure 8. The average vertical velocity (cm/s) of particles landing at each location downstream of the crest, where X is the horizontal landing position. The particle quiescent fall speed is 3.4cm/s. It is clear that particles are

deposited at the crest regions by being thrown over the first vortex in the shear layer at a velocity higher than this fall speed.

Figure 9. The average horizontal velocity (cm/s) of particles landing at each location downstream of the crest, where X is the horizontal landing position. The figures are in cm/s for easy legibility. The mean stream speed U is 20cm/s so the particles travel with velocity far lower than this, as is expected in a region of vorticity where the vortices are travelling at about the average speed of the mean flow and recirculating flow (about half the mean stream speed).

Figure 10. Variation in percentage settling rate with distance downstream of the crest for U/V=6. The line is a least squares fit to the data, excluding the leftmost point (as Allen found, the deposition near the crest is low compared to further downstream because the particles are jetted at the stream velocity in fixed bedform tests). The logarithmic fit compares well with that of Allen (1984).

Figure 11. Comparison between our data at U/V=6 (dotted) and that of Allen (1984). The fit is good except at the outer regions where our data shows higher values due to sediment returning to the lee slope through trajectory modes M3-M5 which are presumably excluded from Allen's data set.

Figure 12. Comparison between the deposition data gathered for three runs where U/V is about six. The similarity between the figures for each mode encourages us to choose a scaling based on U/V rather than the individual values of U and V.

Figure 13. Relative concentrations of particles at each horizontal location at U/V=6. The peaks along the line of the shear layer show its crucial role in sediment suspension. The bedform image (grey) overlaps into the graph to show the orientation of the concentration lines in space.

Figure 14. Table showing the relative sediment deposition through modes M1-M7

at various values of U/V from 2.7 to 12.8. Higher U/V leads to lower lee slope and higher stoss slope deposition rates.

Figure 15. The data in figure 14 is plotted above as the sum of the deposition figures for modes M1-M5 (which are the ones where sediment returns to the lee slope) against U/V. Higher values of U/V lead to sediment being stripped from the bedform and moved downstream.

Figure 16. Distribution of particle landing sites when U/V=9. Most of the particles settle within 2 seconds, on the lee and lower stoss slopes.

Figure 17. Particle concentration diagram for U/V =9. Notice the greater spread of the distribution compared to figure 13.

Figure 18. The table shows the percentage difference between the concentration recorded for two sets of 100 particles at U/V=9. This is a direct measure of the convergence of the statistics for 100 particles and a pessimistic measure for 200 particles. The data is certainly not converged in the outer flows where few realisations are made, but is fair close to the lee slope. H and S refer to the figure above.

Figure 19. Distribution of particle landing sites for U/V=10.8. Notice the more even spread over the bedform than in figure 6.

Figure 20. Comparison between our data at U/V=12.8 (dotted) and Allen's data at U/V=14.4. Compare with figure 11.

Figure 21. Concentration distribution for U/V=12.8. Notice that sediment is dispersed over a greater depth of the flow compared to figures 13 and 17 (at lower U/V).

Figure 22. Percentage of particles taking each of the trajectory modes 1-7 at various U/V from 5.7 to 12.8. The peak at M4 is artificial because it covers a greater stoss slope length than the other modes. M4 is a pivotal

mode since the number of particles deposited after following M4 changes only slightly with U/V, unlike the other modes

Figure 23. Parameters in the log fit $S=bX^m$ where X is the downstream distance and S the sedimentation rate at point X relative to the total sedimentation rate. The parameters in the fit follow a roughly linear ratio with U/V with a good fit at the higher values.

Figure 24. After Atkins & Soulsby (1992). Suspended sediment size distribution after a river Taw sandwave. The sediment size is between about 100 and 400 microns.

Figure 25. The Interactive Fraction for the four data bands of Atkins & Soulsby (1992). For band 1, particles with diameters between 0.40 and 0.17 form the FI and are neither all deposited on the lee slope nor all swept downstream to the next bedform.

Figure 26. The table shows how our deposition data can be applied to a data set to predict, knowing the jetted sediment size distribution, the proportion of jetted sediment moving to the downstream bedform and beyond.

Chapter 4

Figure 1. Inspired by Wille & Fernholz (1965). The upper picture shows the jet attached to the trailing flap due to restriction of the entrained flow shown in the bottom picture. Here the trailing flap makes a larger internal angle with the jet and the shear layer is not drawn to the surface.

Figure 2a-g. The Coanda-flapping event at a flow speed of 0.60m/s (Froude No.=0.6). In frame b) we see an increase in vertical velocity just after the crest (flow right to left) and a region of circulation comparable in height to the height of the bedform which is swept from the view field by frame g).

Figure 3a-j. The plates show particles transported by periodic flows caused by Coanda-flapping of the free shear layer. The particles (light spots on centreline, dark spots just off centre-line of the rig) have a fall speed of 0.034m/s and the depth-averaged flow speed is 0.31m/s.

Figure 4. The plates show three views of the recirculation region behind an experimental bedform. The shots are 0.35 sacs. apart and clearly visualise the sweeping away of the turbulent region, leading to re-attachment close to the trough. We term this sequence of events Coanda-flapping.

Figure 5. Intervals between Coanda-flapping events, between the passage of strong shear layer vortices (SLVs) and between other turbulent events at U=0.20m/s. There is a strong correlation between the Coanda-flapping events and the passage of upstream turbulent events.

Figure 6. Intervals between Coanda-flapping events and between the passage of turbulent events, including shear layer vortices, at U=0.31m/s. This highlights the fact that not all upstream turbulence can trigger the Coanda-flapping event.

Figure 7. The intervals between Coanda-flapping events and between strong shear layer vortices at U=0.36m/s.

Figure 8. The intervals between Coanda-flapping events at various values of inter-crestal spacing L-nLo where n=1.0, 1.5, 2.0, 2.5, 3.0 at U=0.43m/s. Notice the peak occurs in the 2.5s interval range for L=3.0Lo rather than the 1.5s interval range.

Figure 9. The interval(s) between Coanda-flapping events plotted against the cumulative sum of the intervals for inter-crestal spacing L=Lo. The point with the lowest gradient is the modal interval which can be seen on the graph below, indicated by the dotted lines.

Figure 10. The gradient of the line in the above figure averaged over eleven neighbouring points so as to remove the peaks and troughs where only two or

three intervals are similar in value and simultaneously highlight the lowest gradient over a small interval range. The modal value occurs between interval sum of about 20 and 60s, corresponding to 0.9-1.3s on the graph above.

Figure 11. The modal intervals between Coanda-flapping events at various values of inter-crestal spacing from $L=L_0$ to $L=3.0L_0$. At increased crest separation the interval between Coanda-flapping events is seen to double, consistent with the theory that they are triggered by the passing of shear layer vortices. The percentage figure above the line represents the percentage of all measured intervals that fall within this range, whereas the percentage figure below the line represents the percentage of events we would have expected to find in this range if the data was evenly spread over the entire range 0-6.5s(we only show 0-5s here).

Figure 12. The concentration distribution due to lee slope suspension of particles by Coanda-flapping flows at U=0.20m/s. The grey region represents the bedform and is added to aid positioning of the concentration lines in space.

Figure 13. The concentration distribution due to lee slope suspension of particles by Coanda-flapping flows at U=0.31m/s.

Figure 14. The concentration distribution due to lee slope suspension of particles by the Coanda-flapping and lee-shear capture at U=0.36m/s.

Figure 15. The concentration distribution due to lee slope suspension of particles by the Coanda-flapping and lee-shear capture
at U=0.43m/s.

Figure 16. A cloud of particles with quiescent fall speed V=0.06m/s suspended from the stoss slope at a flow speed of U=0.36m/s. The flow is from right to left.

Figure 17. After Soulsby (1989). The shape of a cloud of sediment downstream

of a sandwave crest in the estuary of the river Taw, Devon, England. The flow is left to right, z is height, U current velocity and x horizontal length scale.

Chapter 5

Figure 1. Trajectories (light circles) computed for neutrally buoyant particles a) Inside and b) Outside a Rankine vortex core (heavy circles) to check the validity of the model and the time-step chosen.

Figure 2. The effect of varying starting velocity on particle trajectory. Particle quiescent fall speed is 0.5m/s and initial vertical velocity is a) 0.2m/s b) 0.0m/s c) 0.05m/s d) 0.3m/s. This extreme example shows the sensitivity of the results to the initial conditions.

Figure 3. The trajectories of particle falling near a Rankine vortex core. Here the initial vertical and horizontal velocities are set equal to the local fluid velocity which produces a consistent set of trajectories, unlike those in figure 2.

Figure 4. Varying the particle fall speed for a Rankine core of radius 0.006m and angular speed 100rad/s. The particle quiescent fall speed (m/s) is a) 1 b) 0.6 c) 0.5 d) 0.4 e) 0.35 f) 0.3 g) 0.25 h) 0.2 i) 0.1 j) 0.09 k) 0.07 l) 0.05. The core rotates anticlockwise and the bent trajectories in b and c are due to the local pressure gradient acting towards the centre of the core. The pressure gradient and fluid drag are responsible for transporting the particle around the vortex in k and l.

Figure 5. Effect of varying the particle fall speed on the time taken for the particle to fall to a distance of 5 radii below the core centre (the letters refer to the trajectories shown in figure 4 where they appear in lower case). Notice the low level peak for trajectory d where the particle follows a convoluted path through the vortex core.

Figure 6a-d. Particles falling away and being captured from various starting locations below a Rankine vortex core. a) and c) show the trajectories for particles starting 2 radii below the core mid-plane whereas d) shows the trajectories for starting points four radii below the core where no particles are lifted over the core. b) Shows the relative fall time for each trajectory, which is the actual fall time less the time it would have taken to fall the same vertical distance in quiescent fluid.

Figure 6e-h. The vector force acting on the particle for the first four trajectories in figure 3.10c. Thin solid line=pressure gradient and fluid acceleration, thick line=drag and dashed line=buoyancy.

Figure 7a. Trajectories of particles falling from 3 radii above a vortex core. Trajectory marked *__* falls this vertical distance in the same time as in the absence of the vortex.

Figure 7b. Selected key trajectories from figure 7a.

Figure 7c. The relative fall time distribution for the particles shown in figure 7a. The first peak is caused by trajectory A in figure 7b, the second by trajectory D and the third by trajectory F.

Figure 7d-e. The vector forces acting on the particle at various points along trajectories B and C. The red line=fluid and pressure gradient force, yellow=constant buoyancy force and blue=drag force. The long red lines demonstrate graphically the importance of the instantaneous fluid and pressure gradient forces when compared with the buoyancy force.

Figure 7f-g. The temporal fluctuations in the magnitude of the forces in the horizontal and vertical directions respectively on a particle falling along trajectory C in figure 7b. The pressure and fluid gradient forces pull the particle to the right as it approaches the core. The buoyancy force is constant at -2.31.

Figure 7h-i. The temporal fluctuations in the magnitude of the forces in the horizontal and vertical directions respectively on a particle falling along trajectory D in figure 7b. The pressure and fluid gradient forces pull the particle to the right as it approaches the core, producing the second peak in figure 7c.

Figure 7j. The temporal fluctuation in the magnitude of the particle and fluid velocities in the core region for a particle falling along trajectory D in figure 7b. The lift force component in the vertical direction changes sign at around the vortex mid-plane because the difference between the horizontal fluid and particle velocities changes sign.

Figure 7k. The temporal fluctuations in the magnitude of the horizontal and vertical components of the lift-force due to the change in relative fluid-particle horizontal velocity shown in figure 7j.

Figure 7l. The relaxation time between the particle and fluid horizontal velocities for a particle following trajectory D. The particle's inertia prevents instantaneous response to spatial changes in the fluid velocity in this steady flow.

Figure 7m. The vector forces acting on the particle at various points along trajectory E.

Figure 7n. The temporal fluctuations in the magnitude of vertical components of the forces acting on a particle falling along trajectory F in figure 7b. The third peak forms on figure 7c because the particle reaches the cusp point where it is virtually stationary for an extended period.

Figure 7o. The sum of the forces balances the buoyancy force on the particle at the cusp point.

Figure 8a. Graph of the critical particle terminal fall speed for a range of core sizes. A particle with terminal fall speed less than this critical value will not enter the core from any starting location.

Figure 8b-e. The diagrams show the similarity in trajectory plots for particles with various fall speeds near a 5mm Rankine core. The four cases correspond to the triangles in figure 8a.

Figure 9a-c. The above plates show the effect of keeping the velocity at the core radius constant whilst increasing the core size. The graph on the right shows the fall time for each of the trajectories in the picture on the left.

Figure 10. The pictures show a) a particle that is not captured by the core, b) a particle that is captured and c) a particle that is just captured. The value of AR/V_T here is the criterion C below.

Figure 11. Values of the capture criterion C for various values of (X,Y), the particle starting position at initial velocity $(V_X,V_Y)=(0,0)$.

Figure 12. Variation of the critical vortex strength criterion C AR/V_T with vortex radius R at constant vortex tip speed AR.

Figure 13. Time-averaged horizontal velocity induced below the mid-plane of a moving Rankine vortex over 100 time-steps.

Figure 14. Time-averaged vertical velocity induced below the mid-plane of a moving Rankine vortex over 100 time-steps.

Figure 15. Time-averaged horizontal velocity induced below the mid-plane of a moving Rankine vortex over 10 time-steps.

Figure 16. Time-averaged vertical velocity induced below the mid-plane of a moving Rankine vortex over 10 time-steps.

Figure 17. Time-averaged and time-dependent trajectories of a particle in a moving Rankine vortex. The trajectories in the time-averaged flows are

inclined downwards whereas the time-dependent trajectory follows a near cycloid path.

Figure 18. Table of maximum fluctuating velocities u,v=f. Johns (1991) prescribes u=E and v=0.35E where E is the turbulence energy density in $(m/s)^2$ which has a peak value 0.018. We then assume a sinusoidal distribution for the fluctuating parameters which classically gives $(f^2)max = 1.414(f^2)mean$. Data from Nakagawa & Nezu (1987) gives u,v directly.

Chapter 6

Figure 1. Schematic of the shear layer that develops after the crest of a sandwave with oncoming mean flow U. The first generation vortices form at a distance d_0 downstream of the crest with a radius R_0. Two such vortices pair, after travelling a distance x, forming a second generation vortex with double the length scale and hence half the vorticity (circulation/area).

Figure 2. The parameter space diagram for a particle of quiescent fall speed V=0.076m/s at a vortex growth rate G=0.01m/s. The pictures A-F show the particle trajectories, in a frame of reference moving with the vortex, at the point in parameter space where the centre dotted circle (core radius) lies. The vortices rotate in an anti-clockwise direction. Below the low (L) and high (H) values of A, at one specific radius, the particle trajectory contains a number of loops (the capture trajectories).

Figure 3. Seven trajectory plots corresponding to the points in parameter space marked by the circles in figure 2. G&H correspond to trajectories in the particle dominated region whereas K,L & M correspond to three in the fluid dominated region. I & J are capture trajectories seen in the central region of the parameter space where neither fluid forces nor gravity is dominant.

Figure 4. An example of the internal structure within the region of parameter space enclosed by the heavy lines in figure 2. The number on each line corresponds to the number of times that the particle loops up to the

Chapter 7

starting position (X,Y) at zero initial particle velocity.

Figure 5. The parameter space diagram for a particle of quiescent fall speed V=0.076m/s at a vortex growth rate G=0.01m/s. The pictures A-F show the particle trajectories, in a frame of reference moving with the vortex, at the point in the parameter space where the centre dotted circle (core radius) lies. The vortices rotate in an anti-clockwise direction. Below the low (L) and high (H) values of A, at one specific radius, the particle trajectory contains a number of loops (the capture trajectories).

NOMENCLATURE

Chapter 1

a	Particle diameter (m)
A	Bubble trapping width (m)
A_n	Notational area of nth generation vortex (m^2)
A^*	Bubble trapping width (-)
C^*	Vortex strength parameter (-)
d	Thickness of shear layer at point of separation (m)
Fr	Froude number (-)
g	Gravitational acceleration (m/s^2)
h	Flow depth (m)
H	Dune mean crest height (m)
L	Dune mean wavelength (m)
L'	Length scale (m)
q	Velocity vector (m/s)
r_n	Notional radius of nth generation vortex (m)
t	Time(s)
u	Local fluid velocity (m/s)
U	Depth-averaged flow velocity (m/s)
U_*	Friction velocity (m/s)
v	Particle velocity (m/s)
V_T	Particle quiescent fall speed (m/s)

W'	Velocity scale (m/s)
X	Downstream distance (m)

α	Shear layer spreading angle (degrees)
Γ	Circulation (m^2/s)
δ	Viscous sublayer thickness (m)
λ_n	Notional wavelenth of nth generation vortex (m)
ν	Kinematic viscosity (m^2/s)
ρ	Fluid density (kg/m^3)
τ_0	Bed shear stress (N/m^2)
ω	Vorticity (s^{-1})
$\underline{\Omega}$	Circulation (m^2/s)

Chapter 2

D	Flow depth at crest (m)
DP	Pressure difference (Pa)
Fr	Froude number (-)
h	Bedform crest height (m)
U	Depth-averaged flow velocity (m/s)
u	Local flow velocity (m/s)
g	Gravitational acceleration (m/s^2)
L	Bedform length (m)
L_{DEV}	Flow development length upstream of working section (m)
L_R	Flume length (m)
W	Flume width (m)

ρ	Fluid density (kg/m^3)

Chapter 3

C	Concentration of particles (-)
C_i	Concentration of particles in mesh square i (-)
C_0	Total particle concentration in mesh (-)

d	Sand grain diameter (m)
F_i	Number of footprints left by a particle in square i (-)
FI_0	Grain size where U/V=7 (m)
L	Mesh square length (m)
m	Exponent in fitting equation (-)
N_i	Number of particles passing through mesh square i (-)
N_0	Total number of particles passing through mesh (-)
S	Local deposition rate (-)
S_T	Total deposition rate (-)
t	Time step (s)
U	Free stream velocity (m/s)
V	Particle quiescent fall speed (m/s)
V_{P0}	Mean velocity of particles in mesh (m/s)
V_{Pi}	Mean velocity of particles in mesh square i (m/s)
X	Downstream location (m)

Chapter 4

L	Time-averaged length of separation bubble (m) and Inter-crestal spacing (m)
L_0	Bedform length (m)
U	Depth-averaged flow velocity (m/s)
V	Particle quiescent fall speed (m/s)

Chapter 5

A	Rankine core angular speed (-)
C	Criterion for particle capture (-)
C_{MIN}	Minimum of graph C vs X_{SL} (-)
C_L	Coefficient of lift (-)
C_{VM}	Coefficient of virtual mass (-)
D	Translation distance (m)
f_{MAX}	Maximum fluctuation in horizontal or vertical velocity (m/s)
$\underline{F}$	Force on spherical body (-)

g	Gravitational acceleration (-)
H	Bedform crest height (m)
K	Turbulent Kinetic Energy (m^2/s^2)
r	Particle radius (-)
R	Rankine core radius (m)
t	Time (-)
T	Time (-)
T_{ND}	Particle fall time less T_Q (-)
T_Q	Equivalent time to fall same distance in quiescent liquid (-)
$\underline{u}$	Local liquid velocity (-)
U_{MAX}	Maximum U (m/s)
U_X	Horizontal component of fluid velocity (-)
U_Y	Vertical component of fluid velocity (-)
$\underline{v}$	Particle velocity (-)
V_T	Quiescent fall speed of particle (m/s)
V_{TA}	Apparent slip speed of particle (m/s)
V_{Tcrit}	Critical V_T for entry into the core (m/s)
V_X	Horizontal component of particle velocity (-)
V_Y	Vertical component of particle velocity (-)
$\underline{w}$	$\underline{v}-\underline{u}$, particle slip speed (-)
X	Horizontal location (-)
X_{SL}	Horizontal starting location (-)
X_{SL0}	X_{SL} where $V_T=V_{TA}$ (-)
Y	Vertical location (-)
$\rho_{P/L}$	Particle/fluid density (kg/m^3)
ω	Vorticity (s^{-1})

Chapter 6

A (A_0)	Rankine core (initial) angular speed (rad/s)
$A_{L/H}$	Low/high limit values of A_0 at any R_0 for capture region (rad/s)
d_P	Sand grain diameter (m)
d_0	Distance from crest of first generation incipient vortex (m)

G	Vortex core growth rate (m/s)
k_{1-3}	Constants in fit to data (-)
K	A constant (-)
L	Length scale (m)
n, m	Exponents in fit to data (-)
R (R_0)	Rankine core (initial) radius (m)
R_i	Notional radius of vortex generation i (m)
R_P	Particle radial distance (m)
St	Stokes number (-)
Δt	Time step (s)
$\bar{u}$	Velocity scale (m/s)
u_0	Vortex Eulerian velocity (m/s)
U	Mean stream speed (m/s)
ΔU	Velocity difference across shear layer (m/s)
V	Quiescent fall speed of particle (m/s)
X	Downstream distance (m)

α	Shear layer half angle (degrees)
Γ (Γ_0)	Circulation (initial) (m^2/s)
δ	Shear layer width (m)
μ	Fluid dynamic viscosity (Pas)
ρ_P	Particle density (kg/m^3)
ω	Vorticity (s^{-1})

Chapter 7

A	Vortex angular speed (rad/s)
R	Vortex core radius (m)
U	Depth-averaged flow speed (m/s)
V_T	Particle quiescent fall speed (m/s)
V_X	Horizontal component velocity (-)
V_Y	Vertical component velocity (-)
X	Horizontal location (-)
Y	Vertical location (-)

CHAPTER 1: LITERATURE SURVEY

SUMMARY

Bedform undulations formed by unidirectional flows over sandy beds are categorised and dunes are discussed in detail. Flow over dunes is dominated by the separated shear layer in which discrete vortices grow by entrainment and pairing. We discuss the interaction of these vortices with sand particles, making comparisons with similar interactions exhibited by other discrete elements such as bubbles and particles in shear flows.

Modelling methods employed have generally been based on either integral approaches or two equation turbulence models using Reynolds averaged equations. As explained in our proposal for this PhD study (Thomas, 1990 and appendix 2), these strategies sacrifice the very flow features responsible for exciting the sediment motions. Workers in allied fields, particularly in bubble dynamics, have used models (eg Sene et al, 1993) which account for the structural features embedded in the mean flow field by using calculations based on discrete vortex models. Application of this modelling methodology to sandwave dynamics offers an appropriate alternative to the methods reviewed here.

1 INTRODUCTION

Sand forms the bottom boundary of many rivers, estuaries and coastal waters. Where this is the case, there are invariably bottom undulations ranging from centimetres to tens of metres in height (Allen, 1984). Factors determining this topography include the flow depth, current strength, the grain size and the grain size distribution. These undulations were generically termed *sand waves* by Yalin (1972), incorporating such specific cases as ripples, dunes and antidunes (Engelund & Fredsoe (1982) as shown schematically in figure 1 and discussed in section 2. Other authors, for example Raudkivi (1967), have used the term 'sandwave' to describe more specifically long wavelength, (flatter) dunes. This confusion in terminology is also discussed in section 2. We make the distinction that *sand waves* are the generic grouping and *sandwaves* are bedforms occupying a significant fraction of the flow depth (ie distinguished from ripples) where the Froude number (defined in section 2) is less than 1 (ie not antidunes).

Literature produced over the last century on these bottom features is briefly reviewed below. Extensive accounts have been given by, for example, Dyer (1986), Allen (1984), Stride (1982), Yalin (1972) and Raudkivi (1967). Sandwave studies were traditionally based upon physical observations relating to wave growth, decay, propagation rates and morphological evolution. More recent literature has concentrated on the fluid interaction mechanics of these two-phase systems, which generally incorporate a zone of convergent flow followed by a recirculation zone overlaid by a free shear layer, as idealised in the backstep shown in figure 2 (Simpson, 1989). Recent application of quantitative flow visualisation techniques (Muller & Gyr, 1986) has begun to reveal the underlying mechanisms, but precise links to the suspension mechanisms has been given little detailed attention to date.

Section 2 below briefly reviews main classes of sand waves found in the river environment. However, as our main interest lies in details of the flow interaction with sand particles on crested bedforms, section 3 concentrates on these aspects. Section 4 outlines current calculation methods and relevant modelling techniques (which have yet to be systematically applied in this field).

2 CLASSIFICATION OF SAND WAVES

There are excellent general texts (recall section 1) on bedforms in uni- and multi-directional flows, but our interest here is confined to uni-directional flows. Raudkivi (1967) stated that above a threshold flow velocity particles in a loose granular boundary are transported at a rate which increases rapidly with increasing flow speed. Such beds usually exhibit the transverse wavy features depicted in figure 1. Quantitative classification of these different behaviours has traditionally been in terms of the non-dimensional Froude number Fr, defined as

$$Fr = \frac{U}{\sqrt{gh}}$$

where U is the depth-averaged velocity, g is gravitational acceleration and h the flow depth. Allen (1984) asserted that, for subcritical flow (Fr<1), the sand waves can be classified into two types: namely, *current ripples and dunes*. On the other hand, for supercritical flow (Fr>1), the sand waves are termed *antidunes*. Further classification has been with reference to classical turbulent boundary layer modelling in terms of the viscous sublayer thickness δ, commonly (Engelund & Fredsoe, 1982) represented as

$$\delta = 11.6\frac{\nu}{U_*} = 11.6\frac{\nu}{\sqrt{\tau_0/\rho}}$$

where U_* is the friction velocity, τ_0 the bed shear stress, ρ the fluid density and υ the kinematic viscosity. δ thus provides a scale ratio against some measure of the sediment particle diameter. Indeed, Simons & Richardson (1961) asserted that ripples form when a viscous sublayer is present (ie hydraulically smooth conditions), providing that a threshold of particle motion is exceeded whereas sandwaves form when the bed is hydraulically rough, that is, for particle diameters exceeding several δ's. These different bedforms are discussed below.

2.1 Current Ripples

Current ripples (figure 3) are generally found with the finer grades of quartz sand, typically less than 0.125 mm diameter. However, they are also known to exist with 0.5 mm quartz sand (RJS Whitehouse, private communication). These features are transverse ridges with steep downstream (*lee*) slopes and shallower upstream (*stoss*) slopes. Their height is invariably less than 40 mm and their wavelength less than 600 mm ie, very small compared to typical scales of the flow. Ripples migrate downstream at velocities which are small compared with the stream velocity (Yalin, 1972). Sediment is eroded from the stoss slopes and deposited on the lee slopes (shown schematically in figure 4). Thus, each grain travels intermittently and is then buried (Raudkivi, 1967).

2.2 Dunes/sandwaves

Dunes (figure 5) (equivalent to sandwaves in our terminology) also migrate downstream at speeds which are small compared with the mean flow speed. They are much larger than current ripples - reportedly reaching up to 20 metres in height and 1000 metres in length with straight crests as much as 40 miles long (Raudkivi, 1967). Such dunes have roughly triangular longitudinal profiles, as depicted in figure 4. Their lee slopes subtend angles less than 35 degrees to the horizontal, approximately the angle of repose for quartz sand, with stoss slope angles less than 5 degrees to the horizontal.

The wavelengths of dunes primarily depend on flow depth and velocity, with a weak dependence on grain size. Allens' (1984) correlation from 24 data sources (figure 6) of dune mean wavelength L versus water depth h shows wide scatter around L/h=5, with individual systems giving positive, negative or zero correlation. Correlation of mean crest height H against water depth h (figure 7) gives the best-fit value suggested by Yalin (1964): namely, H/h=0.167. Grain size has only a secondary influence on both height and length of dunes, generally accepted as practically insignificant (Yalin, 1964).

2.3 Antidunes

Antidunes, as found in supercritical flow, are bed waves of near-sinusoidal streamwise profile which are usually in phase with surface waves, as in figure 1. They can migrate downstream, be stationary, or migrate upstream according to relative rates of scouring and deposition on the lee and stoss slopes (Yalin, 1972). For further discussion, refer to texts cited in section 1.

2.4 Sandwave terminology

Sandwaves arise in environments where the ratio of flow breadth to depth is large. This geometry offers much scope for irregularities in sandwave shape because even notionally steady flows are seldom if ever spatially uniform across the breadth of rivers and seas. Though superficially different in appearance there is no evidence to suggest that their formation mechanisms are different. Accordingly, we choose not to distinguish between these different morphologies in the present classification. However, we note that dunes are distinguished in two categories, as discussed by Allen (1984). The first category relates to more three dimensional dunes with steeper lee faces, termed megaripples, simple dunes, dunes or sandwaves. The second category relates to flatter dunes, straighter crested with longer wavelengths and traditionally termed sandwaves, rippled sandwaves, diminished dunes, scaloid sandwaves and transverse bars or bars.

3 THE FLOW OVER SANDWAVES

The main features of flow over a sandwave comprise boundary layer separation at the crest, shear layer growth, reattachment in the trough and establishment of a new boundary layer on the stoss slope, all as included schematically in the back step flow of figure 2. Here we discuss the shear layer and the interaction of its embedded vortices with sediment particles viewed as a discrete second phase in the style of literature on the dynamics of multiphase flows. Discussion of boundary layer aspects appears in appendix 1.

3.1 The Shear Layer

The stoss boundary layer separates from the bed at the crest, where the vorticity generated on the upstream boundary becomes detached and then confined within a free shear layer between the outer flow and the inner recirculation region. This 'feeding sheet' is unstable and rolls up to produce uni-directional eddies as clusters of vorticity (Muller & Gyr, 1986). The nature of the initial instability and the vortex growth rate is discussed below, as are the spreading angle of the shear layer, the spanwise distortion of the primary vortex elements and, finally, the interaction between these vortices and the downstream bedform.

a) Initial Instability and Shear Layer Growth. As noted by Muller & Gyr (1986), the boundary layer upstream of the crest contains decaying relics of the shear layers from sandwaves and ripples further upstream. It separates at, or near, the sandwave crest depending upon the local pressure excursions, which are either fluctuating or mean gradients caused by the relics or by free surface or internal waves (NH Thomas, private communication). Whatever the details, the free shear layer thus formed is typically unstable to Kelvin-Helmholtz amplification (Lamb, 1932) of any small perturbations such that the feeding sheet rolls up into localised vortices which interact with each other forming larger (paired) structures downstream.

Freymuth (1966), reported highly regular vortex motions in the nonlinear transition of a laminar free shear layer, such that uni-directional vortices rotated around a common axis before coalescing to produce a single vortex, an example of which is shown schematically in figure 8 (from Jiminez, 1980). Brown &

Roshko (1974), observed that a turbulent mixing layer also contains large-scale spanwise vortex motions which persist in the presence of smaller scale turbulence. Winant & Browand (1974) went further in reporting that vortex pairing was the main mechanism behind shear layer growth at low Reynolds numbers. Brown and Roshko found the same process to be equally important at high Reynolds number. Dimotakis & Brown (1976) found this behaviour to be a dominant feature even at Reynolds numbers of 10^7. As detailed above, Hernan & Jiminez (1982) found that fluid is engulfed during pairing and is entrained by the vortices between pairing, typically with most of the growth occurring by entrainment rather than engulfment. A comprehensive study of the entrainment phenomenon by Panides & Chevray (1990), identified key elements of the mechanisms from simultaneous flow visualisation and one point two-component laser doppler anemometry. Ho & Huerre (1984) indicated that not only pairing interactions may occur, but also three-fold interactions or higher order events, especially for locations close to the initial instability.

b) Spreading angle and three dimensional instability. Muller & Gyr (1986) used an analysis by Jiminez (1980) to calculate the spreading angle of the shear layer. Jiminez found (figure 9; from Muller & Gyr, 1986) that the ratio of the area A_n of vortices of neighbouring generations was about 4 giving a ratio of 2 for the linear scale since

$$A_{n+1}/A_n = \underset{\text{pairing}}{2} \times \underset{\text{entrainment}}{1.75} \times \underset{\text{engulfment}}{1.17} = 4.1$$

The vortex radius r_n and apparent wavelength λ_n for generations n to n+1 are related according to the simple formula:

$$r_{n+1}=2r_n=2^n r_0, \quad \lambda_{n+1}=2\lambda_n=2^n\lambda_0$$

A simple analysis then gave the spreading angle α as

$$\alpha=2\tan^{-1}\left[\frac{\sqrt{\frac{d}{\pi\lambda_0}}}{1.6}\right]$$

here with d as thickness of the initial vortex sheet (undefined).

Konrad (1976) reported three dimensional instabilities manifested as axially oriented counter-rotating vortex pairs on the braidings between the primary vortices, as shown in figure 10 (from Lasheras & Choi, 1988). Bernal (1981) confirmed these were indeed streamwise vortices, comparable with Townsend's "horseshoe" structures (Townsend, 1976). Lasheras & Choi (1988) created stable two-dimensional laminar shear layers in water to which they introduced small regular perturbations using a horizontal, sinusoidally indented splitter plate. Their visualisations showed that formation of the streamwise counter-rotating pairs does not significantly interfere with the formation of spanwise vortices. One such visualisation, presented in Figure 10, showed how the streamwise pairs channel the faster stream fluid into the slower stream, also that their spacing is less than oppositely oriented pairs channelling the slow stream fluid into the faster stream. They also found that the streamwise vortices align with the direction of the maximum strain introduced by the primary vortices, such that spanwise manifestations in the primary vortices will tend to produce secondary structures which follow the local direction of maximum stress. We might reasonably expect this behaviour to be manifested with the curved crests of sinusoidal sandwaves found in estuaries. The term 'strain-oriented' is more appropriate than the term 'streamwise' here, as indeed had been recognised by Townsend (1976). The effect of these secondary vortices is unclear, but Muller & Gyr (1986) reported bending of the primary vortices into horseshoe vortices (figure 11), an evolution due to the strain-oriented vortices (Townsend, 1976).

c) **Vortex-bed interactions.** Development of the shear layer in sand dune systems is checked by proximity of the adjoining boundary of the downstream sandwave and the free surface. Impingement of the vortex structures on the reattachment is also a complicated and ill-understood system. Jackson (1976) reported surface ordered motions of two to four metres diameter that raised the water surface up to 10 cm and persisted for as long as 20 seconds in the Lower Wabash river, Illinois. He termed these events boils, and attributed them to one metre high sandwaves in the five metre deep water. Jackson invoked the loosely defined 'Kolk' vortex which is presumed to consist (figure 12; from Nezu & Nakagawa, 1991) of vertically oriented vortices of low strength and about one tenth the boil in diameter, collected into a vertical tube (by analogy with the slowly rotating 'sand devils' seen in deserts).

Recent work by Nezu & Nakagawa (1991) has helped to clarify the mechanisms behind boil formations in steady and unsteady flow. They defined a so-called "boil of the first kind" as a direct surface manifestation of primary shear vortices which have grown to fill the depth of flow and are constrained by the free surface as indicated in figure 13. Horseshoe vortices (figure 11), caused by three dimensional instabilities discussed above, channel fluid from below the vortex upwards to the free surface. This fluid may well contain suspended solids entrained into the horseshoe vortex during its impingement on the stoss slope of the downstream sandwave, and this would account for high sediment concentrations seen in boils of relatively low intensity (Jackson, 1976). Other weak boil structures identifed by Nezu and Nakagawa are not considered further here.

3.2 Vortex-particle interactions

Numerous studies have been conducted on the dynamic interactions of discrete elements and vorticity, usually with the conclusion that this aspect is vitally important to a proper description of sediment transport. Grass (1974) studied sand motion in boundary layers using high-speed movie film from which he produced pictures of sediment laden horse-shoe vortices (figure 14). He presented convincing evidence of particle entrainment and transport within migrating vortex loops and also estimated the particle ejection velocities presented in figure 15. These velocities were found to be lower than the overall mean stream velocity which is consistent with the notion of particle ejection from low momentum fluid and now identified quite precisely with the boundary layer ejection mechanism (see appendix 1).

Jackson (1976) observed sand up to 1% by weight in the highly vortical boils behind river dunes, again focusing on the crucial role they played in sediment suspension. Studies undertaken by Sleath (1982), Tunstall & Inman (1975) and Ikeda & Asaeda (1983) all showed that high-vorticity regions shed periodically from crests in oscillatory flows were also responsible for sediment suspension and transport. It is worth remembering here that bubbly flows also manifest comparably high correlations of vorticity and discrete phase transport. Thus, Thomas et al (1983) discussed mechanisms of entrapment of bubbles by transient large eddies, and described dynamic equations for bubble transport by such features with special reference to plunging jet flow as shown in figure 16. The bubbles here accumulate in discrete clusters along the edge of the submerged jet, clear evidence of the important role played by the vorticity. We return to this discussion in section 4.

As another example of the general underlying principles, Lazaro & Lasheras (1992) investigated the entrainment of water droplets (from mist generators) travelling in turbulent, plane mixing layers. The instantaneous particle distribution field comprised large, evenly spaced streaks enclosing areas of very low particle concentration (figure 17). The low concentration areas were identified with the cores of vortical structures which contained quantities of finer particles, whereas the larger particles were found in the outer streaks.

4 MODELLING TWO-PHASE TURBULENT TRANSPORT

Appendix 2 (Thomas, 1990) outlines our starting hypothesis for consideration of bedform dynamics. Essentially we are proffering a modelling hypothesis to account for high sediment concentrations above the trough at the height of the sandwave crest, as observed by Atkins & Soulsby (1992). Wider considerations such as experimental and field studies (eg West et al, 1990; Hill et al, 1988) have generated data sets useful for semi-empirical modelling for every conceivable application from wave-induced suspension to bridge pier, sea bed pipeline and oil platform leg scour (Whitehouse, 1992). Also, there have been numerous studies using engineering codes calibrated against laboratory and field studies for the prediction of, for example, flat bed suspension profiles (Mclean, 1991, van Rijn, 1985, Celik, 1982) and channel degradation by scour (Phillips & Sutherland, 1986). Also, semi-mechanistic models for threshold pick-up (eg van Rijn, 1984; de Ruiter, 1982; Grass, 1982; Fleming & Hunt, 1976). This contextual work is not reviewed in detail since from the outset our study was prescribed to address and incorporate the wider literature on free shear/particle interaction modelling. We do, however, review Johns et al's (1990) model of crest sediment flows and transport because of his direct comparison with Atkins & Soulsby's (1992) field data. Johns et al's modelling methodology is discussed against a wider background of general Eulerian and Lagrangian approaches.

All practically relevant bedform flows are turbulent and so direct Navier-Stokes modelling is computationally impossible because turbulent motions exist on scales down to at least 1/1000th of the mean flow scale. Clearly then, in the order of at least 10^9 grid points would be necessary to capture the whole flow in three dimensions, and this is still beyond the capability of even the largest of supercomputers. The modelling methods which have been most frequently employed are either Eulerian or Lagrangian, as reviewed sequentially below.

4.1 Continuous phase Eulerian modelling

The current strategy for single phase flows involves Reynolds averaging of the equations over time scales which are long compared with all of the turbulent motions. As outlined in appendix 3, this procedure gives a set of equations describing the mean fields of velocity and pressure, etc. However, due to nonlinearity of the equations, Reynolds averaged equations contain undefined terms representing the eddy fluxes of momentum, heat and mass, and these eddy fluxes have then to be prescribed either empirically or heuristically (Rodi, 1979). Such closures have been adopted in terms of integral or field schemes as discussed below.

a) Integral closures. These methods rely on the assignment of empirical profiles for the turbulent fluxes supplemented with empirical formula for the entrainment of external fluid and the interior dissipation as described by Rodi (1979). Tsuji et al

(1987), for example, modelled gas-solid flow in a horizontal channel using a Lagrangian particle method with the simplifying assumption that the continuum gas flow could be described by a boundary layer integral equation. They incorporated gas-particle momentum transfer as a statistical implementation, calculating the particle trajectories and introducing compensating momentum exchange averaged in their computational mesh.

Their particle dynamic equation incorporated a lift term including both the effects of particle spin (Magnus effect) and fluid shear, although both were found to be small in comparison with other forces. They assumed a constant eddy viscosity model to estimate the shear stress for the boundary layer equations. Figure 18 shows the concentration profiles calculated using their model compared with experimental data. The agreement was inevitably quite good at U=7m/s for which the model parameters were calibrated but is poor for the prediction at U=15m/s. They offered no reasons for this discrepancy but we note that their calculated particle velocity profiles (figure 19) display a poorer fit with experimental data at U=15m/s suggesting that the coupling dynamics were probably poorly represented in their model.

b) Field closures. By appealing to a local 'turbulence model', these methods retain a field description in terms of partial differential equations for turbulent quantities as well as mean quantities. Heuristically assigned algebraic or differential equations purport to describe the coupling of the eddy fluxes with the mean field. It should be clear that these models do not actually simulate details of the turbulent motion but only their averaged effect. Such turbulence models are broadly acceptable for defined classes of flows and depend on suitable selection of empirical constants to recover realistic solutions (Rodi, 1979). Such turbulence closure schemes can be zero (algebraic) or one- or two- (transport) equation models. Here we discuss a typical two-equation model, and refer to appendix 4 for comments on other methods.

The two-equation model employed most frequently is the 'k-ϵ' model. Its basis is outlined in appendix 3; (see Rodi, 1979). When two phase flows are considered, there are many proposals for modelling the transport of discrete phase elements such as particles and bubbles. We shall concentrate on Johns et al's (1990) diffusion model, and outline other options on Lagrangian and Eulerian models in appendix 5. Johns et al (1990) simulated bed load and sediment load over a sandwave using the k-ϵ model described in appendix 6 and incorporated a sediment pick-up function after Van Rijn (1984). As pointed out by Johns (1991) the main problem with this model was that it did not predict separation in the vicinity of the sandwave crest. This has since been attributed to the omission of certain hydrodynamic components (see appendix 6) and rectified - although this is not reported in the open literature with reference to implications for sediment transport.

Profiles of shear stress and turbulent kinetic energy (tke) from Johns et al's earlier model (neglecting the horizontal pressure gradient associated with free surface elevation) are shown in figure 20. The absence of separation in this prediction is manifested in the tke graph at X/L=0.1 where the experimental values at crest height are more than twice the predicted values. This discrepancy disappears by X/L=0.5 due to viscous dissipation in the experimental flow. Similar problems apply to the shear stress profiles. However, including the pressure gradient (as in figure 21) effectively eliminated these major discrepancies: compare figure 21a with figure 20b and figure 21b with figure 20c.

So far as sand transport is concerned, the usefulness of this model relies entirely on the quality of the prescribed pick-up function. The formulation used by Johns et al (1990) was developed for flat beds so it seems improbable that particle transport calculations will be accurate in the vicinity of the crest regions. One might hope for some agreement above the stoss slope where pick-up may be better approximated by the mean-shear-lift-off model used for flat beds. Indeed, the results presented in Johns et al (1990) fairly accurately described the suspended sediment concentrations in these areas, but wide discrepancies were demonstrated in the trough zones due to the shortcomings in their representation of the behaviour.

4.2 Continuous phase Lagrangian modelling

Helmholtz (1858; see Sarpkaya, 1989) showed that inviscid vortex lines are also material lines, and therefore always composed of the same fluid elements. This provided the basis for the modelling of vortical flows represented as assemblages of vortices of infinitesimal cross section embedded in a potential flow. By tracking the vortices between time steps in a Lagrangian manner the whole flow field is known in principle, so long as the inviscid approximation is reliable. This method is now termed the Discrete Vortex Method (DVM), of which a brief account and one specific application to two-plane flow are discussed below. For detailed descriptions refer to Sarpkaya (1989) and Leonard (1980).

We begin with the vorticity equation describing advection, rotation or, more strictly, redistribution, and diffusion of vorticity ω

$$\frac{\partial \boldsymbol{\omega}}{\partial t} + (\boldsymbol{q}.\nabla)\,\boldsymbol{\omega} - (\boldsymbol{\omega}.\nabla\boldsymbol{q}) = \nu\nabla^2\boldsymbol{\omega}$$

Here $\mathbf{q}$ is the velocity vector and ∇^2 the Laplacian operator. In two dimensional flows, the vortex rotation/stretching contribution (last term LHS) is identically zero so the equation reduces to a simple advective-diffusive balance which, when non-dimensionalised on representative length and velocity scales (L', W' say) gives

$$\frac{\partial\overline{\boldsymbol{\omega}}}{\partial t}+(\overline{\boldsymbol{q}}.\nabla)\,\overline{\boldsymbol{\omega}}=\frac{1}{Re}\nabla^2\overline{\boldsymbol{\omega}}\qquad Re=\frac{W'L'}{\nu}$$

In the limit of large Re, the right hand side of this equation approaches zero away from flow boundaries, so the equation then describes vorticity convection in inviscid fluid.

There are a number of problems encountered in using the discrete vortex method. Firstly, as the method is based on inviscid theory, extended techniques (or perhaps merely ad hoc assumptions) must be added to incorporate the reality that vorticity (in homogenous fluids) is only generated through the action of viscosity on solid boundaries, as shown in figure 22. Secondly, the models imply ad hoc assumptions as to the starting locations of nascent vortices shed from salient edges, also as to their initial velocities, strength and rates of shedding, all constrained by the Kutta condition which must be satisfied by the separation streamline (as suggested by the inset on figure 22). More problematic is the accumulation of vorticity trapped in recirculating zones, for which only heuristic elimination models are available at present. Many ingenious methods have been developed to address these difficulties, some of which are reviewed in appendix 7.

The model has been applied in wave dominated sedimentary systems by Hansen et al (1991). Although they did not consider the important particle equation discussed in section 4.3, which would have been a more rigorous approach, the prediction of (periodic) clouds forming near the ripple crests (in broad agreement with experimental wave-ripple studies) certainly justifies our proffering that this model should be applied to sandwaves.

4.3 Modelling of particle forces

The particles of interest to us (which could equally be bubbles, droplets or solid particles) are usually smaller than 5mm, but should strictly be smaller than the smallest significant length scale in the flow. Immersed in moving fluid a particle experiences a family of forces, of which the most important is often from pressure gradients in the ambient flow and acts as a perturbation in the steady settling speed associated with buoyancy-drag equilibrium.

The approximations traditionally adopted in developing an analysis of the flow forces acting on a particle generally included the following: that the particle is spherical (or possibly two-dimensional), that the fluid is inviscid, and that the flow is irrotational or of vanishing Reynolds number. Classical viscous (Stoke's flow) analysis at low Reynolds number (eg Clift et al, 1978), is not relevant to particles of 1 mm diameter or so in flows at 1m/s or so (ie with Reynolds numbers perhaps ranging from 1,000 to 10,000). Moreover, extrapolations of these analyses have generally neglected inertial forces that are crucially important for these flows. Here we concentrate on the more appropriate inviscid analyses such as that of Auton (1987), as first described in Thomas et al (1983), which assumed that the particle radius was much smaller than significant gradient length scales in the unperturbed flow.

In this inviscid limit, the equation of motion in weak shear flow under the above length scale restriction, ie

$$|\underline{\Omega}|a \ll |v-u|$$

can be expressed in terms of 4 forces due to pressure gradient, vorticity-lift, buoyancy and drag as follows:

$$\underline{F} = -V\underline{\nabla}P - \rho V[C_{vm}(\dot{\underline{w}}+\underline{w}.\underline{\nabla u})+C_L\underline{w}\wedge\underline{\omega}] - \rho Vg\left(\frac{\underline{w}}{V_T}\right)\left|\frac{\underline{w}}{V_T}\right|$$

As shown in detailed calculations by Auton (1987) and others, the virtual mass and lift coefficients are given by $C_{VM}=0.5$ and $C_L=0.5$ (their time mean values). This equation is discussed in more detail in chapter 5.

Whilst this force law is undoubtedly correct asymptotically in the limits as prescribed, it nevertheless omits two forces which may be of practical significance. The first is the Basset force manifested as wake history integral, which is certainly important at low Reynolds number. The second is the Magnus force, associated with particle spin and potentially important when wall collisions are being addressed. Departures from sphericity may also be important for modelling of sediment transport, but, whereas the analysis can be rigorously extended to accommodate non-sphericity at considerable expense to formulative simplicity, there are probably more important physical factors such as migration of particle separation points in viscous flows around both spherical and non-spherical particles. This last aspect has not been properly addressed in the established literature.

Thomas et al (1983) used the above force law to compute bubble trajectories around a spinning rod as a first approximation to an isolated 'potential' vortex. The experimental results (figure 23) for bubbles rising from below the rod were presented in terms of a non-dimensional trapping width A^* as function of non-dimensional vortex strength C^* such that

$$A^* \equiv \frac{A}{\left(V_T^2/g\right)} = f\left(C^*\right) \equiv f\left(\Gamma g/V_T^2\right)$$

where Γ is the vortex circulation, V_T is the bubble rise speed in quiescent water and g is the gravitational acceleration. Figure 24 shows how this trapping width A^* varied with vortex strength parameter C^* for bubbles and other discrete phases such as oil drops. Figure 25 compares inviscid theoretical predictions with experimental results demonstrating acceptable agreement considering the (necessary) simplifications introduced. Certainly, it is persuasive evidence of the key role played by vortices in capturing discrete phases. As an extension of this study, Sene et al (1993; first reported in Hunt et al, 1988), used a discrete vortex model to represent free shear layer flow, an early version of which is shown schematically in figure 26 taken from Thomas et al (1983). The flowing layer travels at speed U, such that the vorticity sheet generated has strength

$\Omega=\frac{1}{2}U$ and travels downstream at speed $\frac{1}{2}U$. The sheet is unstable to Kelvin-Helmholz modes as discussed in section 3 and 'rolls up'. Following established practices in discrete vortex modelling, Sene et al (1993) approximated this thin shear layer with a sequence of discrete vortices and followed the evolving instabilities in space and time. Typical computational 'tricks' were employed, including the use of viscously cored vortices and random 'jitter' on the locations at each time step. As a downstream boundary condition the vortices were simply removed from the flow in this early version (Thomas et al, 1983). Subsequent improvements in the arrangement of both upstream and downstream boundary conditions are described in Sene et al (1993).

The five numerical runs reported in Thomas et al (1993) are shown in figure 27, giving the trajectories of bubbles released into the shear layer of vertical downflow. The results clearly show how bubbles can be captured and transported in the large scale eddies formed from the roll-up of the shear layer vorticity. Although more precise characterisation of this behaviour has since been reported in Sene et al (1993), the essential point is that our starting hypothesis that such events are also manifested in the crest zones of sandwaves (Thomas, 1990) - is shown to be valid. Furthermore, Soulsby & Bettess (1990) noticed that the recirculation zone size of sandwaves was unsteady with time. We consider the limited quantity of literature in this area in chapter 4.

5 CONCLUSIONS

We began this chapter with an outline discussion on typical bedforms found in uni-directional flows, focusing particularly on sandwave morphology and traditional classification schemes. As discussed, established methods of modelling the flow over these bedforms have been by the extension of flat bed approaches which are totally inappropriate for flows featuring pronounced separation. More recently some basic concepts of shear layer dynamics have been incorporated, but there is presently no adequate engineering calculation method appropriate for these flows. It seems unlikely that Eulerian integral models and two-equation turbulence models alone will adequately reproduce the important features responsible for sediment capture and transport.

Related developments have also been discussed, concerning the coherent eddy features responsible for sediment motion. Many aspects of this are now reasonably well understood and incorporated into modelling methodologies. However, there is still a need for introducing more refined methods such as have been developed for analogous aspects of bubbly flows; in particular Lagrangian calculations based on discrete vortex modelling, which can deliver a representation of the transient large eddies and their propensity for attracting and retaining particles.

This study focuses specifically on this propensity for particle capture by transient large eddies shed from crested bedforms, following Atkins & Soulsby's study of estuarine sandwaves, which revealed captured sand transport in transient structures. Understanding and characterisation of basic dynamical elements was the prime mover in our project, as presented in the technical proposal (Thomas, 1990; appendix 1 here).

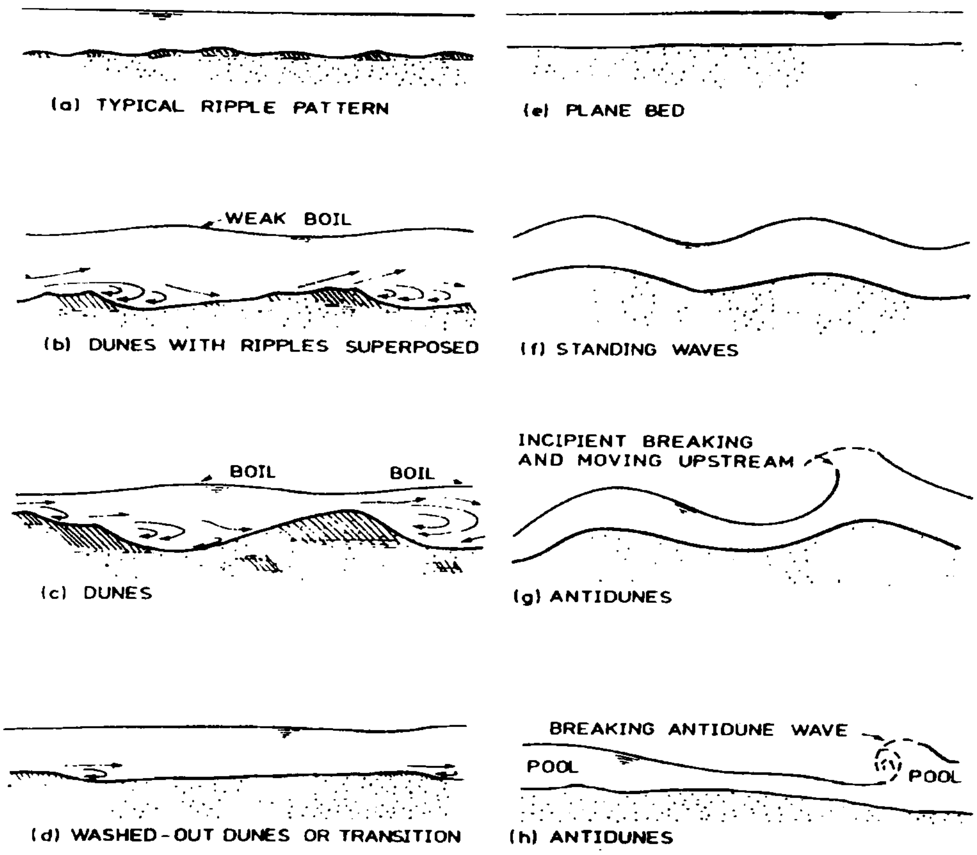

Figure 1. Engelund & Fredsoe (1982). Typical bedforms found in unidirectional flows. Notice the transition from ripples through dunes to wash-out and antidunes with increasing stream power.

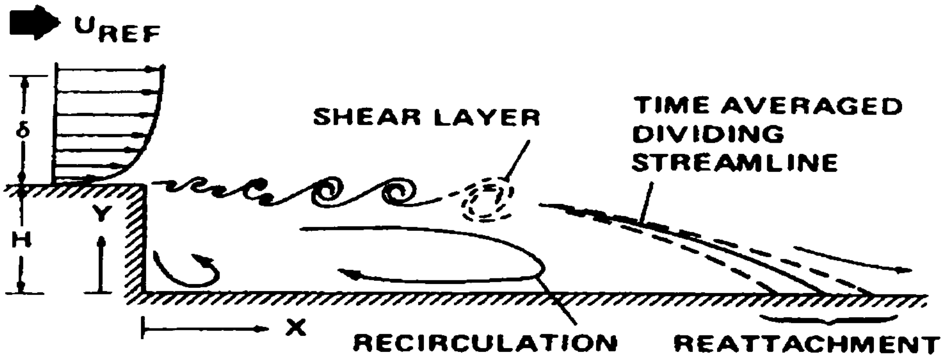

Figure 2. Simpson (1989). Schematic of the flow over a backward facing step showing the shear layer, recirculation zone, reattachment zone and the time averaged separation streamline.

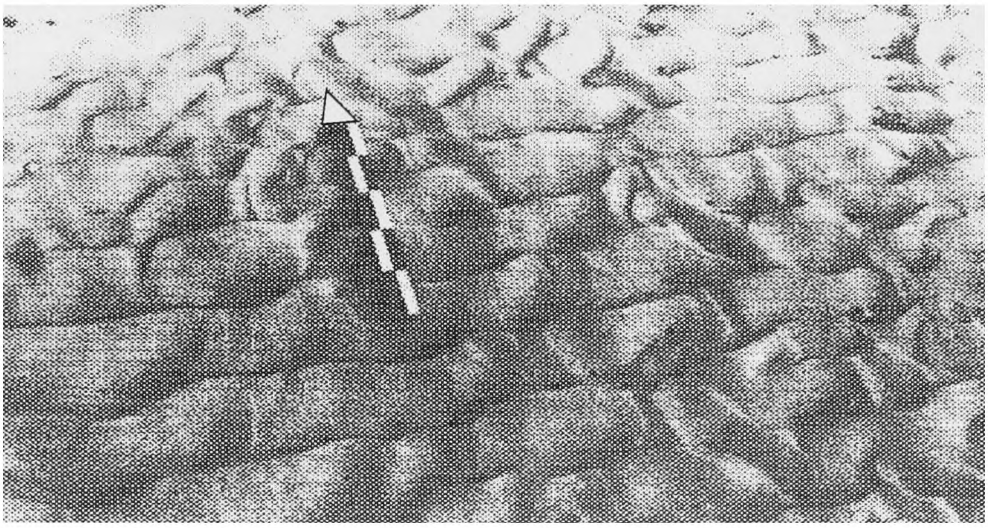

Figure 3. Allen (1984). Long-crested current ripples in fine sand. The scale is 0.5m long and points in the direction of the flow.

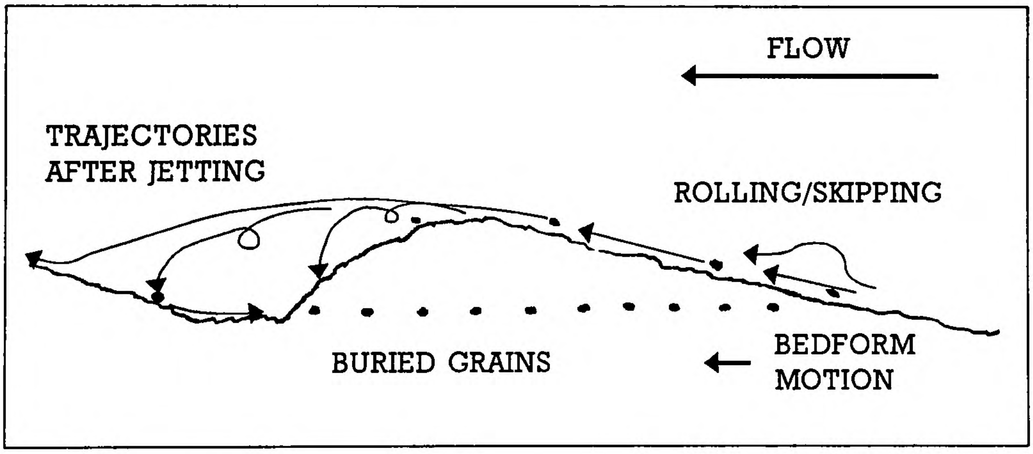

Figure 4. Schematic showing the motion of typical grains in ripples and dunes. The buried grains are uncovered by erosion of the stoss slope. Some of the jetted grains remain with the sand wave and some are transported away to the next bedform.

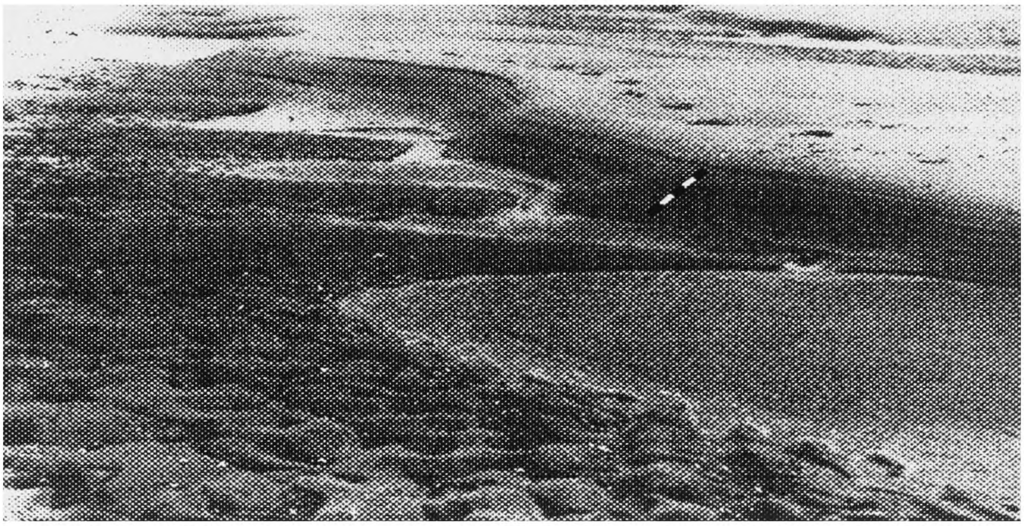

Figure 5. Allen (1984). Oblique dunes in fine sand, Wells- next- the-sea, Norfolk. The scale length is 0.5m and flow is top-right to bottom-left.

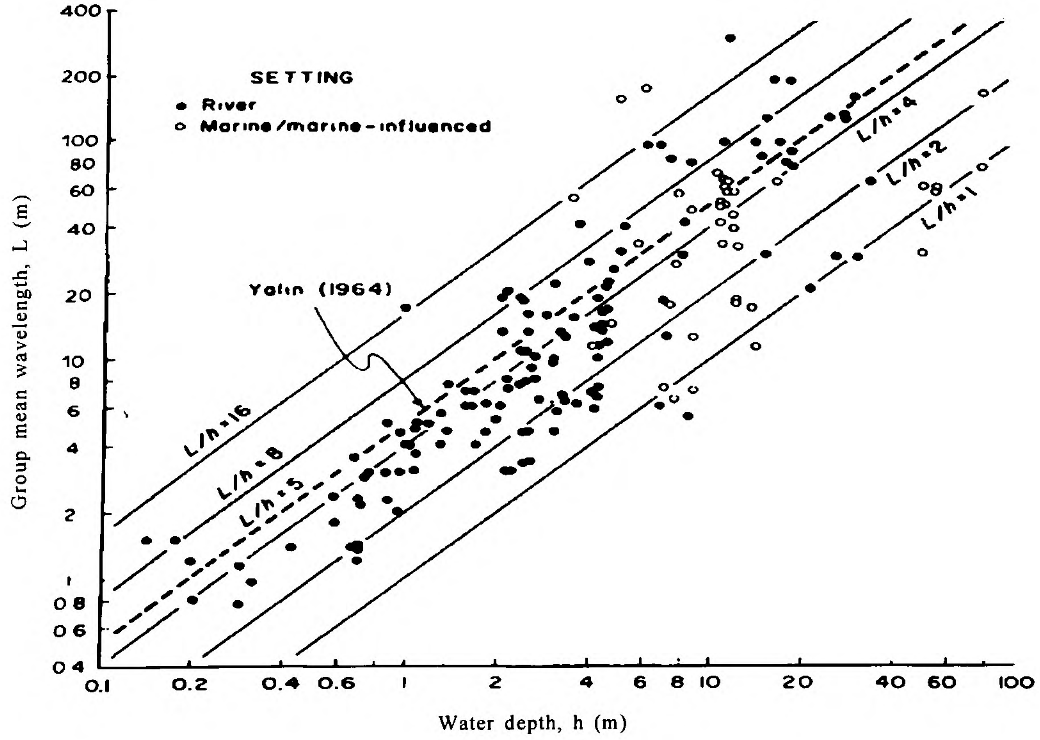

Figure 6. Allen (1984). Correlation between the group mean wavelength and water depth for dunes in rivers and marine settings. Though the scatter is large the trend towards bigger dunes in deeper water is clear.

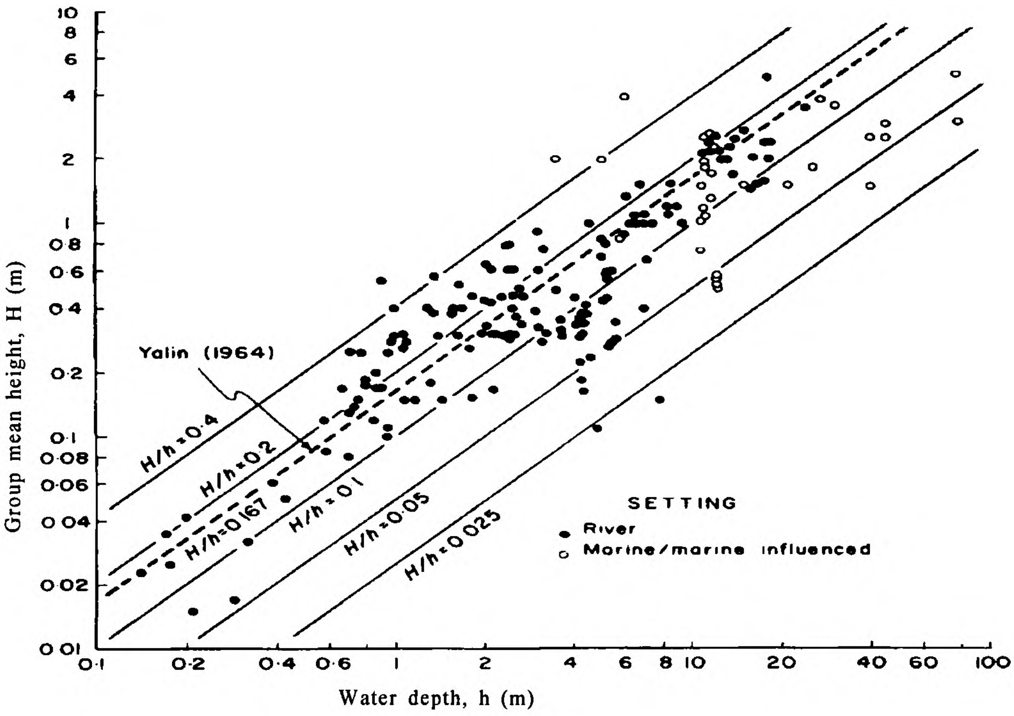

Figure 7. Allen (1984). Correlation between the group mean height and water depth for dunes in rivers and marine settings. Though the scatter is large the trend towards bigger dunes in deeper water is clear.

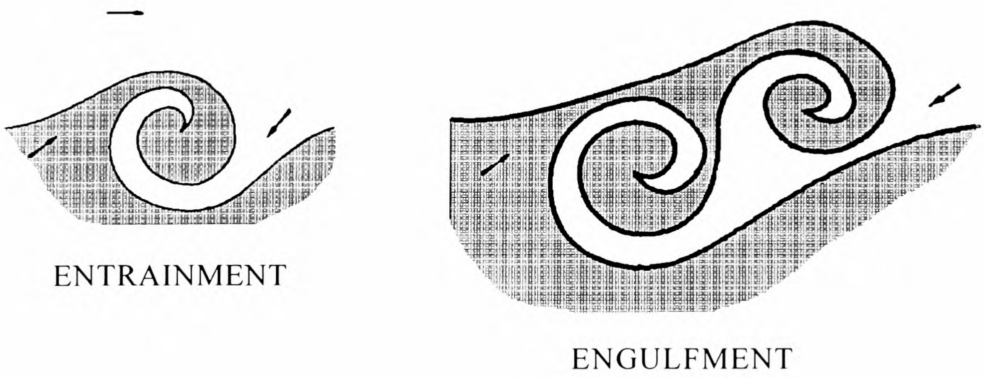

Figure 8. Jiminez (1980). The diagram on the left shows entrainment into a vortex whereas the right shows engulfment during vortex pairing. Most fluid is entrained rather than engulfed in growing shear layers.

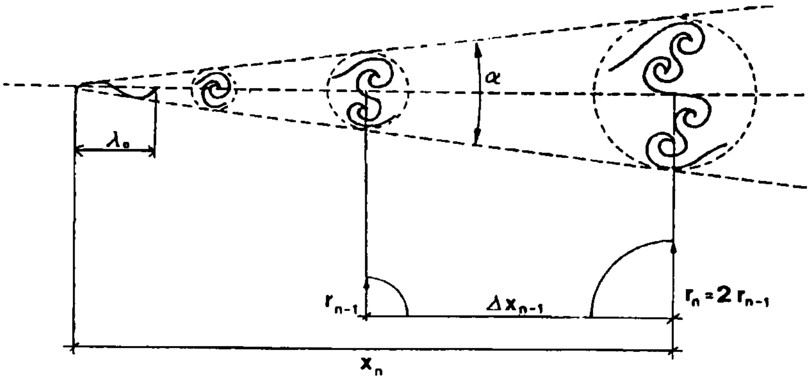

Figure 9. Muller & Gyr (1986). The diagram shows the spreading angle, size and distance between pairings of vortices in a mixing layer. The initial disturbance length causes the shear layer to roll up into discrete vortices of radius r, which subsequently doubles between generations due to entrainment and pairing.

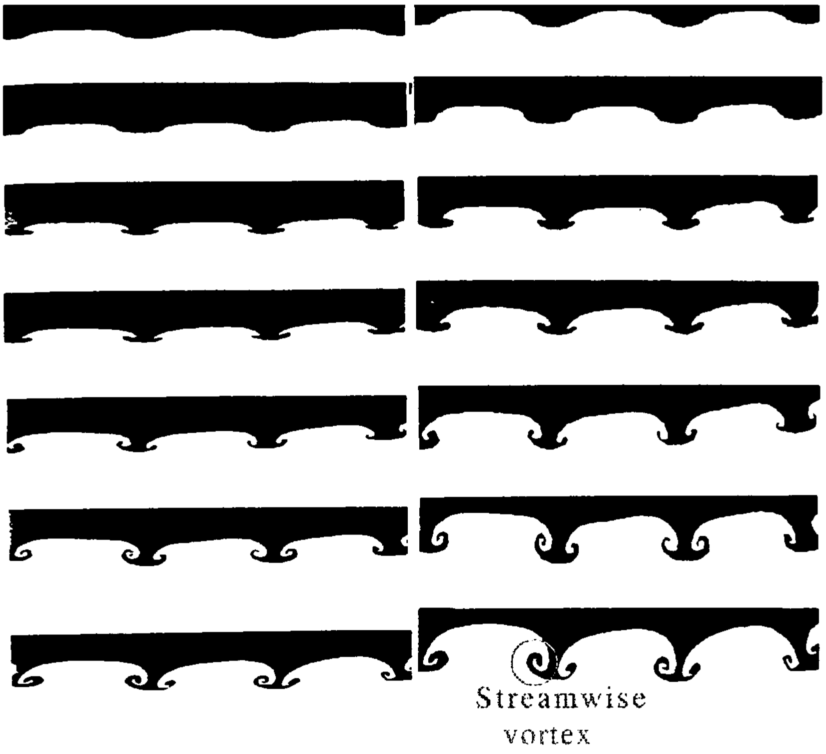

Figure 10. Lasheras & Choi (1988). The series on the left shows the visualisation of the shear layer at 5, 7.5, 10, 12.5, 15, 17.5 and 20cm downstream from the splitter plate. The series on the right are stretched to account for the camera angle. Notice the streamwise vortices that have developed in the latter frames.

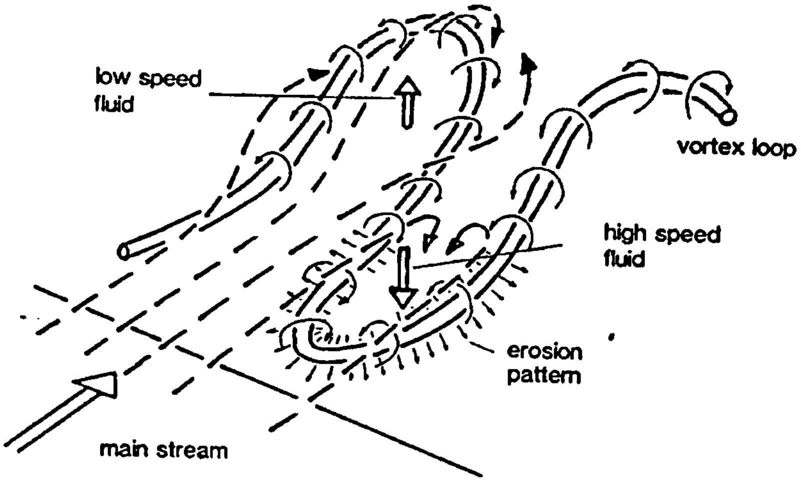

Figure 11. Muller & Gyr (1986). Schematic of the three dimensional distortion of a vortex tube downstream of the crest into the classical horseshoe structure.

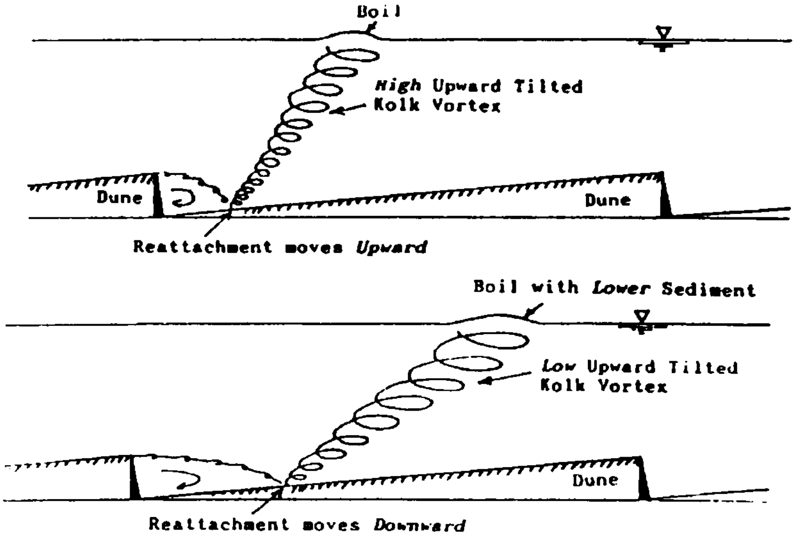

Figure 12. Nezu & Nakagawa (1991). The kolk and boil features postulated by Nezu and Nakagawa in increasing and decreasing stages of the tide. Notice that they show a difference in reattachment point on the stoss slope. The kolk vortex is probably the remnants of shear layer vortices from an upstream crest.

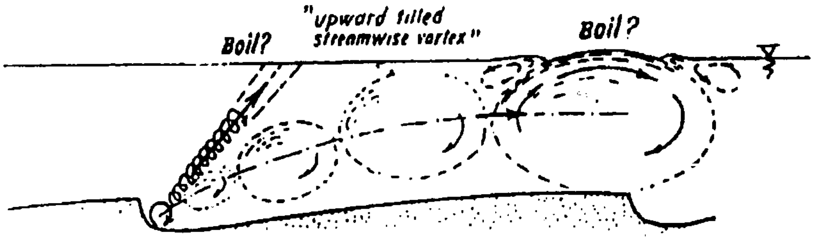

Figure 13. Nezu & Nakagawa (1991). Schematic of the growing vortex tube impinging with the free surface. This picture, though rather simple, captures the main idea that the head structure of distorted vortex tubes could rise in the flow until constrained by the free surface.

Figure 14. Grass (1974). Sand suspended by ejection events in a flat plate turbulent boundary layer. The sand visualises the coherent flow structures.

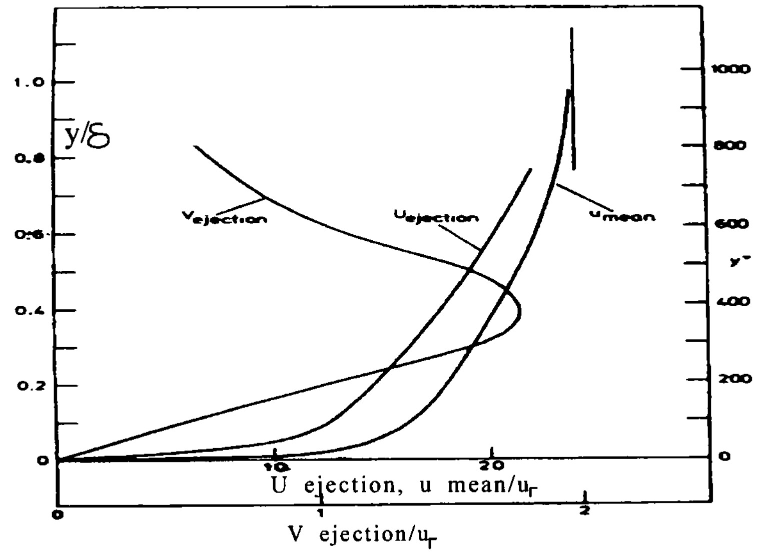

Figure 15. Grass (1974). Streamwise and vertical velocity profiles recorded by sand particles suspended by ejection events in a flat plate turbulent boundary layer. y is the height and delta is 30mm at Re=2300. u_τ =34.9mm/s and the sand grain quiescent fall speed w=12.7mm/s in the mean flow velocity U=830mm/s.

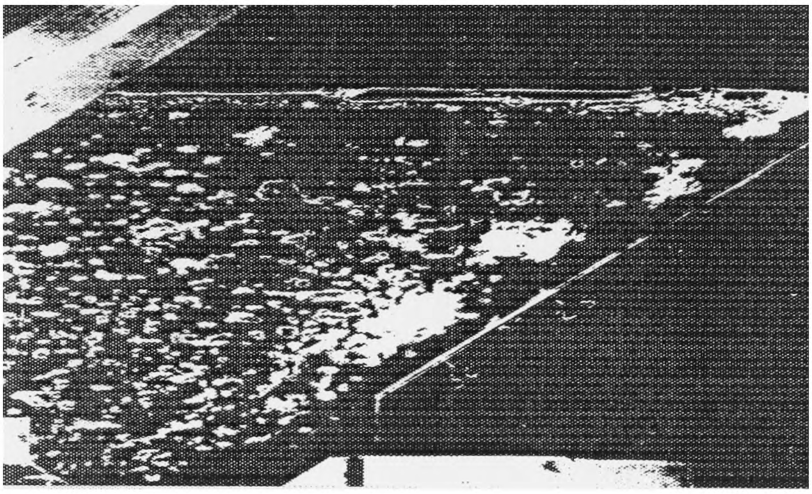

Figure 16. Thomas et al (1983). Air entrainment by a plunging water jet. The white areas are bubbles entrained into and transported by large eddies in the free shear layer.

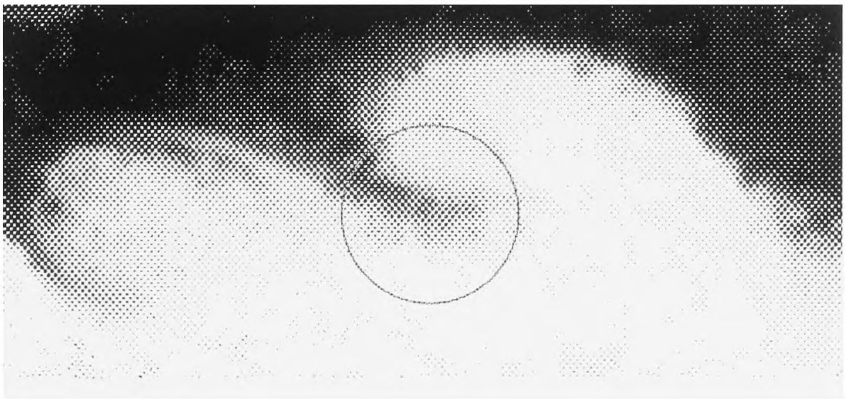

Figure 17. Lazaro & Lasheras (1992). Air-liquid flow visualised by stroboscopic lighting shows that the water droplets (white region) are densely packed in certain regions of the mixing layer but sparse in others. The sparse area circled is a vortex in the mixing layer.

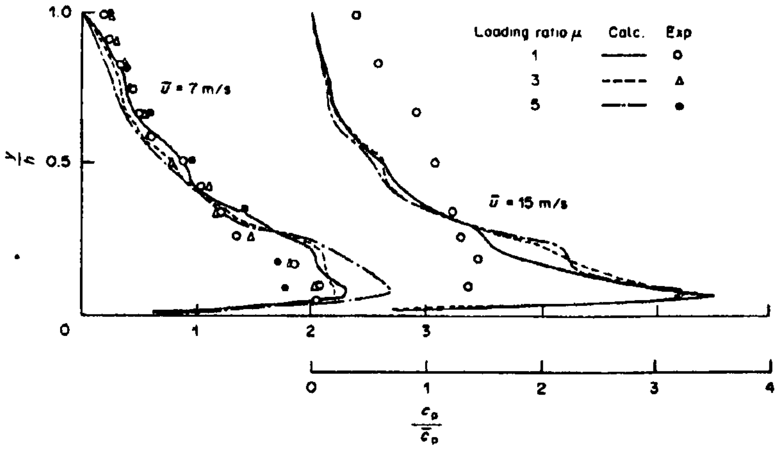

Figure 18. Tsuji et al (1987). Particle concentration distribution for gas-solid flow in a horizontal channel at 7 and 15m/s. Notice that the integral equation gives a good fit at 7m/s, at which velocity the model was correlated, but a poor fit at the higher velocity.

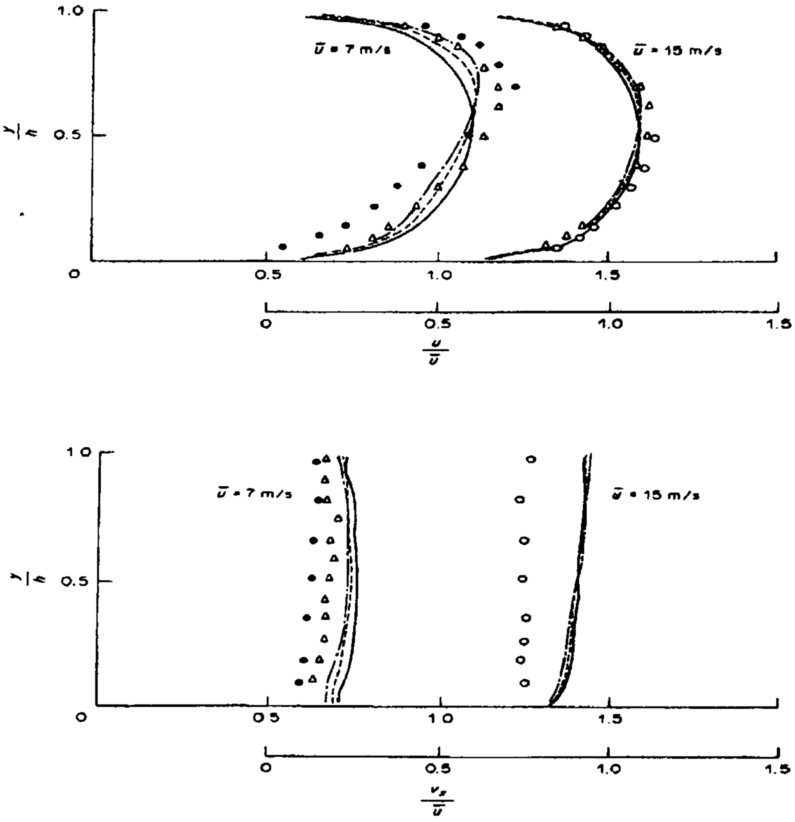

Figure 19. Tsuji et al (1987). The air and particle velocities as computed for the two mean stream speeds in figure 18. The error at 15m/s in figure 18 would appear to be due either to the particle model or to the use of the integral method which ignores the fluctuations from the mean that are so important for two phase modelling.

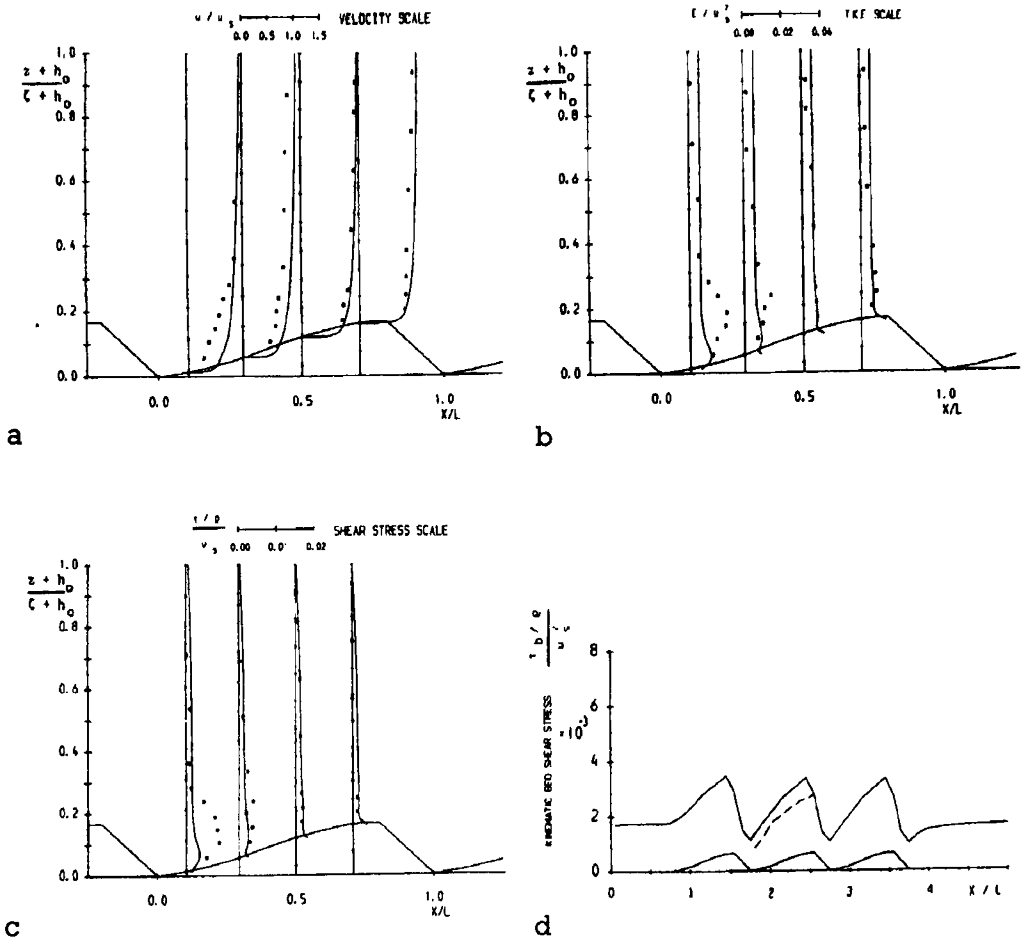

Figure 20. Johns et al (1990). Computed and experimentally determined distributions of mean and turbulent quantities over sandwaves. a) Velocity profiles b) TKE density c) Kinematic shear stress d) Kinematic bed shear stress. The failure of this model to predict separation (as shown by poor fit in graphs b and c) was put down to the assumption of hydrostatic pressure. Nevertheless the model was used to predict sediment transport over a series of three bedforms. Any agreement with sediment transport data must therefore be fortuitous.

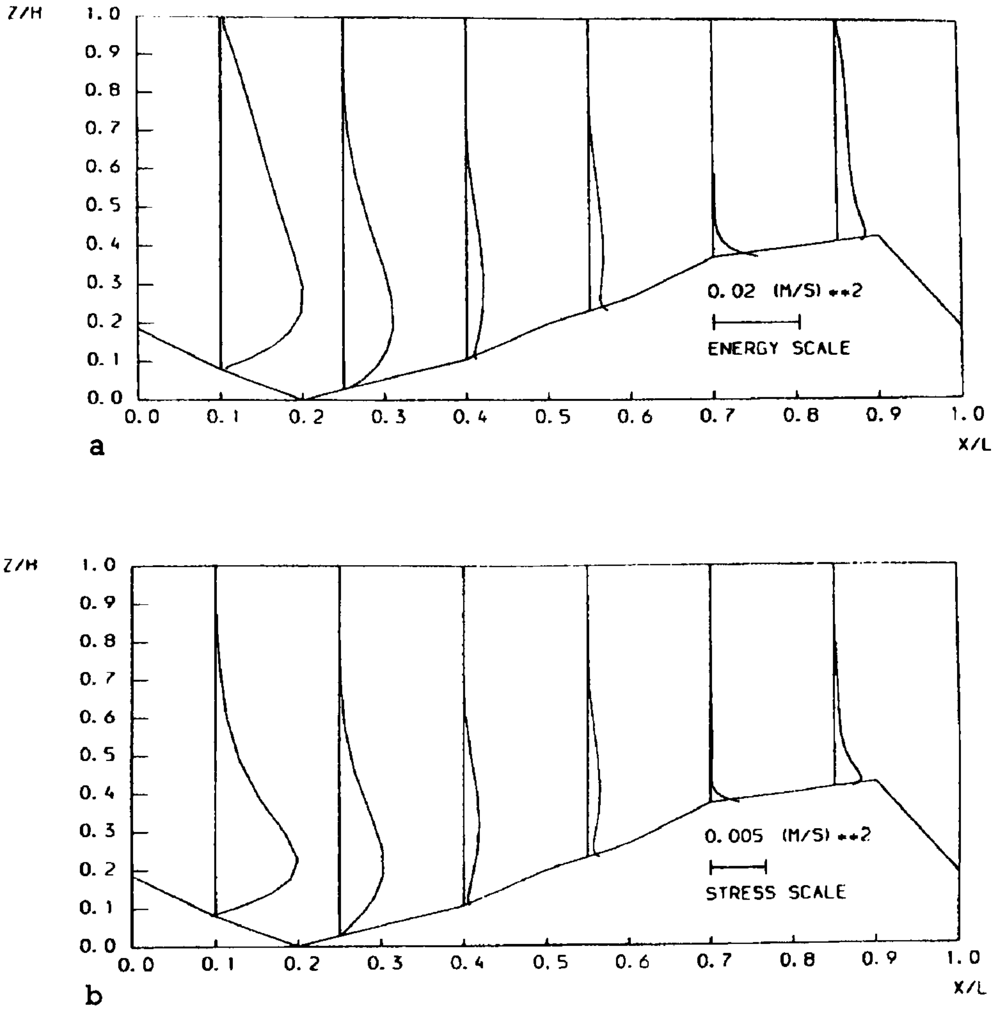

Figure 21. Johns et al (1991). Computed distributions of a) turbulent energy and b) kinematic stress profiles in steady state non-hydrostatic flow over sandwaves at H=3.8m, L=20m. Compare with figure 20. The inclusion of the hydrodynamic component of the pressure gives the required separation at the crest. The model has yet to be applied to sediment suspension modelling.

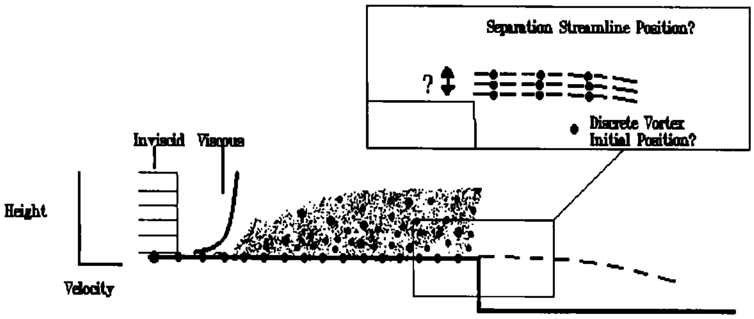

Figure 22. Schematic depicting the theoretical discretisation of the vorticity generated at a boundary wall. The dark spots represent discrete vortex elements that sum to model the effect of the diffuse vorticity cloud (shaded area). Some problems for discrete vortex modelling of free shear layers are where to place the first vortices after the salient edge and how to set criteria for the free streamline.

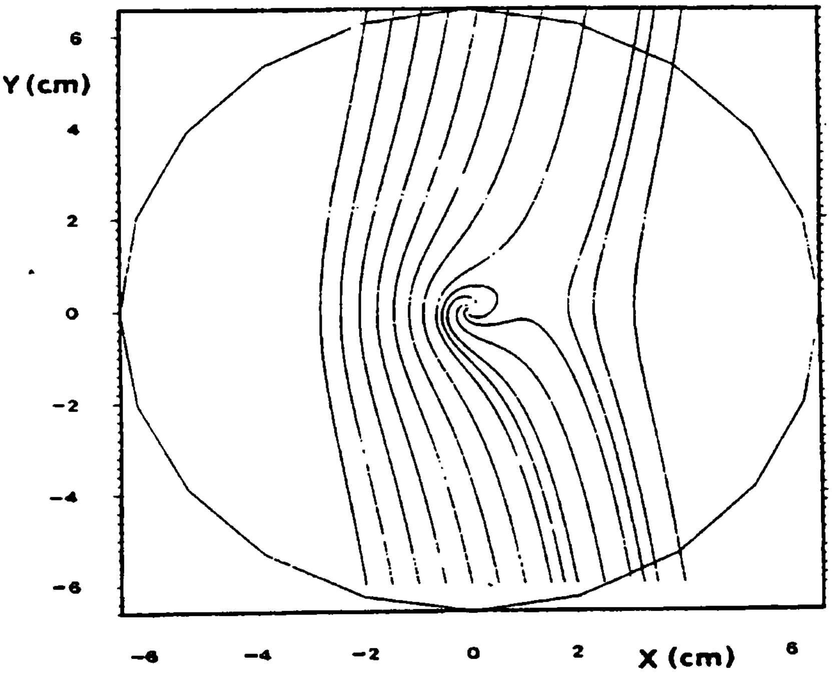

Figure 23. Thomas et al (1983). Bubble trajectories computed near a line vortex. Notice that a narrow band of X starting points lead to bubble capture.

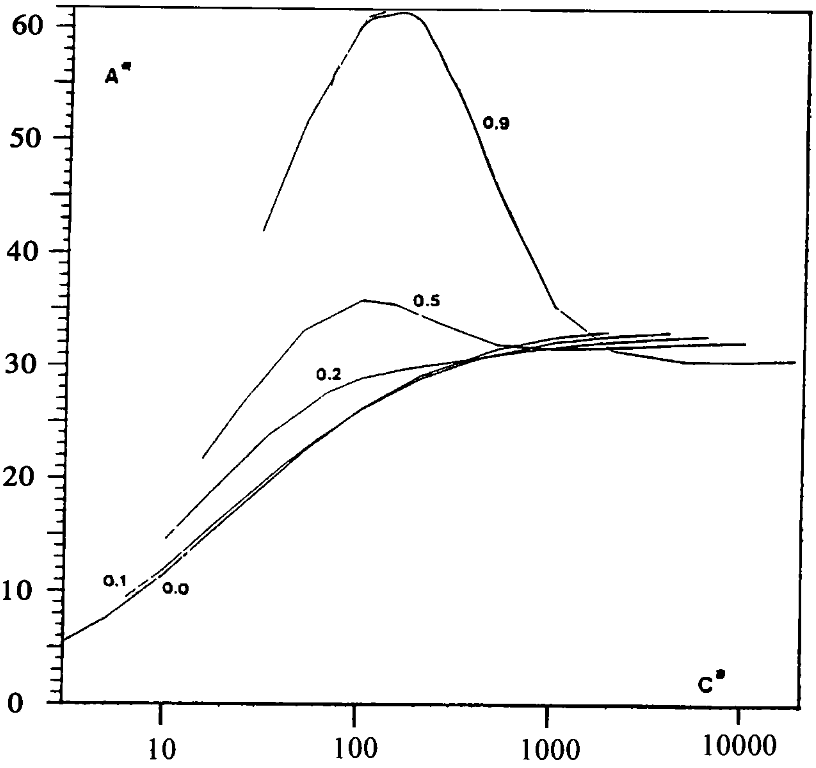

Figure 24. Thomas et al (1983). Dependence of the trapping width on the vortex strength parameter for discreta with various specific gravities.

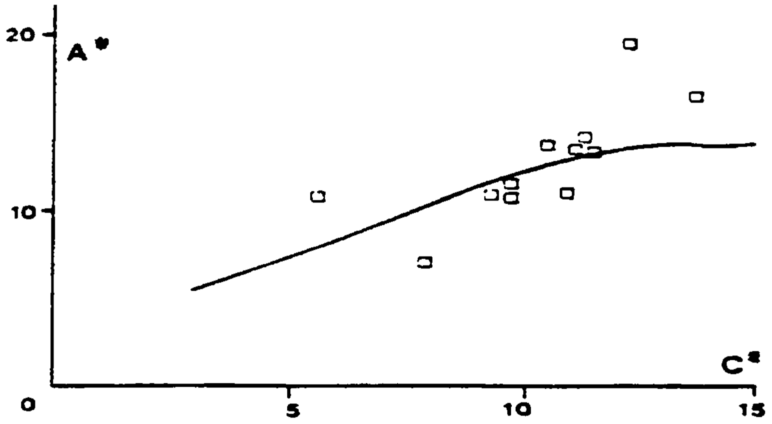

Figure 25. Thomas et al (1983). Comparison between computed and experimental trapping width with vortex strength for bubbles in water.

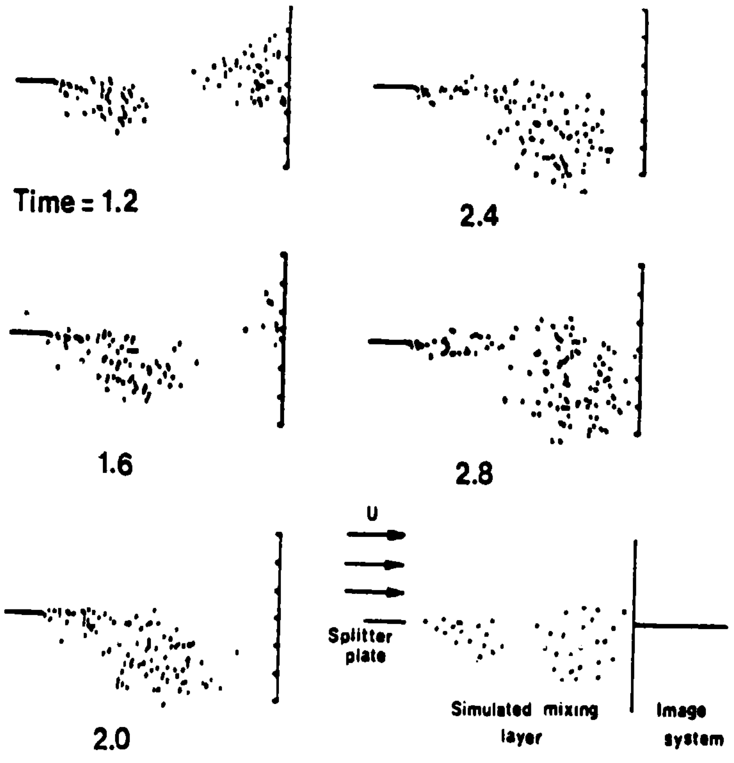

Figure 26. Thomas et al (1983). Examples of the developing shear layer after a splitter plate at various times, as computed using the discrete vortex method.

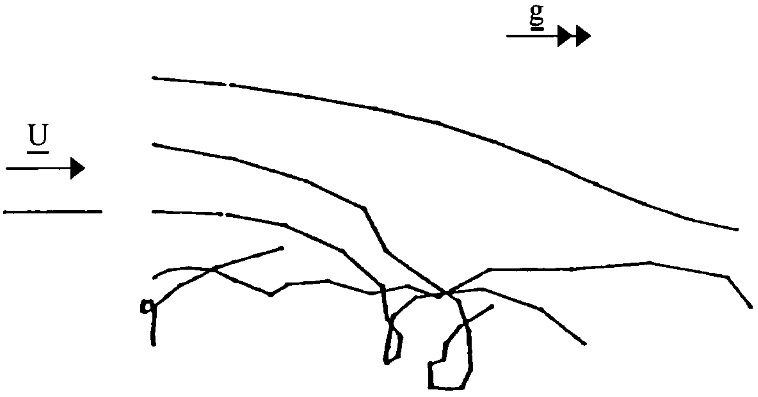

Figure 27. Thomas et al (1983). Computational simulation of bubble trajectories in counter-buoyancy flow (buoyancy force is right to left, flow left to right in this figure). Notice that the model allows capture of bubbles (signified by the cycloid-like trajectories). In such flows this capture delays detrainment of the bubbles into the outer flows. Compare this with the regions of high bubble voidage in figure 16.

CHAPTER 2: EXPERIMENTAL EQUIPMENT AND METHODS

SUMMARY

An experimental flume was designed and constructed to be adaptable and of sufficient size to allow the study of reasonably scaled sandwave bedforms. The facility was 6.7m in length and 0.45m square cross-section, with perspex side walls and base. The inlet flow was calmed using Raschig rings which were adjusted until even flow across the width of the flume was achieved. A series of three perspex triangular-cross-section bedforms were fitted in the working section to model sandwaves.

Experimental techniques concerning fluid and particle visualisation, particle trajectory analysis and concentration profiling, which were applied to particle motions from the crest, lee and stoss slopes, are also detailed. These techniques were developed in existing equipment and during a summer visit to HR Wallingford, where extensive practical trials were carried out (as detailed in appendix 8).

Suggestions for future modifications to the rig include fitting a stainless steel pump to prevent water discolouration and provision of permanent flow and depth metering equipment.

1 INTRODUCTION AND DESIGN CONSIDERATIONS

The experimental aspect of our study required a water flume for evaluation of sediment suspension mechanisms over representative bedforms. The only existing facility was poorly constructed and small in size at 0.1m wide and 0.05m deep, hence a new flume was needed to satisfy our requirements of deeper flow at reasonable velocity. Studies in this existing rig and those done at HR Wallingford underpinned the design philosophy described below.

There were three major sizing constraints: namely, space, cost and suitability for current and future applications; the maximum length of space available was eight metres, total cost should be no more than £2,500 and it should be designed for adaptability. Technical considerations concerning the application to sandwave studies are discussed below.

To select the length, height and width we considered the application to free surface flow over bedforms and found a number of important parameters. Firstly, Schreider & Amsler (1992) state that sandwaves found in estuaries tend to have a maximum steepness h/L of 0.06 (where h and L are the bedform height and wavelength). Secondly, sandwaves occupy a significant fraction of the flow depth D; Lyn (1993) used a value h/D=0.1 in his model study and Soulsby (1989) found h/D=0.33 for estuarine dunes, which are typical values for such bedforms.

Thirdly, the Froude number $Fr=U/(gD)^{½}$ -based on the depth integrated flow velocity, U (g is the gravitational acceleration)- is typically of the order 0.1-0.3 and a Reynolds number -based on the flow depth- greater than $3x10^6$ is usual. Fourthly, we should operate the flume at a depth where corner effects are negligible, optimally with a width (W) to depth ratio exceeding the value of 4 suggested by Lyn (1993). Finally, we should allow a minimum of 40 flow depths of development length $L_{DEV} \approx L_R$ (rig length) upstream of the working section.

The 5 factors above serve to limit the minimum size of the facility once a bedform dimension is set (figure 1). Here the minimum values of D, U, W, L_R and pump size are calculated using the mid-range relationships h/D>0.2, W/D>4, L_R/D>40 and Fr=0.1-0.3 for each value of h in the second column. Since we have no space for a rig of length greater than eight metres and pumps with flow rates above 80l/s would exceed the power capacity of the electrical system available to us, our choice of dimensions was option four in figure 1.

The flume walls and base needed to be transparent throughout to allow visualisation of developing flows. This fixed the material to perspex since it could be handled easily in our workshop. Also, the flow development section could have been constructed either as a contraction-expansion or the flow could have been manipulated with screens to give an even distribution across the flume width. We chose the latter option as a space saving device.

Initial costing for a flume of the above dimensions was only favourable so long as the pump could be acquired at no cost and the ancillaries (such as the wier, valves, hose clips and flow straighteners) were either made from scrap material or otherwise acquired without cost. A sacrifice in flume width was also necessary due to the cost of perspex sheeting of the required size, again at reasonable cost. The final dimensions were chosen as 6.7m length, 0.45m width and 0.45m depth as a necessary compromise between all of the above constraints. The depth was chosen for adaptability, as we did not intend to run at full depth for this study where the desirable W/D ratio is no less than 4. Implications of this choice for our five limiting criteria are discussed in section 4.1.

2 DESIGN

Figure 2 shows the layout of the major components of the flume. It comprised a suction tank with weir, an inlet tank, a flume section, a pump and motor, a discharge spool and hose, a suction spool and a bypass and flow valve. The discharge line from the pump was looped over the flume and then ran underneath the working section to the flow valve and inlet tank.

2.1 Flume section

A 5.5m long channel section of width and depth 0.45m was constructed. The main support was provided by two lengths of 75mmx50mm channel iron supported on four trestle benches of 38mm angle iron (figure 3a,b). The perspex base was bedded down on putty[1] along these main channels, supported at its middle by a 75mmx50mm joist and at 0.46m intervals either side of this joist by neoprene rubber mounted on 6mmx25mm bars.

Each side was constructed in two 2.75m sections as a rectangle of 38mm angle iron with 6mmx38mm bar at 0.46m intervals. A 2.75m perspex sheet was bedded on putty and fixed with set pins to the side piece, the threads being sealed with putty. Two sections were joined in situ with putty seals to form a side-wall, which was placed on a putty layer on top of the perspex base sheets and bolted into place. Side arms were added to hold the flume walls upright under the weight of water.

2.2 Suction and discharge tanks

The end tanks were constructed from a number of trays formed by bending and welding 304 stainless steel sheets (figures 4a,b and figure 5). The trays were spot-welded together to form a box and the edges of this box tungsten welded to give a watertight seal, mechanical strength being added with angle iron straps around the girth of each tank. Each tank was then mounted on an angle iron stool and bolted to the flume with putty added to give a seal.

2.3 Pump and piping

A 12kW cast iron pump with 200mm suction and 150mm discharge

---

[1] Compound B sealing putty from Braithwaite Ltd, Newport, Gwent.

flanges and a maximum flow rate of 60 litres per second at a head of 3m was obtained from a decommissioned chemical plant (Shell Stanlow, Ellesmere Port, Wirral). It was manufactured by Sigmund Pulsometer Pumps (type LK-NN5) in 1967, and was fitted to the flume as in figure 5. The wetted parts were sand blasted and coated with resin to prevent excessive rusting.

The pump suction feed was taken from the front bottom left hand corner of the suction tank, as far away from the flume spill zone as possible, to allow time for entrained bubble disengagement (figures 2 and 5). The spool piece was made of neoprene rubber wrapped around two copper neck-pieces which were flanged to the pump and the suction tank with backing flanges (figure 6). This rubber section prevented vibration transmission to the welds in the suction tank. The flange bolts were used to secure the stainless steel suction filter meshing to the inside of the suction tank. This filter was designed to prevent 0.5mm and larger debris from entering the pump and damaging the mechanical seal.

The discharge line was 100mm flexible tubing, joined to the pump discharge flange by a 150mm diameter copper pipe reduced to 100mm by cutting and braising (figure 5). A 75mm diameter branch was inserted in this copper pipe and joined to a valve which controlled the bypass flow.

The main discharge flow was controlled by a gate valve situated in the discharge hose below the flume as in figure 2. The hose from the pump passed over the rig in a 0.70m diameter loop and then underneath the flume section to enter the inlet box at its front face (figure 2). The hose was joined to the flanges using 50mm wide hose clips with a smear of sealant on the copper or brass necks of the backing flanges. Wire coils were wrapped around the ends of the reinforced hoses and stood proud of the reinforcing spiral (the two spirals formed a double helix). The hose clips pressed on the wire spiral which, in turn, forced the soft rubber (between the reinforcing coil loops) onto the flange necks to form a seal.

2.4 Flow control

The inlet tank was filled with 25mm stainless steel Raschig rings held down by a grid of galvanised iron, as shown by the shaded region in figure 4a. Three net bags filled with rings were placed around the inlet to the tank to prevent the formation of a cavity in the packing due to the local high velocity, and a layer of netting covered the upper surface of the rings to help hold them in place. The upper layers of rings could then be adjusted to give an even flow across the width of the rig. An expanded polystyrene board was floated on the water surface to damp out any waves.

The aluminium weir at the end of the flume ran in two channels either side of the flume walls, but situated in the suction tank so as not to constrict the flow (figure 4b). It was operated by a central screw thread supported by a bush above the flume and could be wound above or below the level of the flume base to allow sluice (underflow) or weir (overflow) operation.

2.5 Flow measurement

We used a pitot tube system to measure the local total and static heads in order to obtain the dynamic head and hence calculate local time-averaged flow velocity. This pitot tube was designed after Blevins (1984) to the dimensions shown in figure 7. The pitot was supported in a traversing cradle (figure 8) which could be positioned at any point along the working section by sliding the cradle along its runner. The difference between the static and total pressures was measured using a differential pressure transmitter[1] (DP cell) which was flushed before each set of readings with degassed water stored in a tank above the rig.

The DP cell was calibrated using static water columns and a voltameter to a range between 0 and 750 Pa which corresponded to the 256 bit, 4-20mA range of the BBC micro-computer logger. This gave a measurement interval of 0.25mm water ie about 0.5% error on our velocities. A short computational routine gathered 1000 readings of the pressure difference DP at 5 per second for averaging and the flow velocity u at the point of the pitot nose was calculated using the formula

$$u = \sqrt{\frac{2DP}{\rho}}\ , \quad \rho = 1000\,Kg/m^3 \qquad u = m/s \quad DP = N/m^2 \tag{1}$$

---

[1] Honeywell type 41101.

3 FLOW VALIDATION

The basic requirement for the rig was that the flow should be symmetrical in the cross stream direction with a flat central profile. In the absence of packing in the inlet tank we expected to have a basic flow with a certain bias along one side of the flume caused by the spiralling discharge pipe. This unwanted swirl and vorticity would be largely dissipated by the Raschig rings and the expansion-contraction of the flow in the inlet tank. The effective expansion in the inlet tank is 70:1 followed by a contraction of 6:1 as the flow enters the flume (assuming that the flow is distributed over the full area), which should be adequate for destruction of this swirl (Thomas, private communication, 1991). To achieve the required profile we measured the mean flow velocity at various cross stream locations at various flow depths and adjusted the Raschig rings until an acceptable flow was attained.

Initial measurements of the velocity profile across the stream at the start of the working section are shown in figure 9. A slight bias along one side of the flume is visible. Trial and error adjustments to the Raschig ring distribution, amounting to a redistribution of about 5% of the rings, gave the corrected profile shown in figure 9. Also, visual observation of the motion of plastic spheres on the water surface of the inlet tank proved that the whole tank area was used by the flow and their subsequent paths along the flume confirmed that there was no appreciable cross stream component of flow velocity.

4 EXPERIMENTAL SETUP AND METHODS

Here we describe the bedforms used for our experimental studies in chapters 3 and 4 and the flow visualisation methods employed. Also, we describe the general techniques used in the particle suspension studies, again presented in chapters 3 and 4.

4.1 Bedforms

Three perspex bedforms were made to the dimensions shown in figure 10. The stoss slope angle was 5 degrees (Allen, 1984) and the lee slope was 30 degrees since this is close to the angle of repose of common quartz sand (RJS Whitehouse, HR Wallingford, private communication). The bedform height was 0.043m and length was 0.65m giving h/L=0.066, similar to the empirical values used by Lyn (1993), Karahan & Peterson (1980), Schreider & Amsler (1992) and found by Soulsby (1989) for estuarine dunes which were 0.08, 0.06, 0.06 and 0.07 respectively.

The set of experiments reported in chapter 3 were conducted at four depth-averaged flow velocities shown in figure 11, which had the vertical profiles shown in figure 12. It should be noted that the profiles show accelerated flow near the crest, about 10% higher than the mean flow, due to flow area constriction by the bedform.

The Froude numbers ranged from 0.16 to 0.29 in the experiments, well within the limits found in natural flows, as were the values for h/D which varied between 0.21 and 0.27. The flow development length to depth ratio (L_{DEV}/D) ranges from 24 to 19 which is low, but not unprecedented since Lyn (1993) reports as yet unpublished work carried out at Delft where a value as low as 17 was used. This parameter was not as important as the others because even if the flow had arrived at the first bedform fully developed it would have undergone an acceleration up the first stoss slope. This situation would be repeated over each bedform so a 'fully developed flow' was never a realistic proposition. Indeed, Soulsby (1989) reports accelerating velocities along sandwave stoss slopes which form low level jets near the crest, comfortingly similar to those in figure 12. We add here that the interesting 'Coanda-flapping' effect studied in chapter 3 is an unsteady flow feature present in separated flows regardless of the extent of flow development length (we reported identical findings in report FAST9108.RJO\NHT -appendix 1- at L_{DEV}/D about 60) as are the discrete shear layer vortices present in the flow after every crest.

The ratio of the flow width to depth varies from 2.2 to 2.8, less than the desired value of 4, so we proceed with a caution that all of our results should be derived from the central region of the flow. Qualitative evidence from the lee slope capture studies in chapter 3 show that particles have a very slow drift rate towards the corner of the rig which is insignificant compared to the convection velocity (less than 1%).

4.2 Flow visualisation and model particles

Our initial efforts were directed at the simultaneous visualisation of flow tracing particles and quartz sand grains, but this proved to be too difficult to achieve except for view fields smaller than about 0.02mx0.02m. This scale was too small to be used in our trajectory studies, so larger model particles (which were viewable at the decimeter scale) were used in place of the quartz sand. These particles were selected on the basis that their fall speed in quiescent water was equivalent to that of sand grains of size known to be actively suspended over our model bedforms, ie quartz grains in the range 100 to 800 microns (Soulsby, 1989). Sediment grains above this size are not present in the suspended load whereas below this size they are distributed as wash load throughout the flow. The suitability of the model particles is discussed at length in chapter 3.

The terminal fall speeds of the three particle types (which had the physical properties given in figure 13) were measured by dropping them in a water filled tube of length 1.5m and diameter 0.05m. Particle fall through a section 0.2m from the bottom of the tube was videoed and the time taken for them to pass between two lines drawn 0.2m apart was retrieved by replaying the video and counting the number of frames of 1/25th second taken by the particle to travel this distance. 100 particles of each type were measured, a representative sample obtained by repeatedly quartering a bulk sample.

The spread of fall speeds is shown in figure 14 for each particle type. The table shows the standard deviation for each and the mean values are 0.034, 0.060 and 0.076m/s. Similar values were found for the same experiment performed on the particle with fall speed 0.076m/s when the measurement interval was at 1.0m from the tube entrance, showing the particles had reached their terminal fall speed by the time they entered our lower measurement region.

We used two different flow tracers; firstly Rilsan powder, a commonly used compound obtained from Atochem UK Ltd, Newbury, Berkshire; and secondly Amberlite XAD-2 resin from Rohm & Haas (UK) Ltd, Croydon, England. The Rilsan powder had a size range 40-200 microns whereas the Amberlite was larger at 300-400 microns, both having a specific gravity close to 1.0 (fall speeds order 1mm/s). The Rilsan powder was used as the flow tracer when we viewed the crest regions on a centimetre scale and the Amberlite was used for visualisation of the outer flows at decimeter scale.

A slit of light was generated in one of two ways. The method used for the jetting experiments was to project a beam of light from a 500W Aldis slide projector onto a mirror underneath the perspex flume base. The mirror was covered with black masking tape except for a 0.01m strip along its centre-line. This strip deflected the beam up through the base of the flume and through the perspex bedforms to illuminate the flow tracers. The width of the beam could be adjusted by removing tape from the mirror. A slit aperture under the base of the flume was used to remove any divergence from the beam and to provide a fine adjustment on the width of the light sheet. This method is advantageous because it produces a light sheet that is not disrupted by water surface deformations.

The above lighting method could not be used for the lee and stoss slope capture experiments because the particles were initially at rest on the bedform, thus obscuring the beam. For these experiments the mirror was suspended above the rig at 45 degrees and the light from a 2000W halogen lamp was reflected down through the surface of the water. The slit aperture was placed above the flume to give the same control as before. The visualisations were taken using a Panasonic NV-G202B VHS-C movie camera and recorded on a Sony SLV-353UB video recorder.

4.3 Chapter 3 experimental methods (jetting capture)

The model particles were soaked in water for a period of about 20 minutes and bubbles were removed from their surface by sharply tapping the bottles. They were then dropped into the flow upstream of the bedforms such that they landed close to the centre-line of the flume on the stoss slope of the bedform before crest 2. A number of these particles were drawn into the recirculating flow behind the first crest but the majority were washed downstream over the second crest. A proportion of the latter group travelled off the centre-line of the flow and could not be visualised. Those particles that did remain on the centre-line were illuminated by a light sheet of width 0.02m and their positions were video-recorded. The recorder was left to play for the duration of the experiment, in which time at least 200 trajectories were recorded.

These video records were analysed manually to give two data sets. The first set concerned the trajectories of individual particles; they were grouped into seven primary modes as described in chapter 3. Also, the point at which the particle was deposited on the downstream lee or stoss slope was recorded along with the duration of the particle trajectory from the crest to this landing site. Such distributions are presented in chapter 3 for varying values of depth-averaged flow speed and particle quiescent fall speed. The second set concerned each particle's contribution to the notional concentration beyond the crest during its flight. The description of the methods used here are detailed in chapter 3.

4.4 Chapter 4 experimental methods (Lee and stoss slope capture)

The bedforms were arranged as for the jetting experiments except that an initial test was carried out with only two bedforms. All subsequent tests used three bedforms as above. A detailed account of the experimental methods are given in chapter 4.

5 CONCLUSIONS

A 6.7m long flume designed for the study of the flow and particle trajectories over sandwaves was constructed and found to give an even flow over 0.45m width and up to 0.45m depth. The flume has been used successfully to study the flow over fixed bedforms, from which a number of points concerning adaptions and improvements have been made.

6 SUGGESTED EQUIPMENT MODIFICATIONS

Improvements to the rig are listed below in order of priority.

- Fitting a stainless steel pump to prevent water discolouration.
- Construction of a larger suction tank with sieve or a settling compartment for batchwise removal of the experimental particles.
- Additional flow discharge metering equipment. A simple venturi or orifice plate in the discharge line should suffice.
- Permanent fitting of depth measurement point gauges.
- Increase of flume length should space become available. This would not be too costly since the flume section is built in component form and can be added to as desired.
- Providing a pumped drainage system for cleaning and flushing.

Re-engineering to allow the flume to be tilted. This would probably involve a complete re-build since a tubular supporting beam is considered most suitable for such purposes.

7 ACKNOWLEDGEMENTS

Thanks are extended to Stan Ward for his diligent effort in undertaking such a mammoth construction task alone, for producing such robust equipment from less-than-ideal material and drawings, and for generating so many good ideas. Thanks also go to John

McMullan from Shell, Stanlow, for supplying the pump and motor, without which our project would have stalled.

Opt	h (m)	Max D(m)	Max U(m/s)	Min W(m)	Min L_R(m)	Min pump rate(l/s)
1	0.01	0.05	0.14	0.20	2.0	2
2	0.02	0.10	0.20	0.40	4.0	8
3	0.03	0.15	0.24	0.60	6.0	22
4	0.04	0.20	0.28	0.80	8.0	45
5	0.05	0.25	0.32	1.00	10.0	80
6	0.06	0.30	0.35	1.20	12.0	126

Figure 1. Table of design values for flume sizing. The maximum and minimum values are desirable only. Option 4 was chosen on the basis that the available electricity system would not cope with a higher flow-rate and such a large pump would be difficult to find gratis.

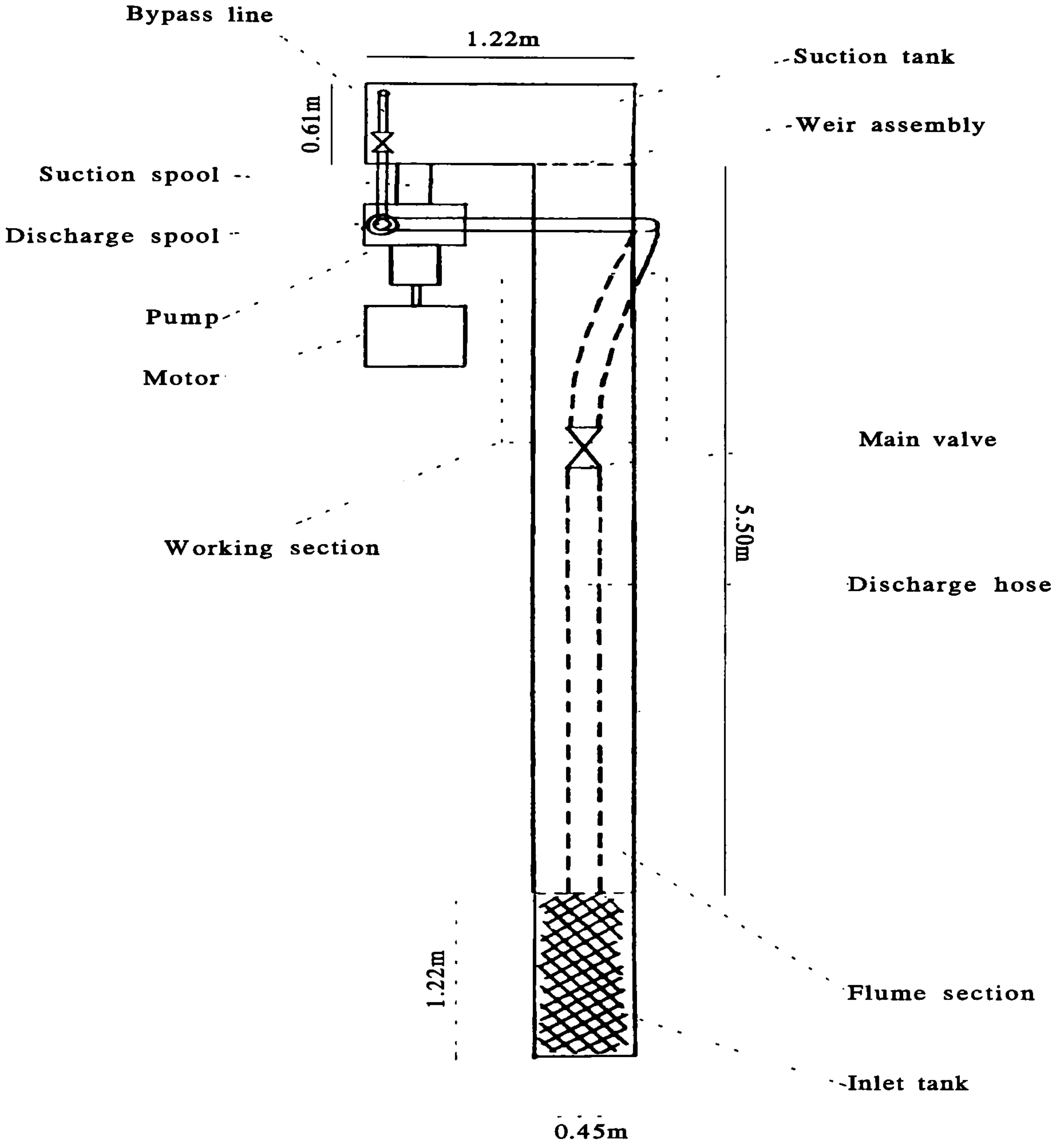

Figure 2. Layout of main flume components.

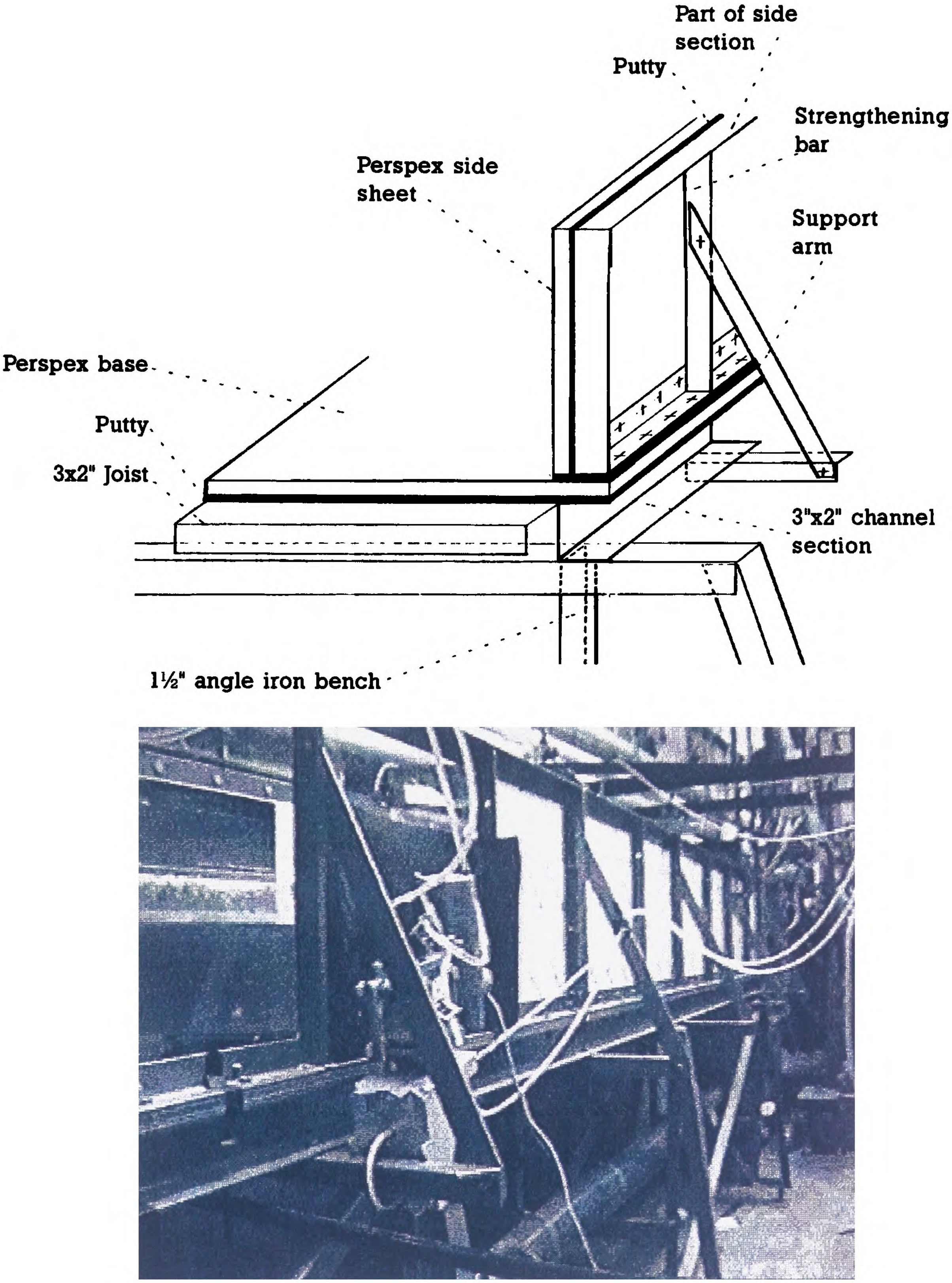

Figure 3a-b. The diagrams show the construction of the flume section of the equipment.

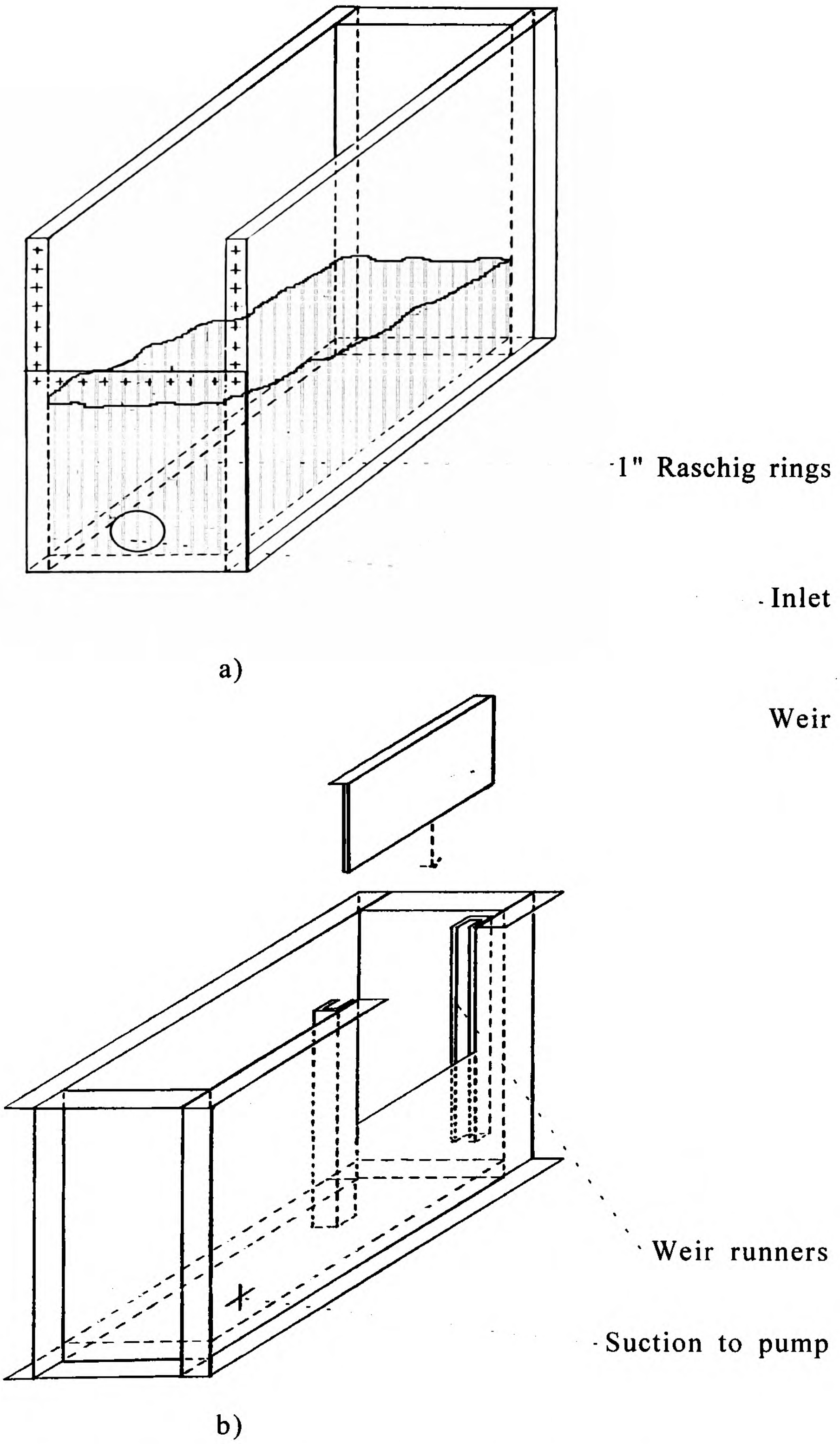

Figure 4a-b. Inlet and suction tanks showing weir and Raschig ring packing section (shaded area).

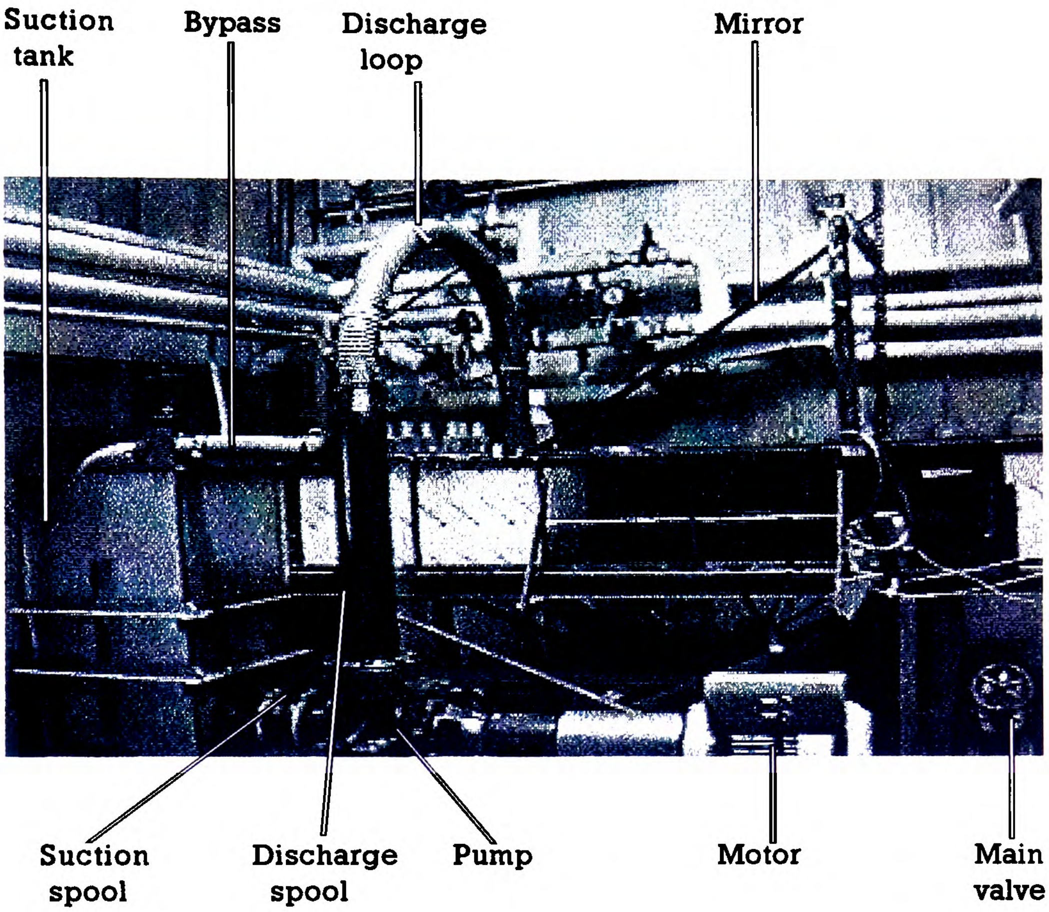

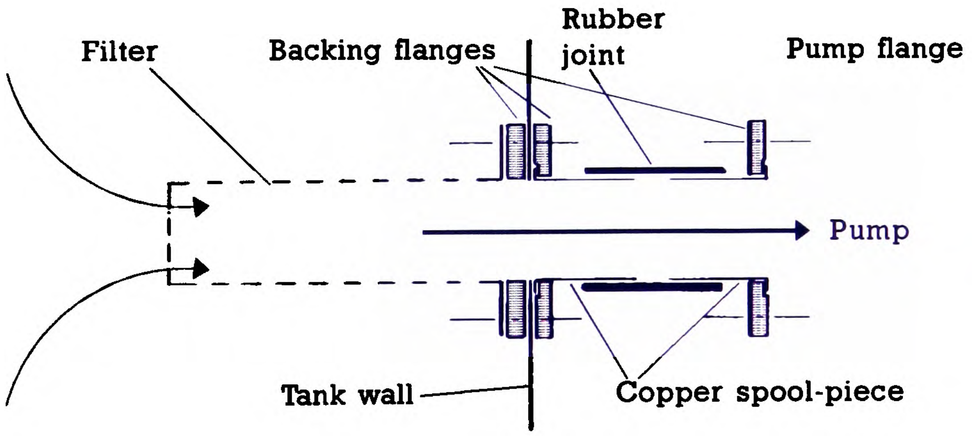

Figures 5&6. The suction tank, pump and valve and a schematic of the suction filter.

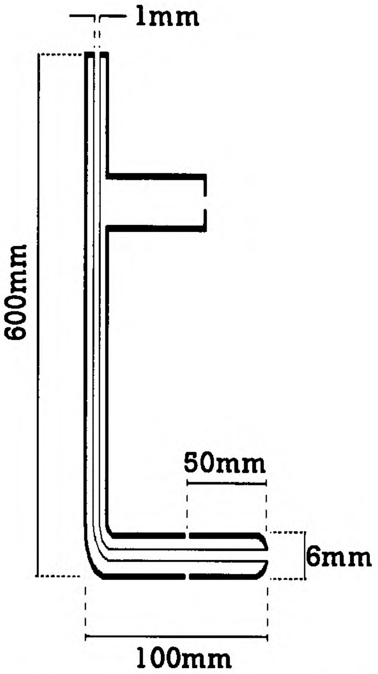

Figure 7. Dimensions of the pitot tube used for measuring the time-averaged flow velocity.

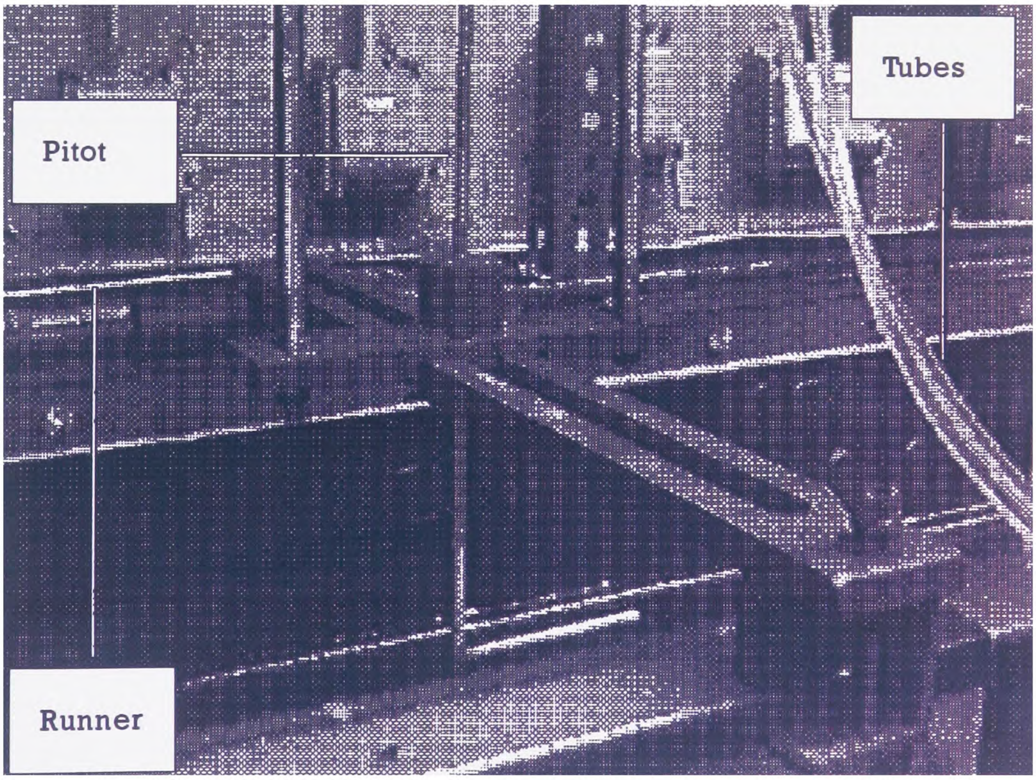

Figure 8. Cradle supporting Pitot tube allowing both lengthwise and widthwise traverse.

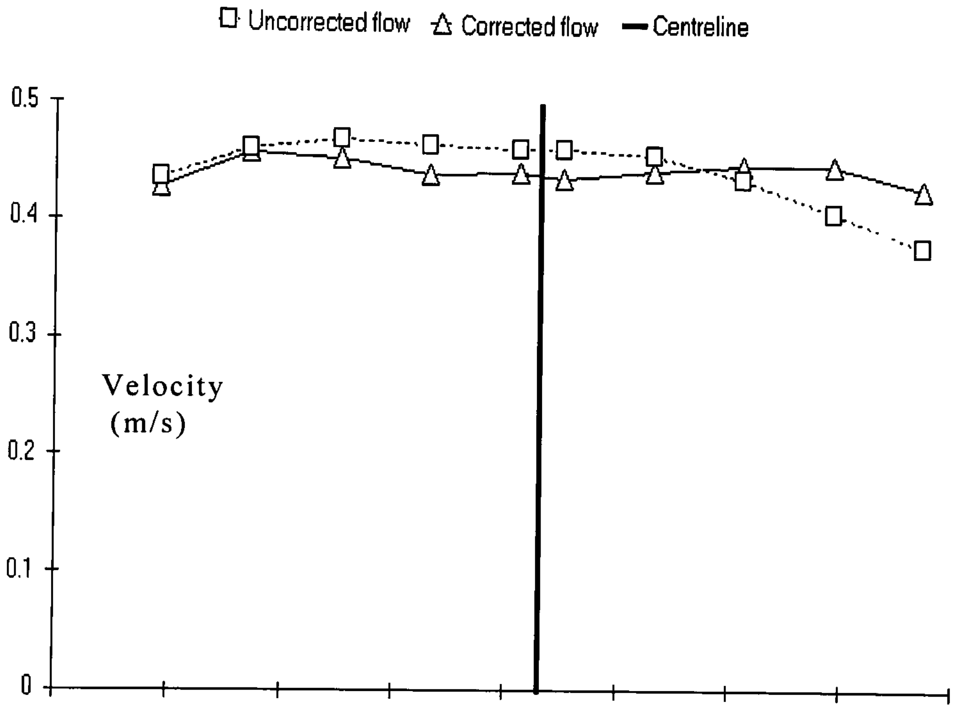

Figure 9. Velocity at various locations across the stream before and after adjustment of the Raschig rings in the inlet tank.

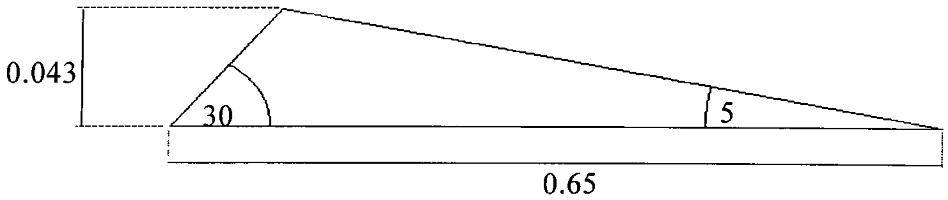

Figure 10. Experimental bedform dimensions (lengths in m, angles in degrees).

U(m/s)	D (m)	Froude num.	W/D	DevL/D	h/D
0.20	0.162	0.158	2.80	24	0.27
0.31	0.177	0.235	2.55	22	0.24
0.36	0.188	0.265	2.40	20	0.23
0.43	0.205	0.289	2.20	19	0.21

Figure 11. Experimental flow parameters at the four depth-averaged flow velocities used for experiments in chapters 3 and 4.

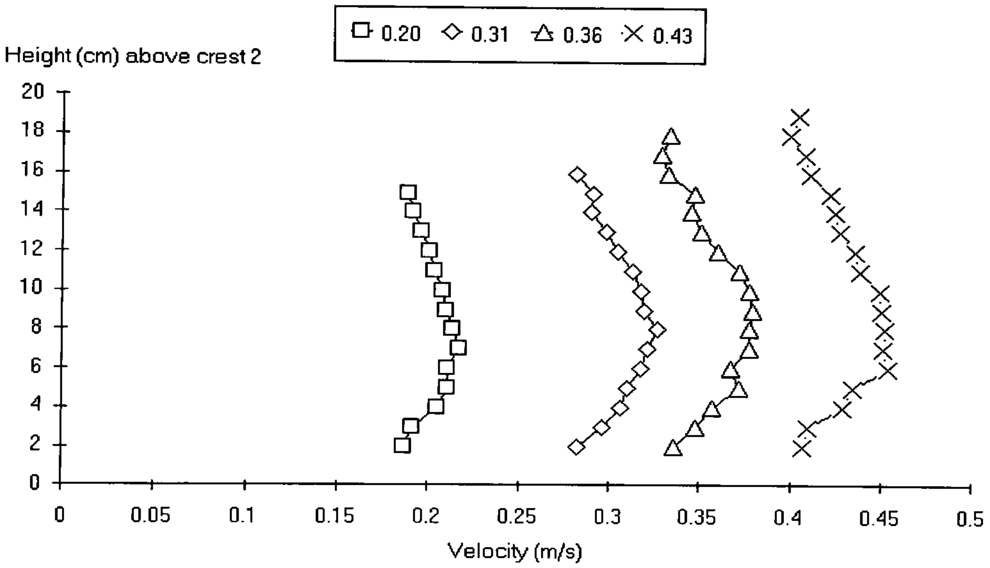

Figure 12. The four velocity profiles at crest two corresponding to the mean flow velocities in the table above. Notice the accelerated flow around 8cm above the crest.

Fall sp (m/s)	Length (mm)	Diam (mm)	S.g.
0.034	3.0+/-0.3	2.0+/-0.3	1.13
0.060	2.5+/-0.3	2.0+/-0.3	1.18
0.076	3.0+/-0.3	2.0+/-0.3	1.25

Figure 13. Physical properties of the experimental particles.

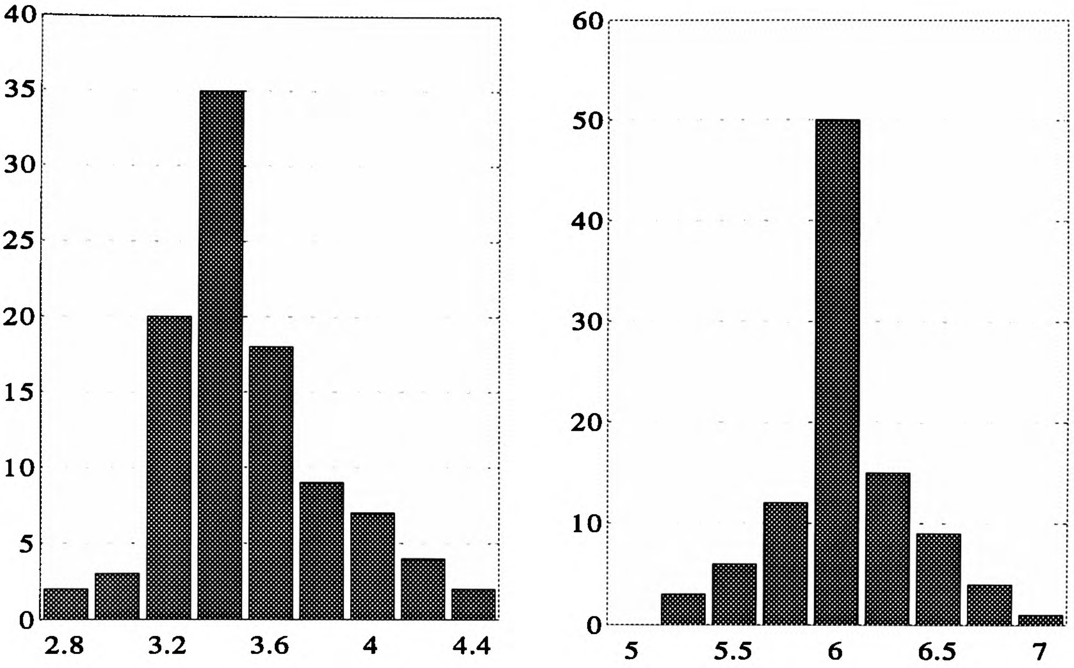

a) Mean=0.034m/s.

b) Mean=0.060m/s

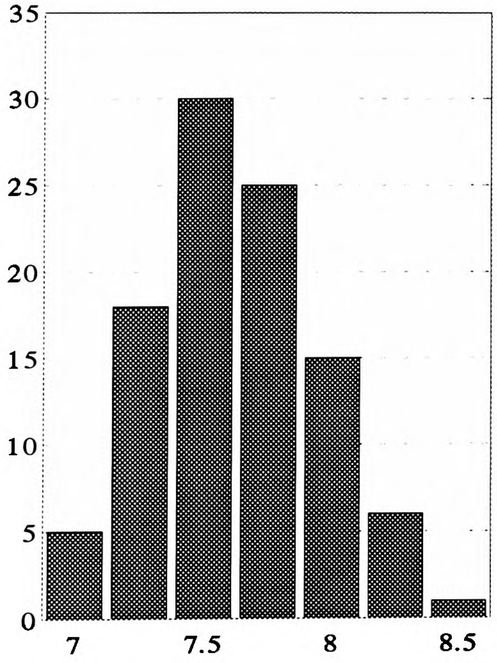

c) Mean=0.076m/s.

Mean Vel	S.D.
0.034	0.102
0.060	0.103
0.076	0.106

d)

Figure 14. a, b and c) show the distributions of the measured fall speed of 100 particles of each type. The mean velocities and standard deviations of these distributions are shown in d).

CHAPTER 3: JETTING EXPERIMENTS

SUMMARY

Our experimental studies address the question of sediment transport over fixed bedforms in an effort to elucidate the mechanisms responsible for sediment motion over mobile sandwaves. This chapter is confined to studying the contribution made to the suspended sediment budget downstream of the sandwave crest by sediment jetting from the upstream stoss slope. We model the sandwave using a fixed bedform and model the sediment grains with plastic prills of suitable quiescent fall speed. The particles are released on the upstream stoss slope and their trajectories are followed from the crest to landing sites either on the lee face or on the downstream stoss slope. Their contribution to the suspended sediment budget downstream of the crest is estimated. Seven trajectory types are identified. A concentration peak along the line of the shear layer is identified which highlights its important effect on the dynamics of the sandwave. The concept of an interactive fraction is developed; basically a range of sediment grain size where the ratio of fluid mean velocity to grain quiescent fall speed ranges from 4 to 10; which is in good agreement with similar work by Sene (1985; reported in Sene et al, 1993) and Nielsen (1984). The concept is used as a diagnostic tool to assess the suspended sediment budget at various flow velocities over a sandwave in an estuary.

1 INTRODUCTION

The main features of flow over sandwaves were reviewed in chapter 1 where we identified the crest shear layer as a dominant flow transport feature. Recall specifically the work of Muller & Gyr (1986) who showed that coherent vortices arising from instability of this shear layer subsequently pair, entraining and engulfing fluid until their growth is constrained by the dimensions of the flow, presently due to the proximity of the base plane: ie reattachment to the bottom topography. The shear layer is also unstable in the cross-stream direction, with the vortices typically distorting into horseshoe structures further downstream and emerging as the dominant feature after three to four pairings. The recirculating fluid below the shear layer, sometimes termed the separation bubble, is also unstable at lower frequencies corresponding to flapping motions of the shear layer. This behaviour has received little attention in the literature but is discussed at some length in chapter four.

Laboratory studies of these flows have often been conducted with fixed bedforms simulating the sandwaves (Lyn, 1993; Schreider & Amsler, 1992; Karahan & Peterson, 1980). The approximation is good since sandwave migration velocities are small when compared with the free stream velocity (typically one fiftieth), so deformations in the sandwave shape occur over timescales far longer than the flight time for individual grains (Johns et al, 1990). It has generally been recommended that four such waves are used in series so that the flow is approaching equilibrium

(Whitehouse RJS, HR Wallingford; private communication).

Allen (1984) studied sediment motion from the crest of model sandwaves. Narrowly sized grain samples were released at the crest and trapped where they landed downstream, either on a greased plate or in a segmented collector. In the first type of experiment the ratio of the free stream velocity U to particle-quiescent-settling speed V was varied through ratio values U/V = 2.57, 5.81, 14.4. The fraction of total particles landing on the greased plate at each downstream location on the lee face is shown in figures 1 and 2. Figure 1 shows that increasing U/V increases the distance over which sediment is suspended and reduces peak deposition near the crest. The lateral dispersion displayed in figure 2, which increases with increasing U/V, shows that three dimensional features have an effect on sediment transport.

Another set of experiments introduced a segmented collector in place of the solid lee and downstream stoss slopes. Three sediment samples were used with mean grain diameters of 870, 520 and 190 microns (V=0.12, 0.07, 0.03m/s). The finer grades were shown to travel further downstream and the deposition rate was found to relate to distance downstream according to a power law with a negative coefficient at low stream velocities. At higher velocities this "fit" was less satisfactory, though why such a law should be applicable was not explained.

2 EXPERIMENTAL METHODS

A detailed description of our experimental equipment and methods was presented in Chapter 2. Recall that three triangular section perspex wave forms of length 0.66m and height 0.05m were secured onto the floor of the experimental flume and sheet light was reflected off a mirror along the centre-line of the bedform, between the second and third crests. Only one crest was present upstream of the test section so as to ensure that any dynamical coupling between shear layers was not obscured by coherent structures from crest shear layers further upstream, as recommended in appendix 8. This method, which departs from the traditional view that three or four upstream bedforms be used, has been justified by the results, especially relating to Coanda-flapping where coupling between shear layer flapping motions and the passage of upstream shear layer vortices has been identified, as presented in chapter four.

The three types of particle used were all cylindrical plastic prills of diameter 0.001-0.002m and length 0.002-0.003m. They were selected to deliver fall speeds in quiescent fluid which allowed suspension at the flow speeds (0.2-0.8 m/s) available in our experimental equipment. Their sizes were discussed in chapter two: viz, they represent a compromise between the reality of micron sized sand grains and the millimetre resolution scale needed for our visualisation methods. Their suitability as regards shape will be defended by comparing present results with published work (sections 3.2a and 3.3c). Here we note that sand grains are not spherical and so must have defined separation points depending on their instantaneous orientations to the local flows. This is not the case for spherical particles which are often used as model substitutes for such grains, so we might argue that it is a reasonable compromise to use cylinders falling somewhere between these two extremes, perhaps even that our model particles may be more appropriate than spheres?

The methods employed in the trajectory experiments of section 3 were described in chapter 2; recall that the landing position and flight time of individual particles was recorded from video records of the trajectories of particles released on the upstream stoss slope. Their contribution to the particle concentration C in the lee fluid was measured by following individual particles. The time averaged relative concentration C_i/C_0 in any reference mesh is then related to the number of particles N_i that have passed through at mean velocity V_{pi} by the expression (Sene, 1985).

$$\frac{C_i}{C_0} = \frac{N_i}{N_0} \cdot \frac{\overline{V_{p0}}}{\overline{V_{pi}}} \tag{1}$$

where N_0 is the total number of particles tracked, C_0 is total particle concentration in the measurement grid and V_{p0} is mean velocity of the particles travelling through the grid. V_{pi} is related to the number of times that any single particle is counted in a square, here termed the number of footprints F_i that it leaves. For a square grid of side L(m) and time step t(sec) the relationship is then simply

$$\frac{1}{V_{pi}} = \frac{F_i t}{L} \tag{2}$$

V_{po}, the mean particle velocity in the grid is simply the mean of all V_{pi}

$$V_{po} = \sum V_{pi} = \frac{L}{t}\sum \frac{1}{F_i} \tag{3}$$

Hence the distribution of F provides a direct measure of the concentration distribution. It should be remembered when comparing data sets that the concentrations are percentages of the total concentration in the grid and not absolute values. The latter is determined entirely by the rate at which sediment is fed into the system through bedload transport, itself dependent on flow speed and grain size. A test for convergence is presented in section 3.3b. Two independent data sets, each calculated from 100 particle trajectories, are compared grid-square by grid-square to give percentage differences which provide a direct measure of the convergence for 100 particles and a pessimistic measure of convergence for the entire data set of 200 particles.

Our results comprise a survey over three particle sizes (slip speeds) at four flow velocities U=0.2, 0.31, 0.36 and 0.43m/s. Three such runs had coincident values of U/V (around 6) and gave very similar distributions for jetted sediment deposition sites.

To demonstrate that U/V represents a suitable scaling parameter for such surveys we present these three data sets together in section 3.2. The remaining data is surveyed in section 3.3 in order of increasing value of U/V from 2.7 to 12.8, the latter representing maximum achievable value in our equipment for reasonably representative Froude numbers, (see chapter 2).

3 EXPERIMENTAL RESULTS

We divide our results into three sections, firstly presenting visualisations of shear layer vortices and particle capture, secondly considering jetting at U/V=6 and finally assessing jetting at other values of U/V.

3.1 Shear layer and particle capture visualisation

Visualisation of shear layer vortices is complicated by the fact that they are moving targets. The fluid elements in the vortex prescribe near circular orbits in a frame of reference moving at the vortex speed so these orbits are cycloidal in an Eulerian frame. At low stream velocities (<0.1m/s) the vortices can be visualised adequately since they rotate slowly and are coherent but at higher speeds they tend to be more diffuse and irregular and are thus difficult to visualise. The ten plates in figure 3 are taken at 1/25 sec intervals with a shutter speed 1/50 sec. They show the development of a shear layer vortex over a triangular section bedform (0.2m high, length 0.2m, 50° internal angle lee slope) at a flow velocity about 0.1m/s and Froude number about 0.14. They were taken using older, uninstrumented experimental equipment not reported in detail here, but have been included because of their clarity.

Figure 4 shows the trajectories of two particles (fall speed 0.034m/s) suspended from the crest region of the bedforms as described in section 2. The flow velocity at 0.36m/s is too high for vortex visualisation, for reasons discussed previously. The particles follow cycloidal paths around a vortex whilst travelling downstream as expected. Notice that they move upwards during part of their trajectory, an important point for comparison with chapter 5 data and discussed in chapter 7.

3.2a) Jetting trajectories at U/V=6

Landing sites (intervals 1 to 24) are grouped into triplets, as shown in figure 5. The deposition data are presented as distribution diagrams in figure 6. This raw data show that most of the particles settle on the lee face (positions 2 and 5) and in the recirculation zone (positions 8, 11, 14 and 17), within two seconds of entering the measurement section. The modal (most frequent) trajectory deposits on the upper lee region whereas the median (average) trajectory is onto the lower lee region.

The particle trajectories could be split into primary modes based on where they landed and to where they were swept after landing, seven in all as follows. The first mode M1 contains trajectories similar to that shown in figure 7a, characterised by paths to the crest regions (ie sectors 1,2 and 3 in figure 5) in times between 6/25 and 20/25th of a second. This mode contains the modal trajectory. The second mode M2 is shown in figure 7b and includes all other particles settling on the lee slope (ie at positions 2 and 5) in times greater than 20/25th of a second. This includes the median trajectory where particles have generally been engaged by one or more eddy events in the free shear layer.

Mode M3 (figure 7c) contains all paths to sites 7, 8 and 9, identified as location 8 in figure 5. These particles have been transported across the shear layer but are rapidly deposited having once travelled further downstream: ie they have experienced upstream drag from eddies in the recirculating region. The fourth and fifth modes contain particles that have experienced turbulent motions before settling at positions 11, 14 and 17 but have been swept back towards the lee face, as in figures 7d & e. The sixth mode represents particles that settled at positions further downstream than station 6 and were swept away over the next crest (as in figure 7f) whereas mode seven (figure 7g) contains all particles not landing within the field of measurement: ie travelling further downstream than station 25.

Figure 6 shows that 18% of the particles take M1 trajectories to the upper lee slope regions, 46% take M2 trajectories to the lower lee, 30% take M3,M4 and M5 trajectories onto the stoss slope but are returned to the lee by the recirculating flow and only 5% are swept down stream, either suspended or travelling along the stoss slope.

Figures 8 and 9 tabulate the mean vertical and horizontal velocities (cm/s) during the entire flights of particles reaching the various landing sites. M1 particles have characteristically high downwards velocities, approximately equalling the fall speed, whereas M6 particles possess average downwards velocities of about one quarter the fall speed. Horizontal velocities are about half of the depth-integrated velocity, which differs by only about 10% from the local crest velocity for modes 4,5 and 6 and less than 25% for modes 1 and 2.

Figure 10 graphs the settling rate with respect to distance downstream. The logarithmic fit employed here appears adequate except near the crest where particles jet into the flow. This comparison justifies our choice of particle since it agrees well with the logarithmic dependence obtained by Allen (1984). A direct comparison between our data set and results for Allen's greased plate experiments (U/V=5.8) appears in figure 11. Quantitative agreement is not expected since Allen used eight collectors on his lee slope whereas we used six, so we should receive percentages averaging 100/6=17% whereas Allen's should only average 100/8=13%. Nevertheless, the similarity is most encouraging, with discrepancies essentially confined to the base of the lee slope where our data shows higher values. These behaviours can be attributed to particles sedimenting on to the lee through M3 and some M4 modes which, presumably did not stick to the greased plate in Allen's experiment but are included in our data set.

Figure 12 tabulates the three runs where U/V≈6. The consistency in the percentage of particles taking each of the trajectories M1 to M7 confirms our initial assumption that the absolute values of U and V are unimportant and that scalings should be based on the ratio U/V.

3.2b) Jetted load concentration distribution at U/V=6

Figure 13 shows the concentration distribution for U/V=6, generated by marking the particle positions every 0.2s from the time that they move over the crest to the time that they land on the lee or stoss slope downstream. 164 particles were tracked giving 1785 footprints on the 43 grid squares. The particles spent an average of 2.2s in suspension before settling to the bed.

As expected, the M1 and M2 trajectories show the highest concentrations and only low concentrations are found above the crest height, showing that particles are not ejected into regions above the shear layer. The peak concentration occurs at the same elevation as the crest and at the end of the lee slope. This peak is convincing evidence of the capacity of the shear layer to support dispersed particles against the buoyancy forces acting upon them.

3.3a) Jetting trajectories when U/V<6

The percentages of particles following the seven trajectory modes at various values of U/V are tabulated in figure 14. There is a cut-off point for U/V between 3.3 and 4.1, below which the particles are only deposited on the lee slope. A second point, where particles land on the downstream stoss slope but are swept back to the lee slope and not carried off downstream, is shown in figure 15. This demonstrates how the fraction of particles that are returned to lee slope depends on U/V; recall that in modes M6 and M7 the particle is transported to the downstream bedform. The significant change occurs around U/V=5. Thus for U/V<5, there is deposition such that all the sediment remains with the sandwave from which it came. Recall that the sandwave migrates downstream and eventually covers the grains deposited close to the lee slope. At higher values of U/V, the grains are progressively stripped from the bedform and moved to the downstream bedform. The distribution diagram for U/V<3 is not reproduced because the particles travel almost solely to the crest.

3.3b) Trajectories and concentration profiles when U/V=9

The settling distribution here is displayed in figure 16 where we see that the bulk of the particles have settled within 45 frames, mostly near to the crest but in considerable numbers further downstream. The modal trajectory is M2 and the median is M4. M1 trajectories to the upper lee slope are taken by 10%

of the particles, whereas 26% take M2 paths to settle on the lower lee slope with 44% taking M3, M4 and M5 paths to the stoss slope before returning to the trough region. The remaining 20% are swept from the flow measurement section.

The concentration distribution here was obtained by tracking 200 particles with time intervals of 0.04 sec, registering 7918 footprints. The particles were in suspension for an average of 1.6s, and produced the concentration profiles shown in figure 17. Here, the vertical grid lines are spaced at 1% concentration intervals, so the first line on the right has peak concentration of 1.5% whereas the fourth line has a peak concentration of 4.7%. Vertical dispersion is manifested in the broadening of profiles with downstream distance up to X=0.17m, after which point it attains apparently constant depth. The peak value increases rapidly for X upto 5 and then decreases more slowly for larger X. The particles register amplified concentration above the crest indicative of vortices capturing particles for the initial conditions used here. This aspect is discussed more fully in our numerical studies (chapter 6) and is broadly in line with expectations outlined in Thomas' (1990) proposal on this project.

As a convergence test for these data, figure 18 tabulates the percentage difference between the concentration profiles for two subsets of 100 particles in the total sample of 200. Key regions over the crest and within the shear layer show up to 20% variations, suggesting our results are adequate to reveal trends with about 10-15% error. Further away from the peak regions the errors increase substantially due to the decreasing number of footprints registered.

3.3c) Trajectories and concentration profiles when U/V>9

Deposition distribution for U/V=10.8 is shown in figure 19. The dominant modes are M4 and M7 with the modal and median trajectories being M4. Of the particles transported downstream in the shear layer, 43% escaped into the return flows to the lee slope and 35% were swept downstream.

At U/V=12.8 the modal trajectory is M7 and the median M5. Here, 43% of the particles were swept downstream and 44% were returned to the lee slope. Figure 20 compares this data with Allen's (for U/V=14.4) and good qualitative agreement is demonstrated; recall figure 11. Figure 21 shows vertical concentration profiles for which the peak value is 4.8%. Notice that the sediment is distributed more evenly here (ie less trapping) than at lower U/V (recall figures 13 & 17), reflecting the shift to the higher number modes.

3.3d) General effects of varying U/V

Figure 22 summarises all our information for U/V from 6 to 12 classified according to the trajectory modes shown in figure 7. It displays an artificial peak for the M4 trajectories, "artificial" since they cover double the number of landing sites compared to the other modes. The overall picture is now clear:

namely, increasing U/V reduces the proportion of the jetted sediment that lands in the lee slope (modes M1 and M2) and increases the proportion that is carried to the downstream crest (M6 and M7). The M3 and M4 trajectories are changed only slightly perhaps because this model coincides with the time-averaged reattachment point. We say this because the ratio of separation length to bedform height is often said to be about 3 (Nezu & Nakagawa, 1991), corresponding to the M4 model (ie at 0.15m). The sedimentation rate onto each site expressed as a percentage of total sedimentation for these runs has been discussed previously.

As a correlation basis for practical applications, our data sets were fitted with the exponential function $S=bX^m$ where S is the sedimentation rate and X is the distance downstream. Figure 23 shows best fit values of exponent (m) and intercept (Lnb) plotted against U/V. They vary nearly linearly with U/V, giving a good fit at high U/V values. This implies that the local sedimentation rate at any U/V can be expressed as a function of U/V and X. From the gradients of the two lines in figure 23 we have as correlation fit to our data:

$$\frac{S}{S_T} = e^{\left(0.8\frac{U}{V}-8\right)}.X^{\left(0.43\frac{U}{V}-5\right)} \qquad \textbf{(4)}$$

where S_T is the total sedimentation rate of the jetted load, ie the bedload transport rate. There is no obvious significance to this formula, but at least it provides an approximation for likely distributions.

4 DISCUSSION

For any given flow rate over a flat bed or over a bedform carrying a wide particle size range we can divide the total sediment transport into bedload, suspended load or wash load; Gyr (1983). Flow separation causes essential differences in the bedform system, mainly by producing a distinctively inhomogeneous vorticity distribution which is available to interact with the sediment. Our experiments were designed to highlight visually this behaviour and to characterise important suspension mechanisms around such bedforms.

Although direct visualisation made for tedious retrieval of quantitative information (25,000 footprints from 2500 trajectories), it nevertheless provided an opportunity to identify a new phenomenon in sandwave transport which is reported in chapter 4. The use of fixed bedforms and model particles facilitated independent observation of sediment suspension from different areas of the bedform.

In closing this section we define an "interactive fraction" for sediment suspension from jetted load and consider how this concept may be utilised for field application.

4.1 Interactive Fraction (FI)

Our jetting studies identified seven main modes of suspension ranging from short paths onto the upper lee slope to long trajectories over the recirculation zone. From figure 14 we see that increasing U/V is associated with increasing proportion of longer (higher M value) trajectories. For bedforms with a wide particle size range our data suggests the bedload will experience a broad dispersive sorting process during ejecting over the crest. The largest particle grades (U/V about 4) will follow trajectories onto the lee slope; whereas the finest grades (U/V about 10) will be suspended by the shear layer and deposited further downstream. Particles for which U/V is between 4 and 10 will deposit in more or less rank order between these limits and this represents an 'interactive fraction'. Here the forces acting on the particles are sensitively balanced such that slight adjustments in U/V determines whether gravity or the flow forces are dominant.

We may also define FI_0 as the grain size for which U/V=7: ie the midpoint of the range within FI. In accelerating flows, such as tidal estuaries, the FI concept may be helpful as an indication of effective mobility. Knowing the stream speed and sediment size distribution we can extract the proportion that travels with each bedform as opposed to moving between bedforms. This distinction has direct implications for the total sediment transport rate and the bedform migration velocity both of which are of concern in civil engineering hydraulics.

Our suggestion here is akin to that detailed in Sene (1985), also Sene et al (1993), who deduced numerically from a discrete vortex model of bubbly flow that inertial force was critical in retaining trapped bubbles in shear layers with U/V above 2, with significant confinement for U/V=3.5. Nielsen (1984) also found that the vertical suspension length scale (defined as the ratio of the height reached by suspended sediment to the height of the ripple) varies linearly with U/V between constant values for U/V<3 and U/V>10, where U now is the maximum orbital wave velocity.

4.2 Example test using the FI concept

We now turn to the field data of Atkins & Soulsby (1992) who carried out a survey of sediment suspension over a sandwave in the estuary of the river Taw, North Devon. The bedform sediment had diameters 0.06mm<d<2.00mm distributed over these sizes as indicated in figure 24. Flow velocity and sediment concentrations over this sandwave were measured during flood tide when appreciable bedform motion occurred and the results were grouped into four bands for which the depth-integrated flow velocity was 0.1-0.3m/s, 0.3-0.5m/s, 0.5-0.7m/s and 0.7-0.9m/s. The FI for each of these bands is tabulated in figure 25. Here the centralised velocity is used to define U/V limits for the FI so as to retrieve estimates of the particle settling speed V and hence the sediment grain diameter d.

The FI contains particles from 0.17 to 0.4mm, with FI_0=0.24mm for band 1 velocity as compared with maximum size of 2mm. This indicates there is a high proportion of particle sizes which probably travel only onto the lee slope and a far narrower band which probably travels over to the downstream sandwave. In band 2 the FI ranges from 0.33 to 0.74mm, with FI_0=0.44mm which is about the maximum size present in the bedform in any quantity (recall figure 24). Band 3 has FI ranging from 0.47 to 1.26mm, with FI_0=0.64mm and band 4 gives FI from 0.61 to 2.25mm, with FI_0=0.84mm. We recognise there may not actually be any grains of diameter FI_0 in the bedform, especially at high flow velocities when a high fraction of the transport is by suspended load transported by jetting from crest to crest.

Figure 26 tabulates our analysis of the jetted sediment in sizes from 100 to 400 microns as extracted from figure 24. In this particular case the sediment is 99% sub 400 micron such that FI_0 exceeds commonly found grain diameters for band 3 and 4 velocities. The second column in the table shows fall speed V (from Hallermeier's (1981) correlation of grain fall speed vs size) for each sediment size and the third column gives the ratio U/V. By comparing this U/V value with our experimental values and by linear interpolation where necessary, we obtain an estimate of the fraction of jetted load which follows M6 and M7 trajectories onto the downstream sandwave. This is presented as the fourth column in figure 26. The fifth column shows the mass fraction of each size in the sandwave, implicitly assumed here to equal the jetted mass fractions. Whilst this may be a fair assumption for sampling taken from the uppermost layers, it does not accommodate the differing migration velocity of each fraction along the stoss slope. However, in the absence of further information to improve on this supposition, we proceed as follows.

Multiplication of column five by column four gives the percentage of each sediment fraction following M6 and M7 trajectories, as shown in column six. The sum of column six entries represents the total jetted sediment that travels from the crest to the stoss slope where it is then transported downstream, in this case 21% of the total jetted load. A similar calculation for band 2 suggests about 84% escapes as jetted load. Our data set does not extend above this range because higher values of U/V implies smaller particle size and introduces uncertainties about the assignment of V for finely sized particles in our experiments.

In summary then, we deduce that as the velocity is increased there is not only an increase in the jetted particle flow rate but also an increase in grain diameter that is suspended. Also, there is a decrease in the proportion of sediment that remains with the sandwave as it travels downstream. In chapter 4 we propose this as an important factor for dune washout.

5 CONCLUSIONS

The concentration data reported here display peaks at elevations corresponding to the crest height, confirming how crucial is the role played by the free shear layer in engaging, capturing and transporting the sediment downstream. Also, there is evidence of particle ejection from the shear layer at higher U/V, another method for elevating particles to heights above the bed which could not otherwise be achieved by the mean flow. The diversity of modal trajectories for any given U/V indicates that temporal excursions from the mean flow behaviour play an important role in sediment distribution beyond the crest.

The jetting experiments described above have allowed us to formulate the concept of an interactive fraction corresponding to U/V value in the range 4 to 10. Values below 4 result in trajectories which deposit on the lee slope ie the fluid forces are exceeded by the gravitational force whereas values greater than 10 lead to particles being jetted away from the lee slope onto the downstream stoss slope or even to the next bedform: ie the fluid forces here dominate gravity. The interactive fraction covers values of U/V for which there is a balance between the flow forces and gravity. We gave an example of the use of this concept for sediment transport in a real flow and linked the notion to earlier findings reported in Sene (1985) and Nielsen (1984).

The bottom line seems clear: namely, that any numerical modelling technique failing to incorporate a structured representation of the shear layer vortices will exclude the effects discussed above. At best this is misguided, except for cases of limited interest when U/V<<3 and U/V>>12, when the suspended load is unlikely to be important. Such an entrainment law has not been considered by proponents of numerical models; recall our review in chapter 1.

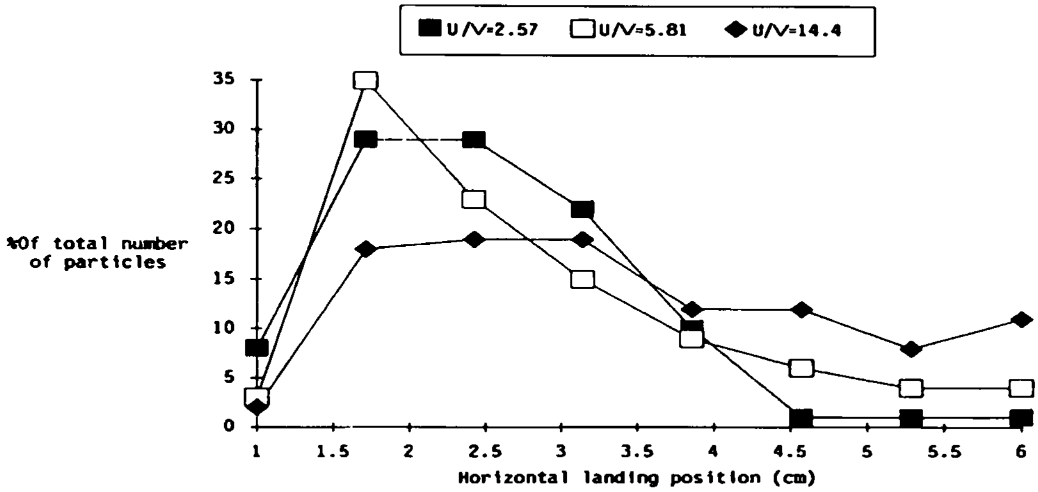

Figure 1. After Allen (1984). Lee slope landing sites for sediment jetting over the crest of a sandwave. Sediment is deposited further along the lee slope with higher values of U/V.

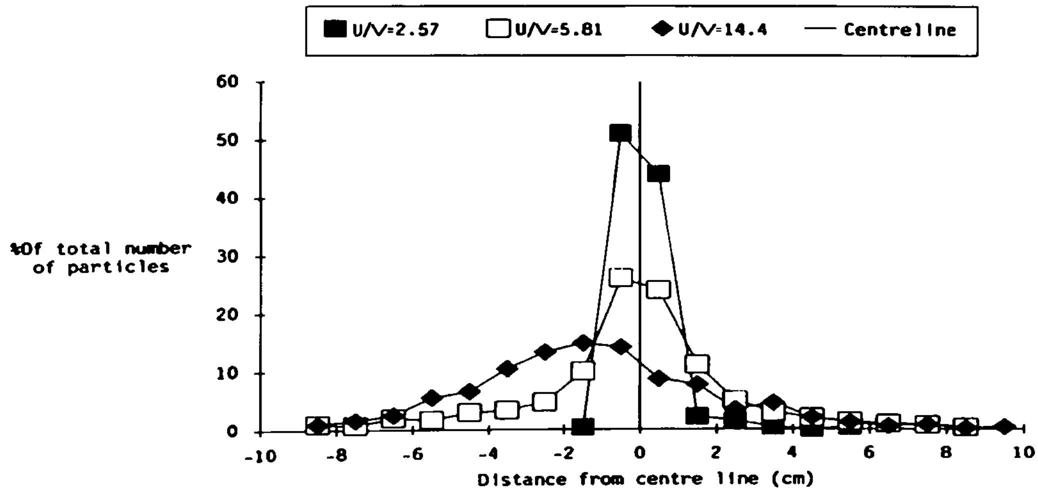

Figure 2. After Allen (1984). Widthwise dispersion of sediment jetting over the lee slope of a sandwave.

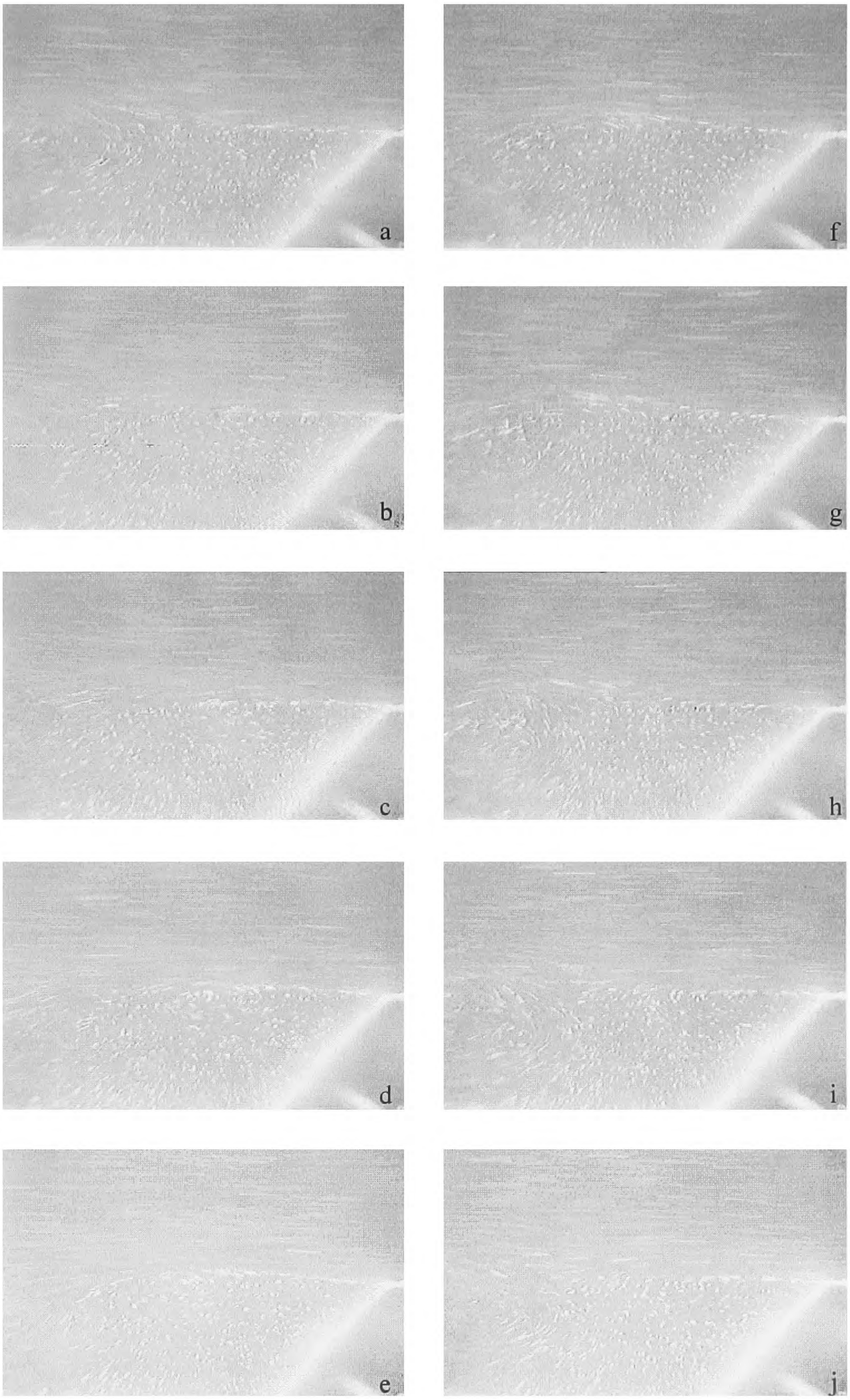

Figure 3a-j. The plates show the development of a shear layer vortex over a steep-lee-faced dune at a crest velocity of about 0.1m/s. Had the camera been slightly further to the left we would see the vortex in plate a) move off downstream.

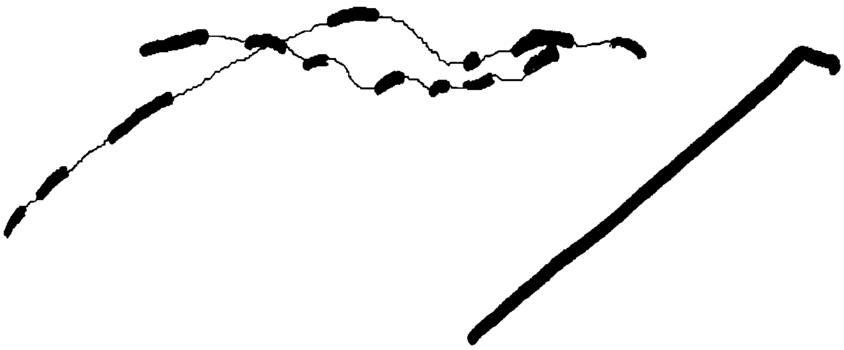

Figure 4. The cycloid-like trajectories of two particles entrained into the shear layer and transported downstream. The crest velocity is about 0.36m/s. The bedform angle is 30 degrees to the horizontal but appears larger due to graphical manipulation.

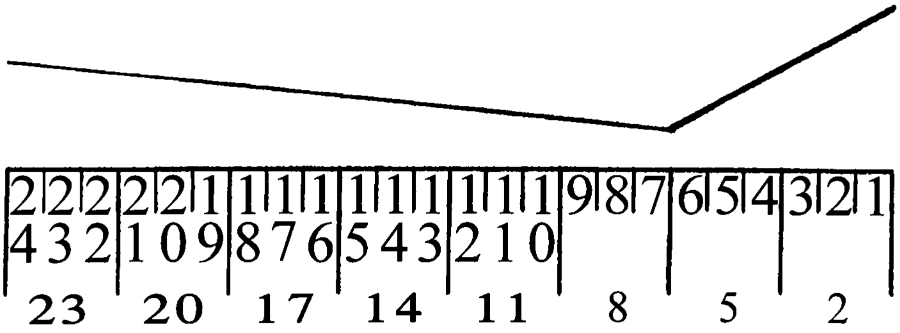

Figure 5. The view field, positioned after the second crest (the rightmost point of the bedform above) was divided into 24, 0.012m long categories for gathering of the trajectory data, giving a total view field length of 0.29m ie 44% of bedform wavelength). Subsequent analysis used groups of three landing sites denoted by the central value in the range, ie 2, 5 etc.

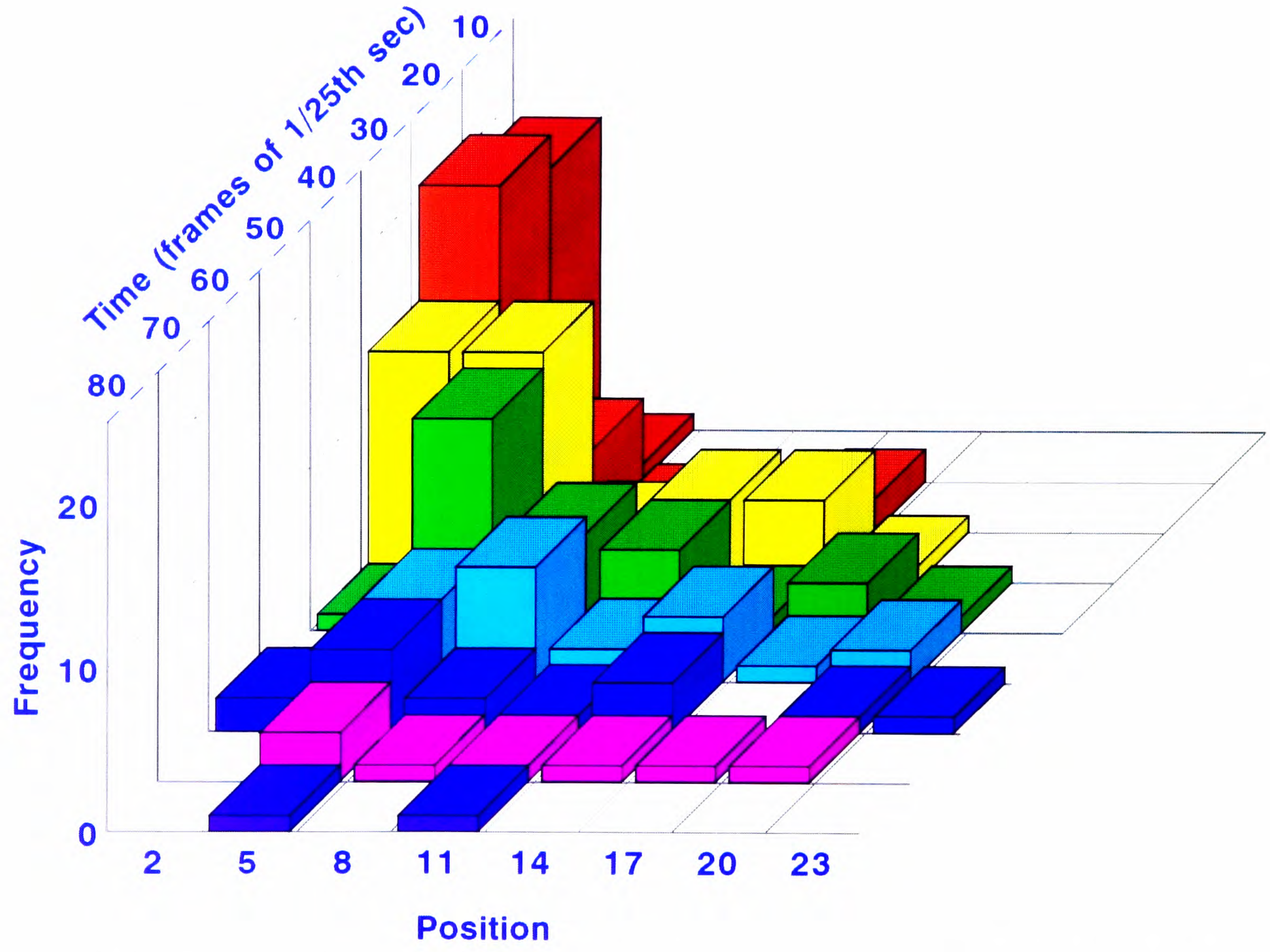

Figure 6. Distribution of particle landing sites for U/V=6. Most of the particles land on the lee slope within two seconds of leaving the crest.

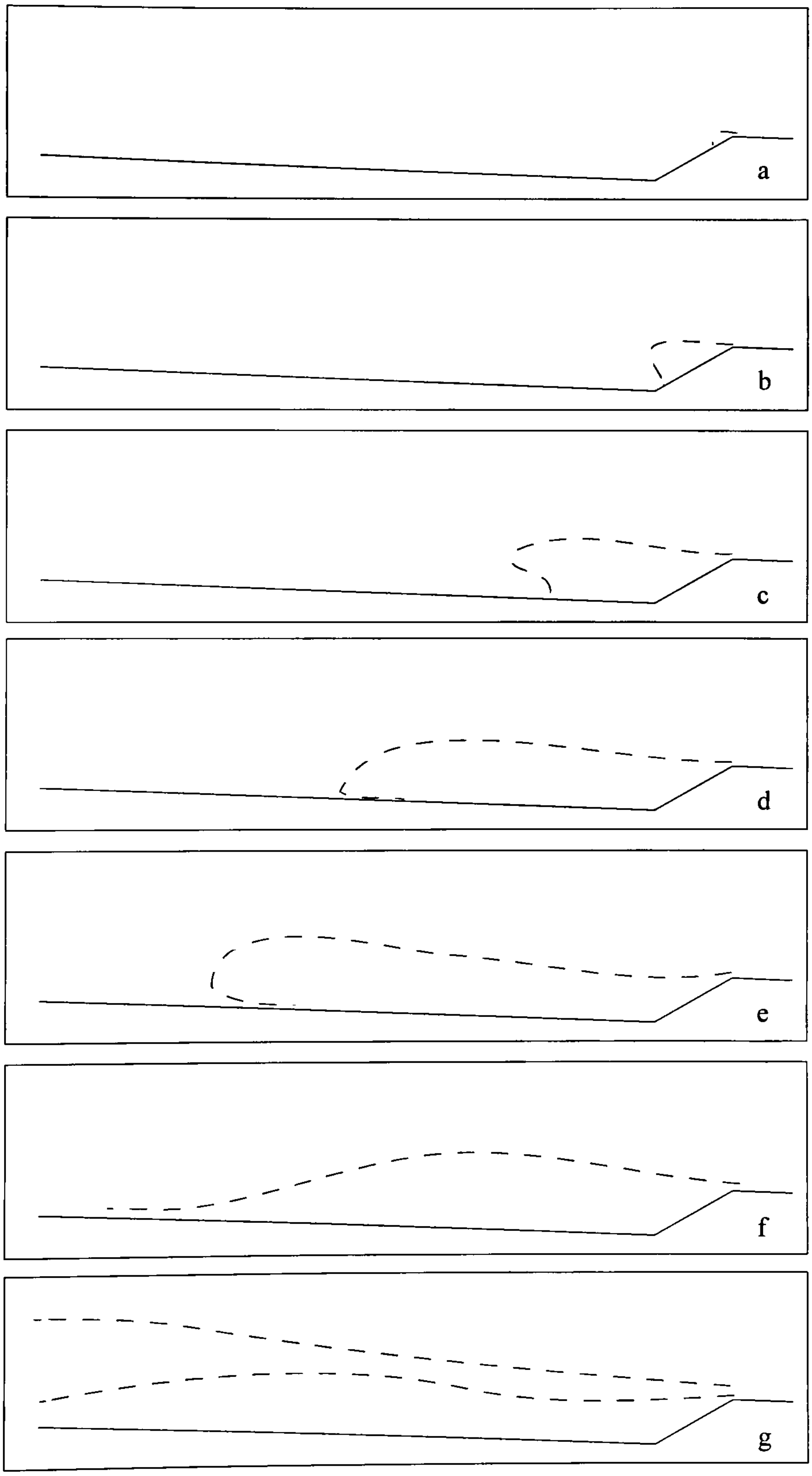

Figure 7a-g. The seven trajectory modes for jetted particles. a) M1 b) M2 c) M3 d) M4 e) M5 f) M6 g) M7.

Number of 1/25th sec video frames taken to travel to position X(cm)

X(cm)	8	13	18	23	28	33	38	43	48	53	58
1	2	1	1								
2	4	3	2	2	1	1					1
3			3	2	2	2		1			1
4		5		3	2	2	2	2	1		
5			4		2	2	2				1
6					2	2	2	2		1	1
7				3	2			2		1	1
8						2	2	1	1	1	1
9								1	1		
10				3	2		2				
11					2				1		

Figure 8. The average vertical velocity (cm/s) of particles landing at each location downstream of the crest, where X is the horizontal landing position. The particle quiescent fall speed is 3.4cm/s. It is clear that particles are deposited at the crest regions by being thrown over the first vortex in the shear layer at a velocity higher than this fall speed.

Number of 1/25th sec video frames taken to travel to position X(cm)

X(cm)	8	13	18	23	28	33	38	43	48	53	58
1	3	2	1								
2	6	4	3	2	2	2					1
3			4	3	3	2		2			1
4		8		4	4	3	3	2	2		
5			7		4	4	3				2
6					5	5	4	3		3	3
7				8	6			4		3	3
8						6	5	5	4	4	3
9								5	5		
10				11	9		7				
11					10				6		

Figure 9. The average horizontal velocity (cm/s) of particles landing at each location downstream of the crest, where X is the horizontal landing position. The figures are in cm/s for easy legibility. The mean stream speed U is 20cm/s so the particles travel with velocity far lower than this, as is expected in a region of vorticity where the vortices are travelling at about the average speed of the mean flow and recirculating flow (about half the mean stream speed).

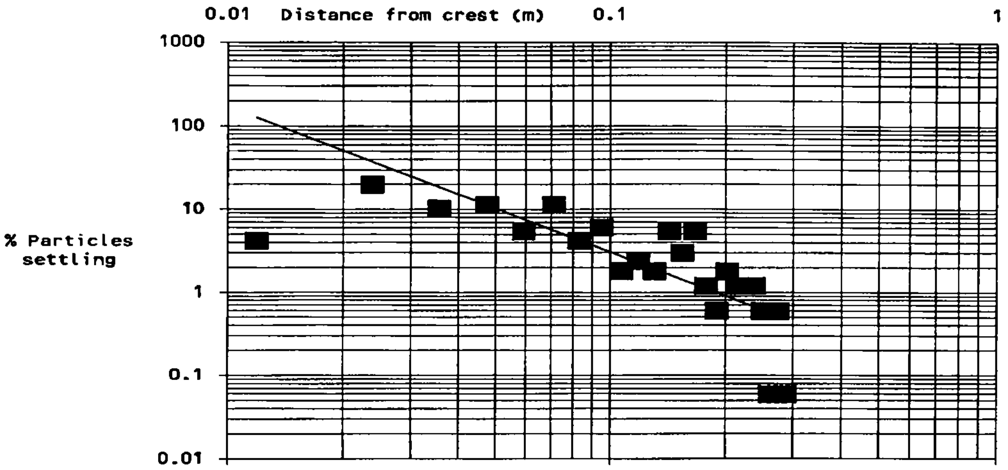

Figure 10. Variation in percentage settling rate with distance downstream of the crest for U/V=6. The line is a least squares fit to the data, excluding the leftmost point (as Allen found, the deposition near the crest is low compared to further downstream because the particles are jetted at the stream velocity in fixed bedform tests). The logarithmic fit compares well with that of Allen (1984).

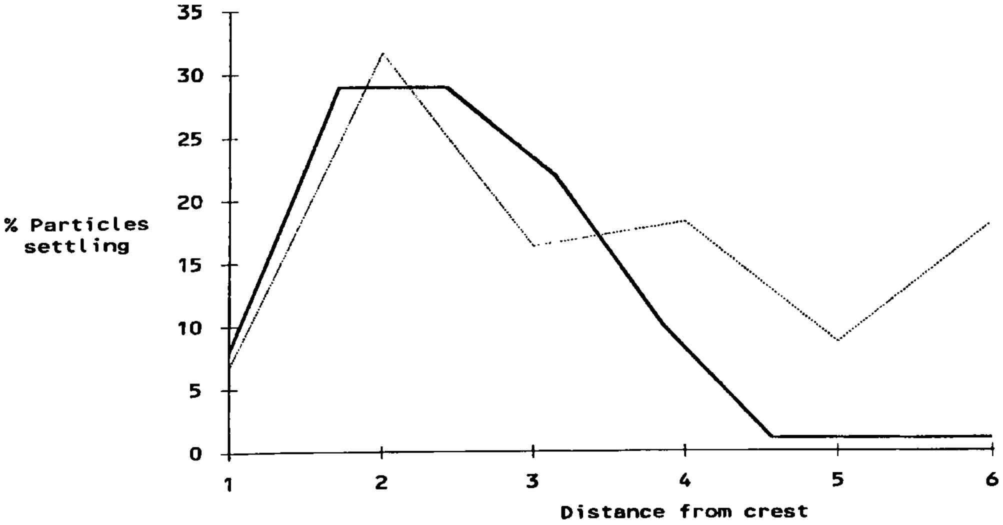

Figure 11. Comparison between our data at U/V=6 (dotted) and that of Allen (1984). The fit is good except at the outer regions where our data shows higher values due to sediment returning to the lee slope through trajectory modes M3-M5 which are presumably excluded from Allen's data set.

U(m/s)	V(m/s)	U/V	M1+M2	M3	M4	M5	M6	M7
0.20	0.034	5.9	64	10	16	4	4	2
0.36	0.060	6.0	75	12	9	1	2	1
0.43	0.076	5.7	68	7	13	3	6	3

Figure 12. Comparison between the deposition data gathered for three runs where U/V is about six. The similarity between the figures for each mode encourages us to choose a scaling based on U/V rather than the individual values of U and V.

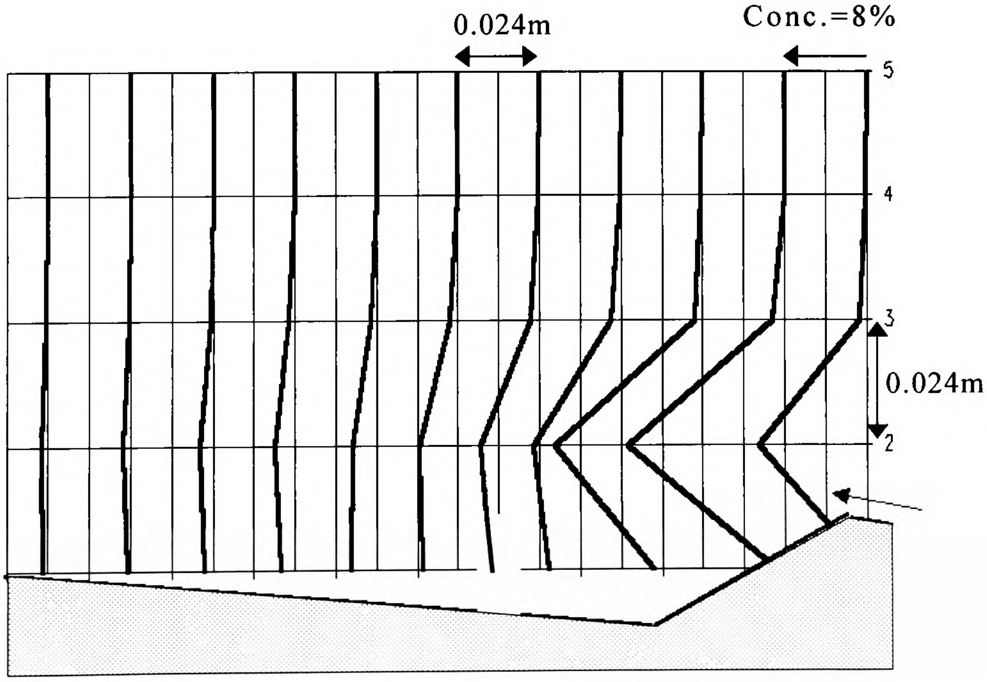

Figure 13. Relative concentrations of particles at each horizontal location at U/V=6. The peaks along the line of the shear layer show its crucial role in sediment suspension. The bedform image (grey) overlaps into the graph to show the orientation of the concentration lines in space. The lowest point of each thick line represents the concentration in the grid square (or partial square, eg grey square) just above the bedform surface.

U/V	M1+M2	M3	M4	M5	Mg	M7
2.7	100					
3.3	100					
4.1	95	4	1			
4.8	80	7	9	2	2	
5.2	88	6	4	1	1	
5.7	68	7	13	3	6	3
5.9	64	10	16	4	4	2
6.0	75	12	9	1	2	1
7.2	61	12	12	3	6	6
9.3	36	13	25	6	9	11
10.7	22	9	25	9	11	24
12.8	13	8	24	12	11	32

Figure 14. Table showing the relative sediment deposition through modes M1-M7 at various values of U/V from 2.7 to 12.8. Higher U/V leads to lower lee slope and higher stoss slope deposition rates.

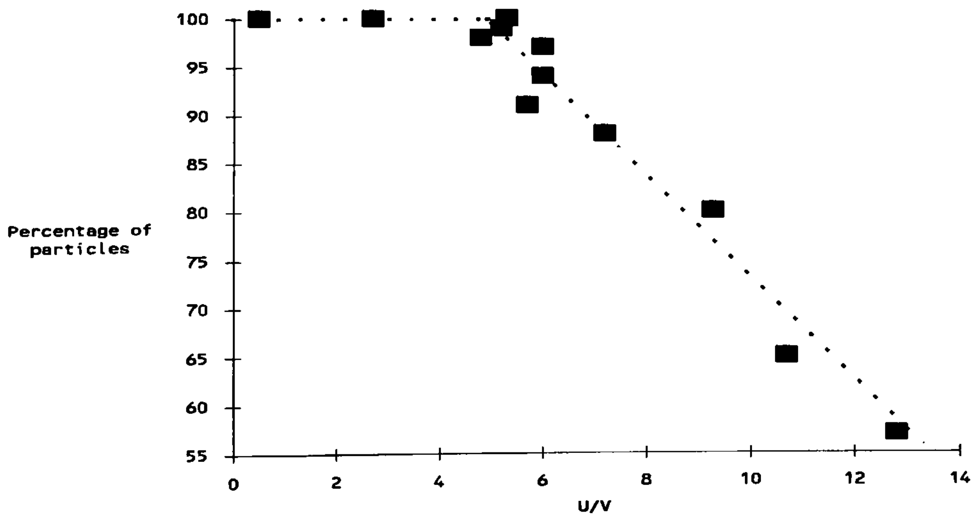

Figure 15. The data in figure 14 is plotted above as the sum of the deposition figures for modes M1-M5 (which are the ones where sediment returns to the lee slope) against U/V. Higher values of U/V lead to sediment being stripped from the bedform and moved downstream.

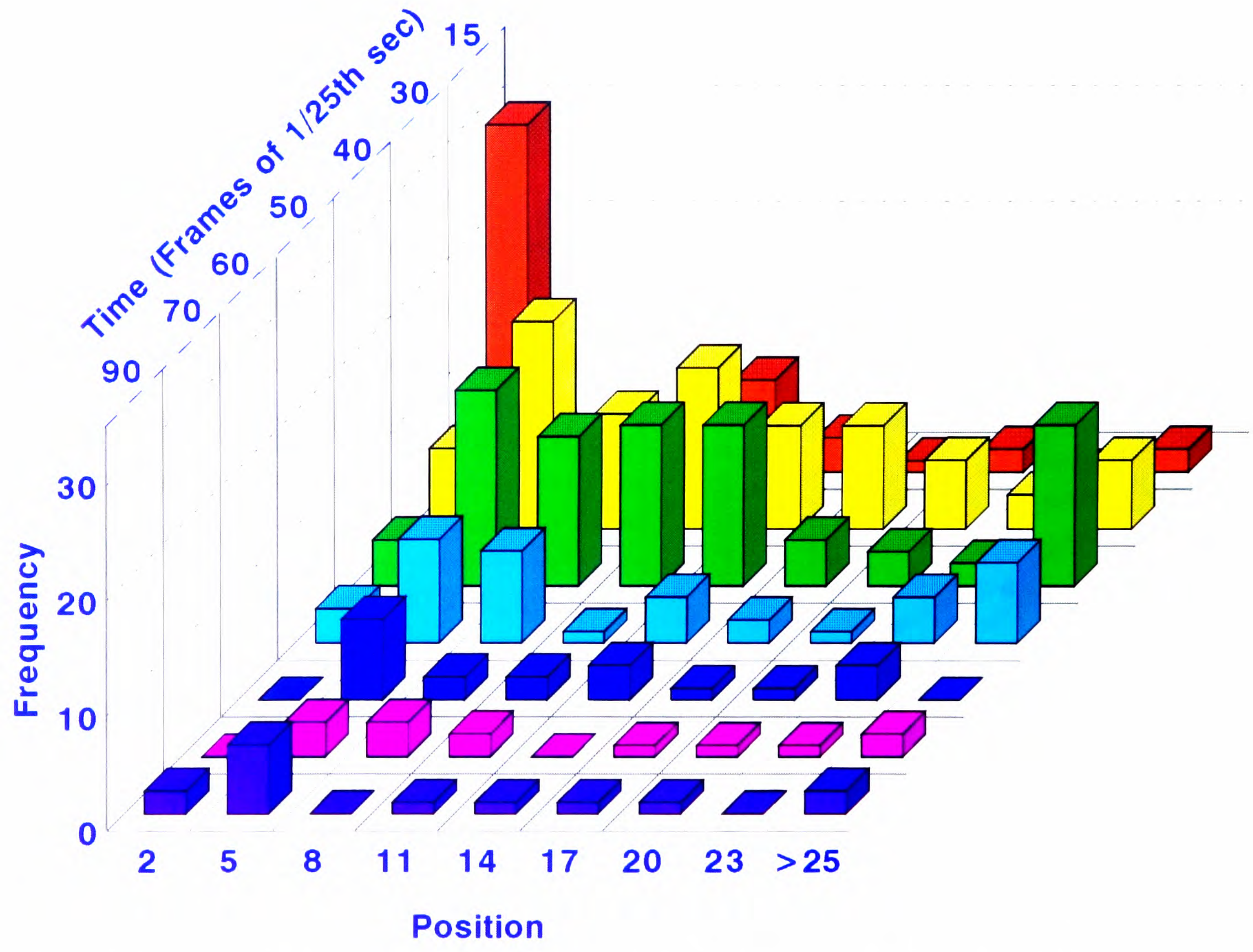

Figure 16. Distribution of particle landing sites when U/V=9. Most of the particles settle within 2 seconds, on the lee and lower stoss slopes.

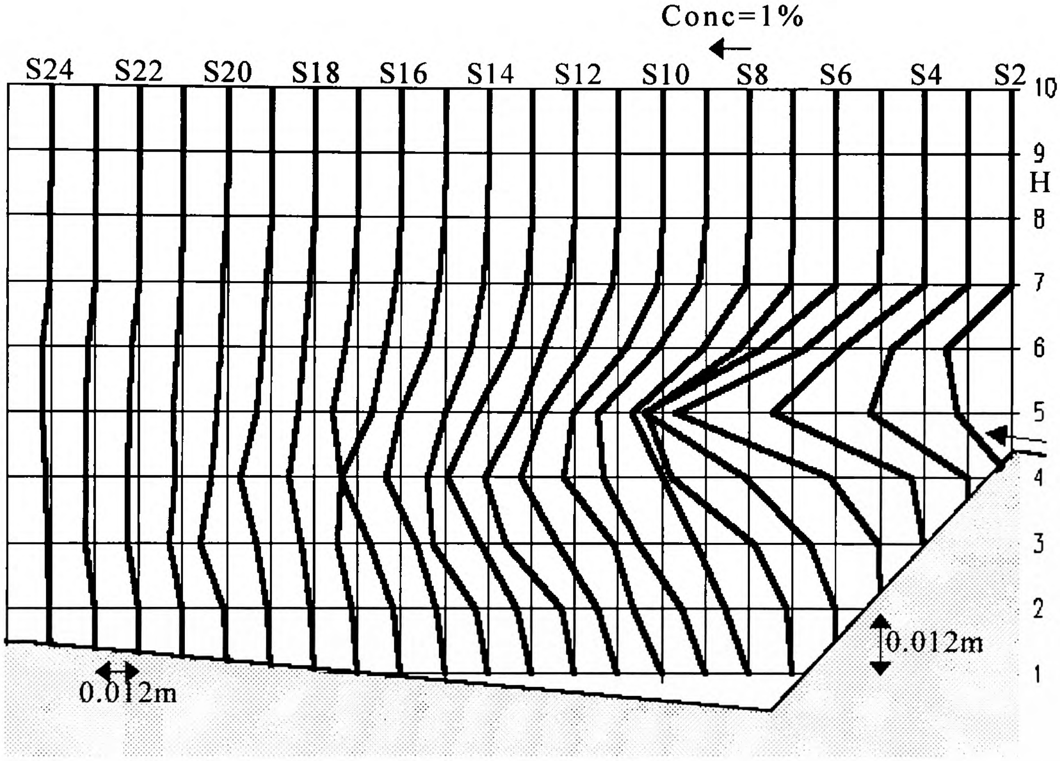

Figure 17. Particle concentration diagram for U/V=9. Notice the greater spread of the distribution compared to figure 13.

S 24	S 23	S 22	S 21	S 20	S 19	S 18	S 17	S 16	S 15	S 14	S 13	H
										99		7
		96	96	96			96	96	57	2	96	6
	96	96	99	35	18	96	96	96	99	61	16	5
96	96	22	96	96	99	99	99	44	51	56	25	4
96	35	99	-		99	99	99	96	40	61	35	3
					99	99				47	96	2
										99		1
S12	S11	S10	S9	S8	S7	S6	S5	S4	S3	S2		H
2	2	96	99	2	99	2	96					7
64	31	57	8	7	15	16	14	2	8	7		6
35	2	47	11	14	51	24	14	54	36	16		5
12	43	18	35	23	46	37	2	99				4
14	9	6	31	13	47							3
47												2

Figure 18. Convergence table for figure 17. The data is not converged in the outer flows where few visualisations are made, but is fair around the crest regions. This table shows the percentage difference between the concentration recorded for two sets of 100 particles at U/V=9. This is a direct measure of the convergence of the statistics for 100 particles and a pessimistic measure for 200 particles in figure 17. H and S refer to the vertical and horizontal grid locations in figure 17.

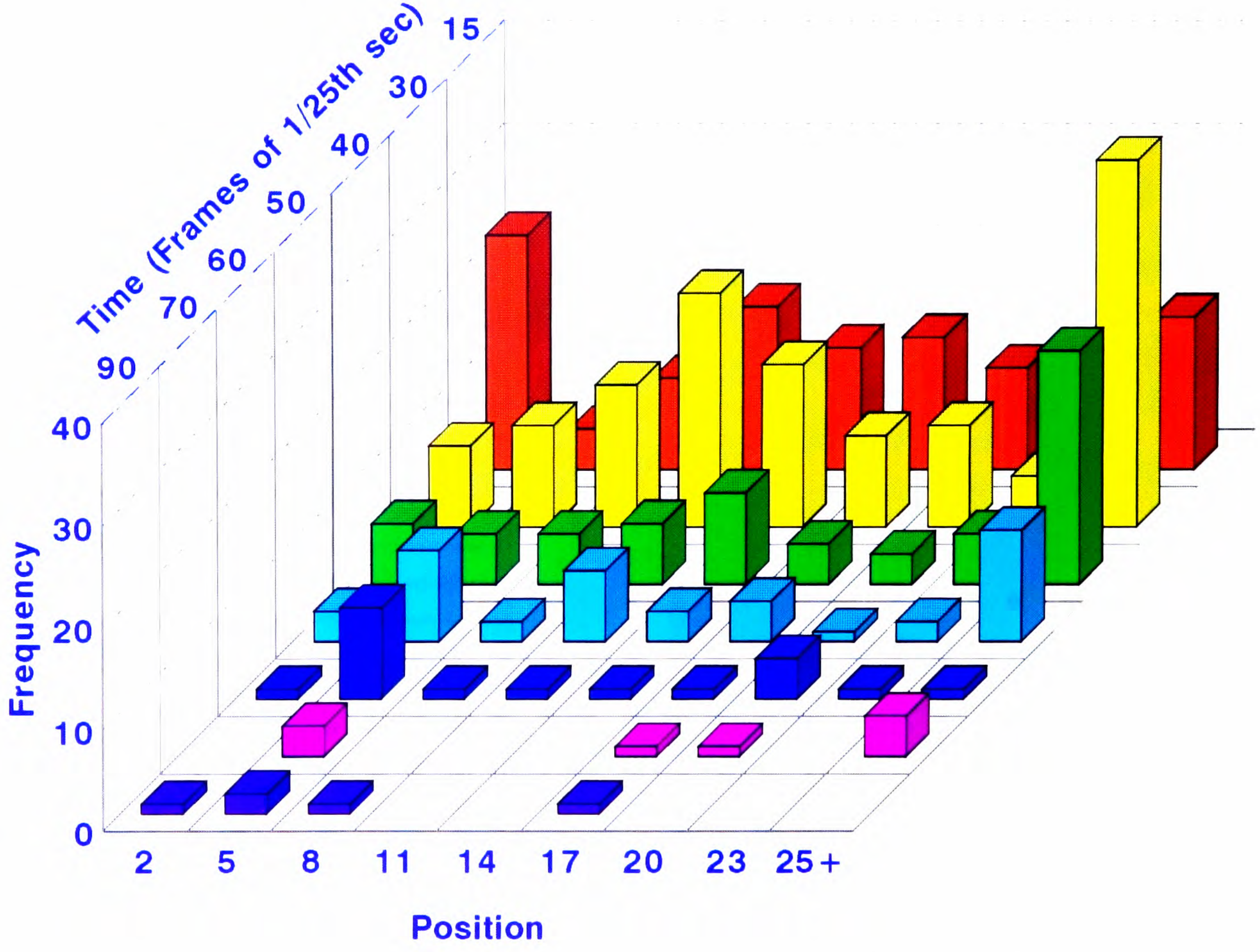

Figure 19. Distribution of particle landing sites for U/V=10.8. Notice the more even spread over the bedform than in figure 6.

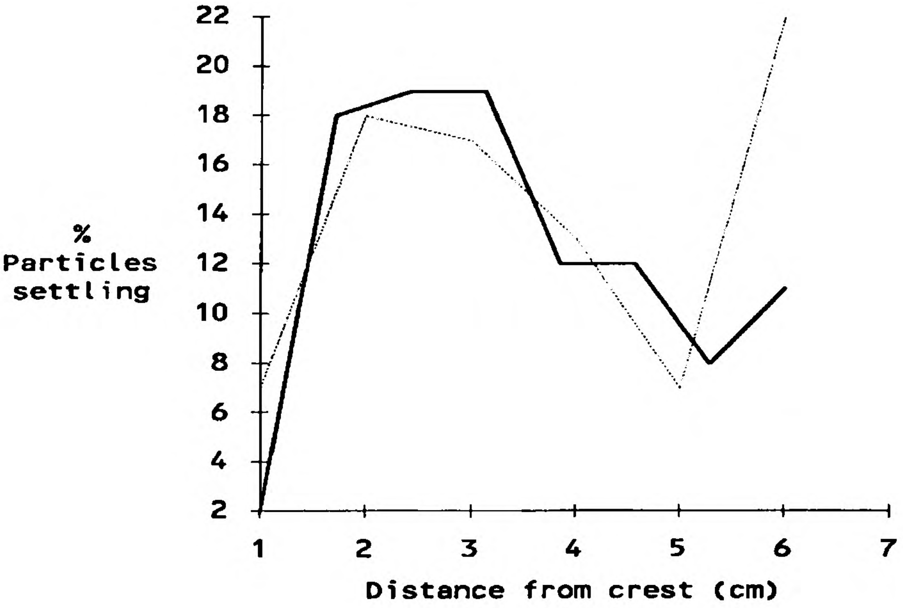

Figure 20. Comparison between our data at U/V=12.8 (dotted) and Allen's data at U/V=14.4. Compare with figure 11.

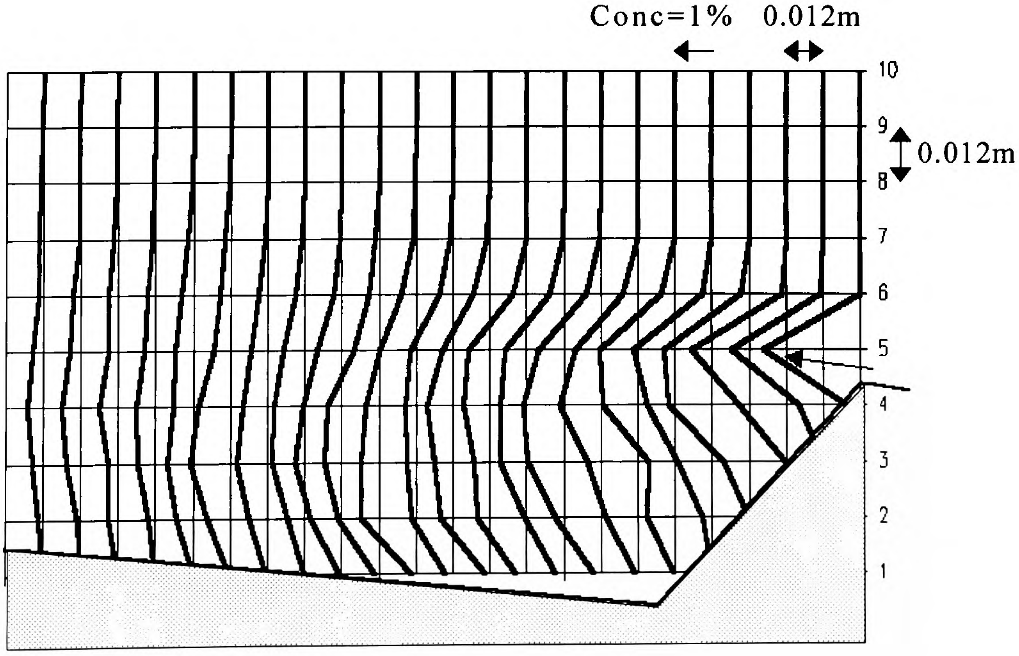

Figure 21. Concentration distribution for U/V=12.8. Notice that sediment is dispersed over a greater depth of the flow compared to figures 13 and 17 (at lower U/V).

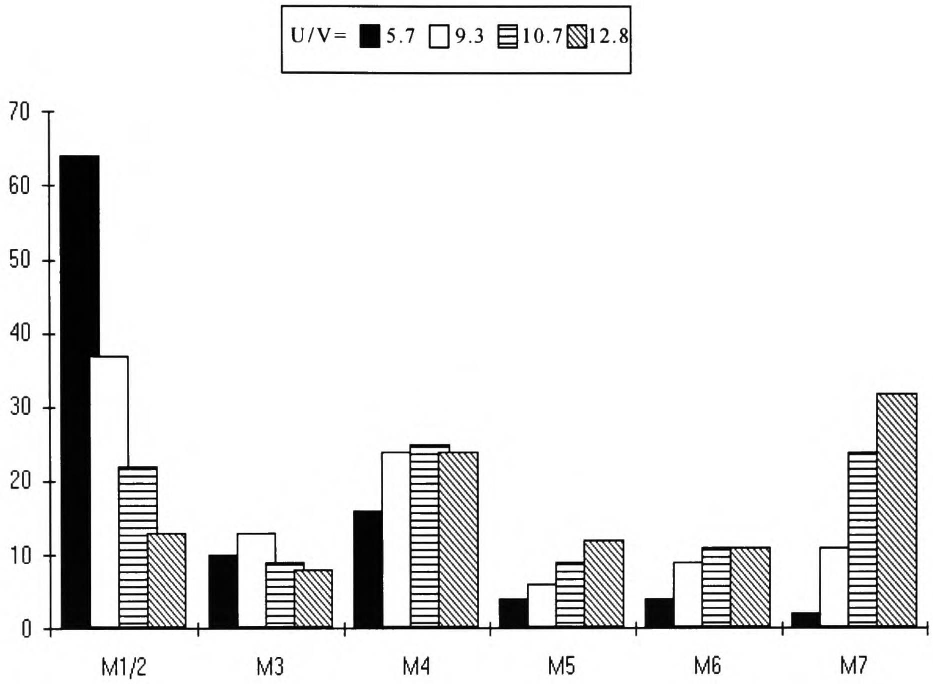

Figure 22. Percentage of particles taking each of the trajectory modes 1-7 at various U/V from 5.7 to 12.8. The peak at M4 is artificial because it covers a greater stoss slope length than the other modes. M4 is a pivotal mode since the number of particles deposited after following M4 changes only slightly with U/V, unlike the other modes.

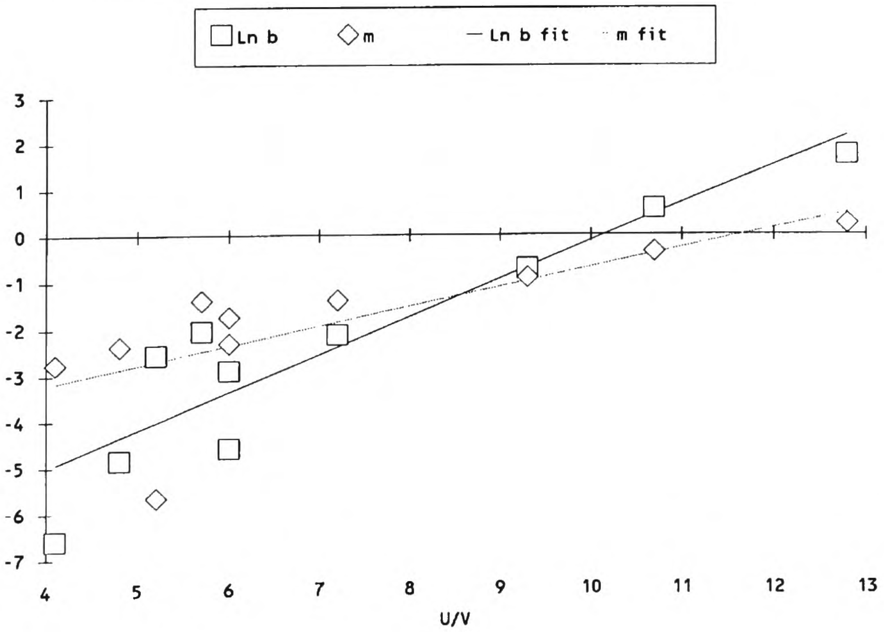

Figure 23. Parameters in the log fit S=bX^m where X is the downstream distance and S the sedimentation rate at point X relative to the total sedimentation rate. The parameters in the fit follow a roughly linear ratio with U/V with a good fit at the higher values.

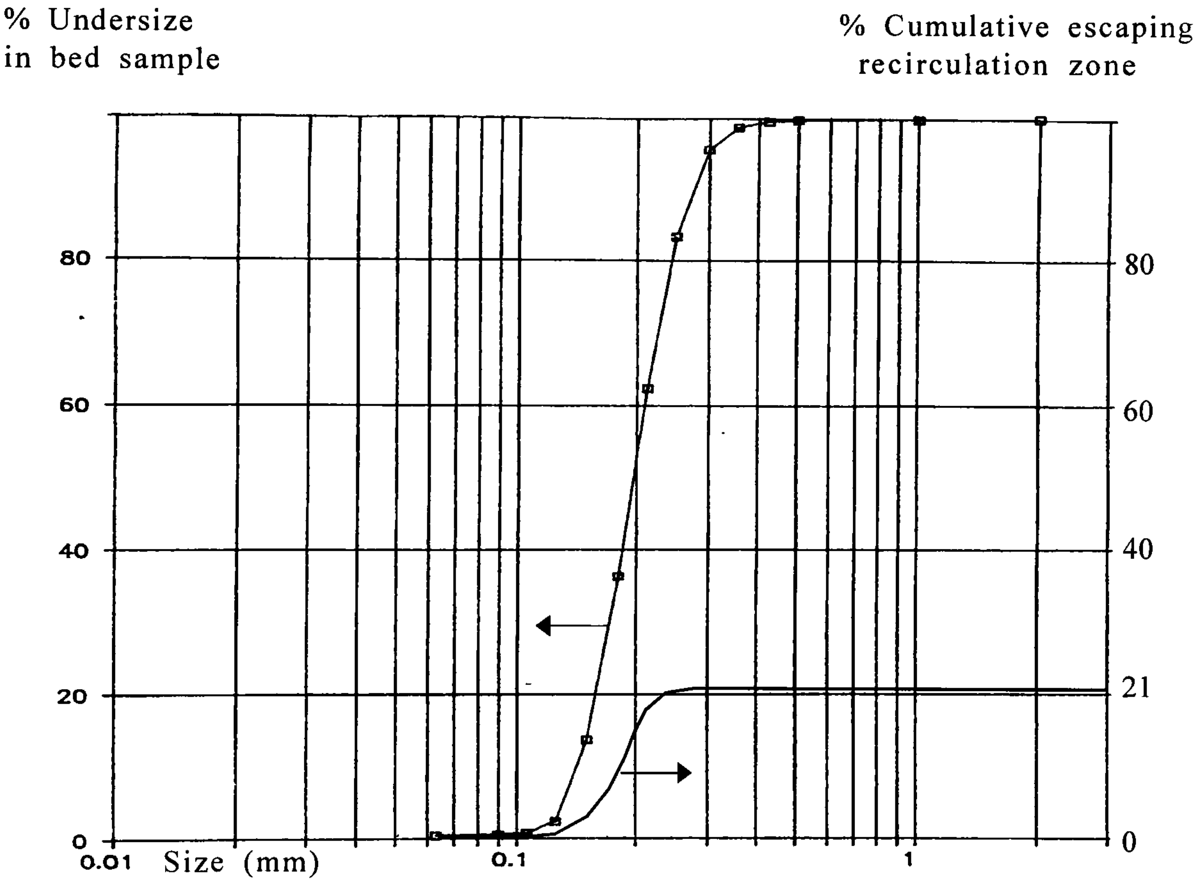

Figure 24. After Atkins & Soulsby (1992). Bedload sediment size distribution of a river Taw sandwave (left axis). The sediment size is between about 100 and 400 microns, with a maximum of 2000 microns. Predicted cumulative percentage carried over the recirculation bubble to be washed downstream at U=0.2m/s from figure 26 (cumulative column 6) on the right hand axis.

Band	U(m/s)	V(m/s) U/V=4	d(mm) U/V=4	V(m/s) U/V=10	d(mm) U/V=10
1	0.2	0.05	0.40	0.02	0.17
2	0.4	0.10	0.74	0.04	0.33
3	0.6	0.15	1.26	0.06	0.47
4	0.8	0.20	2.25	0.08	0.61

Figure 25. The Interactive Fraction for the four data bands of Atkins & Soulsby (1992). For band 1, particles with diameters between 0.40 and 0.17 form the FI and are neither all deposited on the lee slope nor all swept downstream to the next bedform.

1 d micron	2 V(m/s)	3 U/V	4 % Escape	5 % of bed	6 % bed escape
100	0.008	25.0	100	1.0	1.0
120	0.011	18.1	75	1.5	1.1
140	0.015	13.3	45	11.5	5.2
160	0.018	11.1	36	13.0	4.7
180	0.021	9.5	21	13.0	2.7
200	0.024	8.3	16	13.0	2.1
220	0.026	7.7	14	9.0	1.3
240	0.029	6.9	11	21.0	2.3
260	0.032	6.3	6	7.0	0.4
280	0.034	5.9	5	3.0	0.2
300	0.037	5.4	1	2.0	0
320	0.040	5.0	0	1.5	0
340	0.042	4.8	0	1.5	0
360	0.045	4.4	0	1.0	0
380	0.048	4.1	0	1.0	0
400	0.051	3.9	0	0	0

Figure 26. The table shows how our deposition data can be applied to a data set to predict, knowing the jetted sediment size distribution, the proportion of jetted sediment moving to the downstream bedform and beyond. The cumulative sum of column 6 is displayed on figure 24 and represents the cumulative percentage of bed particles jetting over the recirculation bubble to land downstream and be swept away.

CHAPTER 4: LEE AND STOSS SUSPENSION EXPERIMENTS

SUMMARY

Sediment transport over representative fixed bedforms is investigated to elucidate main mechanisms contributing to sediment motion over mobile sandwaves. This idealisation is satisfactory since the bedform migration velocity is much less than particle transport velocity. We focus on the suspended sediment budget contributed by sediment suspended from the lee and stoss slopes downstream of the crest. The fixed bedform comprises only three crests against the more usual five for 'equilibrium' velocity profiles. This was done so that the coupling between two shear layers could be analysed without effects from the relics of shear layers further upstream. Main finding is that shear layer flapping (ie cyclic separation and reattachment) makes a large contribution to total sediment scour from the lee slope. We term this behaviour 'Coanda-flapping' because of the similarity between the periodically reattached free shear layer here and the Coanda effect where a free shear layer is sucked onto a nearby surface by restriction of the local entrainment flows. Although fractional flow depth at the crest and flow Froude number are recognised as important parameters, the frequency of this flapping nevertheless correlates well with the passage of free-shear vortices generated by the upstream crest. Concentration distributions for particles captured from the lee slope indicate a possible mechanism for sandwave wash-out, as discussed in chapter 1.

1 INTRODUCTION

In chapter 3 we considered the fate of particles jetting from the crest of a fixed bedform. Our attention is now directed at sediment transport from the lee and stoss slopes downstream of the crest, again modelled using fixed bedforms and model particles. We focus on three main mechanisms as follows: capture by the recirculating flows on the lee slope; capture by motions induced by shear layer flapping and capture by interaction between the shear layer vorticity impinging on the downstream stoss slope.

Recirculating fluid in the separation bubble below the shear layer is usually also unstable at a lower frequency which corresponds to the flapping of the shear layer. We term this phenomenon 'Coanda-flapping' because it is akin to the Coanda effect. The latter is the phenomenon where a separated flow moves towards a fixed surface due to the sub-pressure caused by the vorticity within the shear layer which would entrain fluid into the shear zone in the absence of the fixed surface. The Coanda-flapping phenomenon has a marked effect on sediment transport, though it appears not to have been cited in the open literature as a sediment capture mechanism.

Wille & Fernholz's (1965) review of a colloquium on the Coanda effect reported Bradbury's study of an air jet blown over a convex surface with trailing flap; see figure 1. The angle subtended between the flap and the jet was increased until the flow just separated from the convex surface. Bradbury found that vorticity-induced entrainment of the confined fluid caused jet deflection towards the flap for all angles less than some unspecified critical value. For larger angles, there was a different stable pattern in which the jet detached from the convex surface and the confined recirculating flow was directed everywhere upstream towards the convex surface.

Kiya & Sasaki (1983) studied the separation bubble on the front edge of a thick rectangular plate. They found that large vortices were shed at a mean frequency of 0.6U/L where U here is the free stream velocity and L is the time-mean bubble separation length. These vortices appeared in the free shear layer separating from the salient leading edge and grew by entrainment until restricted by the proximity of the plate. A second oscillation was superimposed at a lower frequency of 0.2U/L, associated with large scale flapping of the shear layer during partial shedding of the separation bubble. Kiya & Sasaki do not give a detailed interpretation of this second phenomenon but we believe that boundary restriction of the entrainment flows played an important role.

Soulsby & Bettess (1991) found the time averaged flow velocity over the trough of estuarine sandwaves showed no mean flow reversal at any height above the trough, which they explained as lack of permanent separation at the crest. Further measurements of the fluctuating velocity at 0.1, 0.2, 0.4 and 0.8m above the trough (where the crest height was about 0.8m) showed negative velocity for a maximum of 40% of the time, which occurred during the decelerating phase of the tide after the crest had been sharpened by the accelerating phase. We ascribe this to the low lee slope angle of 15 degrees, which would probably promote reattachment further up the lee slope by the Coanda effect.

Although there is no definitive evidence of sediment transport by Coanda-flapping, it seems likely that the phenomenon played a role in the sediment transport events reported by Soulsby (1989). Indeed the existence of such interactions between the free shear layer and adjoining bedform was postulated as background context for our project. The intermittent ejection of sediment from the vicinity of the crest might be attributed to any of at least four possible mechanisms as follows: firstly, surface or internal waves; secondly, feedback from downstream shear layer/bed interaction (only feasible in very shallow water); thirdly, by upstream events and fourthly, by boundary layer bursting events. In order to assess the relative importance of these possible mechanisms we performed a series of experiments on flow transport over the first of two crests and compared the results with those for transport over the middle crest in a set of three.

We have also studied particle capture by steady shear layer entrainment flows for which, again, there is little published literature explicitly. Some indication as to the relative significance of stoss and lee slope erosion can be found from observations that antidunes form for supercritical Froude numbers

(Kennedy, 1969; recall chapter 1). Antidunes move against the flow, such that the sediment transport rate from the lee slope must exceed that from the stoss slope. Moreover, as the free surface elevation is in phase with the sandwave here, we can probably expect that the free shear layer more readily collapses onto the bottom boundary, thereby enhancing shear suspension and promoting the upstream migration of antidunes.

Whilst sandwaves are generally associated with subcritical Froude numbers and so do not have any in-phase free surface elevations, the strength of their free shear crest flow is nevertheless proportional to the stream velocity and hence also the Froude number; likewise the velocities associated with the entrainment flows. Hence, at higher Froude numbers the shear layer should move closer to the lee slope giving enhanced lee side sediment transport.

From the foregoing it seems reasonable to distinguish between the coupled contributions arising from shear layer vortices above the surface and from vortex reattachment unsteadiness manifested in Coanda-flapping. Clearly the interaction between these aspects plays an important role in determining the overall transport dynamics.

However, there is very little established literature relevant to these mechanistic ideas, as we have already seen from the review given in chapter 1. Nezu & Nakagawa (1991) defined a 'boil of the first kind' in terms of its surface manifestation from shear layer vortices extending over the depth of flow. According to their picture, the horseshoe structure pumps fluid from between its legs, presumably carrying sediment from the stoss slope to the surface, although no quantitative data was presented. Other qualitative evidence comes from Jackson's (1976) study of river dunes, reporting that sediment-carrying surface deformations were caused by flow structures similar to the sand devils which form behind wind-driven sand dunes. This again is likely to be the remnants of horseshoe shear layer vortices following their stretching by the stream as they grow to fill the flow depth.

Below we describe our experimental methods together with results for the flow over two and three bedforms. Experiments over the latter set-up included varying the flow speed and inter-crest spacing, the results of which are used to discuss bedform washout.

2 EXPERIMENTAL METHODS

2.1 General considerations

The experiments were conducted in our flume (described in chapter 2) using videography to track particle motions at four depth-averaged flow speeds U=0.20, 0.31, 0.36 and 0.43m/s over a series of three fixed bedforms all of height 0.05m and length L_0=0.66m such that the Froude number ranged from 0.16 to 0.20. This experimental setup was identical to that described in chapter 3, as were the flow conditions during each of the runs, which were carried out at identical flow depths and velocities.

The three families of particles used, with settling speeds representative of sediment grains, were all cylindrical in shape. The implications of shape and size distortions were discussed in chapter 3 where the particles were shown to deliver good fits with published data on deposition after crest jetting. Data was not presented in terms of non-dimensional parameters (involving, for instance, bedform height and length) because ripples and dunes do not form a continuum of scales and interpolation is not appropriate.

The flow was visualised using a 1cm wide slit light from a mirror suspended at 45 degrees above the bedform. A 2000W halogen lamp provided sufficient light to illuminate Amberlite resin (ie neutral) flow tracers (Rohn & Haas Ltd). As detailed in chapter 2 the camcorder (NV-G202B, Panasonic) images were recorded on a VCR (SLV-353UB, Sony) at a frame rate of 25/s with a shutter speed of 1/50s.

In section 3.1 we show visualisations of the flow and particle suspension induced by the Coanda-flapping, both as obtained from our experimental equipment described in chapter 2 and from similar experiments performed earlier at HR Wallingford and detailed in appendix 8.

2.2 Methods for measuring Coanda-flapping frequency

Section 3.2 examines the frequency of Coanda-flapping. Two sets of experiments were done, the first searched for Coanda-flapping at the upstream crest of two bedforms and compared the results with those from the middle crest of three bedforms and the second set evaluated the effect of inter-crest spacing on the Coanda-flapping frequency.

Individual events were difficult to discern from single frame shots since the sense of motion of the flow was lost. The records were thus analysed in real time using a computational routine to record the time at which the enter key was pressed on the keyboard. Each section of video was watched three times, firstly to get the Coanda-flapping frequency, then the frequency of passage of the shear layer vortices and, finally, the frequency of passage of all discrete turbulent events from upstream. The event intervals were sorted into one second bin sizes: viz 0-1s labelled as 0.5, etc. This classification was subsequently changed to cumulative analysis (section 3.2b) so that the region with the lowest gradient thus defined the modal value for the distribution. This deserves some explanation, as follows. In a continuous system such as a distribution of times the modal value depends upon the size of the discretisation interval. If we had chosen too coarse a discretisation band we would have introduced a discrepancy as to where our modal value lay within the most frequent interval, yet at too small a value there would be no sensible modal value as each piece of data would occupy a different band.

The need to choose a value for the discretisation interval was thus removed by plotting raw data event intervals in size order against their cumulative sum. The most densely occupied region thus had the lowest gradient when the intervals were plotted on the Y axis and corresponded to the modal interval range.

2.3 Methods for particle suspension experiments

The results in section 3.3 show sediment suspension from the lee slope due to the recirculating flow and from Coanda-flapping. Concentration data was obtained in the same way as for the jetting experiments detailed in chapter 3. A total of eight runs were carried out at flow velocities U=0.20, 0.31, 0.36 and 0.43m/s with two particle velocities V=0.034 and 0.060m/s.

One problem not resolved here was that particles could not be held on the lee slope near the crest to allow capture from these regions. Rather, they piled up around the base of the lee slope prior to capture by the recirculation and flapping mechanisms which resulted in a supply side deficit around the crest and upper lee regions. This caused severe distortion in the concentration data, particularly at the lower flow velocities, because the scouring flows on the upper lee had no particles to scour. Recommendations for future consideration are made in chapter 7.

Section 3.4 considers suspension from the stoss slope downstream of the crest. However, the interaction between shear layer vortices and the stoss slope downstream of the trough was particularly difficult to study here because of bedload motion during start-up. Thus, particles pre-spread over the stoss slope were washed away during the start-up flows in our flume, even when the flume was full before the flow was started and regardless of the rate of increase in flow velocity. A partial solution was secured by attaching a grid of galvanised meshing to the centreline of the bedform. The height of the grid above the perspex bedform was about 4mm.

Even with the grid present the starting flow washed away most of the particles at higher flow velocities, however enough remained to allow reasonable estimation of the suspension fluxes. No estimates were made of the concentration distribution due to lack of particle numbers so we give a brief description here of the seven runs in which the flow velocity U and particle fall speed V were varied through U=0.20-0.36m/s at V=0.034m/s and U=0.20-0.43m/s at V=0.60m/s.

3 EXPERIMENTAL RESULTS

3.1 Visualisation of the Coanda-flapping events

The series of plates in figure 2 show the Coanda-flapping phenomenon with great clarity. This sequence was taken over the bedforms described above at a flow velocity of about 0.6m/s

(Froude number 0.60). We chose this higher velocity to show the phenomenon clearly (though passing shear layer vortices from upstream are not visualised at these high speeds). In frame b we see an increase in vertical velocity just downstream of the lee associated with an observed circulation comparable in size to the height of the bedform.

In frame c (2/25th seconds later) we see this recirculating zone move downstream and the beginnings of a vortical structure forming at the crest. By frame d this structure at the crest has grown and begins to move down the lee slope and by frame e it forms a large recirculation bubble on the lee slope. The turbulence downstream is swept out of view by frame g.

As shown by the series of plates in figure 3 this flapping sequence is important with respect to sediment transport. Here the Coanda-flapping-induced flow, similar to that described above but not visualised on these plates, interacts with the bed of particles (dark and light spots) of quiescent fall speed 0.035m/s on the lee slope of the same bedform, causing a plume of particles to be suspended into the flow and move downstream. The particles appear both light and dark because they are both on and just off the centre-line of the flume (ie inside and outside the light sheet). This sequence also demonstrates that the process is cyclic to the extent that two such events are pictured. The sediment structure attains a height about equal to that of the bedform and carries the bulk of sediment transported downstream from the lower lee slope during the cycle.

This same flow structure has also been seen over larger bedforms, as described in appendix 8. The pictures in figure 4 clearly show striking excursions in the recirculation region during Coanda-flapping.

3.2a) Effect of varying flow speed

i) Two bedforms The free shear layer at the first of two bedforms was strikingly stable and seen to flap only slightly regardless of the oncoming flow velocity, essentially manifested as a slight pulsing of the velocity of the return flow up the lee slope.

ii) Three bedforms We now turn to Coanda-flapping at the second in a series of three crests relating its frequency to the frequency at which upstream shear layer vortices pass over the downstream crest at flow velocities 0.20, 0.31, 0.36m/s. The shear layer vortices at 0.43/s could not be adequately discerned so we do not report results at this value. The Coanda-flapping motions were clearly visible at this velocity, as discussed in section 3.2b.

The interval distribution for Coanda-flapping events at stream velocity 0.20m/s is shown in figure 5. Also shown is the interval distribution for the passage of shear layer vortices and also for the passage of other discrete turbulent events (probably boundary layer bursts) which we have yet to identify but were order 0.03m high and 0.06m long. 158 shear layer vortices were timed along with 39 of the unidentified turbulent events and 46 Coanda-flapping events. Figure 5 shows that the Coanda-flapping interval has a fairly wide distribution up to about 12s with a peak at 2.5s. This compares with Kiya & Sasaki (1983) who find frequency 0.2U/L, ie interval of 4s, but recall that their experiment had no periodic upstream disturbances for the flapping to lock-on to. The Coanda-flapping interval correlates well with the turbulent spot interval distribution but does not show the striking peak at 1.5s relating to shear layer vortices. Compare this with the value reported by Kiya & Sasaki (1983) who found the frequency of primary vortex shedding to be 0.6U/L, ie interval of 1.25s. We also mention that the Coanda-flapping events tended to occur in pairs, as manifested in the peak of 11% for the 0.5s interval (see figure 5).

The interval distributions for Coanda-flapping and both types of upstream event (ie the shear layer vortices and turbulent spots combined) at U=0.31m/s are shown in figure 6. We show this figure with the events combined to see if there is any correlation between Coanda-flapping and general free stream turbulence. The fit is not good since the Coanda-flapping and turbulent events have different peak intervals. Figure 7 shows the interval distribution for Coanda-flapping events and for the shear layer vortices at U=0.36m/s. The peak here is at an interval of 1.5s for both events and the frequency of events occurring at longer intervals show a remarkably good fit.

3.2b) Effect of varying inter-crestal spacing

Below we consider how the shedding frequency is affected by changes in L, the inter-crestal spacing. For this study we chose a flow velocity of 0.43m/s (where the Coanda-flapping events are most strong) and varied L in intervals of $0.5L_0$ (half wavelength), from L_0 to $3L_0$. We could not visualise the oncoming flow vortices at this velocity but continued because the Coanda-flapping events are certainly stronger and easily visualisable.

The interval distribution for Coanda-flapping events here, recorded as in section 3.2a, is shown in figure 8 for each value of L. Of major interest is the change in modal location for $L=3L_0$ and broadening of the distribution which is discussed further below. It is clear that our bin size is too large at 1s so we revert to the raw data and plot the interval data for $L=L_0$ sorted in ascending numerical order against the cumulative sum of the intervals in figure 9. The reason for following this procedure was explained in section 2.2. Thus, for $L=L_0$ we retrieve a modal value between 0.9 and 1.3s (ie about 1.1s) corresponding to the minimum point on figure 9 and the gradient plot in figure 10. The limits were defined arbitrarily as any gradient region below 0.02 and any higher or lower limit simply changes the band width. The same region corresponds to the first line in the top left-hand corner of figure 11. The number (32%) above the line corresponds to the percentage of all the measured intervals that fell within this range (ie 0.9 to 1.3s) whereas the figure in italics below the line is the percentage of events that we would expect to find in this range had the event intervals been spread evenly over all the categories (ie 0-6.5s). A modal value is signified by a large number above and a small number below the line. Compare this result with that of Soulsby & Bettess (1991), who found flow separation to occur for a maximum of 40% of the time. We found Coanda-flapping events to cause flow reattachment for about 0.5s (figure 2) which leaves about 0.5s for flow reversal, ie about 50% in this case.

The results are also shown for other inter-crestal spacings. We see that $1.5L_0$ has modal value at 1.5s and $2.0L_0$ has a similar peak at modal value 1.4s. We also see a second, smaller modal value at an interval of 3.2s. $L=2.5L_0$ does not possess a peak near 1.4s but has a strong peak at 2.8s with a smaller peak at 3.4s. $L=3.0L_0$ gives two peaks at 2.4 and 2.9s of equal height. Figure 11 thus shows how the modal interval shifts from about 1.3 to 2.6s as L varies from L_0 to $3L_0$, corresponding to halving of the Coanda-flapping frequency. We discuss this point in section 4.

3.3 Particle capture from lee slopes

In the experiments below we describe results for the motions of particles initially at rest on the lee slope behind the middle of three crests at each of four flow velocities U=0.20, 0.31, 0.36 and 0.43m/s and for two particle quiescent fall speeds V=0.034 and V=0.060m/s. We describe in detail the findings with fall speed of V=0.034m/s at each stream velocity and then add those with fall speed 0.060m/s for comparison. The concentration data was found in an identical fashion to that in chapter 3 where an estimate of the statistical significance of the data found that two sets of 100 particles produced results that were converged to about 20% in the areas of high concentration. Hence the 200 particles represented a better than 20% estimate of the particle relative concentration. In the tests below we caution that similar confidence levels can be attached to the data, but the problem of particle supply at the crest, especially at the low flow velocities, produces a far larger distortion which we cannot estimate.

At V=0.034m/s and U=0.20m/s the particle transport was found to be solely due to Coanda-flapping events. Figure 12 shows the percentage concentration plot for the 83 particles that were suspended. The highest concentrations are found around the lower lee slope regions, which is not surprising since this is where they lie before being suspended. Less than five percent of the particles were suspended for long enough to move off downstream with the vortex.

92 particles were tracked at V=0.034m/s and U=0.31m/s. Here there was a higher proportion of sediment entrained up the lee slope, but the suspension events were still caused by the Coanda-flapping event, as at the lower velocity above. The concentration profiles are shown in figure 13 and again here display a peak just downstream of the lee face. 82% of the deposited particles fell directly onto the lower lee and 18% were

deposited on the stoss slope downstream and subsequently swept away.

95 particles were traced at V=0.034m/s and U=0.36m/s, 40% of which escaped the lee region and 60% returned either directly to the lee or via the stoss slope. The concentration profiles shown in figure 14 have a peak at vertical elevation equal to the crest height at streamwise station half way down the lee slope. This behaviour reflects particle transport occurring increasingly by recirculation up to the crest followed by entrainment into the shear layer and finally downstream transport akin to the jetted load (recall chapter 3). At this velocity the relative importance of the Coanda-flapping is reduced with respect to shear layer capture. Of the 92 particles traced at V=0.034m/s and U=0.43m/s, 50% were swept away to the stoss slope. The concentration profiles in figure 15 again show the importance of the shear layer in removing sediment from the lee at higher U/V ratios.

At V=0.060m/s (ie heavier particles), no motions of the particles up the lee slope and no suspension events due to Coanda-flapping were visualised at U=0.20m/s or U=0.031m/s. The first suspension events by Coanda-flapping were seen at U=0.36m/s, 95% of the particles were returned to the lower lee slope and about 5% were carried downstream. With U=0.43m/s, about 20% escaped the lee slope, all due to Coanda-flapping.

3.4 Particle capture from stoss slopes

Brief notes on the experiments using two particle types, those with V=0.034m/s and V=0.060m/s are discussed here. At V=0.034m/s about 2% of the particles were entrained into the flow and suspended to a height of half the flow depth at U=0.2m/s. About 88% simply rolled along the bedform and about 10% travelled 0.1m or more without returning to the surface. Particles were entrained both upstream and downstream from a bed location about 0.2m downstream from the crest where the shear layer vortices impinged with the stoss slope. Further downstream the particles moved in low-level saltations with periods of dormancy.

At U=0.31m/s, 10% of the particles were entrained into vortex structures and suspended at heights up to half the flow depth. The saltating particles contributed about 60% of the bedload and attained a height of up to 0.04m. Higher velocities could not be used because the particles were washed away too quickly by the starting flows.

When V=0.06m/s and U=0.20m/s the particles moved as bedload with about 1% saltation to a height of 2cm above the bed. At U=0.31m/s there was about 25% saltation, but no sustained suspension events to half the flow depth as had been seen for the previous particles. Such intermittent events were visible at U=0.36m/s, where about 5% of the particles were plucked from the bed and suspended in clouds (such as figure 16) with a height of about half the flow depth. The bed load at this velocity was excited into low level saltations rather than just rolling modes.

4 DISCUSSION

Coanda-flapping was postulated ab initio to be a likely mechanism for sediment capture from lee slopes. The visualisations reported in section 3.1 here lend support to this explanation for the findings of Soulsby (1989) and Soulsby & Bettess (1991) who report the sediment cloud (depicted in figure 17 taken from his paper) and temporary flow reattachment. Further considerations (section 3.2 and 3.3) have shown that Coanda-flapping could be triggered by the passing of upstream shear layer vortices at higher stream speeds. Also, the absence of Coanda-flapping when upstream bedforms are absent points to the shear layer vortices as the Coanda-flapping trigger, though changes in the mean flow profile cannot be excluded. The absence of a correlation between upstream shear layer vortex passage and Coanda-flapping at lower velocities suggests there is a threshold vortex strength needed to achieve temporary lee slope reattachment; other mechanisms such as described in the introduction for Bradbury's jet and Kiya & Sasaki's plate shedding experiments may be appropriate at the lower velocities.

Below we widen the discussion towards offering some predictions on sandwave morphology, in particular the importance of different sediment transport mechanisms (section 4.1) and the mechanism of dune washout at high Froude numbers (section 4.2). These ideas are discussed in the context of established knowledge as reviewed in chapter 1.

4.1 Relative importance of sediment transport mechanisms

Four suspension mechanisms have been identified here and in chapter 3, namely; jetting; Coanda-flapping capture; lee-shear capture and stoss slope capture. Comparing the percentage of particles that escape the recirculation bubble due to Coanda-flapping with the same percentage for jetted load we see that they are fairly similar: ie 5% and 6% at free stream velocity U=0.20m/s, 18% and 20% for U=0.31m/s respectively. These results are consistent with the notion that flapping of the shear layer towards the lee slope induces similar effects on the particles as on the jetted load. One difference is that the Coanda-flapping event is intermittent, apparently with duration and interval of order 0.5s and 1.5s respectively, which suggests that Coanda-flapping capture may occur for approximately one third of any time period. We infer total transport due to Coanda-flapping capture is perhaps at most one third that from jetting, based on these event durations (1.5/0.5=3) and the similarity in deposition profiles mentioned above. The implicit assumption here is that transport rates during Coanda-flapping are equal to that due to jetting. We proceed with caution in the absence of flux data from the lee.

We saw in section 3.3 that lee-shear capture arose for U/V about 10, the upper boundary for FI. This suggests the mechanism may be relatively insignificant since only fine grains are transported up to the shear layer by these flows. The highest concentrations of vorticity reside close to the crest and decline downstream due to entrainment, resulting in declining capacity to capture and transport sediment from stoss slopes. In effect we are suggesting that the FI encompasses a smaller particle size range for stoss slope capture than for jetted load capture. Unfortunately, the lack of quantitative results prevents us from substantiating this conjecture other than commenting that, even for U/V=10, barely 10% of the particles on the stoss slope are suspended.

4.2 Bedform shape and migration

Both shape and migration are inextricably linked to suspension mechanisms. We should also point out that the adjustment of the bedform to changes in flow velocity will be delayed by limited accessibility of smaller particles buried in the sandwave. The resulting 'spatial lag' has been discussed by Phillips & Sutherland (1989). We also caution that the wash load has been ignored here: ie particles with a diameter much smaller than FI_0 (Gyr, 1983).

The Coanda-flapping event provides a possible mechanism explaining the phenomenon of bedform washout described in chapter 1. Here, sandwaves are seen to flatten as $Fr \rightarrow 1$ and are eventually washed out. We propose that as U increases to a value where the largest grain diameters have $U/V \rightarrow 10$, the proportion of jetted grains settling to the lee slope will be small. This is not crucial since, for some equilibrium to exist, those particles held in suspension must largely deposit on the stoss slope downstream. We conjecture the contribution to bedform scouring made by Coanda-flapping is critical because a similar grain size distribution to that being jetted from the stoss will be scoured from the lee slope. Regardless of stoss slope deposition, there is no mechanism available to allow the return of a grain to the lee slope because at high U/V the bulk of the jetted load follows trajectories from crest to stoss to crest and not to lee. A gradual reduction in crest height seems likely, leading eventually to sandwave washout. We add here that this conjecture takes no account of suspension when suspended sediment load is high, nor for the effects introduced by our fixed bedform shape which did not evolve with time to model real sandwaves.

5 CONCLUSIONS

Key conclusions here concern the lee concentration profiles, individual mechanisms responsible for the transport of sediment and their effect on the bedform shape and migration. Coanda-flapping capture on the lee slope is an important phenomenon deserving detailed study since it causes particle entrainment at flow velocities where lee-shear capture is insignificant. It may also hold the key to observed washout of sandwaves as $Fr \to 1$. Stoss slope entrainment was also seen to be insignificant compared to Coanda-flapping capture. Initial tests allude to passing shear layer vortices as the trigger for Coanda-flapping at the high U's, and boundary layer events at low U's.

From the above we confirm the well known but usually ignored point that grain size <u>distribution</u> is crucial when assessing bedform shape and existence and must be considered when predicting changes in bedform morphology over anything other than small timescales compared with that of the dune velocity to length ratio.

Finally we note that the transport role of shear layer eddies cannot be represented using existing engineering calculation schemes based on Reynolds averaged equations with a turbulence model. Methodologies are available to describe the main unsteady features and they should be further explored and applied to these problems: viz discrete vortex models as reviewed in chapter 1.

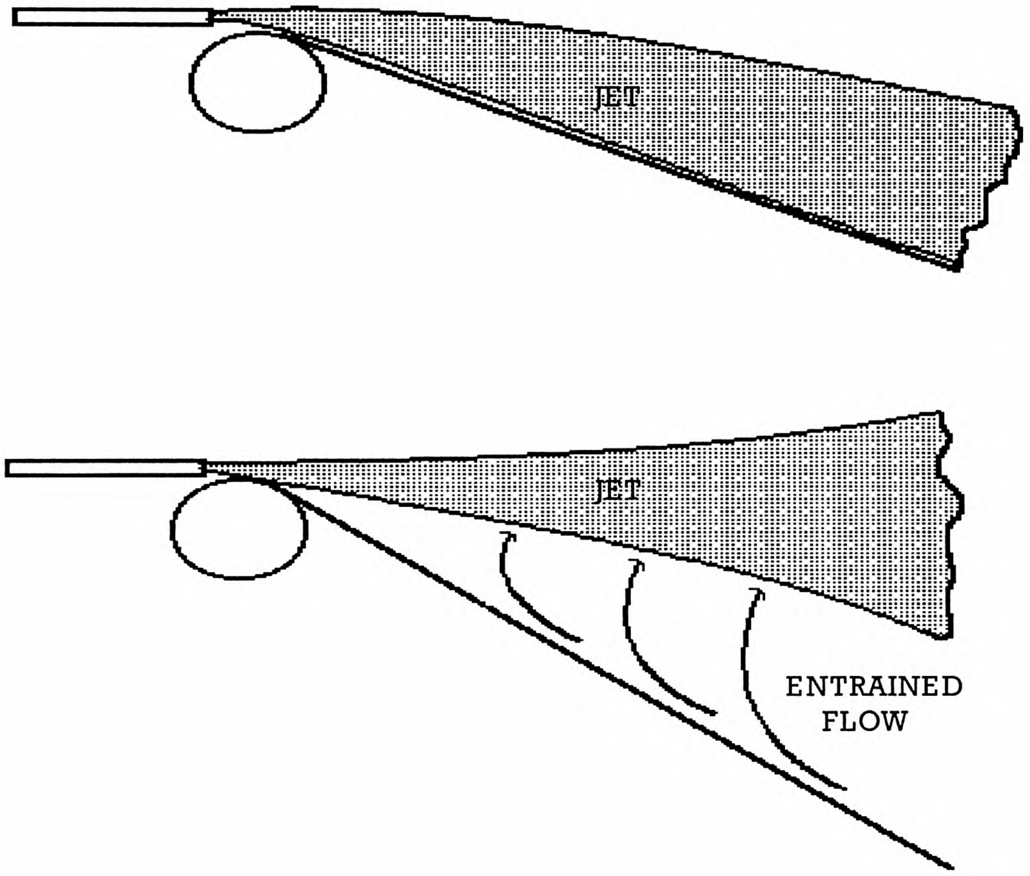

Figure 1. Inspired by Wille & Fernholz (1965). The upper picture shows the jet attached to the trailing flap due to restriction of the entrained flow shown in the bottom picture. Here the trailing flap makes a larger internal angle with the jet and the shear layer is not drawn to the surface.

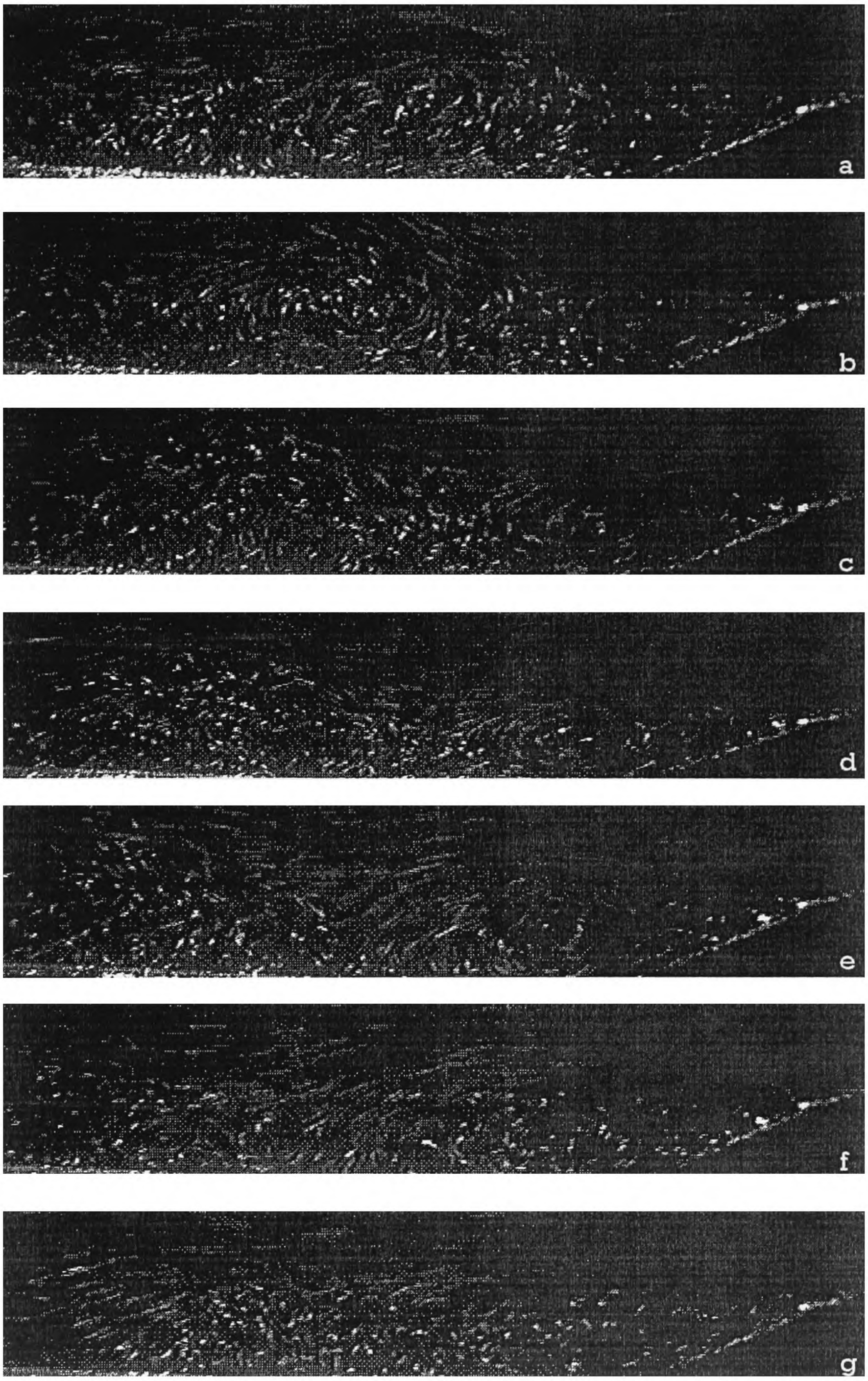

Figure 2a-g. The Coanda-flapping event at a flow speed of 0.60m/s (Froude No.=0.6). In frame b) we see an increase in vertical velocity just after the crest (flow right to left) and a region of circulation comparable in height to the height of the bedform which is swept from the view field by frame g).

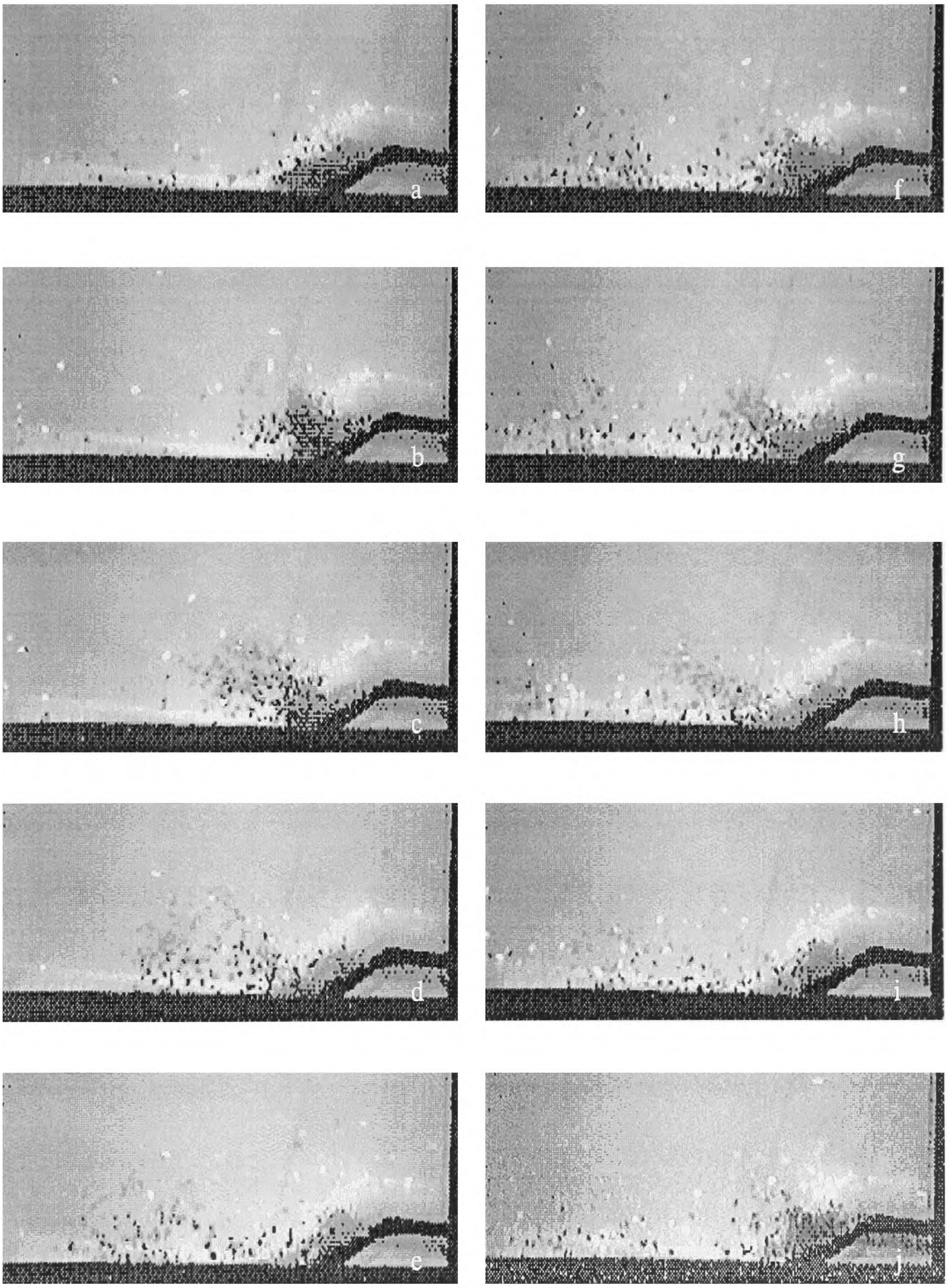

Figure 3a-j. The plates show particles transported by periodic flows caused by Coanda-flapping of the free shear layer. The particles (light spots on centreline, dark spots just off centre-line of the rig) have a fall speed of 0.034m/s and the depth-averaged flow speed is 0.31m/s.

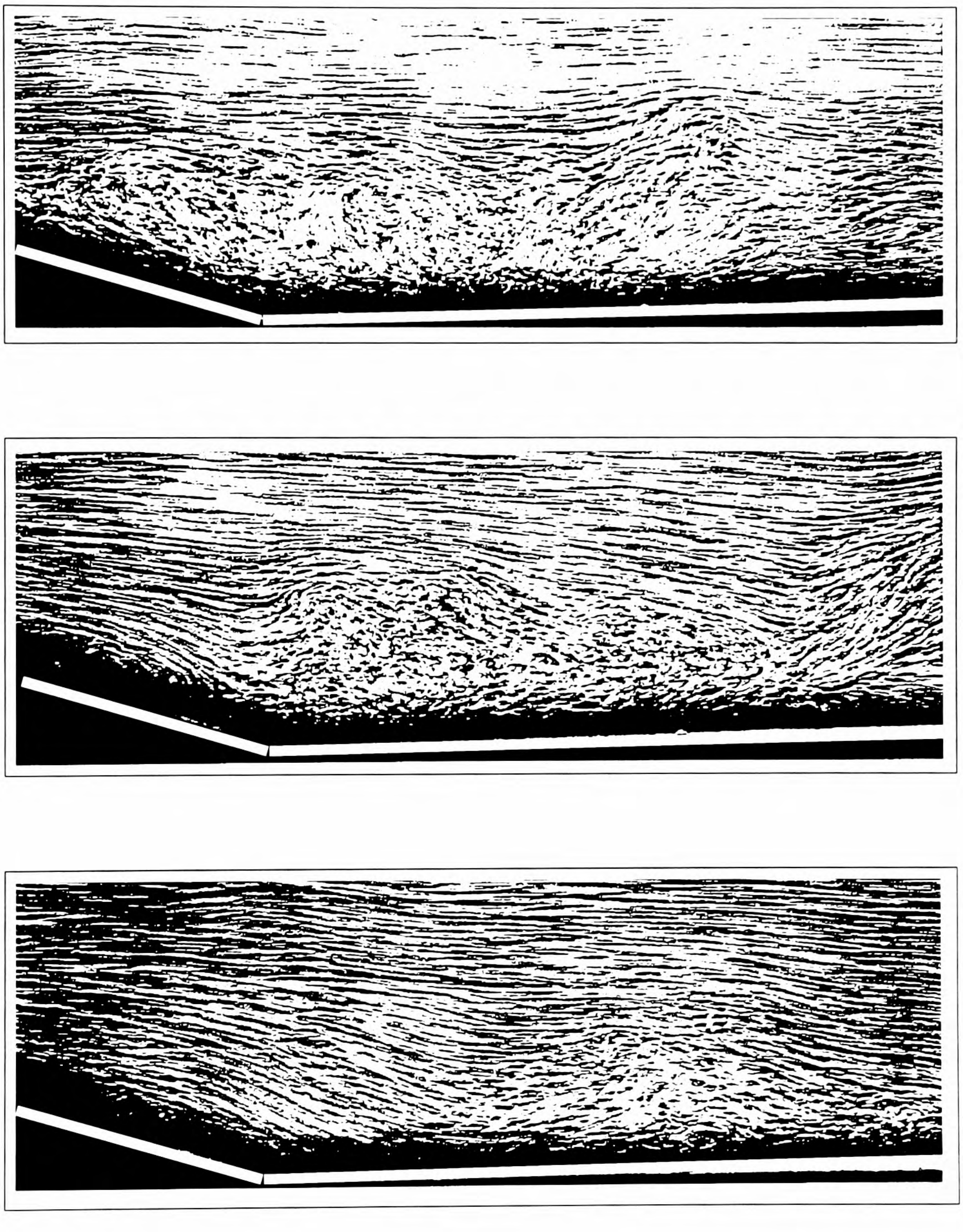

Figure 4. The plates show three views of the recirculation region behind an experimental bedform. The shots are 0.35 secs. apart and clearly visualise the sweeping away of the turbulent region, leading to re-attachment close to the trough. We term this sequence of events Coanda-flapping.

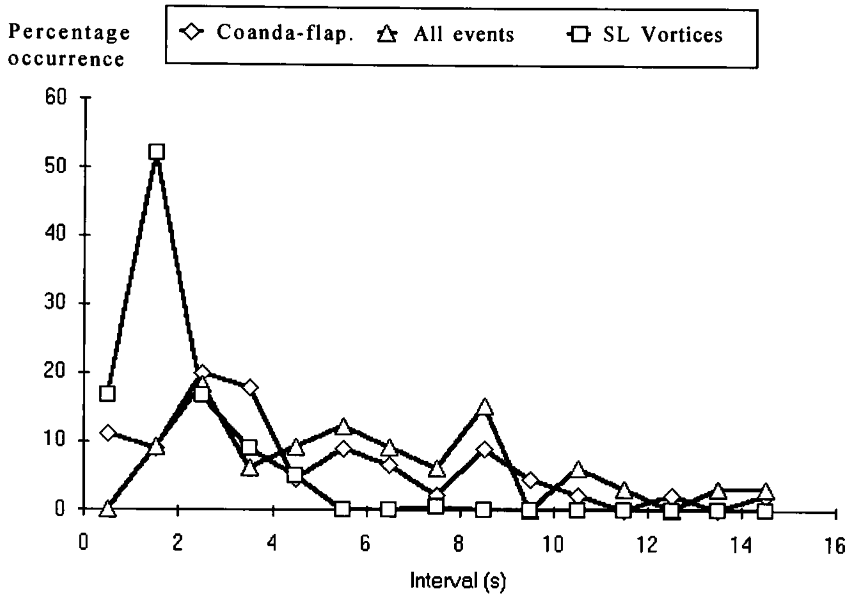

Figure 5. Intervals between Coanda-flapping events, between the passage of shear layer vortices (SLVs) and between other turbulent events at U=0.20m/s. There is a strong correlation between the coanda-flapping events and the passage of upstream turbulent events.

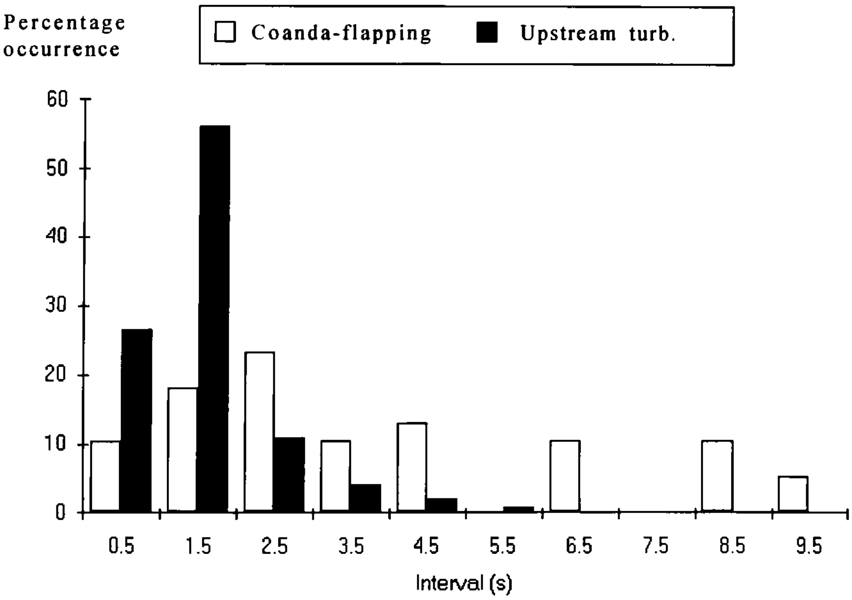

Figure 6. Intervals between Coanda-flapping events and between the passage of turbulent events, including shear layer vortices, at U=0.31m/s. This highlights the fact that not all upstream turbulence can trigger the Coanda-flapping event.

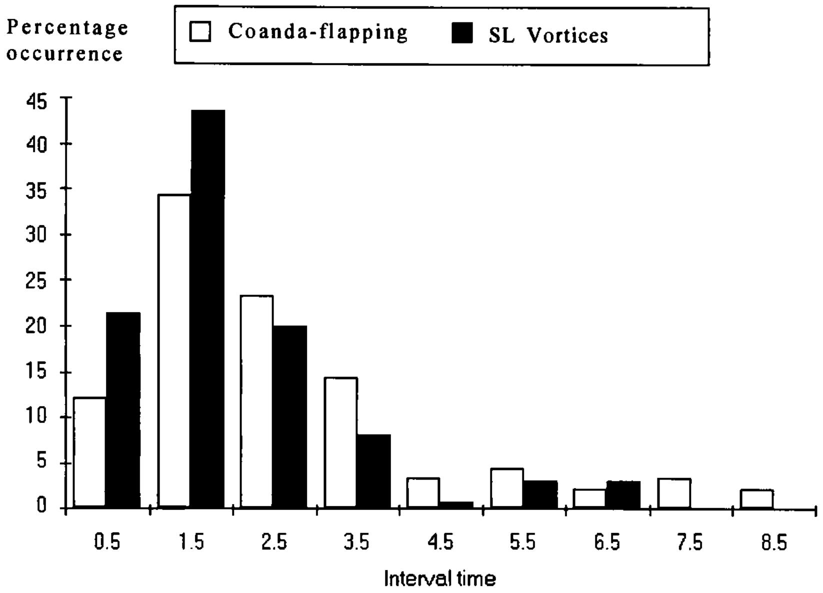

Figure 7. The Intervals between Coanda-flapping events and between shear layer vortices at U=0.36m/s.

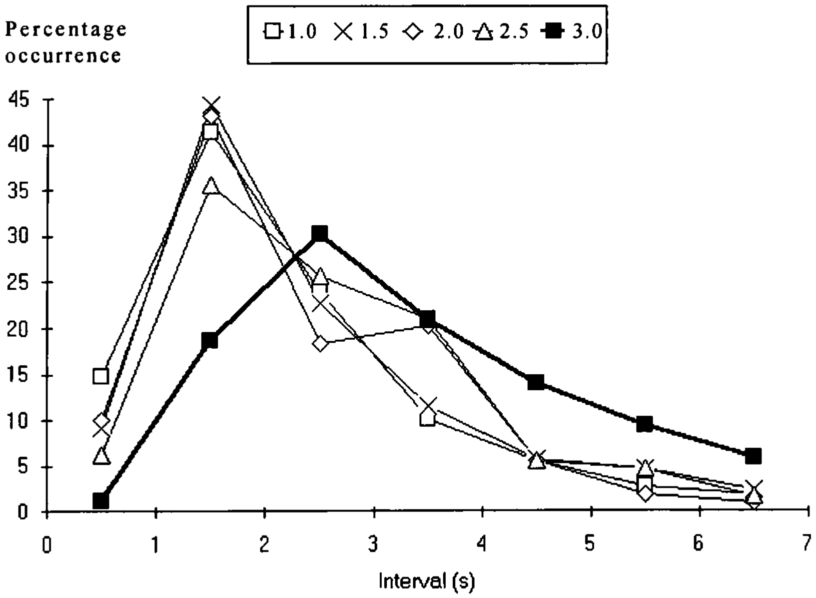

Figure 8. The Intervals between Coanda-flapping events at various values of inter-crestal spacing L=nLo where n=1.0, 1.5, 2.0, 2.5, 3.0 at U=0.43m/s. Notice the peak occurs in the 2.5s interval range for L=3.0Lo rather than the 1.5s interval range.

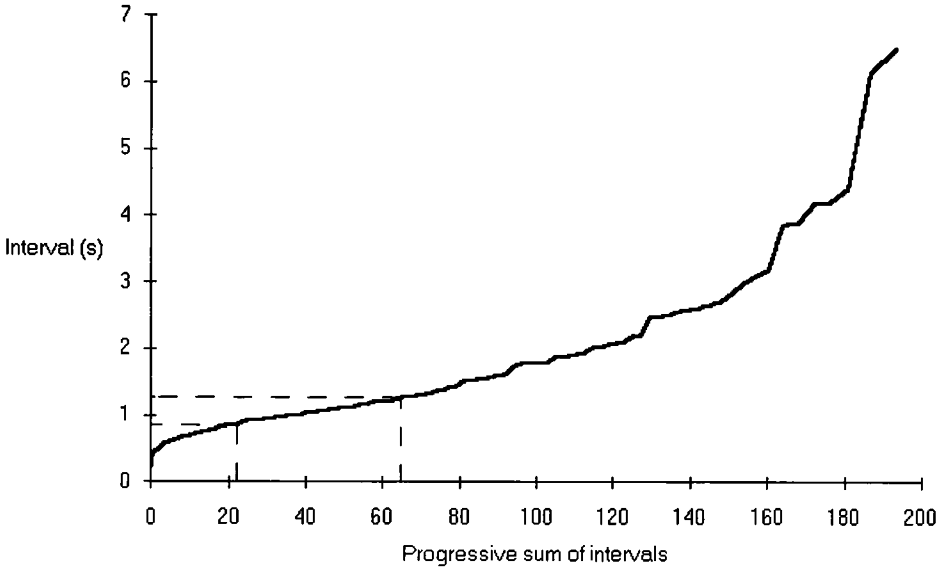

Figure 9. The interval (s) between Coanda-flapping events plotted against the cumulative sum of the intervals for inter-crestal spacing L=Lo. The point with the lowest gradient is the modal interval which can be seen on the graph below, indicated by the dotted lines.

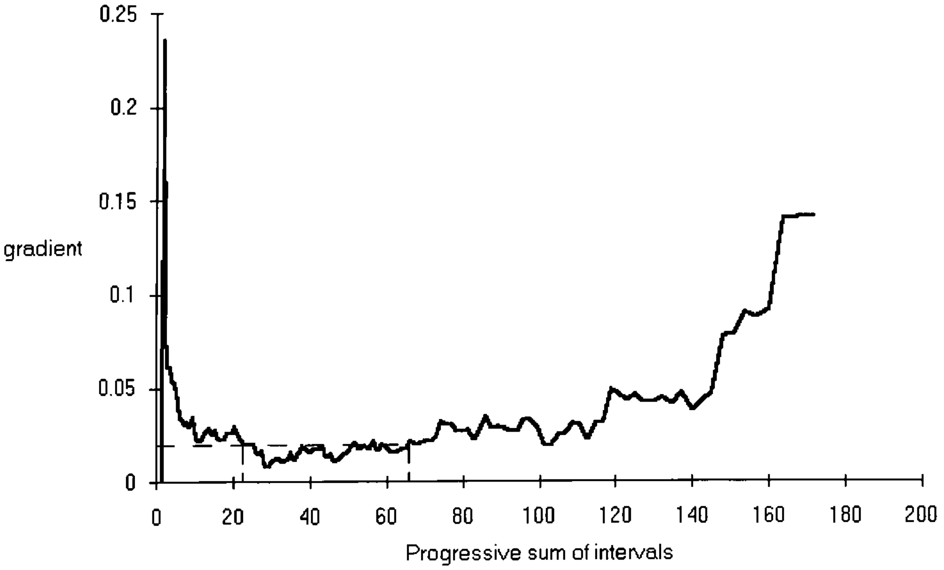

Figure 10. The gradient of the line in the above figure averaged over eleven neighbouring points so as to remove the peaks and troughs where only two or three intervals are similar in value and simultaneously highlight the lowest gradient over a small interval range. The modal value occurs between interval sum of about 20 and 60s, corresponding to 0.9-1.3s on the graph above.

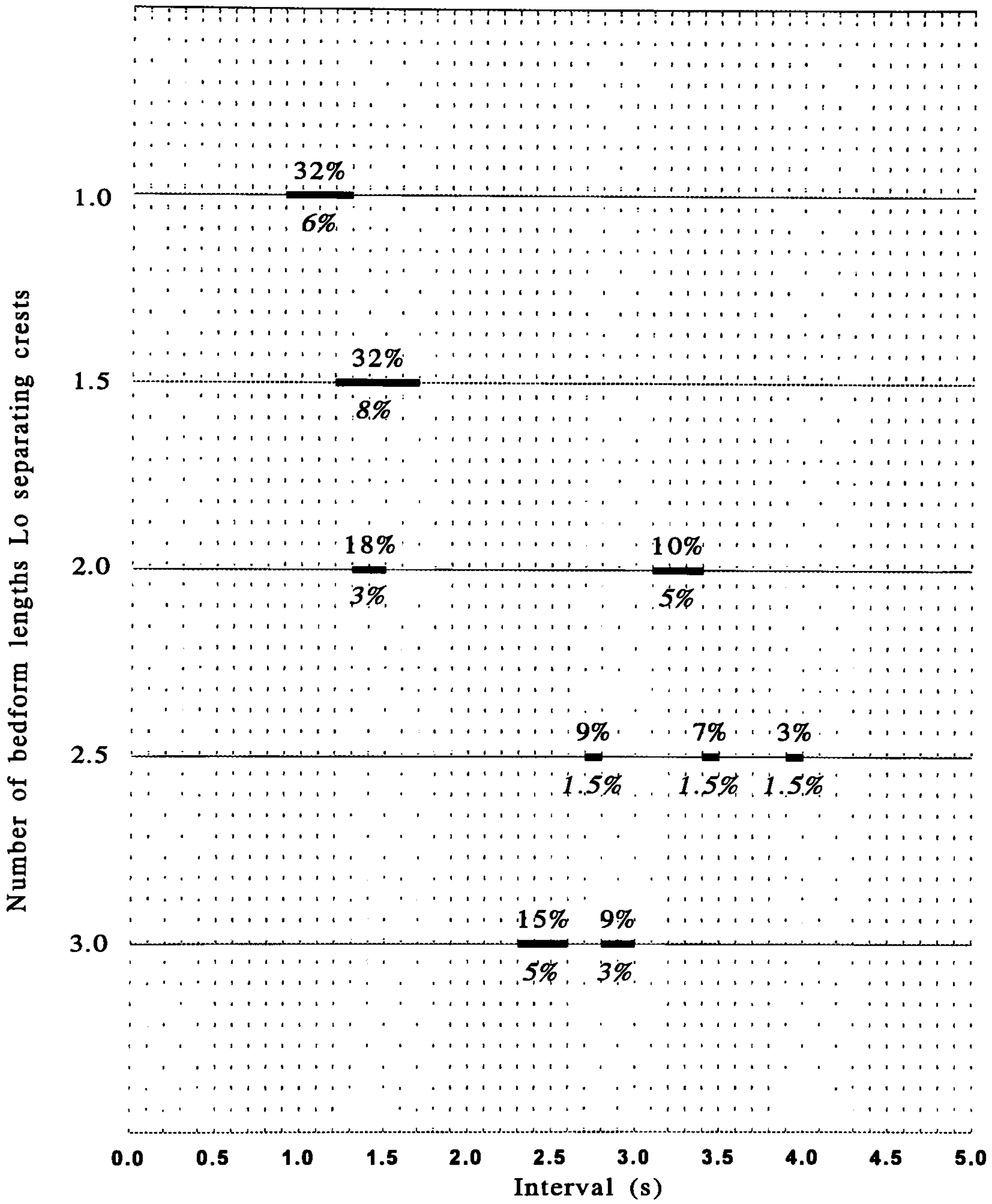

Figure 11. The modal intervals between Coanda-flapping events at various values of inter-crestal spacing from L=Lo to L=3.0Lo. At increased crest separation the interval between Coanda-flapping events is seen to double, consistent with the theory that they are triggered by the passing of shear layer vortices. The percentage figure above the line represents the percentage of all measured intervals that fall within this range, whereas the percentage figure below the line represents the percentage of events we would have expected to find in this range if the data was evenly spread over the entire range 0-6.5s (we only show 0-5s here).

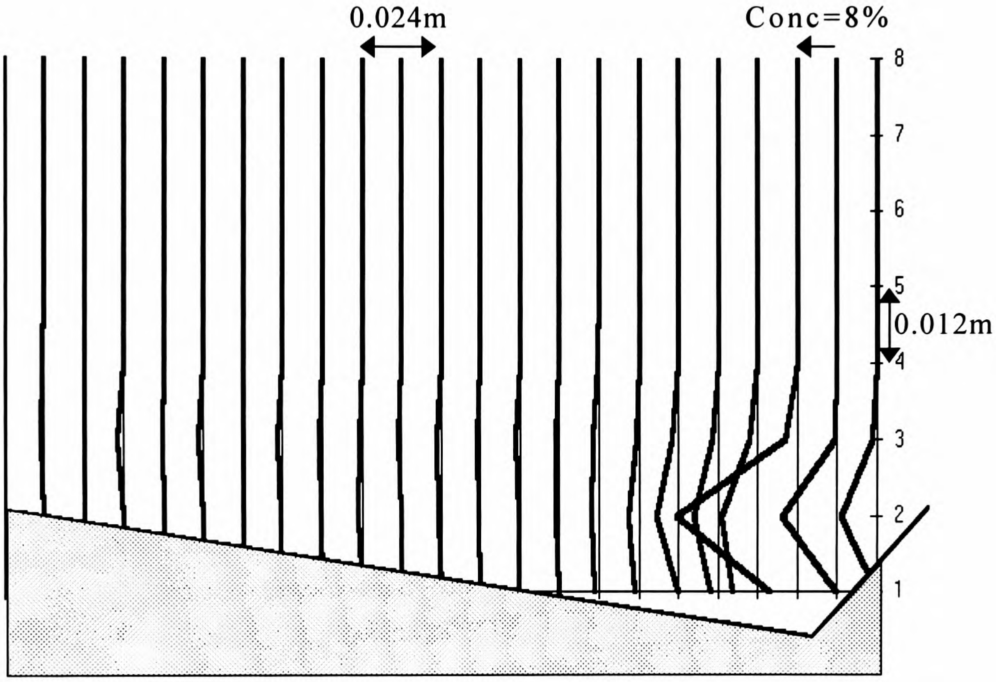

Figure 12. The concentration distribution due to lee slope suspension of particles by the Coanda-flapping flows at U=0.20m/s. The grey region represents the bedform and is added to aid positioning of the concentration lines in space.

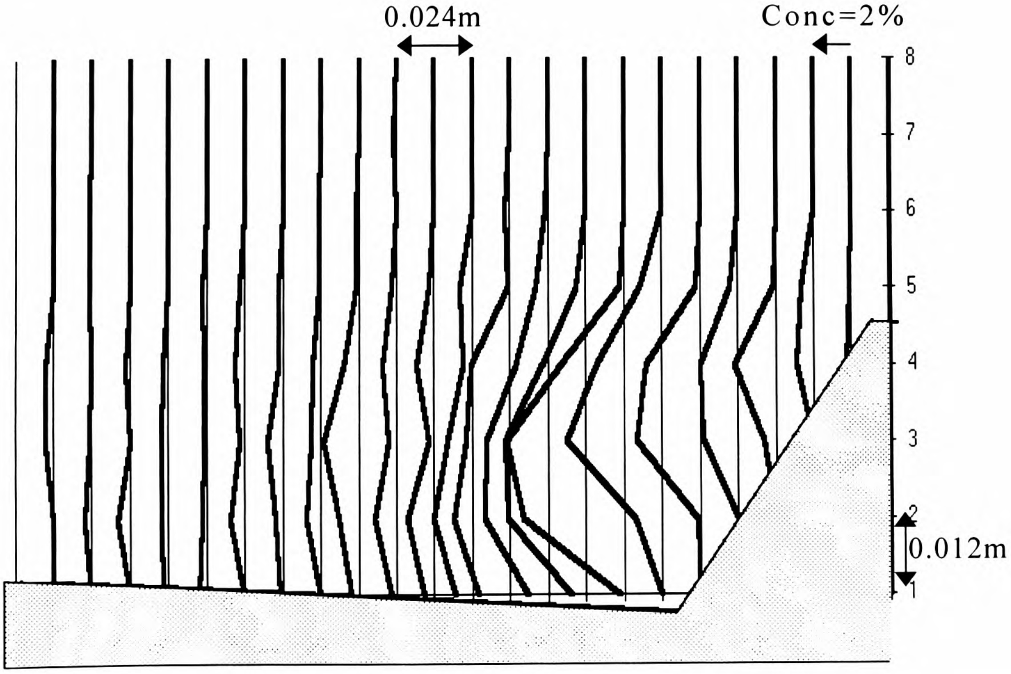

Figure 13. The concentration distribution due to lee slope suspension of particles by the Coanda-flapping flows at U=0.31m/s.

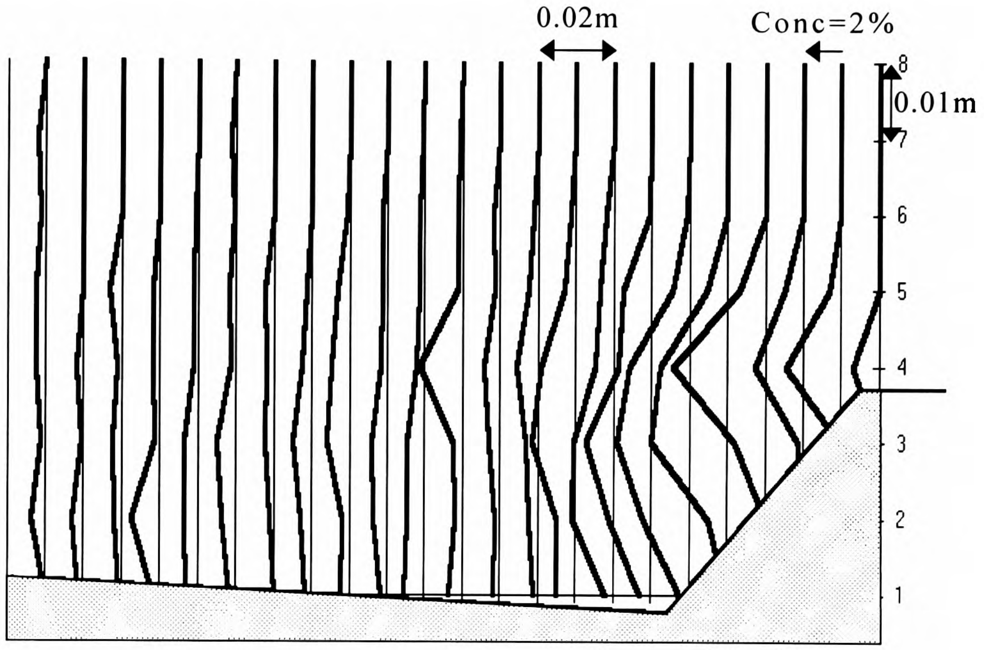

Figure 14. The concentration distribution due to lee slope suspension of particles by Coanda-flapping and lee-shear capture at U=0.36m/s.

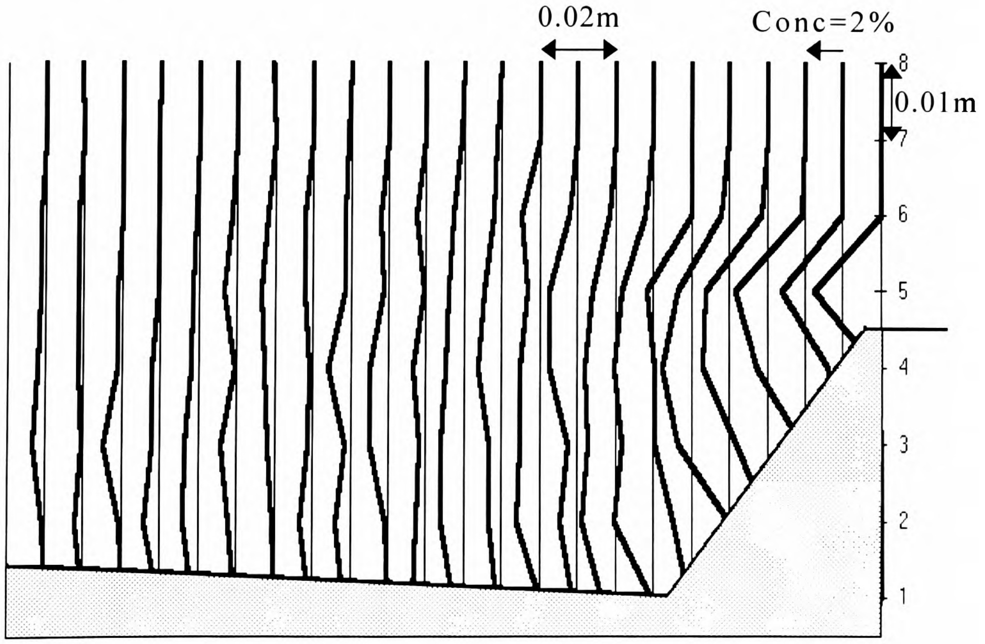

Figure 15. The concentration distribution due to lee slope suspension of particles by Coanda-flapping and lee-shear capture at U=0.43m/s.

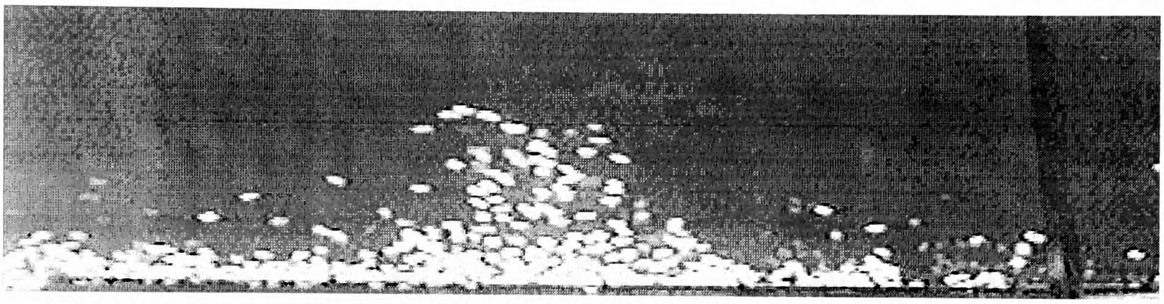

Figure 16. A cloud of particles with quiescent fall speed V=0.06m/s suspended from the stoss slope at a flow speed of U=0.36m/s. The flow is from right to left.

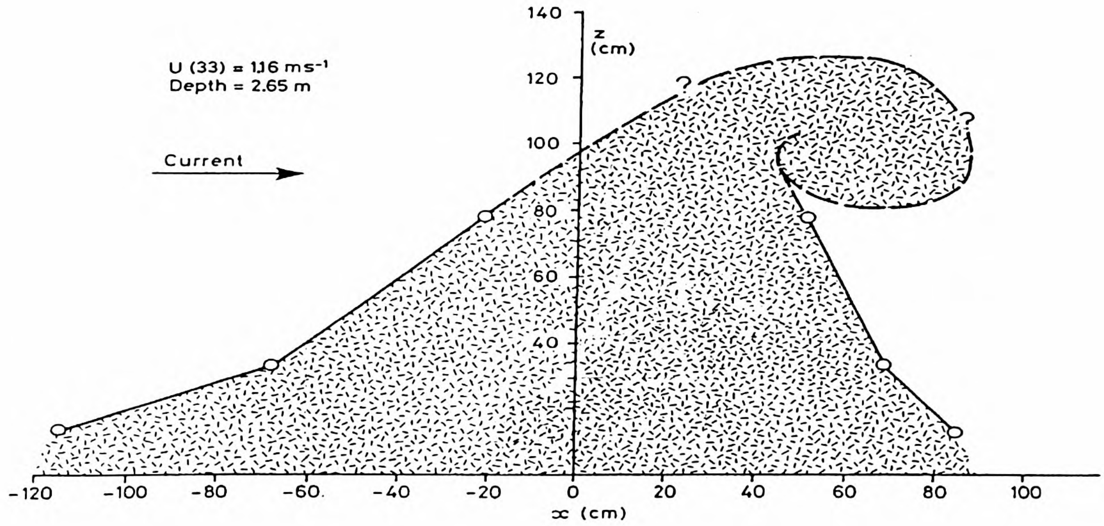

Figure 17. After Soulsby (1989). The shape of a cloud of sediment downstream of a sandwave crest in the estuary of the river Taw, Devon, England. The flow is left to right, z is height, U current velocity and x horizontal length scale..

CHAPTER 5: NUMERICAL SIMULATIONS WITH FIXED VORTEX CORES

SUMMARY

We consider interactions between Rankine vortices and particles as an idealised approximation of particle transport in the shear layer separating from the crest of a sandwave. It is a particularly relevant model to employ since cored vortices (chapter 1) have been widely adopted in the literature on shear layers as a simplified description more amenable to direct calculations than computational alternatives which use, for example, discrete vortex models. This simulation derives from an analysis developed by Auton (1984) for the dynamics of particles in weak shear flows, which has been used for vortex-bubble simulations by Thomas et al (1983). The force law includes asymptotically correct formulations for the lift and inertial forces, but neglects the Basset terms, consistent with the high Reynolds number approximation relevant here.

Our results highlight the importance of pressure gradient and added mass terms in two-phase vorticity dynamics and clearly demonstrate that time averaging of the instantaneous velocity field must have catastrophic consequences for characterising entrainment and entrapment. We present a criterion for sediment entrainment into a Rankine vortex; our formula depends on the particle fall speed in quiescent liquid and the vortex core radius and angular speed. Comparison with published experimental data is encouraging.

1 INTRODUCTION

We use a Rankine vortex core as a model of the first generation vortex downstream of a crest in the developing shear layer to assess capture criterion for particles at the crest. Using a compact support (chapter 1) to represent a discrete vortex has gained wide acceptance in the discrete vortex modelling literature where it is now the standard choice for solving the problem of high induced velocities caused by point vortex interactions over infinitesimal distances (Sarpkaya, 1989). Such a compact support was used by Thomas et al (1983) in modelling the flow of bubbles around a spinning rod as idealised isolated vortex, by Nielsen (1984) to model sediment suspension and by Hunt et al (1988; also Sene et al, 1993) in discrete vortex modelling of shear layers.

Our use for the cored vortex is akin to Julien (1986) who applied a Rankine vortex model to the analysis of fine silt concentrations in a steady, horizontal vortex. His particle equation involved only the pressure gradient and viscous drag terms, and it was assumed that the particles possessed only a very small slip speed. The focusing forces were balanced by a diffusional flux with diffusion coefficient (assumed to be constant) that was deduced from experiments. Julien demonstrated his formulation fitted the shape of the experimental concentration curves.

Yalin & Ferreira da Silva (1991) used discrete vortices to model sediment suspension during a boundary layer burst but supposed a Gaussian sediment distribution within the core rather than considering the interesting and complicated dynamical interactions in detail. Nielsen (1984) gave an analytical solution to the problem of sand interaction within a Rankine vortex, showing that particles could be suspended on closed trajectories in the core region. He noticed that particles could only achieve this closed trajectory if they happened to be there initially, or were entrained during an undefined vortex growth period.

An asymptotically correct formulation developed by Auton (1984) for the force law of discrete elements in weak shear flows at large Reynolds numbers has been used by Thomas et al (1983) as a diagnostic tool to analyse the modes of particle-vortex interactions. The Basset term was not included in this analysis, consistent with the high Reynolds number approximation. Also neglected was the Magnus spin-lift force which is important in such flows as gas-solid pipe flow where the wall impacts are known to induce large spin momentum to the particles (as discussed by Tsuji et al, 1987). We discuss this further in chapter 6.

Below we consider particle interactions with Rankine vortex cores and highlight the sensitivity to initial conditions of the resulting trajectories. We identify the dominant forces on the particle throughout its trajectory, estimate the particle relaxation time to the changing velocity field and assess the effective particle fall speed in these flows. The results relating to particles falling into or gathered up by the vortex flow are then used to infer likely interactions occurring in sediment transport from sandwave crests. More specifically, we identify a criterion which defines the limiting fall speed for which a particle can be captured by the vortex.

2 COMPUTATIONAL PROCEDURE

The particle equation proposed by Auton (1984) incorporated individual contributions to the body force **F** from pressure gradient (P), acceleration (I), vorticity-lift (L) and drag (D), for which the resulting equation (see appendix 9) of particle motion can be written

$$\left(\frac{\rho_P}{\rho_L C_{vm}}+1\right)\frac{d\underline{v}}{dt} = \left(1+\frac{1}{C_{vm}}\right)\left(\frac{D\underline{u}}{Dt}\right) - \frac{g}{C_{vm}}\frac{\Delta\rho}{\rho_L}\left(1+\frac{\underline{w}|\underline{w}|}{V_T^2}\right) - \frac{C_L}{C_{vm}}\underline{w x \omega} \quad \mathbf{(1)}$$

where $\underline{v}$ is the particle velocity, $\underline{u}$ the liquid velocity, $\underline{u}.\underline{\nabla u}$ the (steady) flow acceleration, V_T the terminal fall speed (quiescent liquid), $\underline{w}=\underline{v}-\underline{u}$ the slip speed, $\underline{\omega}$ the vorticity vector, $\rho_{P/L}$ the particle/liquid density, $\Delta\rho=\rho_P-\rho_L$, g gravitational acceleration and t time. Also, the coefficients of virtual mass and lift are assigned their asymptotic quasi-steady values: $C_{vm}=0.5$, $C_L=0.5$. The equation for the fluid field is described in appendix 9.

We solved this equation numerically for the prescribed vortex flow to obtain the acceleration of a particle at discretised time intervals, as discussed below. The equations were non-dimensionalised, (see appendix 1) using the core radius and the terminal fall speed of the particle. They were solved numerically (using an algorithm reproduced in appendix 2) to obtain a range of trajectories with V_T as parameter; the key scaling here being the ratio V_T/RA, where R is core radius and A angular speed $(\omega/2)$.

2.1 Iteration interval

Selection of suitable time steps was crucial, and to identify an acceptable value we initially used a neutrally buoyant particle and required that its local radius r, measured from the vortex centre, should not adjust by more than 2% (arbitrary selection) during any complete revolution due to tangential approximation to the curved trajectory. Such trajectory plots for this convergence test are presented in figure 1a,b where the non-dimensional time step is 0.002.

2.2 Initial conditions

One prerequisite for starting the calculation is selection of particle location and velocity. In the absence of any obvious guiding constraints the choice is arbitrary but the results can be highly sensitive to very small differences in initial values. Consider figure 2, in which the circles represent the vortex core and the open curves show representative particle trajectories. In each case here $V_T=0.5$ and the initial horizontal component particle velocity $V_X=0$. The initial Eulerian vertical component particle relative velocity is then $V_Y=U_Y-V_T$ (eg -0.2m/s in figure 2a), where U_Y is the flow velocity component at the initial particle position. To illustrate the sensitivity to initial slip velocity we show cases a), b), c) and d) in which V_Y is initially -0.20m/s, 0.0m/s, 0.05m/s and 0.3m/s.

Now consider figure 3 showing eight particle trajectories from initial positions varying from two radii horizontally to the right of the vortex axes to three radii directly above the axis. V_Y and V_X initially assigned equal to the local fluid velocity values and the resultant trajectories were non-chaotic. The essential point is that system parameters and initial conditions serve to define uniquely subsequent behaviour which, in figure 2 is chaotic and figure 3 is ordered. Careful selection of initial conditions (if arbitrarily chosen) is advised.

3 RESULTS

We survey various values of V_T with core parameter AR fixed (section 3.1), assess the forces on particles falling from starting points below and above a vortex (section 3.2 and 3.3) and describe a vortex-particle capture criterion (section 3.4).

3.1 Varying V_T at fixed R and A

We chose parameter values A=100 rad/s and R=0.006m for the vortex and varied V_T to assess the sensitivity of particle trajectories.

Examples are shown in figure 4 for V_T varying from 1m/s to 0.05 m/s (ie parameter V_T/AR varying from 0.6 to 12.5). In a) the particle fell with slight curvature taking its trajectory towards the core. This curvature increased in b) and c) until conditions were appropriate for the particle to enter the core in d). Once inside the core, the particle immediately experienced shear lift force, was attracted inwards and was carried around the axis several times until finally ejected by centrifugal expulsion following acquisition of sufficient angular momentum.

Comparative fall times over a descent of 5 core radii are shown in figure 5 for V_T's from 0 to 1m/s, in which the peak marked D corresponds to trajectory d in figure 4. For V_T's less than this value (0.4m/s), the trajectories passed through the core at a higher elevation and exhibited less tortuosity thus reducing the effective residence time, as seen in figure 5. However, as V_T approached zero, the transit time eventually increased and the trajectories exhibited outward spiralling, first following just one orbit, then increasing numbers and eventually approaching neutrally buoyant behaviour as $V_T \rightarrow 0$ for which the residence time tended to infinity. To the right of D in figure 5 the gravitational force overwhelms the fluid gradients and the particle simply falls from the core.

3.2 Forces on particles starting below the vortex

Figure 6a shows example trajectories plotted for a particle starting from numerous locations on a horizontal plane 2R below the vortex axis. Vortex circulation was counter clockwise with magnitude such that peak tangential velocity was $6V_T$ (arbitrary selection), ie the non-dimensional parameter $AR/V_T=6$. We begin our description with the trajectory marked (*--*), initially deflected leftwards with the flow. The relative non-dimensional transit times T_{ND} (equal to actual fall time less the time taken to fall an equal distance in quiescent water; the quiescent fall time, T_Q) for these trajectories appear in figure 6b (recall: non-dimensionalised on R and V_T). Figure 6c shows magnified details of key trajectories whereas figure 6d shows other behaviour to which we shall return later. The forces acting on the particle as it fell along the *'d trajectory are shown in vector form in figure 6e. We see buoyancy force (B) acted downwards throughout its transit whereas the instantaneous drag (D) initially acted in the direction of the flow when the particle was at rest, and at later times acted almost vertically upwards as the particle approached vertical motion with slip speed V_T. Of course, contribution from the local pressure gradient or fluid acceleration (PI) always acted towards the vortex axis.

Returning to figure 6a, and shifting the starting position rightwards, we see the trajectories are increasingly curved due to the higher pressure gradient and drag forces. The trajectory in figure 6f clearly exhibits this behaviour. For a starting point immediately below the vortex axis (figure 6g), this PI force was dominant and the particle was accelerated inwards and around the core until its angular momentum eventually overwhelmed the pressure gradient, when it escaped via the fourth quadrant. Further rightwards in figure 6a, the local flow gradients decline until, for trajectory 6h, particle drag is responsible for the path over the vortex. Eventually, gravity becomes the dominant force, and the particle falls vertically downwards in the weak outer flows.

Returning to figure 6b we see how the net forces act to extend or diminish T_{ND}. In particular, the case shown in figure 6h corresponds to the second peak (at 5 on the abscissa of figure 6b) for starting location (X_{SL}) approximately 6R to the right of the vortex axis. As mentioned above, particle hold up here arises from the balance between local upflow drag and gravity. Figure 6d shows particle trajectories starting from a horizontal plane 4R below the vortex axis. We see that the local pressure gradients are too small to achieve upwards acceleration of the particle (cf figure 6a), and they experience only hindered settling.

3.3 Forces on particles initially above the vortex

As a demonstration calculation we chose V_T=0.28 m/s, R=0.005 m and A=200 Rad s^{-1}; ie parameter AR/V_T=3.6 (cf 6 above; ie a weaker vortex here). Figure 7a shows trajectory plots which should be compared with those shown in figure 6a. The particles here descended from starting locations in the horizontal plane 3R above the core axis. Some key trajectories are distinguished on figure 7b, whilst figure 7c shows the particles relative non-dimensional fall times T_{ND} for different X_{SL}.

a) Reference trajectory and first time-peak trajectory. The particle following the *'d reference trajectory in figure 7a, starting at -1.3R to the left of the core, descended the reference height of 10R in $T_{ND}=0$. For all starting positions to the right of this location $T_{ND}>0$ and to the left $T_{ND}<0$.

The descent times in figure 7c exhibit three peaks and two troughs. The trajectories associated with these peaks and troughs are identified in figure 7b. Thus the slightly curved trajectory A starting from horizontal location $X_{SL}=-2R$ gave $T_{ND}<0$ due to drag enhanced downwards acceleration. Trajectory B with $X_{SL}=-0.8$ is associated with the first peak in figure 7c. The forces acting along this trajectory are shown in figure 7d. Clearly the PI force (in red) was dominant in lengthening the particle transit, resulting in $T_{ND}>0$.

b) First time-trough and second time-peak trajectories. Trajectory C in figure 7b, corresponding to $X_{SL}=0.2R$ and the first trough in figure 7c, crosses the core where it additionally experienced lift force as shown in figure 7e-g. In figures 7f and 7g the local net force, position and speed are plotted versus time. In figure 7f we see explicitly how the lift force (pink line) is switched on following entry to the core (T=1.6) and then switched off at exit (T=2.3). The drag force is dominant from T=0 to T=1 as the particle is accelerated from rest by the outer potential flows. By T=1.5 the PI force increases as the particle encounters the high velocity gradients closer to the axis and we see the drag peaked in opposition to this induced motion. The lift and PI forces were jointly responsible for accelerating the particle around the vortex axis, following which all the flow forces diminished.

The vertical component forces (Y direction) along this trajectory are seen in figure 7g. Here the PI forces accelerate the particle downwards until it enters the core where the lift force repels it from the axis (as explained below) until it crosses the mid-plane when both the PI and lift forces change sign. The neutral component PI force changes sign since it is always directed towards the centre of the vortex, and diminishes with distance from the axis. The drag force was unidirectional throughout this trajectory, always retarding the particle's descent. Clearly, in this case, PI forces dominated the lift force.

The forces associated with trajectory D on figure 7b, relating to the second peak in figure 7c, are plotted versus time in figure 7h and 7i. The vertical component behaviour is broadly similar to that discussed above. Both the drag and the PI forces accelerate the particle leftwards until it enters the core. Here it experiences a lift force which is attractive horizontally and repulsive vertically. This difference arises from the relative velocity, as indicated in figure 7j. We see that the vertical component flow velocity U_Y was always greater than the vertical component particle velocity V_Y, thereby producing a positive horizontal component lift force (figure 7k) acting towards the core centre. Conversely, the relative horizontal component velocities V_X-U_X changed sign, resulting in vertical component lift force that also changed sign (figure 7k) and essentially always acted to repel the particle from the core.

Returning to figure 7h, the horizontal component drag force accelerates the particle rightwards after it exits the core which, combined with the positive vertical component PI force, caused the particle to move upwards and so lengthened its trajectory, resulting in the second peak appearing in figure 7c. Figure 7l shows the horizontal component velocities U_X and V_X. We see the particle relaxation time is increased by larger flow velocity gradients due to particle inertia. For the maximum lag shown here, the particle velocities are less than half the flow velocities.

c) **Second time-trough and third time-peak trajectories.** The second trough on figure 7c relates to starting location $X_{SL}=3.6R$ and corresponds to trajectory E in figure 7b; a vector force diagram is shown in figure 7m for completeness. The third peak in figure 7c, corresponding to trajectory F in figure 7b, is due to the cusp at which the particle remains approximately stationary from T=12 to T=25. This metastable equilibrium is reflected in the force balance shown in figure 7n, and the significantly extended descent path as compared with the other trajectories. Figure 7o illustrates clearly that it is the buoyancy which counteracted the PI, D and L forces during the extended interval from T=5 to T=25. To the right of the third peak in figure 7c the particles undergo hindered settling in the outer upwards-directed flows that weaken with increasing X_{SL} (eg trajectory G), and T_{ND} must tend to zero asymptotically with increasing X_{SL}.

d) Core-entry limiting trajectory and cusp point. Figure 8b illustrates the limiting trajectory V_T selected such that, starting from any horizontal plane 3R above the vortex axis, it passes around the core but does not enter it. For any given vortex prescription in terms of A and R, there is a critical value of V_T, V_{Tcrit} say, above which a particle within a defined range of starting points above the vortex must enter the core. V_{Tcrit} thus provides a criterion to assess the capture capability of vortices with defined A and R. Figure 8a shows V_{Tcrit} versus A for three values of R, from which we see that the relation is not simply linear. Figures 8b-e show typical trajectories for representative examples with R=0.005 m, one of the cases in figure 8a. The location of the cusp marked '*' in figures 8b-e was displaced downwards with increasing A: compare figure 8b with figure 8e.

Figures 9a-c show descending trajectories for three values of R with A and R selected such that the tangential velocity was equal to about $3.6V_T$ at the core edge (parameter $AR/V_T=3.6$, as in a, b and c above). These graphs show the transit time relative to that for descent at V_T, and they all have a peak corresponding to starting locations about 6R offset from the vortex axes. This corresponds to the trajectory traversing the longest, slowest path in the vicinity of the cusp. Indeed, an analytical solution at the cusp would surely produce infinite transit time here (although this is irrelevant for engineering practicalities).

3.4 Vortex-particle interaction criterion

We now consider in more detail the conditions for the limiting trajectories which first travel around the core. Again the particles were assumed to be initially at rest - as appropriate for simulating their suspension from a bed. Starting values of (X,Y) in the range (-4:10,-4:4) were selected for these calculations.

Firstly, consider figure 10. Figure 10a shows the trajectory for a particle starting with (X,Y)=(0,-1) and having critical V_T such that it is not captured by the core ($AR/V_T=2.62$). On the other hand, figure 10b shows the trajectory with $AR/V_T=2.81$. Here the particle was definitely captured by this stronger vortex and looped the core. Figure 10c shows the trajectory of a particle which was 'just captured', here with $AR/V_T=2.7$. It is clear that for other starting conditions X, Y, V_X, and V_Y there will be similar critical values of $AR/V_T=C$.

More specifically, we defined criterion $C(X,Y,V_X,V_Y)$ as

$$C(X,Y,V_X,V_Y) = \frac{AR}{V_T} \tag{2}$$

Thus (to clarify the terminology) the critical value for the proceeding example was

$$C(0,-1,0,0) = \frac{AR}{V_T} = \frac{7.2 \times 0.006}{0.016} = 2.7 \qquad \textbf{(3)}$$

which held for all vortices and particles initially starting from rest at $(X,Y)=(0,-1)$: ie the capture criterion was

$$\frac{AR}{V_T} \geq C(0,-1,0,0) \approx 2.7 \qquad \textbf{(4)}$$

Figure 11 shows calculated values of C(X,Y,0,0) versus X for fixed Y, demonstrating a minimum value and an indefinite increase as $X \rightarrow \pm\infty$. Indeed, by arguing that the local upflow must compensate for V_T as $X \rightarrow +\infty$, we can deduce the behaviour illustrated on figure 11, namely that critical $AR/V_T \propto X$. We also deduced numerically that as $X \rightarrow -\infty$, $C(X,0,0,0) \rightarrow -3.5X$.

Similar criteria were obtained for positive values of Y (ie above the horizontal plane of the vortex axis), for example C(0,1,0,0)=3.2 and C(10,1,0,0)=12.5. The minimum values C_{MIN} exhibited by each graph have X values that are a linear function of Y and $C_{MIN}=2.6Y$ for $Y<0$. C(X,Y,0,0) increased with decreasing Y for all values of X.

Figure 12 shows R dependence of C(X,0,0,0) for constant AR. Increasing R gave lower values of C(X,0,0,0), most noticeably for $X_{SL}>-0.2$. We note the staggered lines are a consequence of stepping the calculation in V_T. Doubling R caused a maximum reduction of only 6% which we regarded as sufficient demonstration that R-dependence is small (for fixed AR). Caution is advised in the blanket assumption that AR/V_T is a non-dimensional parameter over the entire range of A and R.

4 DISCUSSION

Having analysed the forces and trajectories followed by particles departing from various locations above and below defined vortices, we now generalise to inferences for sediment transport in real systems, with regard to the forces in shear flows, the effective fall speed and the significance of our capture criterion.

4.1 Forces acting on a particle in shear flows

We have shown how the dominant forces on particles released near vortices are those due to the flow pressure/velocity gradients and these forces act towards the vortex axis. Further from vortices drag and buoyancy dominate. When the particle is inside the vortex core, the vertical component of vorticity lift is repulsive and the horizontal component attractive.

To discuss the implications of these results we compare our conclusions with trajectories computed using time-averaged modelling methods. We take a simple case to highlight the important effect on the pressure gradient and fluid inertia forces of time-averaging, and the subsequent prediction of second phase dispersion. A more complete analysis would only cloud these issues.

Suppose a Rankine vortex (radius R) appears and translates a distance D before disappearing after time T. Figures 13 and 14 show the resulting time-averaged horizontal and vertical component fluid velocities versus X for fixed Y planes, here with D=100R. Figures 15 and 16 show the same velocity components for D=10R. We choose a particle-vortex interaction for which the capture criterion C was satisfied: viz $AR/V_T=8$. Trajectories followed by this particle travelling in the two time-averaged flows and in the time-dependent field of the moving vortex are shown in figure 17. Note that the particle release condition in each case was $(X,Y,V_X,V_Y)=(0,-2,0,0)$. For time-averaged flow with D=100 (green line) the particle simply descended from its starting point. For D=10 (blue line) the trajectory was initially upwards, but then descended. However, with the time-dependent field (red line) the trajectory was cyclical, corresponding to a nearly circular trajectory outside the vortex core.

The key point to note from this simple demonstration is that the time-averaged flows fail to elevate the particle above the vortex mid-plane because the instantaneous flow/pressure gradients had been averaged out. Moreover, subsequent introduction of a Gaussian fluctuating field, as is often done in calculations with engineering turbulence models, will not compensate for time-averaged exclusion of the coherent travelling capture field represented by our cored vortex (or eddy). This issue is at the heart of the current debate about how to formulate closures for the Lagrangian point pressure-velocity correlation which is often the most important contribution to the interphase momentum transfer term (NH Thomas, private communication).

4.2 Effective particle fall speed

For particle-vortex interactions not meeting the criterion C the vortex caused either an increase or a decrease in the apparent particle slip speed (V_{TA}), depending sensitively on the starting conditions assigned. An increase in V_{TA} was achieved for starting location (X_{SL}) to the left of the vortex centre; ie local upflow. We note there is always a point X_{SLo} for which $V_{TA}=V_T$, and, according to our computations, this always resided in locations between -2R and 2R. For $2R<X_{SL}<6R$ we found $V_{TA}<V_T$ and for $X_{SL}>6R$, V_{TA} asymptotically approached V_T.

These guidelines for effective slip speed dependence on X_{SL} define the approximate field of vortex influence on a particle; ie the region inside which effective particle entrainment occurs. Thus, if $-2R<X_{SL}<6R$ then the particle experiences a significantly hampered descent. Muller & Gyr (1986) suggested vortex spacing in a developing shear layer is around 4.5R so we conclude that strong particle-vortex interactions are generally likely, subject to the constraints of criterion C.

4.3 Comparison of criterion C with published data

Atkins & Soulsby (1992) reported sediment concentrations and flow velocities over an estuarine sandwave at peak flood tide (stream velocity 0.643m/s) with a maximum sediment grain diameter in suspension after the crest of about 700 microns in a population of which 99.2% were sized less than 400 microns (the accompanying bedload comprised material sub 2000 microns). They did not present data for the fluctuating velocities explicitly, but we can make an estimate from two other sources. Firstly, Johns' (1991) k-ϵ model for flow over the sandwave described by Atkins & Soulsby (1992) used mean squared fluctuating vertical and horizontal velocities of 0.35k and k respectively, where k is the turbulent kinetic energy density in $(m/s)^2$. The maximum value of k at X/H=1.25 (X measured downstream from the crest) was about 0.018 $(m/s)^2$ at an oncoming flow velocity of 1 m/s, suggesting rms fluctuations about 15% or so of the mean velocity. Secondly, Nakagawa & Nezu's (1987) experimental data gave a peak rms velocity fluctuation in a back-step shear layer of about $0.18U_{MAX}$ where U is the downstream mean flow velocity before the separation point.

Figure 18 shows estimates of the fluctuating velocities as deduced by assuming, for convenience, a sinusoidal time profile, such that the peak values are $\sqrt{2}$ times the rms values. As a crude guideline we simply average these three values to obtain a fluctuating velocity value $f_{MAX}=0.1\pm0.04$ m/s. If we take f_{MAX} to be the vortex tangential speed AR and adopt the lowest value of

C from figure 11 (ie 2.2) then we have

$$\frac{f_{MAX}}{V_T} = 2.2 \qquad \textbf{(5)}$$

and hence V_T=0.05±0.02m/s which corresponds to a quartz sand grain diameter of 350±100 microns (Hallermeier, 1981) which is lower than, but certainly of the right order as, the observed value of 400-700 microns measured by Atkins and Soulsby.

5 CONCLUSIONS

This chapter has shown that the instantaneous pressure gradients make crucial contributions to particle suspension by shear layers. We have not only demonstrated time averaging suppresses the peak values but transport models as presently employed omit the striking effect of eddy pressure gradients in particle capture and transport inside and outside the core. Also, captured particles acquire angular motion and are then expelled by centrifugal forces so ad hoc assumptions of a Gaussian sediment distribution within the core (Yalin & Ferreira da Silva, 1991) are clearly extremely dubious.

We have also shown that the fall speed is reduced for all starting points $X_{SL}>-2R$ ie upflow regions in the vicinity of the core. Also, the fall speed has a striking minimum for particles released from $X_{SL}=6R$ for Y=0. We found, for any core of prescribed angular speed and radius, there are limiting values of the quiescent fall speed for which such particles will not enter the core from any starting location above the vortex. This critical fall speed depends on both the angular speed and radius of the core.

A criterion has been defined by which the initial particle location and velocity determines whether a particle is carried once around the vortex core. We have assessed this criterion against reported sandwave data. A plausible consistency with published data lends confidence to the calculated results. It would be interesting to extend this evaluation to a variety of practical situations and gauge its worth for estimations of suspended load upper size limit in sandwave flows with given depth integrated velocity.

Perhaps the most important message here is that time-averaged Reynolds closure models - such as that used by Johns (1991) (chapter 1) - do not properly account for flow separation and the intense fluctuating pressure gradients which play a crucial role in the transport of suspended sediment.

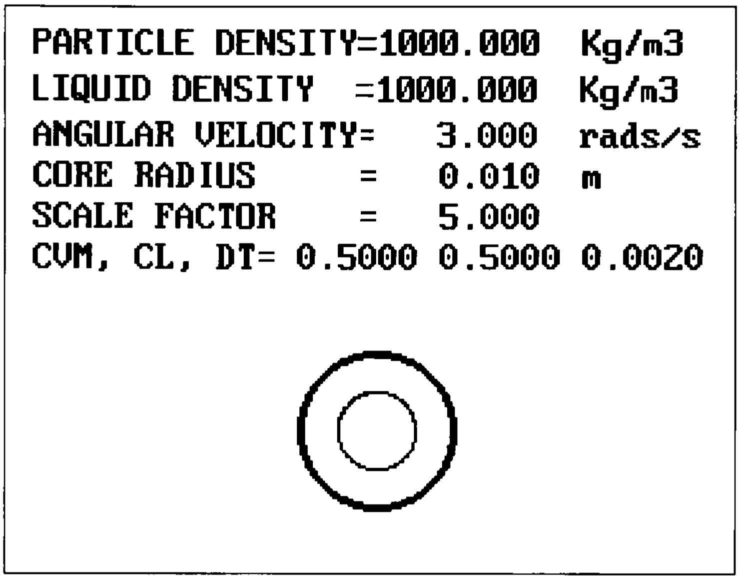

```
PARTICLE DENSITY=1000.000  Kg/m3
LIQUID DENSITY  =1000.000  Kg/m3
ANGULAR VELOCITY=   3.000  rads/s
CORE RADIUS     =   0.010  m
SCALE FACTOR    =   5.000
CVM, CL, DT= 0.5000 0.5000 0.0020
```

Figure 1a.

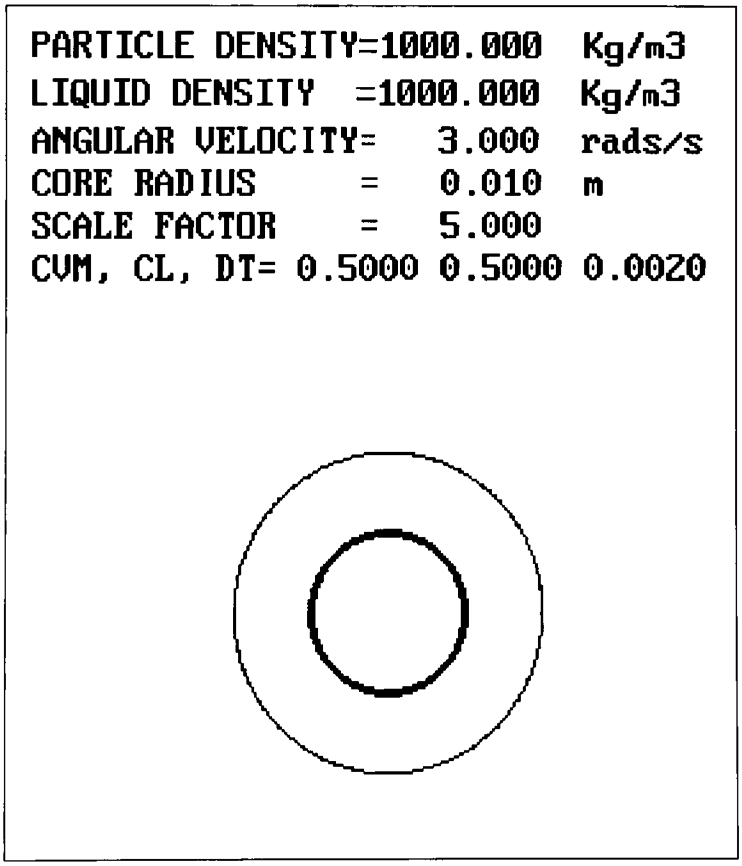

```
PARTICLE DENSITY=1000.000  Kg/m3
LIQUID DENSITY  =1000.000  Kg/m3
ANGULAR VELOCITY=   3.000  rads/s
CORE RADIUS     =   0.010  m
SCALE FACTOR    =   5.000
CVM, CL, DT= 0.5000 0.5000 0.0020
```

Figure 1b.

Figure 1. Trajectories (light circles) computed for neutrally buoyant particles a) Inside and b) Outside a Rankine vortex core (heavy circles) to check the validity of the model and the timestep chosen.

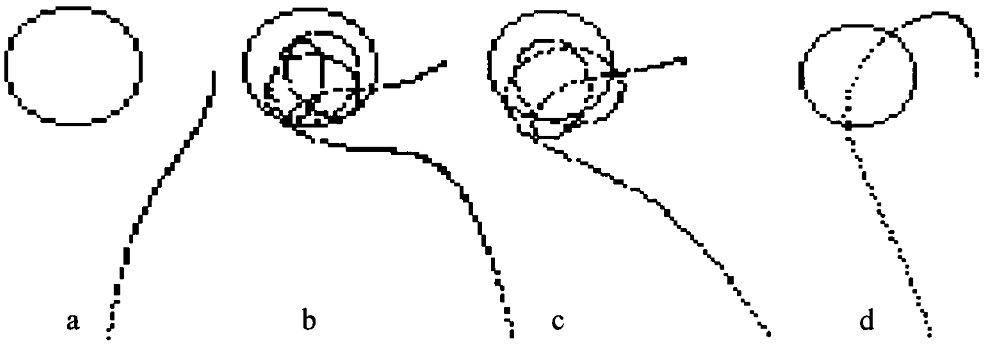

Figure 2. The effect of varying starting velocity on particle trajectory. Particle quiescent fall speed is 0.5m/s and initial vertical velocity is a) -0.2m/s b) 0.0m/s c) 0.05m/s d) 0.3m/s. This extreme example shows the sensitivity of the results to the initial conditions.

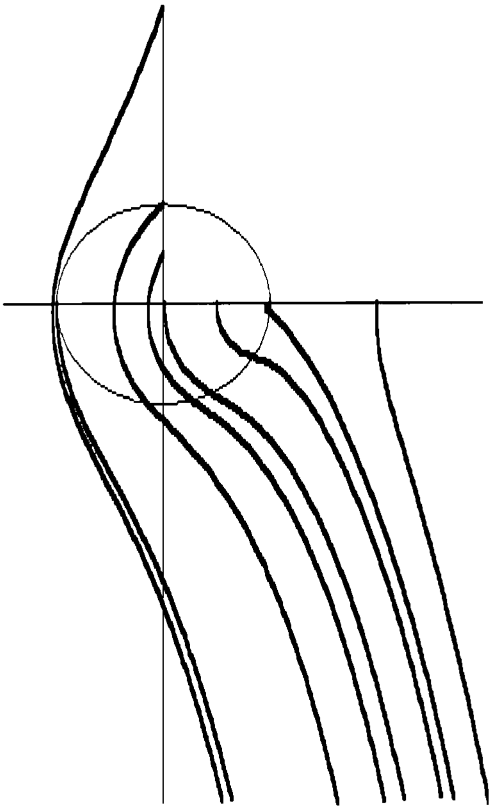

Figure 3. The trajectories of particles falling near a Rankine vortex core. Here the initial vertical and horizontal velocities are set equal to the local fluid velocity which produces a consistent set of trajectories, unlike those in figure 2.

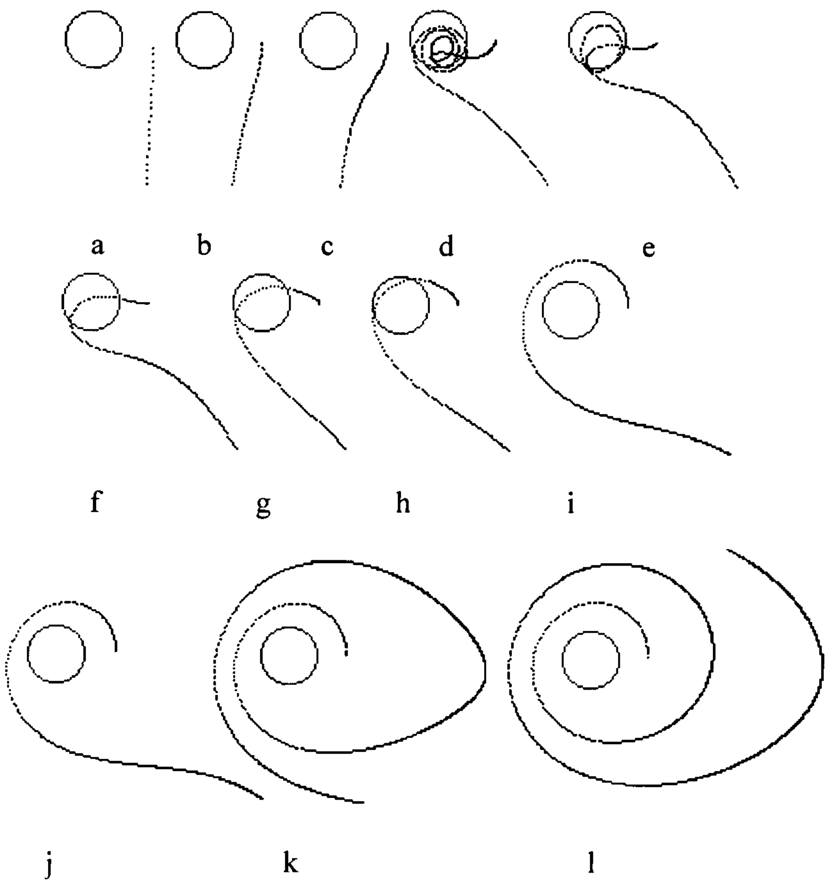

Figure 4. Varying the particle fall speed for a Rankine core of radius 0.006m and angular speed 100rad/s. The particle quiescent fall speed (m/s) is a) 1 b) 0.6 c) 0.5 d) 0.4 e) 0.35 f) 0.3 g) 0.25 h) 0.2 i) 0.1 j) 0.09 k) 0.07 l) 0.05. The core rotates anticlockwise and the bent trajectories in b and c are due to the local pressure gradient acting towards the centre of the core. The pressure gradient and fluid drag are responsible for transporting the particle around the vortex in k and l.

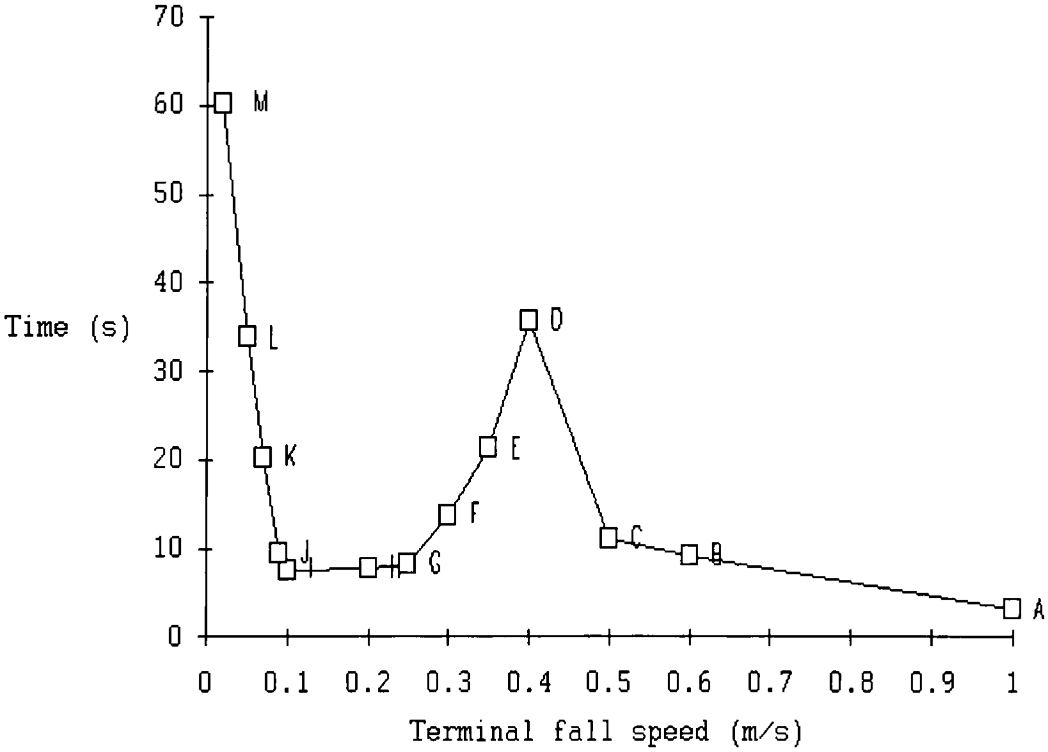

Figure 5. Effect of varying the particle fall speed on the time taken for the particle to fall to a distance of 5 radii below the core centre (the letters refer to the trajectories shown in figure 4 where they appear in lower case). Notice the low level peak for trajectory d where the particle follows a convoluted path through the vortex core.

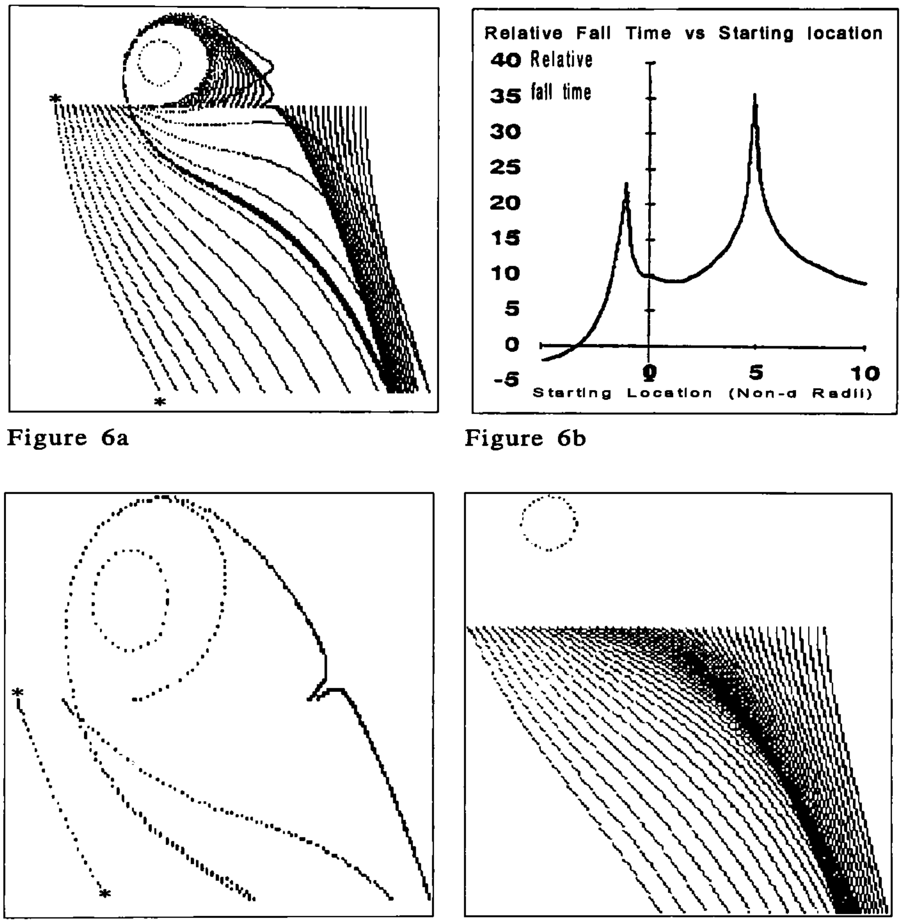

Figure 6a

Figure 6b

Figure 6c

Figure 6d

Figure 6a-d. Particles falling away and being captured from various starting locations below a Rankine vortex core. a) and c) show the trajectories for particles starting 2 radii below the core mid-plane whereas d) shows the trajectories for starting points four radii below the core where no particles are lifted over the core. b) Shows the relative fall time for each trajectory, which is the actual fall time less the time it would have taken to fall the same vertical distance in quiescent fluid.

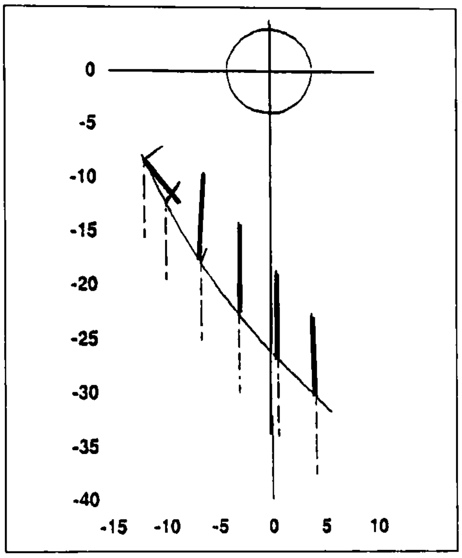

Figure 6e

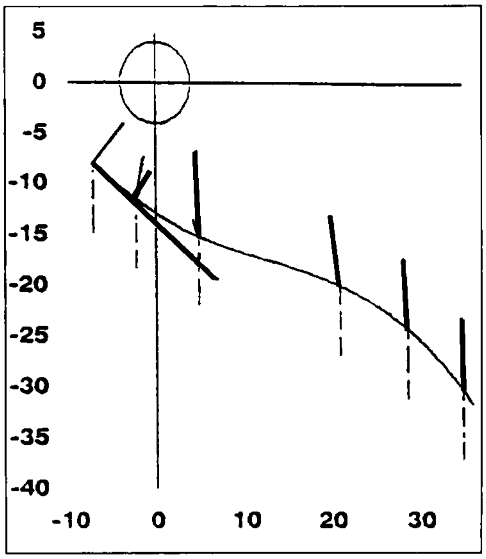

Figure 6f

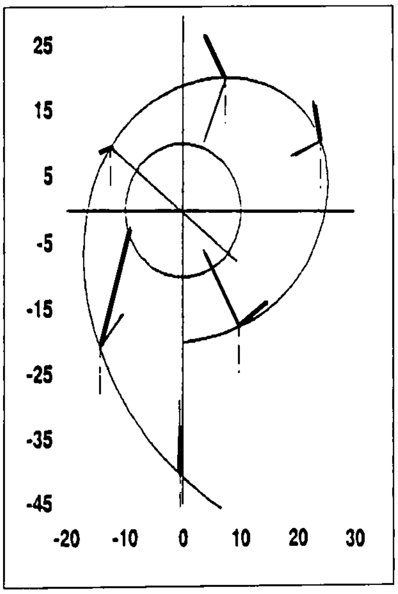

Figure 6g

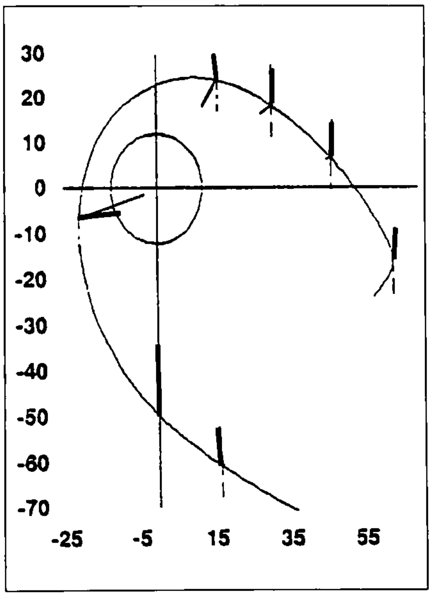

Figure 6h

Figure 6e-h. The vector force acting on the particle for the first four trajectories in figure 3.10c. Thin solid line=pressure gradient and fluid acceleration, thick line=drag and dashed line=buoyancy.

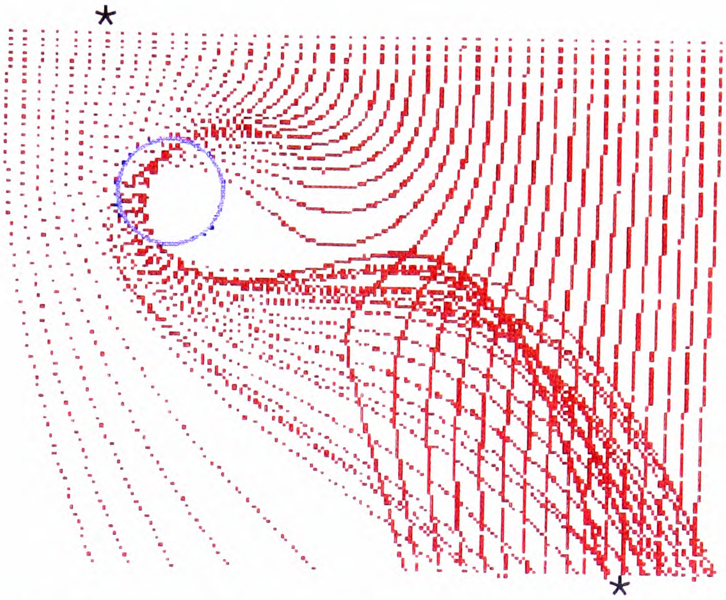

Figure 7a. Trajectories of particles falling from 3 radii above a vortex core. Trajectory marked *--* falls this vertical distance in the same time as in the absence of the vortex.

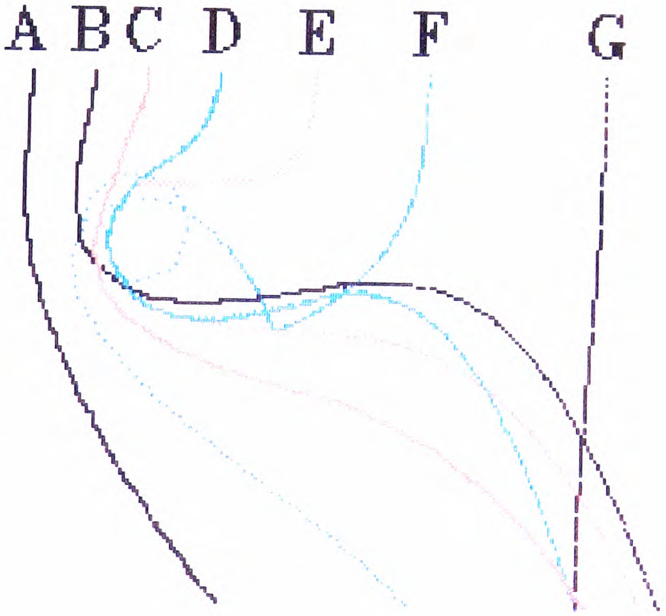

Figure 7b. Selected key trajectories from figure 7a.

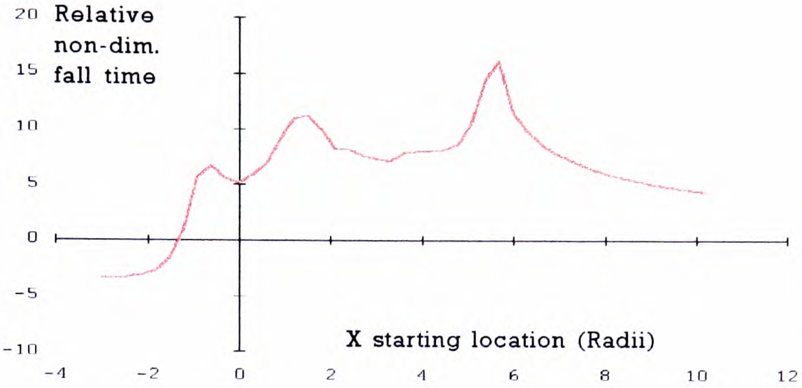

Figure 7c. The relative fall time distribution for the particles shown in figure 7a. The first peak is caused by trajectory A in figure 7b, the second by trajectory D and the third by trajectory F.

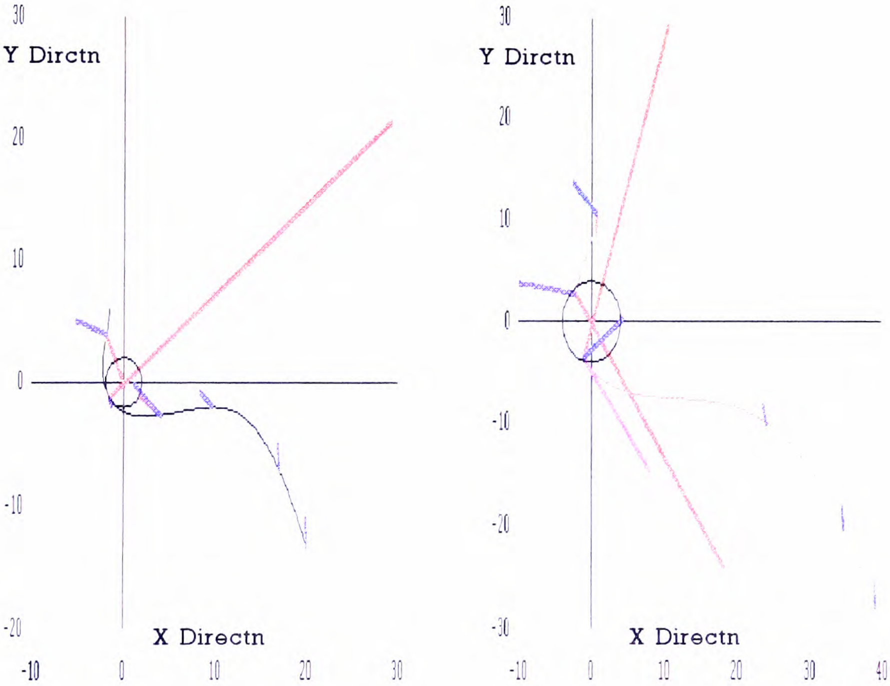

Figure 7d-e. The vector forces acting on the particle at various points along trajectories B and C. The red line=fluid and pressure gradient force, yellow=constant buoyancy force and blue=drag force. The long red lines demonstrate graphically the importance of the instantaneous fluid and pressure gradient forces when compared with the buoyancy force.

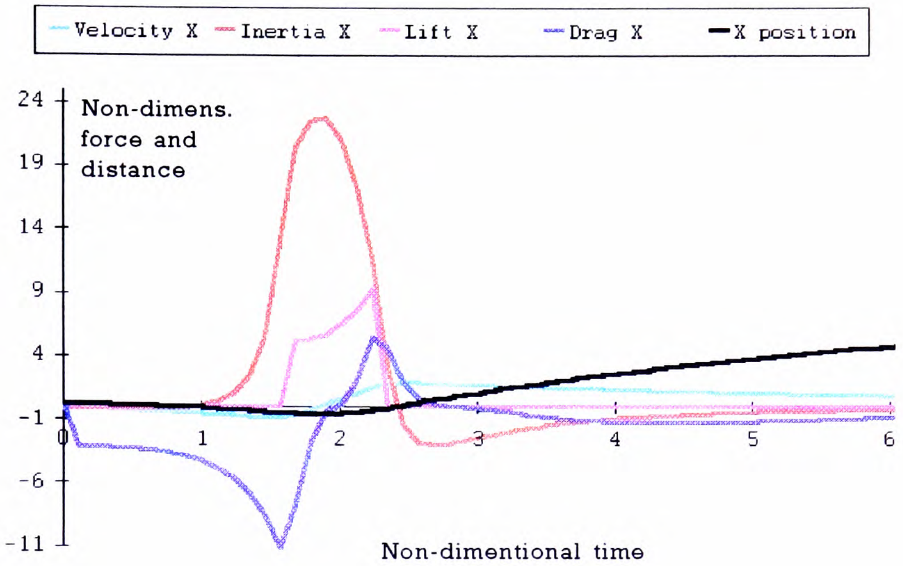

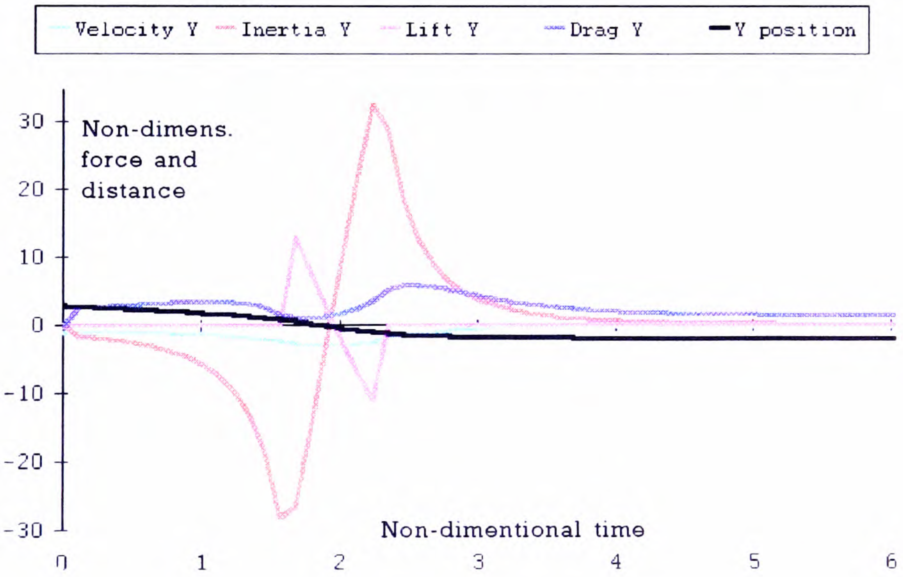

Figure 7f-g. The temporal fluctuations in the magnitude of the forces in the horizontal and vertical directions respectively on a particle falling along trajectory C in figure 7b. The pressure and fluid gradient forces pull the particle to the right as it approaches the core. The bouyancy force is constant at -2.31.

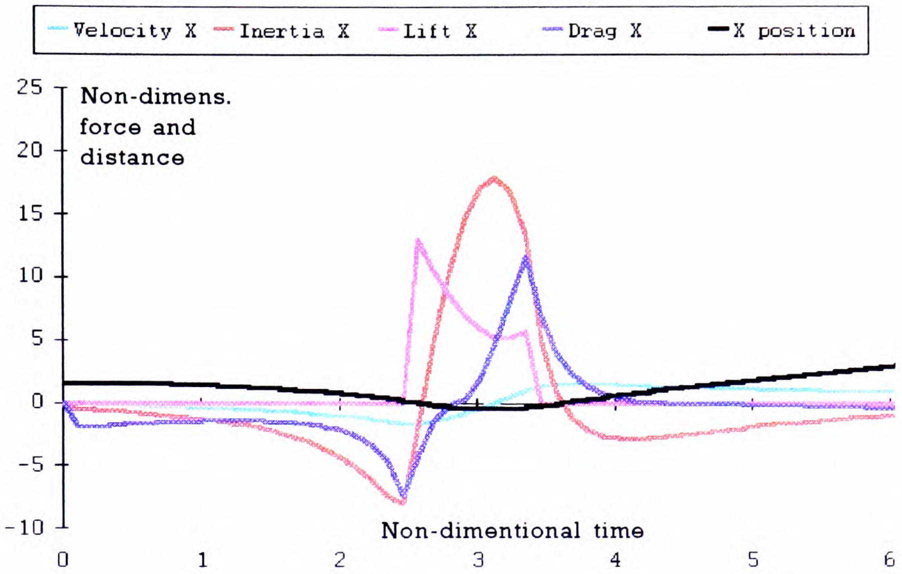

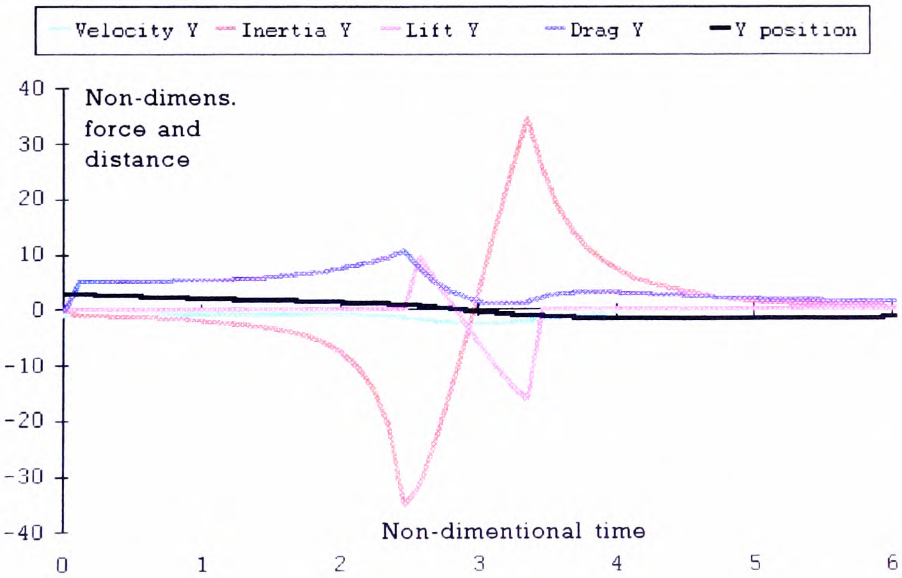

Figure 7h-i. The temporal fluctuations in the magnitude of the forces in the horizontal and vertical directions respectively on a particle falling along trajectory D in figure 7b. The pressure and fluid gradient forces pull the particle to the right as it approaches the core, producing the second peak in figure 7c.

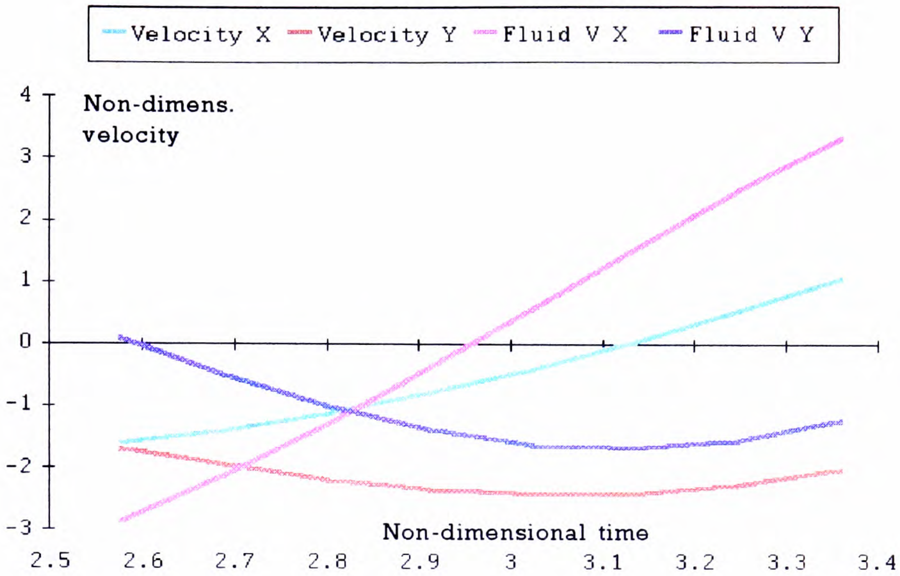

Figure 7j. The temporal fluctuations in the magnitude of the particle and fluid velocities in the core region for a particle falling along trajectory D in figure 7b. The lift force component in the vertical direction changes sign at around the vortex mid-plane because the difference between the horizontal fluid and particle velocities changes sign.

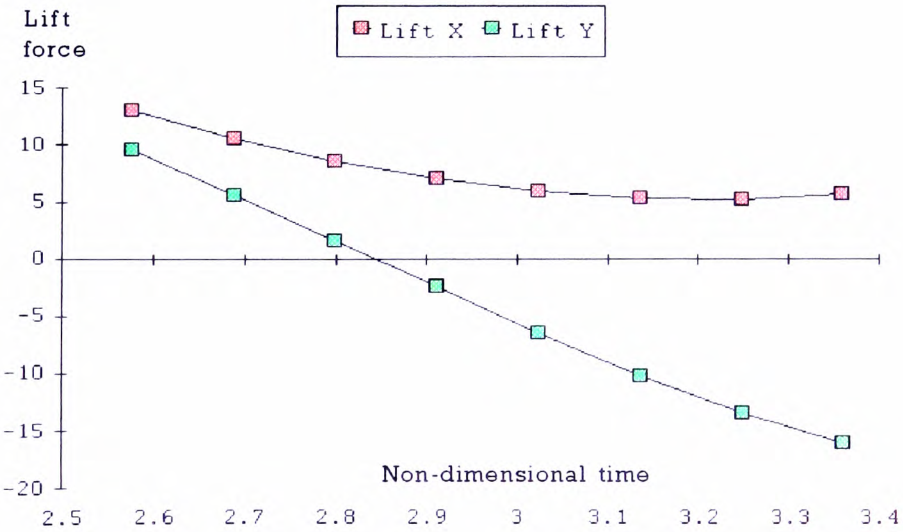

Figure 7k. The temporal fluctuations in the magnitude of the horizontal and vertical components of the lift force due to the change in relative fluid-particle horizontal velocity shown in figure 7j.

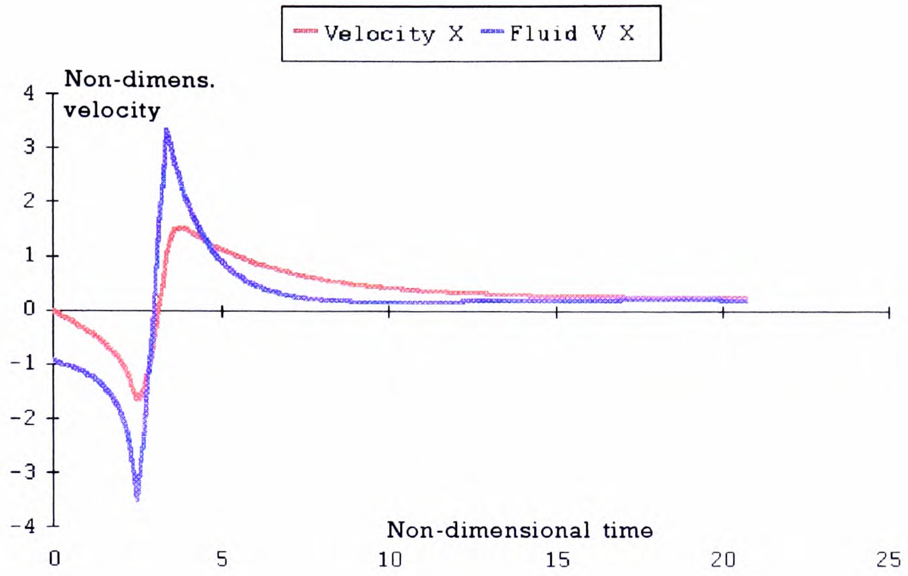

Figure 7l. The relaxation time between the particle and fluid horizontal velocities for a particle following trajectory D. The particle's inertia prevents instantaneous response to spatial changes in the fluid velocity in this steady flow.

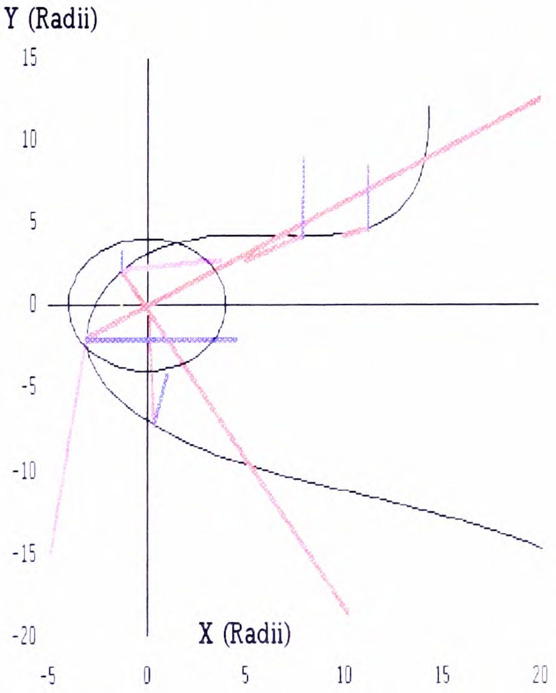

Figure 7m. The vector forces acting on the particle at various points along trajectory E.

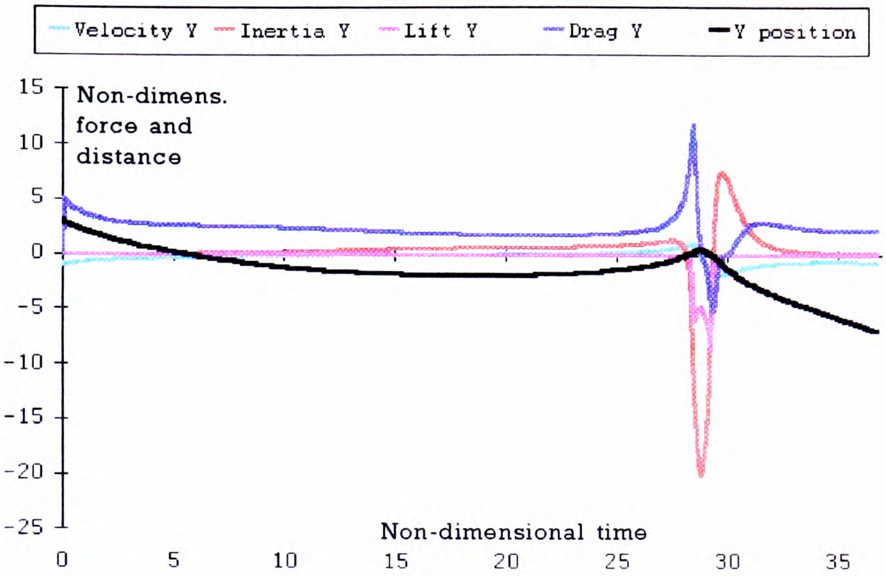

Figure 7n. The temporal fluctuation in the magnitude of vertical components of the forces acting on a particle falling along trajectory F in figure 7b. The third peak forms on figure 7c because the particle reaches the cusp point where it is virtually stationary for an extended period.

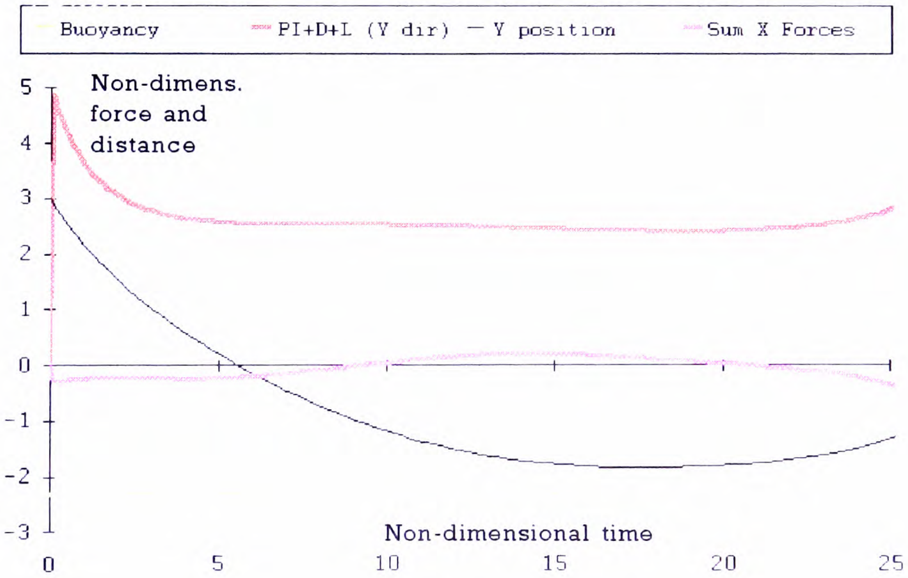

Figure 7o. The sum of the forces balances the buoyancy force on the particle at the cusp point.

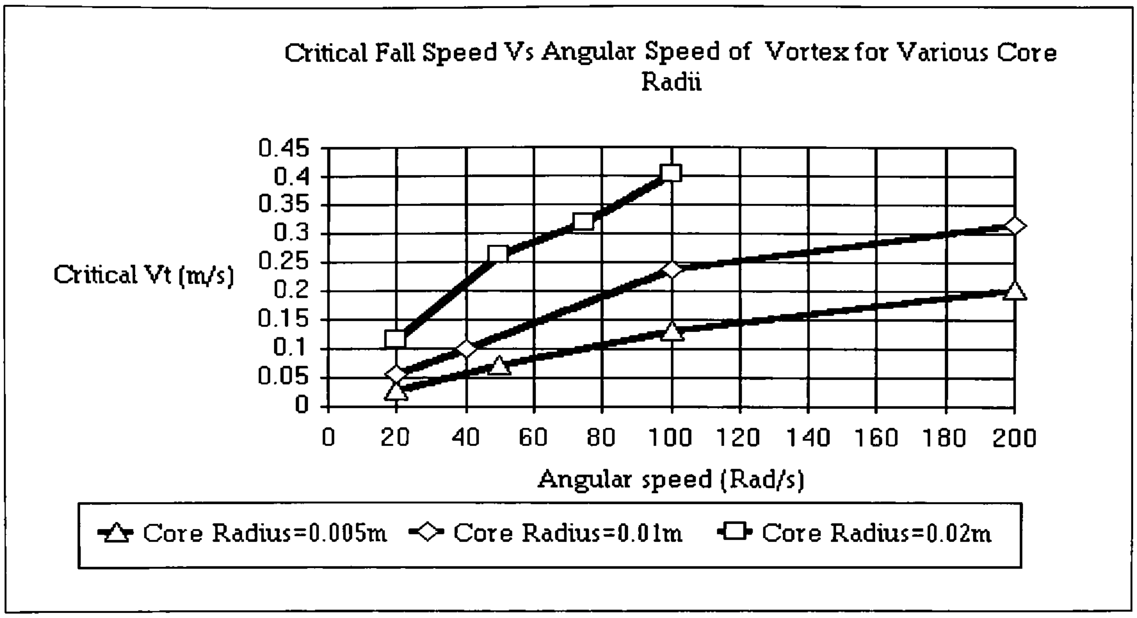

Figure 8a. Graph of the critical particle terminal fall speed for a range of core sizes. A particle with terminal fall speed less than this critical value will not enter the core from any starting location.

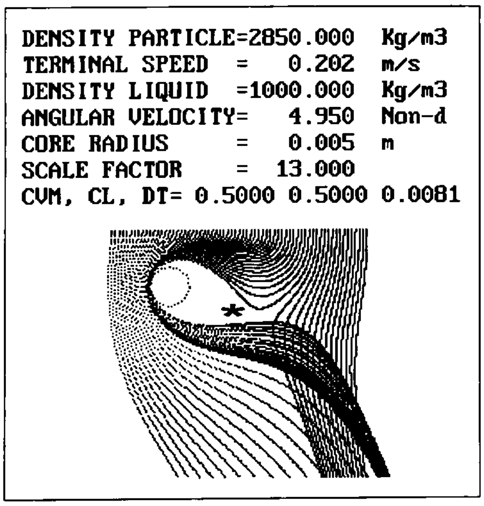

```
DENSITY PARTICLE=2850.000  Kg/m3
TERMINAL SPEED  =   0.202  m/s
DENSITY LIQUID  =1000.000  Kg/m3
ANGULAR VELOCITY=   4.950  Non-d
CORE RADIUS     =   0.005  m
SCALE FACTOR    =  13.000
CVM, CL, DT= 0.5000 0.5000 0.0081
```

Figure 8b.

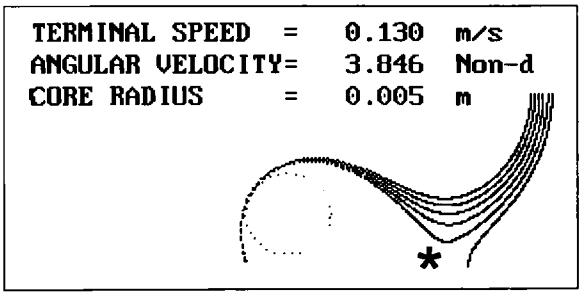

```
TERMINAL SPEED   =   0.130  m/s
ANGULAR VELOCITY=    3.846  Non-d
CORE RADIUS      =   0.005  m
```

Figure 8c

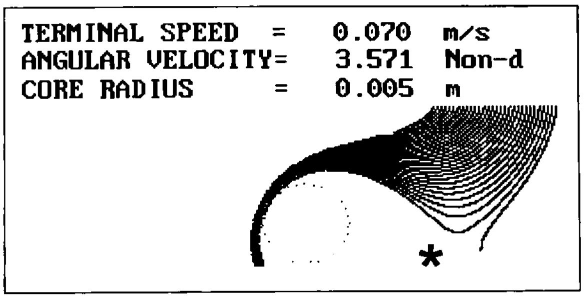

```
TERMINAL SPEED  =   0.070  m/s
ANGULAR VELOCITY=   3.571  Non-d
CORE RADIUS     =   0.005  m
```

Figure 8d

Figure 8b-e. The diagrams show the similarity in trajectory plots for particles with various fall speeds near a 5mm Rankine core. The four cases correspond to the triangles in figure 8a.

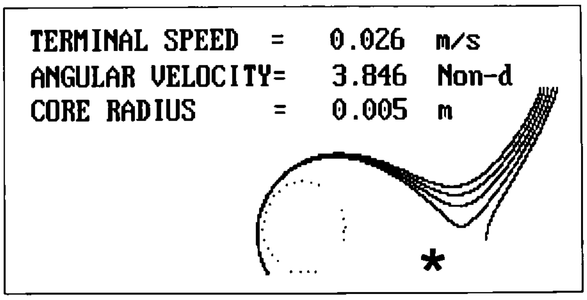

```
TERMINAL SPEED  =   0.026  m/s
ANGULAR VELOCITY=   3.846  Non-d
CORE RADIUS     =   0.005  m
```

Figure 8e

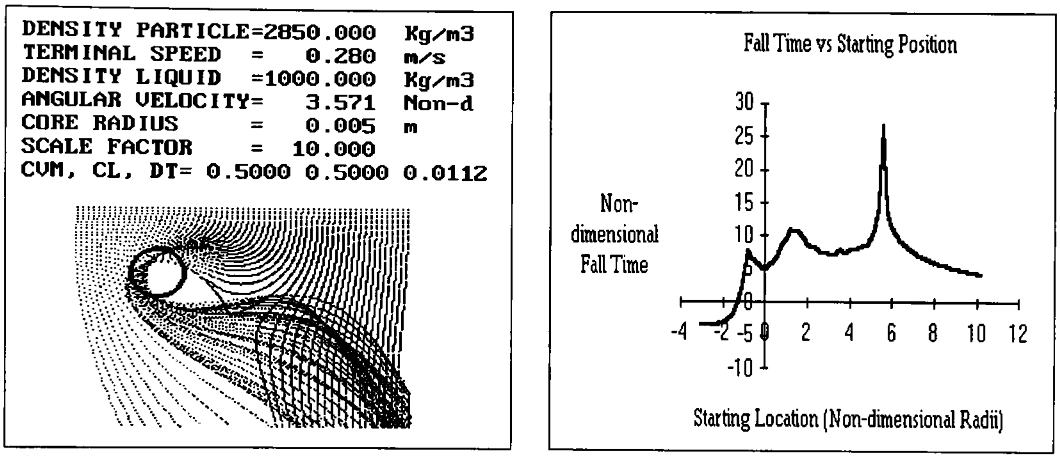

```
DENSITY PARTICLE=2850.000  Kg/m3
TERMINAL SPEED   =    0.280  m/s
DENSITY LIQUID   =1000.000  Kg/m3
ANGULAR VELOCITY=    3.571  Non-d
CORE RADIUS      =    0.005  m
SCALE FACTOR     =   10.000
CVM, CL, DT= 0.5000 0.5000 0.0112
```

Figure 9a

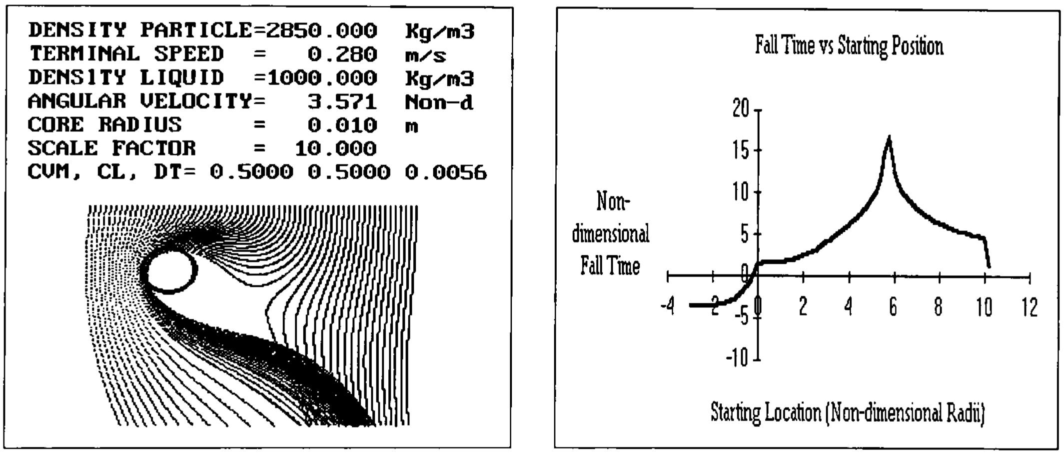

```
DENSITY PARTICLE=2850.000  Kg/m3
TERMINAL SPEED   =    0.280  m/s
DENSITY LIQUID   =1000.000  Kg/m3
ANGULAR VELOCITY=    3.571  Non-d
CORE RADIUS      =    0.010  m
SCALE FACTOR     =   10.000
CVM, CL, DT= 0.5000 0.5000 0.0056
```

Figure 9b

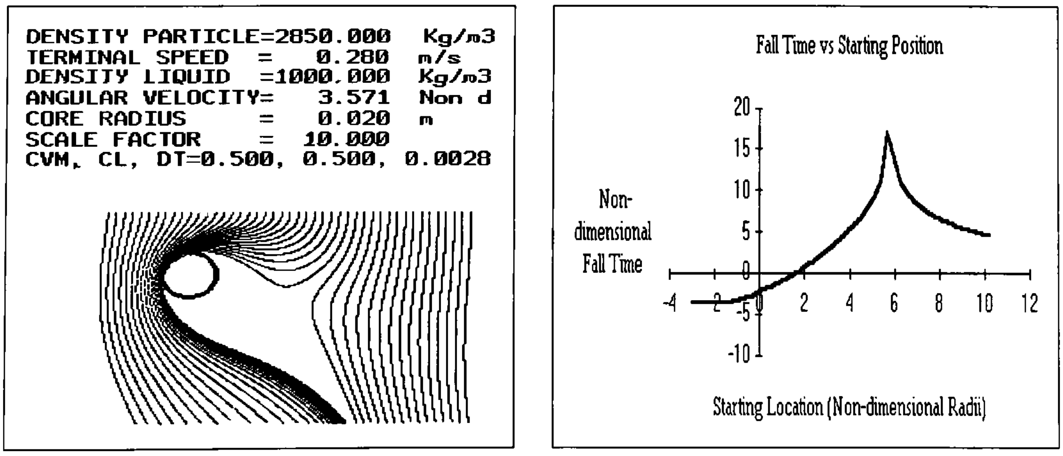

```
DENSITY PARTICLE=2850.000  Kg/m3
TERMINAL SPEED   =    0.280  m/s
DENSITY LIQUID   =1000.000  Kg/m3
ANGULAR VELOCITY=    3.571  Non d
CORE RADIUS      =    0.020  m
SCALE FACTOR     =   10.000
CVM, CL, DT=0.500, 0.500, 0.0028
```

Figure 9c

Figure 9a-c. The above plates show the effect of keeping the velocity at the core radius constant whilst increasing the core size. The graph on the right shows the fall time for each of the trajectories in the picture on the left.

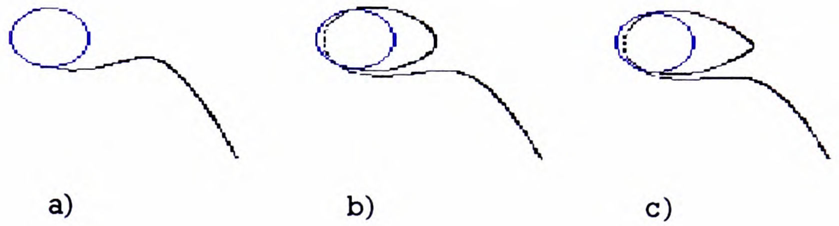

Figure 10. The pictures show a) a particle that is not captured by the core, b) a particle that is captured and c) a particle that is just captured. The value of AR/V_T here is the criterion C below.

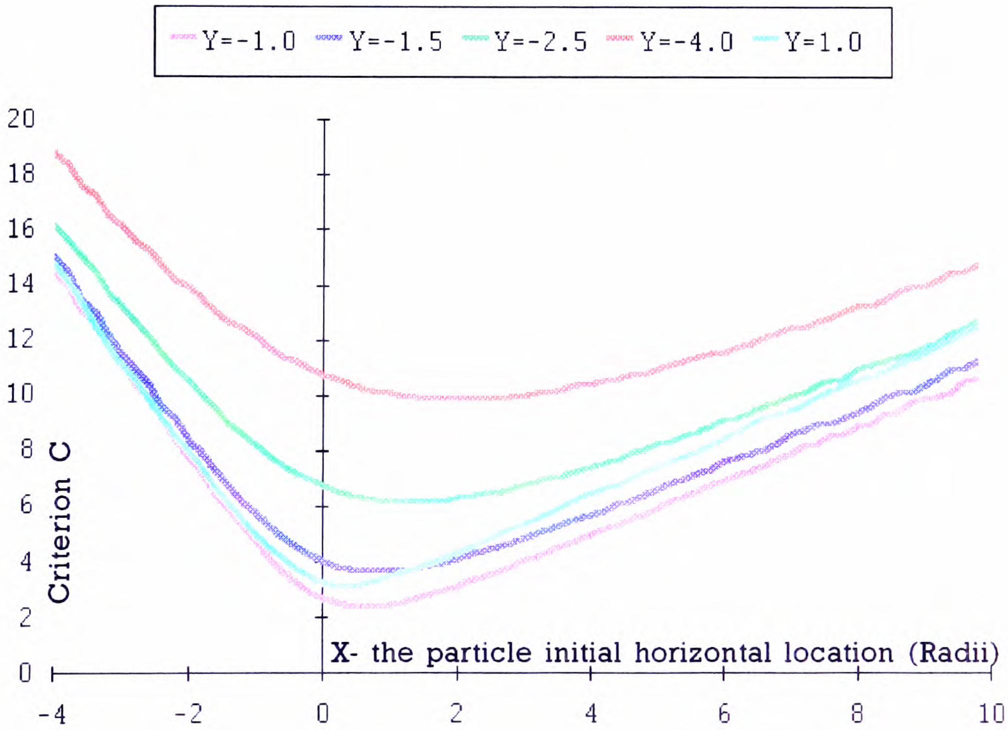

Figure 11. Values of the capture criterion C for various values of (X,Y), the particle starting position at initial velocity $(V_X,V_Y)=(0,0)$.

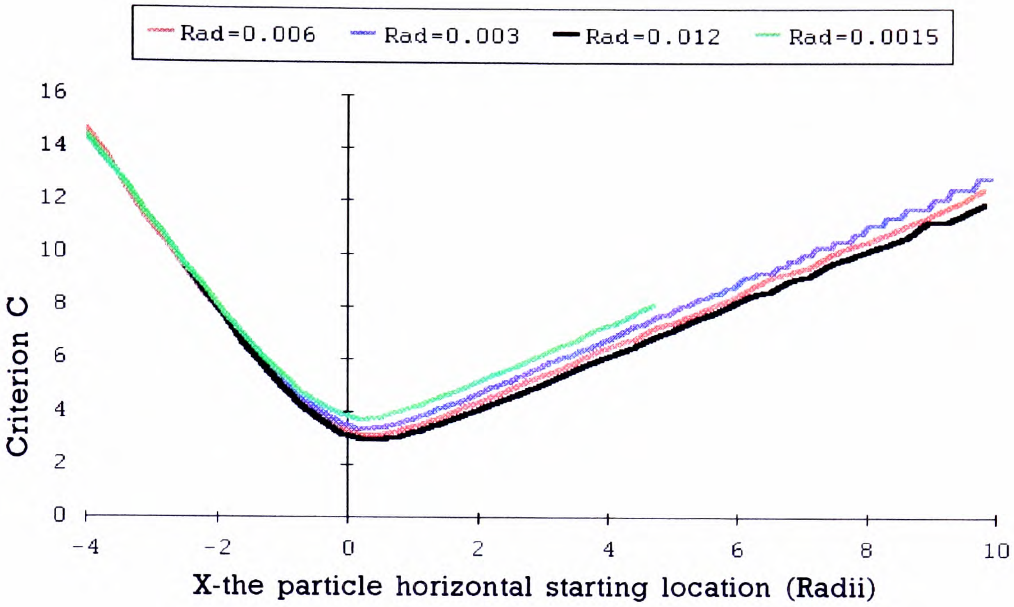

Figure 12. Variation of the critical vortex strength criterion C AR/V_T with vortex radius R at constant vortex tip speed AR.

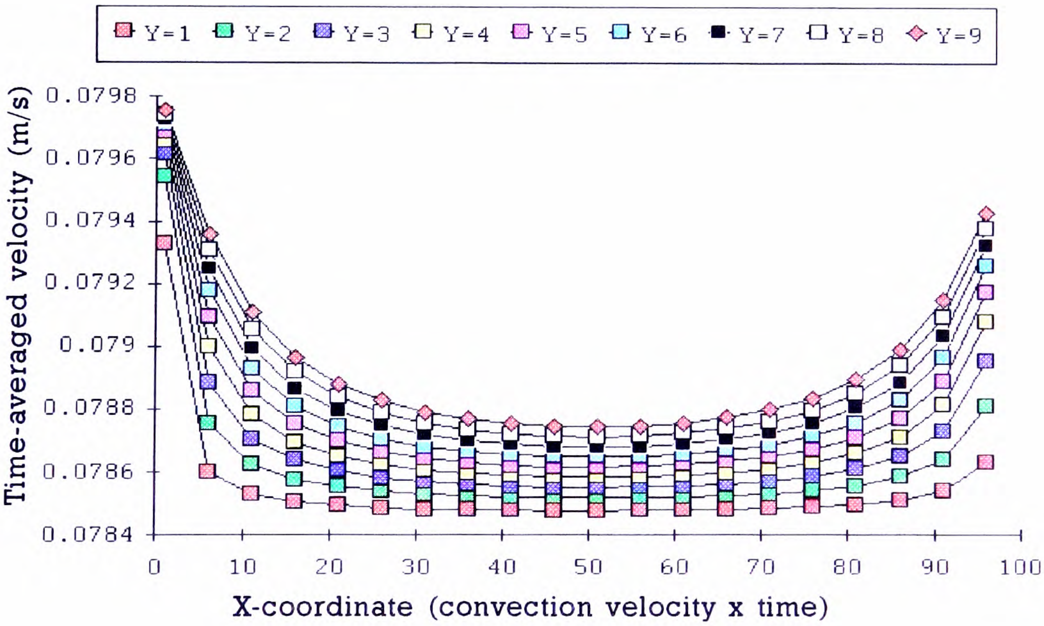

Figure 13. Time-averaged horizontal velocity induced below the mid-plane of a moving Rankine vortex over 100 timesteps.

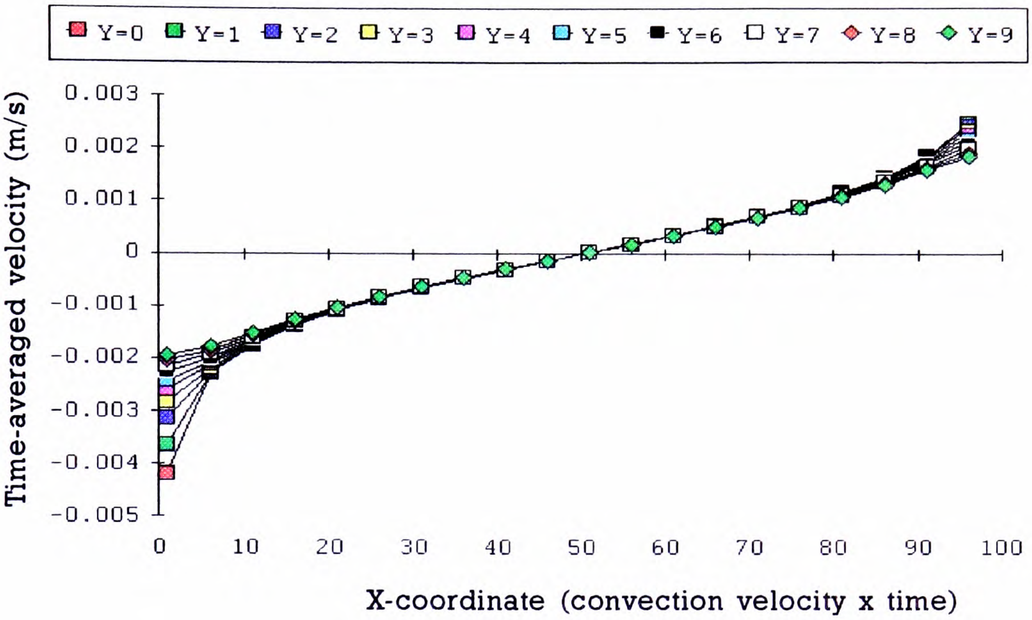

Figure 14. Time-averaged vertical velocity induced below the mid-plane of a moving Rankine vortex over 100 time steps.

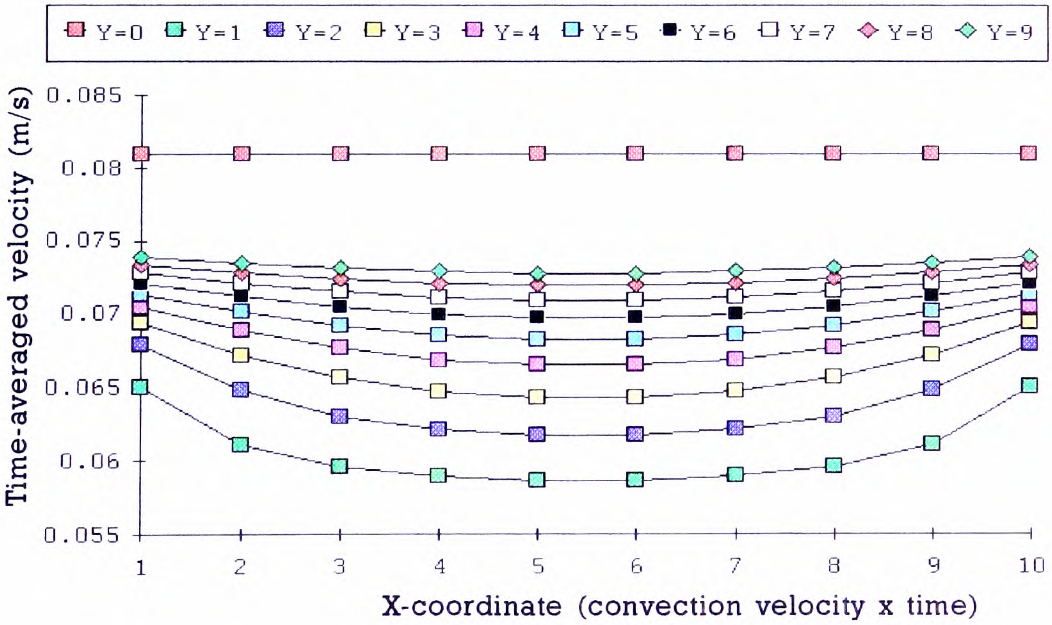

Figure 15. Time-averaged horizontal velocity induced below the mid-plane of a moving Rankine vortex over ten time steps.

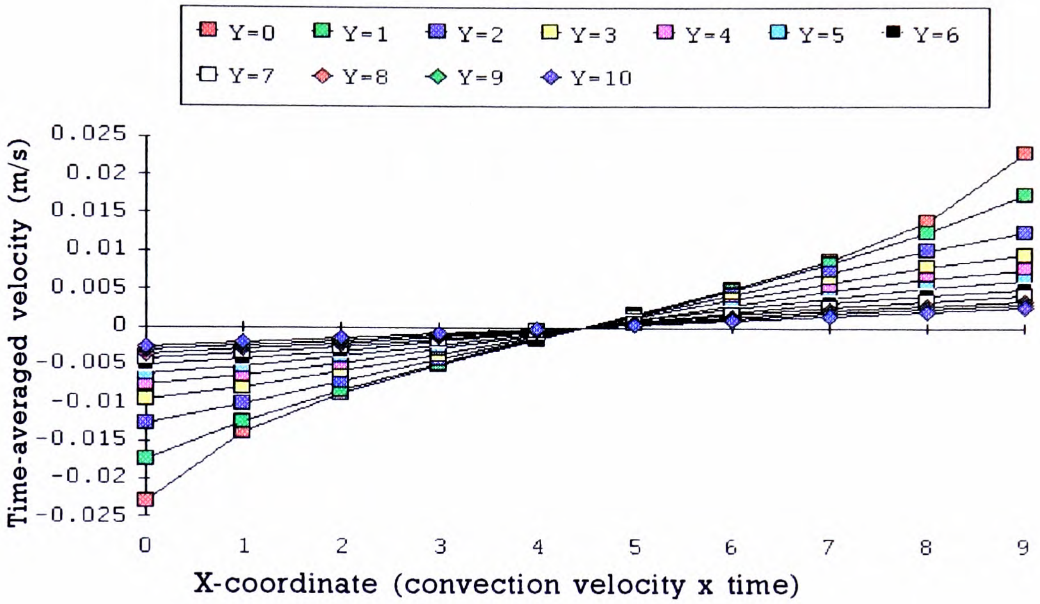

Figure 16. Time-averaged vertical velocity induced below the mid-plane of a moving Rankine vortex over 10 timesteps.

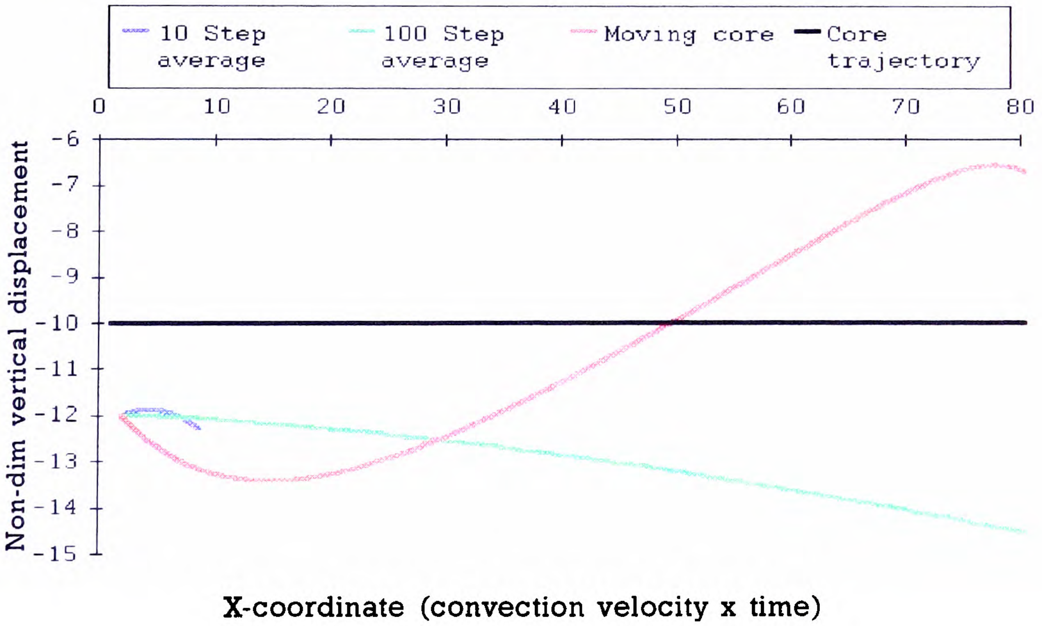

Figure 17. Time-averaged and time-dependent trajectories of a particle in a moving Rankine vortex. The trajectories in the time-averaged flows are inclined downwards whereas the time-dependent trajectory follows a near cycloid path.

Fluctuating vel f (u or v)	u-Johns -1991	v-Johns -1991	u,v-Nak. -1987
U=1m/s mean (f^2)	E	0.35E	{ mean u,v }
U=0.64 mean (f^2)	0.64^2E	0.35(0.64^2)E	{(0.18*0.64)=0.115}
max E (X/H=1.25)	0.018	0.018	
mean (f^2)	0.007	0.003	0.013
max (f^2)	0.010	0.004	0.019
max (f)	0.102	0.063	0.137

Figure 18. Table of maximum fluctuating velocities u,v=f. Johns (1991) prescribes u=E and v=0.35E where E is the turbulence energy density in $(m/s)^2$ which has a peak value 0.018. We then assume a sinusoidal distribution for the fluctuating parameters which classically gives (f^2)max = 1.414(f^2)mean. Data from Nakagawa & Nezu (1987) gives u,v directly.

CHAPTER 6: NUMERICAL SIMULATION OF PARTICLE TRAJECTORIES IN GROWING VORTICES

SUMMARY

We now examine particle Lagrangian dispersion in an idealised shear layer, synthesised as a travelling Rankine vortex whose core expands according to the entrainment law based on classical scalings for free shear layers. The problem has many independent parameters, not least of which is the particle initial conditions which are held fixed in this study. What we do survey here are relevant values of the initial size of the vortex, its angular speed and the shear layer spread rate parameter as determined by velocity difference across the layer, also the particle fall speed, effectively the Stokes number.

Results are shown as parameter space diagrams which are presented as contour plots in the plane of initial vortex radius versus angular speed. Behaviour is classified within three distinct regions. The first region is dominated by gravity, such that particles simply fall out of the vortex. A second region is dominated by fluid angular momentum transfer which leads to centrifugal expulsion of the particles. The third region, an intermediate one, contains particle trajectories looping around the vortex core. The boundary between regions 1 and 3 depends on the particle fall speed (ie drag dominated regime), whereas the boundary between regions 2 and 3 strongly depends on vortex growth rate (ie inertial entrapment forces).

1 INTRODUCTION

Figure 1 shows a schematic of the crest regions of a notional sandwave. The flow separates at the crest as a salient edge. As an idealisation we picture the instantaneous shear layer rolls up into a first generation vortex with angular velocity A_0 and nominal radius R_0 at a distance d_0 from the crest. The circulation Γ of this vortex is in reality distributed non-uniformly over its core. In common with previous models (Thomas et al, 1983, Hunt et al, 1988 and Onslow et al, 1994), we suppose as a first approximation that the distribution is uniform (ie classical Rankine vortex). The other implicit assumption here, that the vorticity is strictly two dimensional, is generally held to be an adequate approximation sufficiently close to the crest (Muller & Gyr, 1986). In reality, the values of R_0, A_0 and d_0 depend on upstream parameters, notably boundary layer thickness at the crest, and intensity and scale of turbulence. For stream speed U, this vortex travels downstream at speed u_0 depending on the velocity of the recirculating flow (Townsend, 1956).

It is well known (eg, Muller & Gyr 1986) that pairing occurs to form second generation vortices possessing approximately double the radius of the initial vortices. Vortex growth is characterised by entrainment due to fine scale turbulence and engulfment as described, for example, by Ho et al (1991) following the seminal studies by Brown & Roshco (1971). Clearly, the circulation also doubles during pairing so the vorticity (circulation area density) must halve from one generation to the next. If we now adopt the classical scaling arguments (eg Townsend 1956) that shear layer width δ is proportional to the downstream distance x and also assume that the vortex velocity u_0 is constant throughout its translation then a useful first idealisation is to replace the stepwise changes with a steady growth rate such that radius R_i increases proportional to time: viz,

$$R \propto \delta \equiv R_0 + x\tan\alpha \equiv R_0 + u_0 t\tan\alpha \equiv R_0 + Gt \qquad (1)$$

and the notional angular velocity A decreases proportional to time: viz,

$$A \propto \Gamma/\delta^2 \propto \Gamma_0 R/R_0 (1/R^2) \propto 1/R_i \propto 1/Gt \qquad (2)$$

where G is the averaged vortex growth rate (velocity). These scalings comply with the requirement that RA, the notional vortex shear velocity, is constant with time: ie, consistent with constant spread rate for constant velocity difference ΔU. Thus

$$A \propto \frac{\Delta U}{\delta} \quad , \quad R \propto \delta \Rightarrow AR = K \qquad (3)$$

where K is constant; see Kaul (1988) and Ho et al (1991).

We should caution that this picture does not allow for boundary interference due to the stoss slope, nor does it recognise curvature of the shear layer toward reattachment. Also excluded is direct representation of vortex pairing which is known to be important for more complete consideration of bubbly flows, reported in, for example, Sene et al (1993) and Yang & Thomas (1994). In particular the 'gaps' between vortex structures here allowed bubbles and particles to escape from the layer: see also Lasheras & Choi (1988) and Sommeria et al (1991). Also, Jacobs & Pullin (1989) reported evidence of three vortex tripling, again unaccounted for here.

Recognising the limitations declared above we now address the fate of a sediment particle (quiescent fall speed V) which is entrained from the crest into the growing vortex and an idealised model of the shear layer. Yalin & Ferreira de Silva (1991) used a similar model to represent sediment concentration distributions during a turbulent burst cycle, though they assumed a normal distribution which is an unrealistic idealisation; see Onslow et al (1994). Also similar to our contribution is the work of Nielsen (1984) who considered Rankine vortex idealisation for transport in sediment laden flows. Nielsen found the particles should travel in equilibrium trajectories within the vortex cores, observing that particles follow closed trajectories as a result of inclusion during vortex formation and growth.

Chien & Chung (1988) used a discrete vortex method to model particle dispersion within a shear layer but their particle dynamics only contained drag/slip speed representation. They also correlated their measurements in terms of particle Stokes numbers, the ratio of the particle drag response time to a characteristic timescale for the shear flow: viz,

$$St=\left(\frac{\frac{\rho_P d_P^2}{18\mu}}{L/\bar{u}}\right) \tag{4}$$

Where ρ_P was the particle density, d_P its diameter, μ the fluid dynamic viscosity and L and $\bar{u}$ are length and velocity scales. They found that low Stokes number particles disperse at rates about equal to the shear layer growth rate whereas high Stokes number particles disperse more slowly. However, intermediate values produced centrifugal expulsion from the vortices, resulting in high dispersion rates.

2 NUMERICAL SCHEME

The model outlined above was coded in Fortran and executed on a 486 PC (Hewlett-Packard Vectra), as presented in appendix 11. The programme provides for a vortex growing at rate G in time steps Δt after each of which the particle trajectory is calculated using the updated values of A and R. The particle dynamic equation is that described in Thomas et al (1983), also as adapted in Onslow et al (1994), and includes the effects of added mass, inertia and lift forces but neglects the Basset and higher order terms, consistent with asymptotically high Reynolds number (symbols as chapter 5): namely,

$$\left(\frac{\rho_P}{\rho_L C_{vm}}+1\right)\frac{d\underline{v}}{dt}=\left(1+\frac{1}{C_{vm}}\right)\left(\frac{D\underline{u}}{Dt}\right)-\frac{g}{C_{vm}}\frac{\Delta\rho}{\rho_L}\left(1+\frac{\underline{w}|\underline{w}|}{V_T^2}\right)-\frac{C_L}{C_{vm}}\underline{w}\mathrm{x}\underline{\omega} \tag{5}$$

The time interval was initially set at 0.001s but subsequently adapted so as to ensure the particle moved incrementally no more than 10^{-3}m and no less than 10^{-5}m, usually corresponding to Δt 0.0001s, see chapter 5 for further discussion of the numerical procedure.

There are numerous parameters defining this idealised problem, not least the particle initial velocity and location; in all a total of 6 (including R_0, A_0, G and V) for prescribed particle density. Starting particle values were selected with zero velocity located on the upstream side of the vortex mid-plane at $0.9R_0$, an arbitrary selection but representative of sediment supplied to the shear layer from the crest. Setting the initial velocity to zero might be regarded as modelling particles that have been captured from bedload. We note that such particles may have significant spin caused by bed impacts in the high velocity shear flow at the bed, as found in gas-solid pipe flow (Tsuji et al, 1987). Whilst analysis of these factors is beyond our scope here we recognise this limitation, although perhaps the priority need for future work would be to survey for sensitivity to initial conditions. Another need here is to assign the inclination of the shear layer and vortex size.

Muller & Gyr (1986) estimated from visualisations that the vortex diameter and included shear layer angle are approximately 0.006-0.008m and 15-25° respectively. Results of our calculations are described below.

3 RESULTS

3.1 Specified G and V

Figure 2 shows results for the case G=0.01m/s and V=0.076m/s (700 micron particles): ie, a shear layer with internal angle (2α) of 15° with vortices translating at 0.08m/s, since $G=u_0\tan\alpha$. This particle fall speed, also 0.0335m/s used later, equals that of the particles used in the experimental studies detailed in chapters 3 and 4. The axes in the parameter space shown in the figure represent initial values assigned to A (A_0) and R (R_0). The inset sketches show a dotted outline of the vortex (tip speed A_0R_0). Also shown is the particle trajectory relative to the centre of the vortex. As illustrated in figure 2, for any value of R_0, (say 0.02m), there will be a range of A_0 ($A_L<A_0<A_H$, say) which gives rise to particle retention, as depicted in the insets C and D. The main graph shows the boundary conditions for particle retention independently, as discussed further below.

a) General points on parameter space. Values of A_0 and R_0 falling below the lower heavy line cause the particle to fall from the vortex; insets A, E and F. Higher values of A_0 and R_0 introduces higher curvature of the trajectory, caused by drag forces acting to the right at locations below the vortex centre. The trajectories in this region are thus dominated by the particle parameters.

In the region above the upper heavy line the particle trajectories are depicted as inset B. Here the vortex forces are dominant and the particle is expelled from the core because it's drag-induced angular momentum provides a centrifugal force which defeats the pressure and lift retaining forces.

Figure 3 shows seven trajectory plots corresponding to R_0=0.02m and A_0 shown by the position of the circles G-M along the x-axis in figure 2. As expected, insets G and H represent extremities of the particle-dominated region, displaying downwards directed trajectories. Crossing the lower boundary takes us to conditions where the particle executes loops incorporating the horizontal mid-plane. The height achieved on subsequent loops follows a decaying curve, similar to that shown as J, but here there is also an initial increase in the maximum elevation. A further increase in A_0 results in trajectory K, where the particle loops once before exiting. Cases L and M confirm that higher A_0 results in earlier ejection of the particle.

b) Detail of inner region of parameter space. Figure 4 shows the number of complete loops that the particle describes: ie here defined as the number of crossings of the vortex mid-plane. The particle eventually falls but appears not to escape from the core even though the ratio of particle fall speed to shear layer growth rate is 7.6. The lower line labelled by red squares is equivalent to the lower boundary line in figure 2 and the upper line labelled by red squares corresponds to the upper heavy line in figure 2. In between we have curves where the particle loops at least once. Thus the green squares relate to single loops, the blue squares to double loops and so on, up to the blue diamonds, representing nine loops. Higher order looping has been excluded for the sake of figure clarity.

All cases up to the upper green line marked LE represent effective trapping within the core, at least up to the 1000s time period computed. Above the LE line and below the line E there is a region where the particle completes one loop before being expelled from the core. There does not appear to be any condition corresponding to multiple loops, perhaps due to the increments selected for increases in A_0. An analytical solution to this problem would certainly aid interpretative diagnosis of the physical sensitivities, including the limiting conditions at each end which may tail asymptotically to infinity or simply terminate on the axis.

3.2 Different values of V & G

The effect on the parameter space of varying V and G are presented below, followed by correlations of the results in terms of equations for the bounding lines denoting capture from escape. The correlations are not physically based on first principles but they do deliver simplicity for the broader discussion with which we close this chapter.

a) Varying particle fall speed. Varying V has a marked effect on the location of the central region as shown in figure 5. Here G=0.01m/s and the four cases show different V=0.0335, 0.076, 0.1185 and 0.161m/s, corresponding to a broad span of fall speeds of practical interest for sediment dynamics (Atkins & Soulsby, 1992). The graph is presented on logarithmic axes having the effect of straightening the boundaries of figure 2 for the range of (A_0, R_0) displayed. We see that as V is increased so the lower boundary is shifted to larger R_0 an A_0. On the other hand the upper boundary moves only slightly with increasing V, at least for higher values of V.

b) Varying shear layer growth rate. Figure 6 shows the effect of varying G. Increasing G has only a small effect on the lower boundary, such that for any R_0, the boundary appears at slightly lower values of initial angular speed. The case G=0.001 is included for comparison since the location of the lower boundary suggests a tendency to converge at high R_0 on to the value at G=0. Whether this is true has not been clarified and indeed would be of little consequence for engineering practicalities. The upper boundary moves in the opposite direction to the lower boundary with increasing G: ie higher values of G shift the boundary to significantly higher values of A_0 for any R_0.

c) Functions fitting parameter space boundaries. We fitted the upper and lower curves of the parameter space with the general function

$$A_0^n R_0^m = k_1 V + k_2 G + k_3 \tag{6}$$

which returned for the lower line

$$A_0R_0 = 1.25V - 0.33G - 0.005 \quad (7)$$

and for the upper line

$$A_0R_0^{0.72} = 41.8G + 0.03 \quad (8)$$

when fitted through values of V from 0.0335m/s to 0.161m/s and G from 0.01m/s to 0.04m/s. The numerical results and values predicted by these equations are shown in figures 7 and 8.

Notice in figure 7 that varying the growth rate G has very little effect on the location of the lower transition line over the range studied. We add here that the two terms not including V are at maximum 30% of the value for A_0R_0, even when V is at the lower end of the range that we studied, and only 5% at the upper end.

Figure 8 shows the fit for the upper transition line at various G and V, and again the fit is good even though V does not appear in the equation. The weak dependence upon V and G for the upper and lower lines respectively allows us to ignore their respective contributions as a first approximation.

4 DISCUSSION

Points of interest discussed below include (section 4.1) dominant forces in each of the three regions of parameter space and (section 4.2) the likely implications for modelling of sandwaves, originally prescribed as the focus for our study.

4.1 Forces dominating the parameter space

Our data presented above has shown that typical behaviours fall into three categories, as follows: firstly, a particle-dynamic region; secondly, a flow dynamic region; thirdly, a bridging region where both contribute. The first region relates to those values of A_0 and R_0 falling below the lower line shown in figure 2, whose location is strongly dependent on particle fall speed and nearly independent of vortex growth rate. This is as expected because the forces accelerating the particle around the vortex scale on A_0 and R_0 and are in competition with the gravitational force on the particle, varied here in terms of V which was used as the independent parameter. Thus entrapment at higher values of V requires higher A_0 and higher R_0 to deliver sufficient flow force acting for sufficient time. Furthermore, the relative insensitivity to vortex growth rate G of this lower transition line provides much information concerning which force is responsible for fixing this lower line in the parameter space.

The pressure gradient and inertial force (PI)$\alpha A^2 R_P$ (where the particle radial distance from the core $R_P \approx R_0$ for spiral trajectories close to the core edge) and drag force varies linearly with A and R_P (refer to appendix 1 in chapter 5), and since $A \alpha A_0/G$ the pressure gradient force must depend on G and the drag must be independent of G. Hence, the lower line's insensitivity to G is indicative of drag dominated dynamics.

Conversely, the upper line of the parameter space in figure 2 is dependent upon G but is insensitive to V (at higher V's studied) and so the pressure gradient must be the dominant force. It appears that greater sensitivity to V and hence to more equal contributions from drag and pressure gradient might appear as $V \to G$ (figure 6), though this is not explored further here. This pressure gradient sensitivity is physically manifested as the requirement for tighter spiral trajectories for lower G, obtained by increasing the magnitude of the pressure gradient force which always acts towards the centre of the vortex.

4.2 Implications for practical modelling of sandwaves

Our deductions above have interesting implications, although we caution that only one set of initial conditions have been considered. Nevertheless, we note that comparisons with our experimental results can be made with regard to the lower transition line which varies with V such that $A_0R_0/V \approx 1.25$. In chapter 3 we concluded that jetted particles are suspended by the shear layer when the ratio of depth-averaged stream speed to particle fall speed, U/V is about 10. Consistency here would require A_0R_0 to be about 0.12U, a value comparable with measured turbulent fluctuations in shear flows: eg measurements by Atkins & Soulsby (1992) and by Nakagawa & Nezu (1987), both recovering values ranging from 0.1U to 0.2U. For $A_0R_0/V<1.25$ the particle falls out of the shear layer and an extensive simulation should be undertaken to assess the extent to which measured distributions of settling points can be recovered by introducing realistic distributions of initial conditions for the particles, also typical ranges of vortex sizes and speeds associated with crest separating shear layers.

Above the upper transition line in the parameter space there is a range of particle trajectories which terminate at different locations around the core circumference, depending on trajectory details of the spiralling motions but primarily defined by the vortex growth rate. This behaviour clearly implies a resulting distribution in particle settling sites, since any small change in R_0, A_0 or G will affect whether the vortex expels the particle downwards into the bed or upwards towards adjoining vortices.

Away from the crest zone there is the complication, not considered here, of shear layer curvature and reattachment. As a crude first approximation we might simply terminate the simulation at an appropriate downstream station, resulting in streamwise length of the shear layer as a further independent parameter. However, more realistically perhaps, we should consider a more formal simulation using a discrete vortex model such as that developed by Kiya for back-step shear layers. Certainly, this approach could accommodate some recognition of the statistical distributions of A_0's and R_0's, including not only eddy growth but also pairing behaviour and eddy fission during impingement at the reattachment point. We urge the point of this extension study is an avenue for realistically complete simulation without the ad hoc assumptions required of existing engineering calculation schemes based on turbulence closure equations. Such a discrete vortex model would also allow for investigation of deposition trajectories and also accommodate representation of the jetting fraction.

Notwithstanding its declared limitations, our simple model has provided valuable insight into assessing the balance of mechanisms responsible for entrainment, retention and deposition in flows that are dominated by crest-shed shear layers.

5 CONCLUSIONS

Our model has shown that any particle entering a shear eddy of growth rate G displays one of three distinct outcomes depending on the vortex initial radius R_0, angular speed A_0 and the particle fall speed V. For values of $A_0R_0/V<1.25$ the particle escapes directly with only slightly deflected trajectories. For $A_0R_0/V>\sim1.25$ and $A_0R_0^{0.72}<\sim42G+0.03$, we find the particle is captured and follows a looping trajectory which gradually descends within the core. For values of $A_0R_0^{0.72}>\sim42G+0.03$ the particle is expelled from the vortex and could subsequently be engaged by adjoining eddies or be deposited on the bedform. Comparisons with published data and our own measurements broadly supports the picture developed here, certainly sufficient for us to reasonably recommend further development. However, more complex zones such as reattachment will probably call for a fuller simulation, for which we recommend the adoption of a discrete vortex model. Perhaps the major message delivered here is that the dynamical interaction between particles and eddies are far more complex than suggested in earlier studies such as by Nielsen (1984) who first argued for closed loop trajectories within vortex cores. Our findings here are closer in spirit to the findings of Chein & Chung (1988) who described modes of transport ranging from core-expulsion to advective transport for which the dispersion rates of the particle and the fluid were comparable. The need now is to bridge the gap between the understanding delivered here and practical realism involving more complex aspects of the interactions.

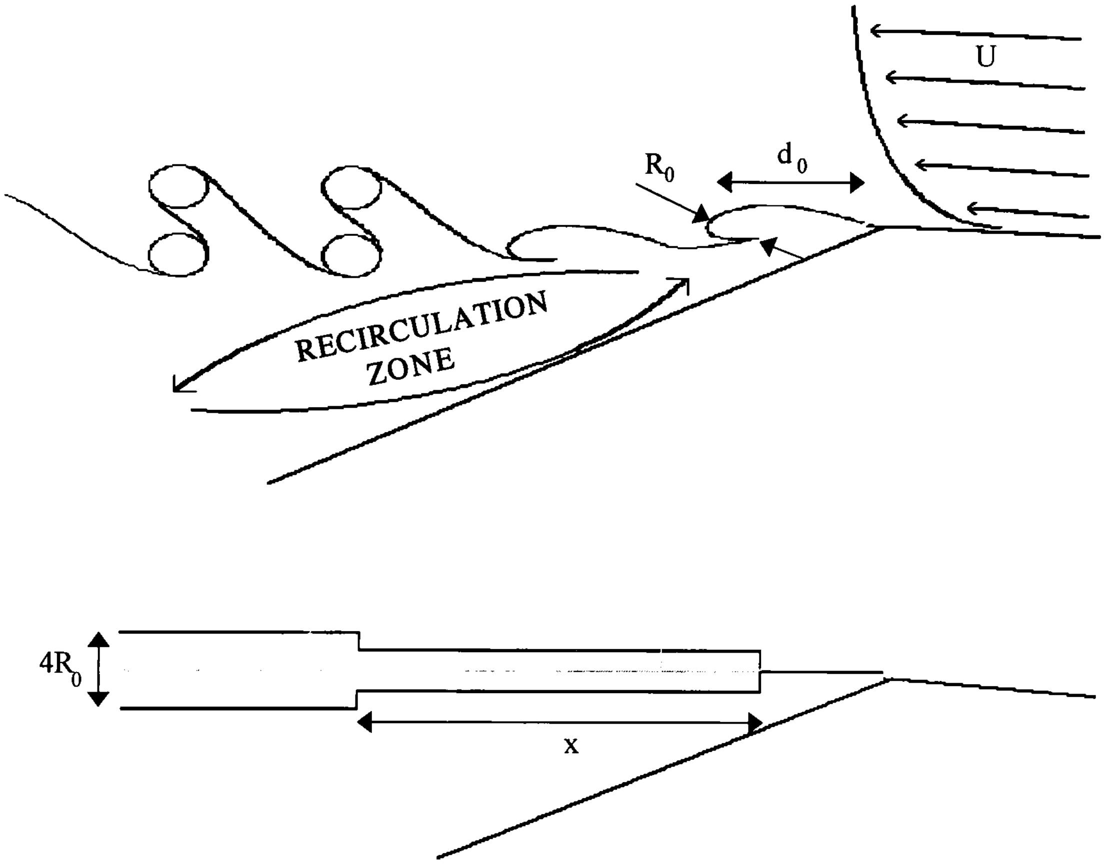

Figure 1. Schematic of the shear layer that develops after the crest of a sandwave with oncoming mean flow U. The first generation vortices form at a distance d_0 downstream of the crest with a radius R_0. Two such vortices pair, after travelling a distance x, forming a second generation vortex with double the length scale and hence half the vorticity (circulation/area).

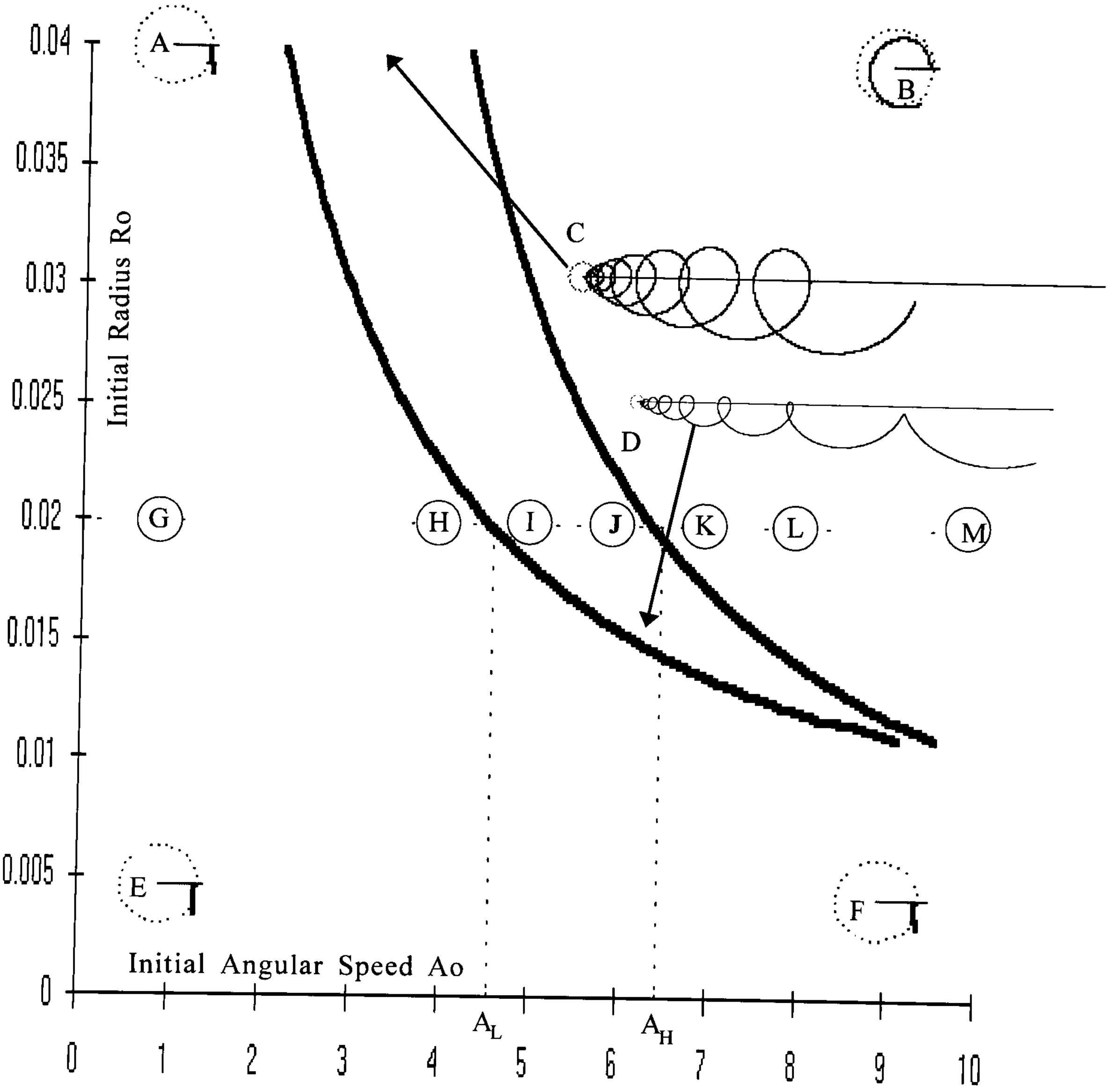

Figure 2. The parameter space diagram for a particle of quiescent fall speed V=0.076m/s at a vortex growth rate G=0.01m/s. The pictures A-F show the particle trajectories, in a frame of reference moving with the vortex, at the point in parameter space where the centre dotted circle (core radius) lies. The vortices rotate in an anti-clockwise direction. Between the low (L) and high (H) values of A, at one specific radius, the particle trajectory contains a number of loops (the capture trajectories).

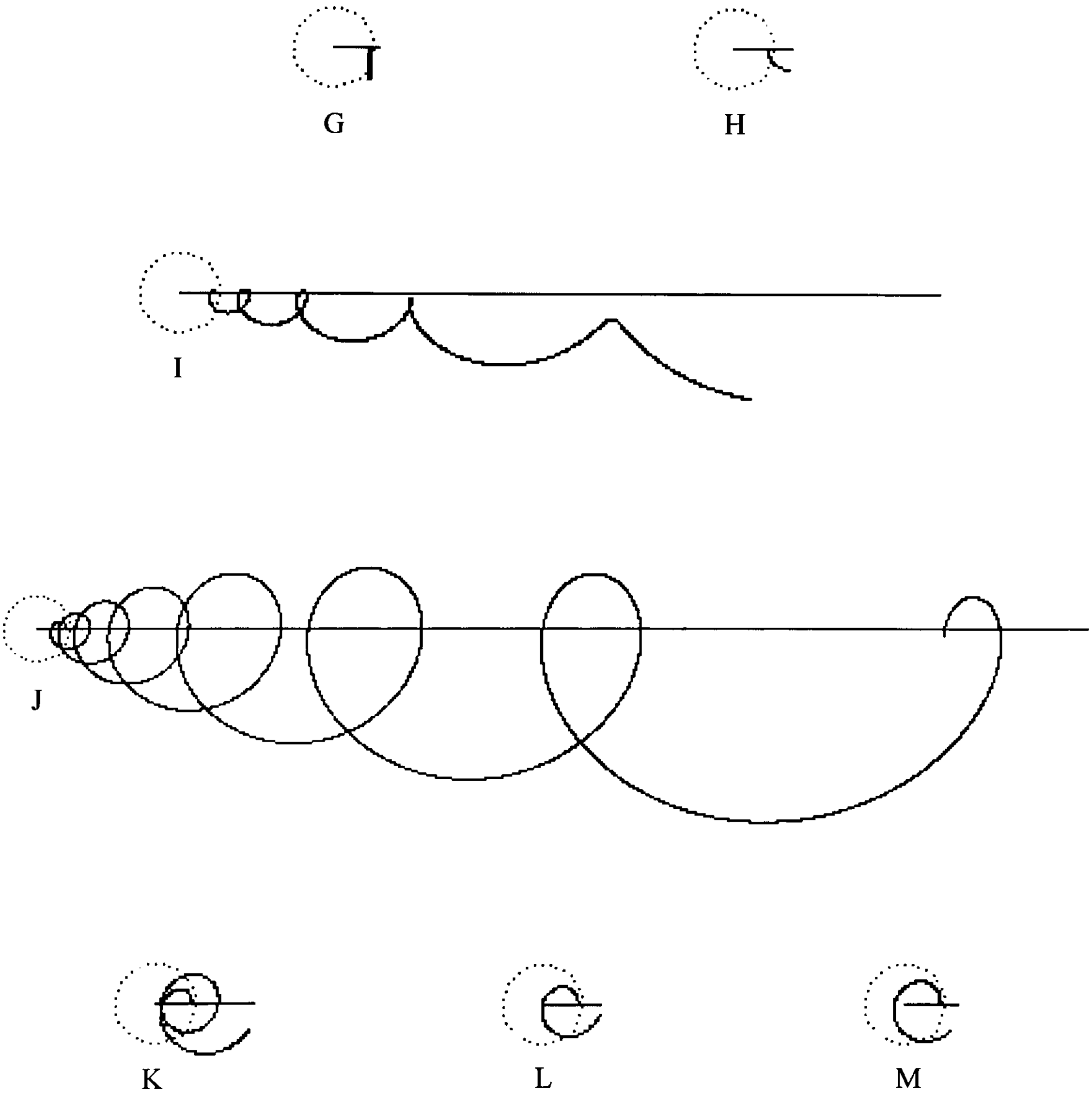

Figure 3. Seven trajectory plots corresponding to the points in parameter space marked by the circles in figure 2. G&H correspond to trajectories in the particle dominated region whereas K, L & M correspond to three in the fluid dominated region. I & J are capture trajectories seen in the central region of the parameter space where neither fluid forces nor gravity is dominant.

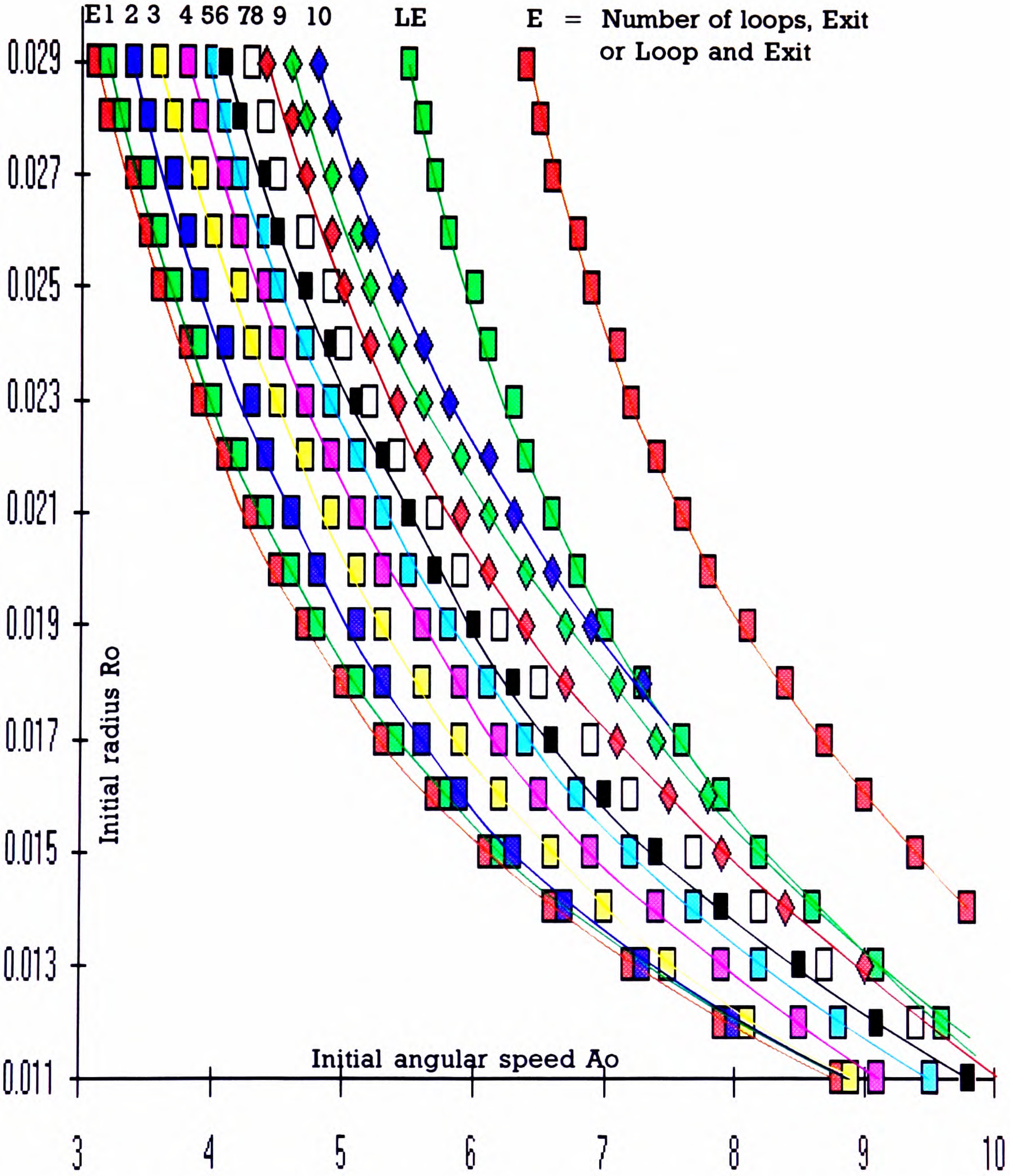

Figure 4. An example of the internal structure within the region of parameter space enclosed by the heavy lines in figure 2. The number on each line corresponds to the number of times that the particle loops up to the horizontal before falling away from the core.

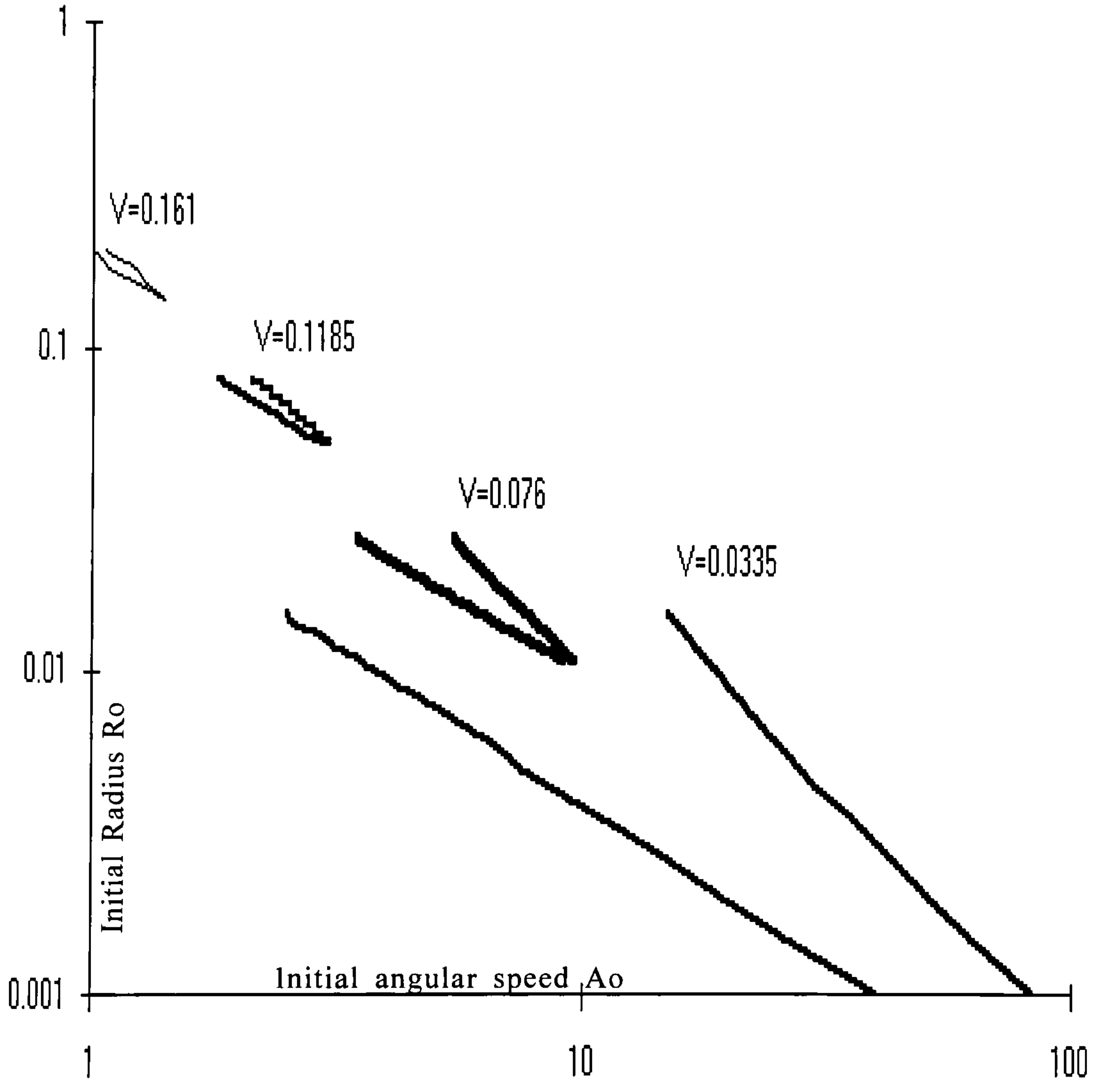

Figure 5. The effect that changing the particle fall speed has on the position of the central capture region of the parameter space for vortex growth rate G=0.01m/s.

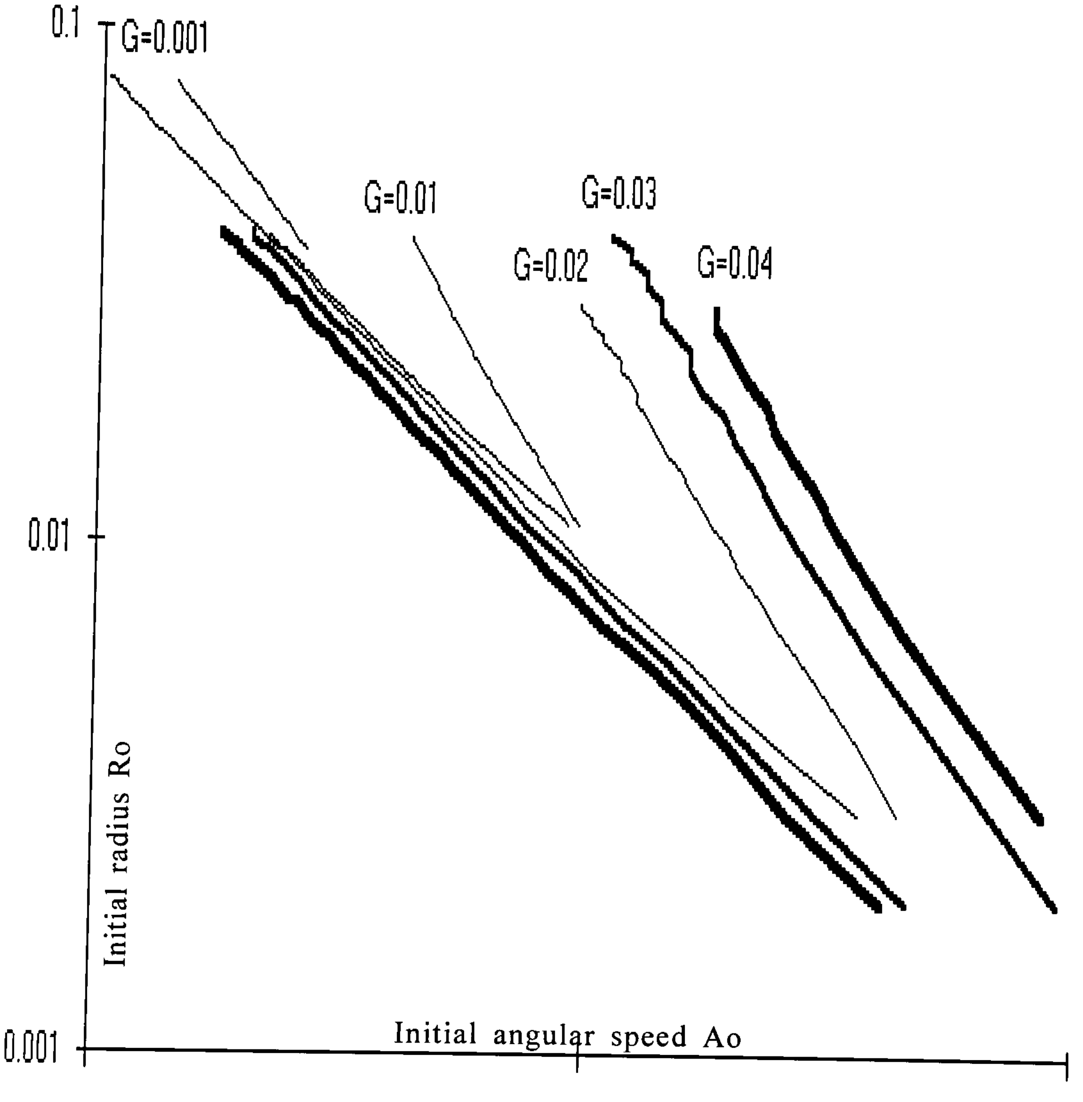

Figure 6. The effect of changing the shear layer growth rate G on the position of the central capture region of the parameter space for particle fall speed V=0.076m/s.

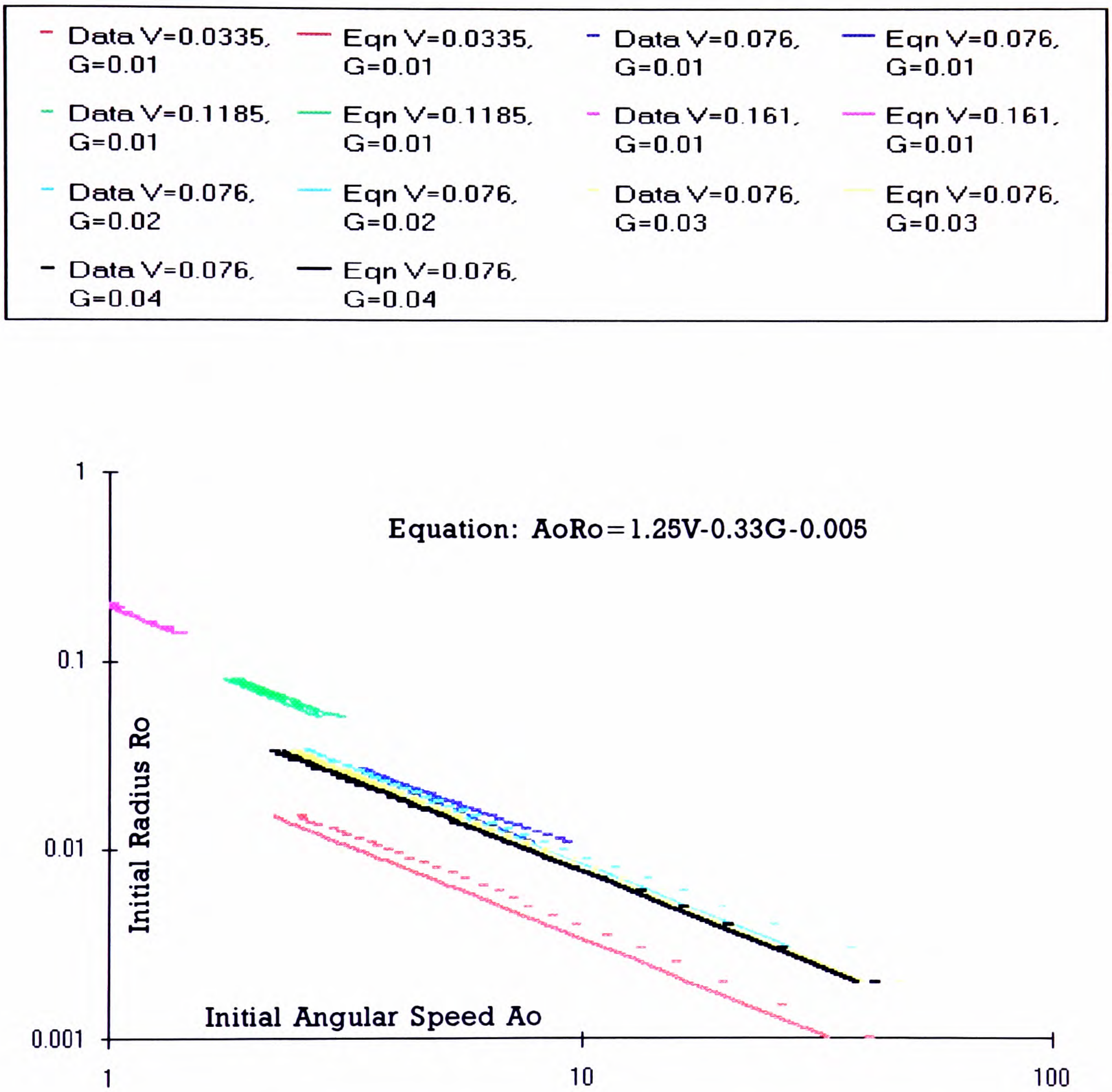

Figure 7. Comparisons between the above equation and data for the lower parameter space line at different values of particle fall speed and vortex growth rate.

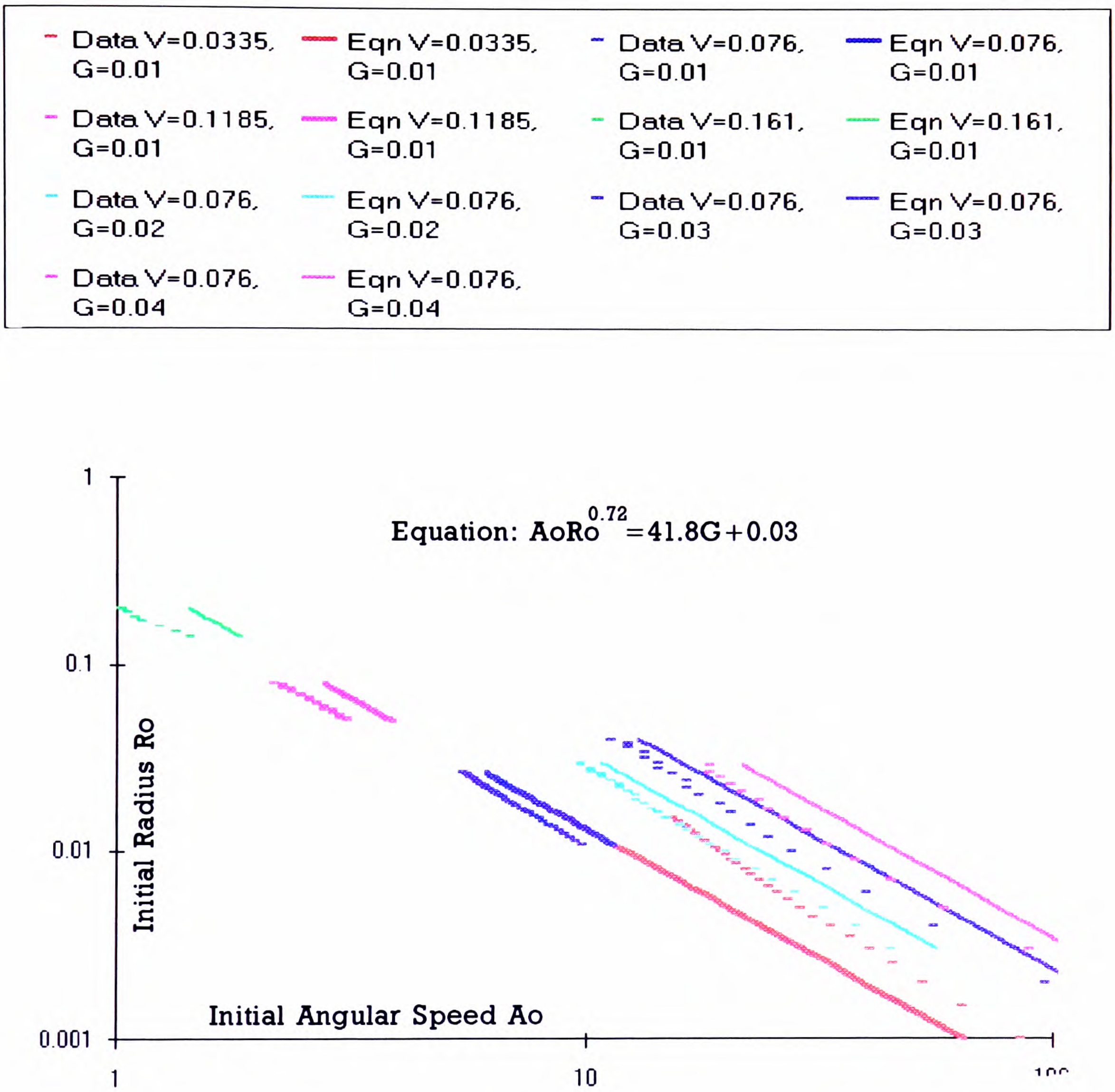

Figure 8. Comparisons between the above equation and data for the upper parameter space line at different values of particle fall speed and vortex growth rate.

CHAPTER 7: RECAPITULATION AND RECOMMENDATIONS

1 STATUS OF SANDWAVE MODELLING

Sandwaves have received much attention from many researchers over the past century. Extended reviews are presented by Dyer (1986), Allen (1984), Stride (1982), Yalin (1972) and Raudkivi (1967). The earlier studies were mainly concerned with the morphology of bedforms, especially in terms of correlating their height, length and steepness with flow depth, velocity and grain size so as to provide practical guidelines on bedform existence and migration.

Chapter 1 here concentrated on more recent literature concerned with the local flow dynamics, particularly shear layer evolution (Muller & Gyr, 1986) and reattachment onto the downstream stoss slope (Nakagawa & Nezu, 1987). Although recognition of the effects of these phenomena on bedform morphology has certainly increased, the modelling techniques have lagged well behind, with integral models concerning surface shear stress and adaptations of engineering k-ϵ models critically regarded as state-of-the-art. These methods suffer from the limitation that they offer only a time-averaged description whereas dynamical coupling between the particles and instantaneous flows radically influences their transport. This latter contribution has been more widely recognised in other fields of two-phase flows, particularly with regard to recent models of fluid-bubble interaction. Lagrangian modelling methods have incorporated these excursions from the mean field and demonstrated their importance when considering discrete second phase transport.

2 PROJECT METHODS AND RESULTS

Our interest has centred around understanding and modelling the dynamical interaction of the shear layer with the sandwave, especially with reference to particle-eddy interactions identified in the project proposal (Thomas, 1990) in connection with field measurements indicative of such interactions (Soulsby & Bettess, 1990). Below we briefly review wider implications of the findings of our experimental studies and computational modelling.

2.1 Experimental studies

We constructed a flume of 0.42m square cross-section and length 6.7m specifically to study the flow and particle dynamics over fixed bedforms. These bedforms represent a good approximation to sandwaves because migration velocity is negligible compared with the flow velocity so bedform deformation timescale is much longer than that for the typical trajectories of bedload sand grains.

We selected model particles of quiescent fall speed V_T equivalent to typical sand grains and surveyed flow speeds U such that the ratio U/V_T varied from 3 to 13. The 2mm squat cylindrical particles were large enough to be visualised videographically and their deposition rate at various sites on the bedform surface were shown to compare well with previous sedimentation data for quartz sand grains. Their suitability for optical tracking, possibly using colour labelling to differentiate between particles of differing fall speeds has promising implications which we mention in section 3.

a) Concentration peak at crest height. Soulsby & Bettess' (1990) observation of a concentration peak over the bedform trough but elevated at the height of the crest has now been shown to derive from interaction between the jetted bedload and the free shear layer. Chapter 3 showed experimentally that this behaviour is due to extended suspension time (ie hindered settling) in the shear layer as compared to the time spent falling through the relatively quiescent recirculating flow region.

Horizontal and cycloidal particle trajectories from the crest demonstrated temporary reductions and even local reversals of the particle fall speed. The results, characterised in terms of parameter U/V_T compared well with earlier findings for bubble transport in shear flows (Thomas et al, 1983) and for wave induced sediment suspension (Nielsen, 1984) where vortex capture was found to occur for U/V_T greater than 3.

b) Modal trajectories. Particles follow the broad classification of trajectories shown in figure 1, travelling from the crest to the downstream lee and stoss slopes. It is tempting to attribute the predominance of these modes to our conclusion that particle escape from vortices is predominantly from the upflow upstream directed quadrant of vortex flow. Certainly the opportunity for escape and deposition is only available for a limited time during each circuit of the vortex core.

Bearing in mind that the shear layer comprises unsteady flow features manifested as vortices of differing sizes and strengths forming, growing and pairing during transit from the crest, any subsequent trajectory of a particle that arrives at the crest, will depend sensitively on the state of the shear layer at the time of its arrival, not merely its fall speed. This consideration goes some way to accounting for the distribution of settling sites on the lee and stoss faces. Thus absence of any mechanistic representation of eddy capture and turbulence transport is certainly one of the greatest flaws in time-averaged models as currently employed.

c) Coanda-flapping. In deducing a characteristic shape for the sediment cloud behind a sandwave, Soulsby & Bettess (1990) noticed major excursions in the size of the recirculation region. In chapter 4 we showed this behaviour could be attributed to shear layer flapping as reproduced in figure 2 here. We have termed this phenomenon 'Coanda-flapping' because it is essentially caused by entrainment suction of the free shear, acting on the liquid volume of fluid in the recirculation region, dragging the shear layer towards the wall, akin to the Coanda effect.

We have shown Coanda-flapping makes a dominant contribution to lee slope sediment transport because the recirculating flow alone only moves particles from the trough to the crest for values of U/V_T about 10 or more whereas flapping excursions can induce particle transport even for U/V_T about 4 or so (see figure 3): ie larger particles are transported by Coanda-flapping than by recirculating flows.

d) Stoss slope particle capture. Our studies may have been only essentially qualitative but sufficed to show that only 20% of the stoss slope particles move as suspended load (rather than bedload) at $U/V_T=10$. Essentially, stoss slope suspension made a negligible contribution to the suspended load downstream of the crest compared to jetting and Coanda-flapping suspension.

2.2 Numerical studies

Our initial studies addressed the interaction between particles at the crest and the first generation vortex formed by roll-up of the free shear layer. Subsequently we modelled the trajectory of particles in a growing travelling vortex. Main points of each aspect are surveyed below.

a) Fixed vortex modelling. We calculated capture interaction between particles and vortices following the methods reported previously for bubbles and vortices (Thomas et al, 1983 and Sene et al, 1993). The vorticity was taken as uniform within the core as a reasonable first approximation of shear layer vortices. The model studies in chapter 5 have enhanced our understanding by confirming temporary reductions and even reversals in the effective fall speed of particles released in the vicinity of vortices, confirming our experimental finding that particles in the vicinity of the crest indeed move upwards.

Capture was shown to be due to local instantaneous pressure gradient forces experienced by the particle. A criterion was deduced for capture in terms of the ratio AR/V_T where A is the vortex angular speed and R its radius. For shear layer vortices forming at a downstream location about 8-12R from the crest, we have a critical value of AR/V_T about 10 or so (figure 4). Since the advection speed of vortices close to the crest is about half the upstream flow velocity U and the tangential compact core speed (AR) also about U/2 we recover $U/V_T=5$ or so, for particle capture at the crest, which indeed compares plausibly with experimentally determined values of about 3.

Here we also computed particle trajectories for a time averaged flow produced by a travelling vortex, comparing this with the trajectories obtained with vortex flow which had not been averaged. This simple demonstration strikingly highlighted the crucial importance attached to modelling details of the fluctuating field.

b) Shear layer modelling. In chapter 6 we introduced greater realism by extending the model to a growing vortex core. We found that the capture domain located between the lines in figure

figure 5, was critically dependant upon the vortex initial strength and size. The lower boundary was dependent on drag forces and the upper boundary on pressure gradient forces. Particle trajectories ranged from short modes depositing near the crest through capture modes depositing within the recirculation bubble to particle ejection over the top of the shear layer.

Of special interest are the capture modes exhibiting looped trajectories in a frame of reference travelling with the vortex. Such trajectories always defined exit paths in the fourth quadrant (ie upwards upstream directed flow) and although our model did not extend to deposition it served to suggest that deposition probably occurs modally ie in various bands centred on discrete time intervals, rather than a continuum of times, behaviour associated with this looping nature of the trajectories. We note here that these bands will almost certainly overlap for real shear layers due to the distribution of starting conditions not considered here. Nevertheless, we feel it is improbable that Gaussian dispersion modelling could deliver a representation of this transport behaviour.

3 RECOMMENDATIONS

3.1 Experimental techniques

Videography of the flow and particle trajectories over fixed bedforms have certainly been found a valuable technique for sandwave research. Our initial efforts at visualisation of the

Coanda flapping phenomenon involved manual analysis which was exceedingly time consuming. Introduction of PIV and frame-by-frame automated analysis would solve this problem. Specifically here, such a system could interrogate frames for the recovery of the effective separation volume by finding the first occurrence of directionally-pulse-tagged streaks formed by flow tracers. The remaining streaks caused by flow tracers looping and travelling in the opposite direction must then be part of the recirculation bubble, giving the time dependent bubble size. This study would surely demonstrate that fluctuations here are directly linked to the Coanda-flapping frequency.

Concurrent video records of the crest flow could also be analysed, allowing, for example, subtraction of the mean flow to produce pictures of the shear layer vortices arriving at the crest and again producing a frequency for the possible driving events.

Chapters 3 and 4 described particle trajectory information which revealed interesting information but statistically converged data is difficult to achieve by manual analysis alone. We now have automatic particle tracking equipment available which should eradicate this problem. It will also allow two-point correlation methods to be used which will probably prove the modal trajectory theory. It will also be useful when considering lee slope suspension and the concentration profiles thereof.

The problem of starting flow washout as encountered during the stoss slope suspension studies of chapter 4 are difficult to overcome. One plausible approach would involve attaching a layer of particles to the bedforms providing a rough surface for retention of a second layer of free particles. Should this prove insufficient to solve the problem then magnetics may provide the answer. Each particle could conceivably be coated with, say, iron powder and held to the bedform during flow development with an electromagnet either beneath the flume or built into the bedform.

3.2 Numerical modelling techniques

The fixed core modelling of chapter 5 should be extended to encompass more starting conditions and different vorticity distributions such as the Gaussian core. Essentially, the criterion $C(X,Y,V_X,V_Y)$ should be found for all relevant values of the initial position (X,Y) of the particle at initial velocities (V_X,V_Y). For the sandwave problem (X,Y) should be considered from (-20,-20) to (20,20) at (V_X,V_Y) from $(0,-V_T)$ to (U,0) where U is the maximum mean stream speed, about say 2m/s for dunes. This comprehensive set would be too large to be of use directly, but would allow rules to be defined concerning particle capture and ejection which should be of more general use to modellers.

The growing vortex model of the shear layer should be extended to include different growth laws ie adapted to account for shear layers that do not have constant velocity difference. This is needed because the shear layer over sandwaves cannot sensibly hold to this law after reattachment as there is no velocity difference. Also, a wider range for particle starting conditions should be surveyed to account for capture of particles suspended upstream of the crest.

Of course, our main recommendation is that discrete vortex or large eddy modelling methods should be applied to this problem so that all of the crucial time-dependent factors can be accounted for in a thorough and mechanistic fashion.

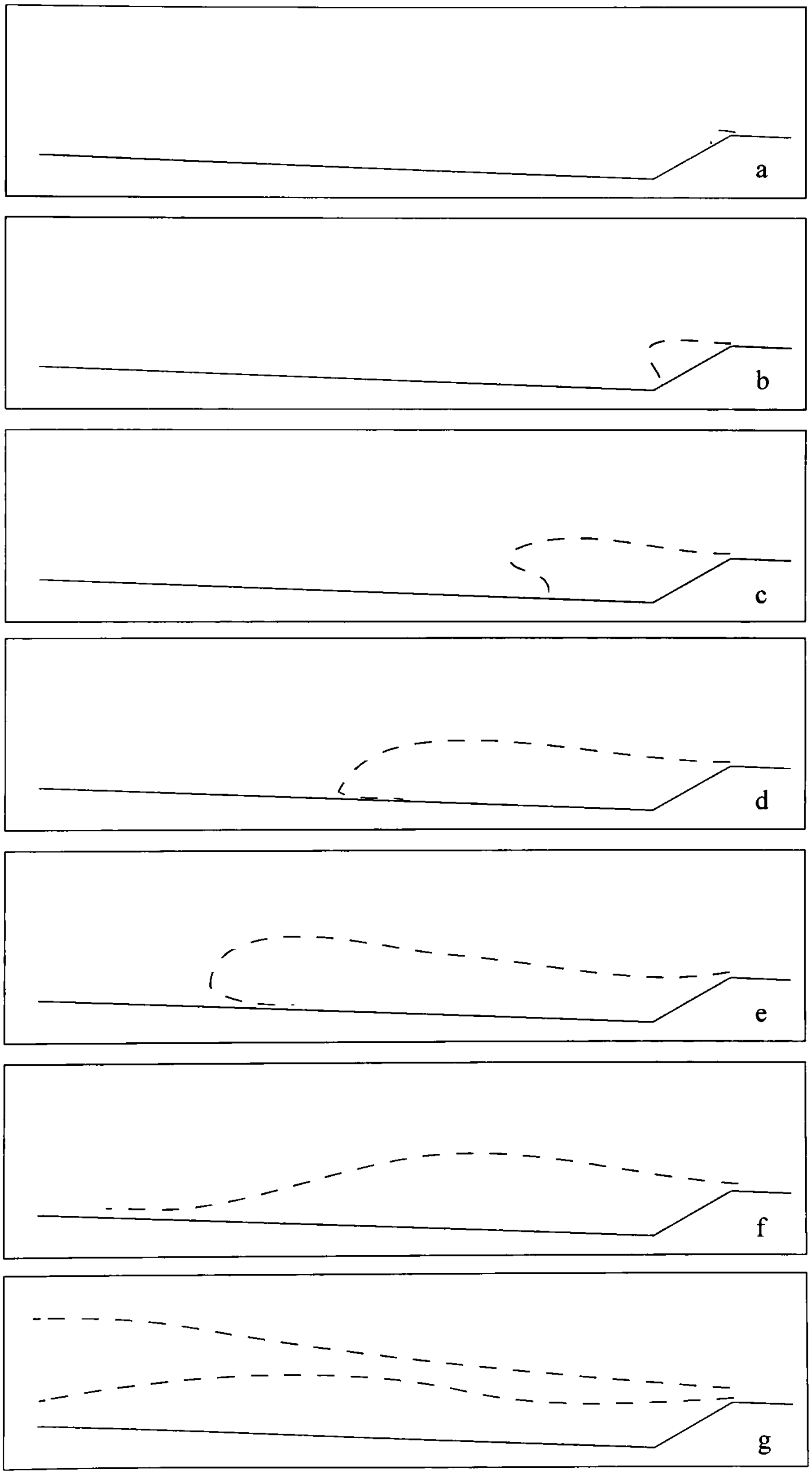

Figure 1a-g. The seven trajectory modes for jetted particles. a) M1 b) M2 c) M3 d) M4 e) M5 f) M6 g) M7.

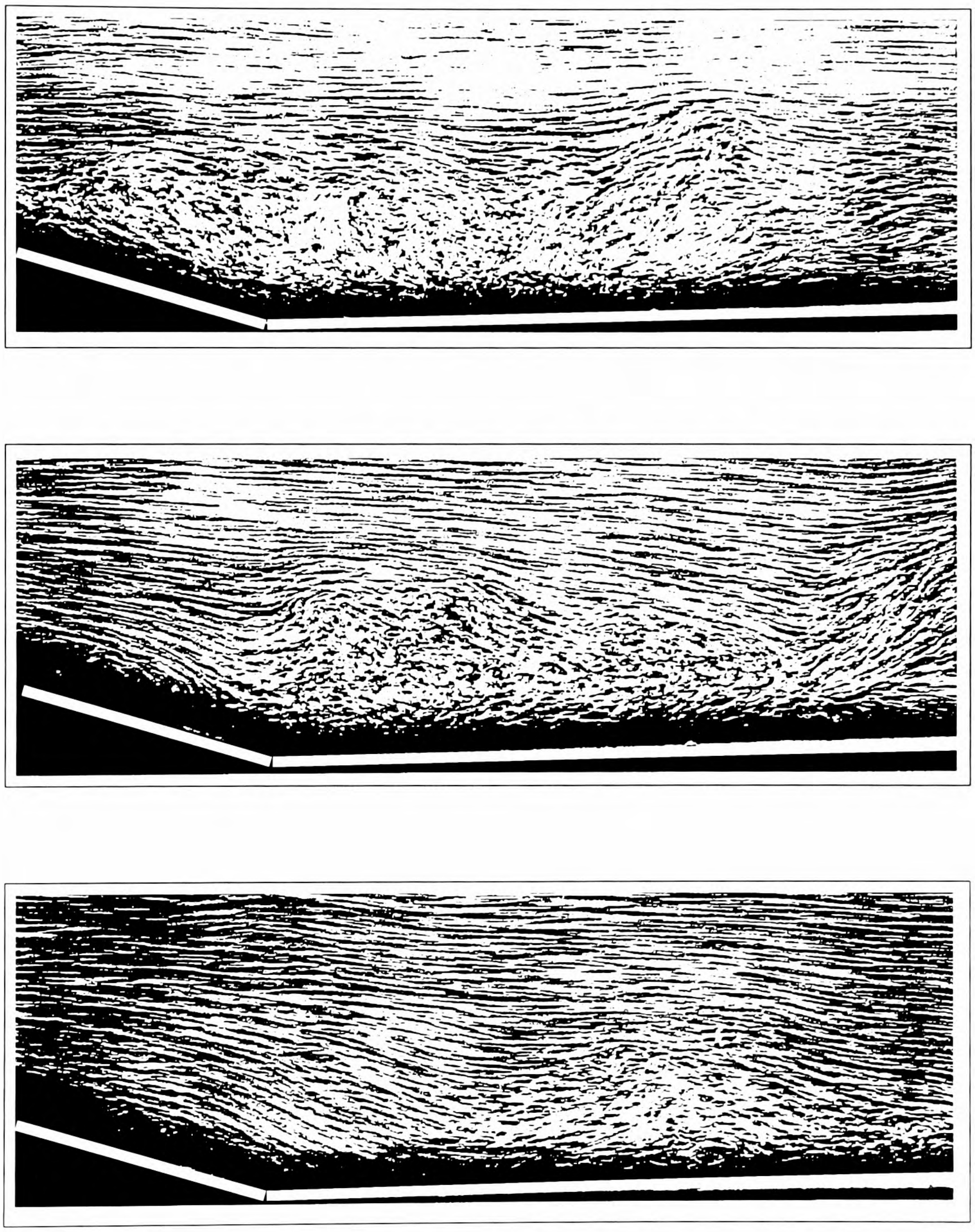

Figure 2. The plates show three views of the recirculation region behind an experimental bedform. The shots are 0.35 secs. apart and clearly visualise the sweeping away of the turbulent region, leading to re-attachment close to the trough. We term this sequence of events Coanda-flapping.

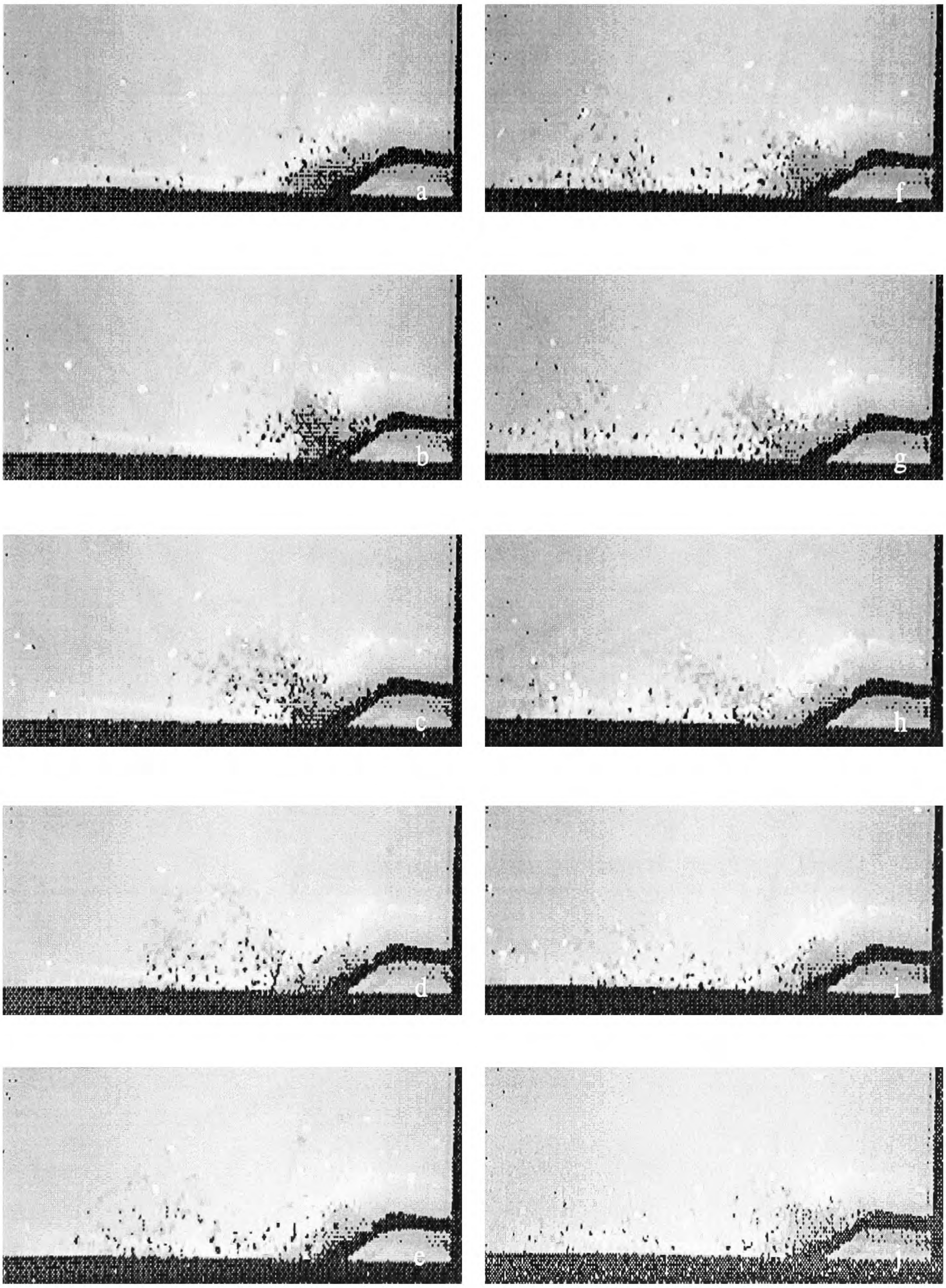

Figure 3a-j. The plates show particles transported by periodic flows caused by Coanda-flapping of the free shear layer. The particles (dark spots, just off centre-line of the rig and light spots on the centre-line) have a fall speed of 0.034m/s and the depth-averaged flow speed is 0.31m/s.

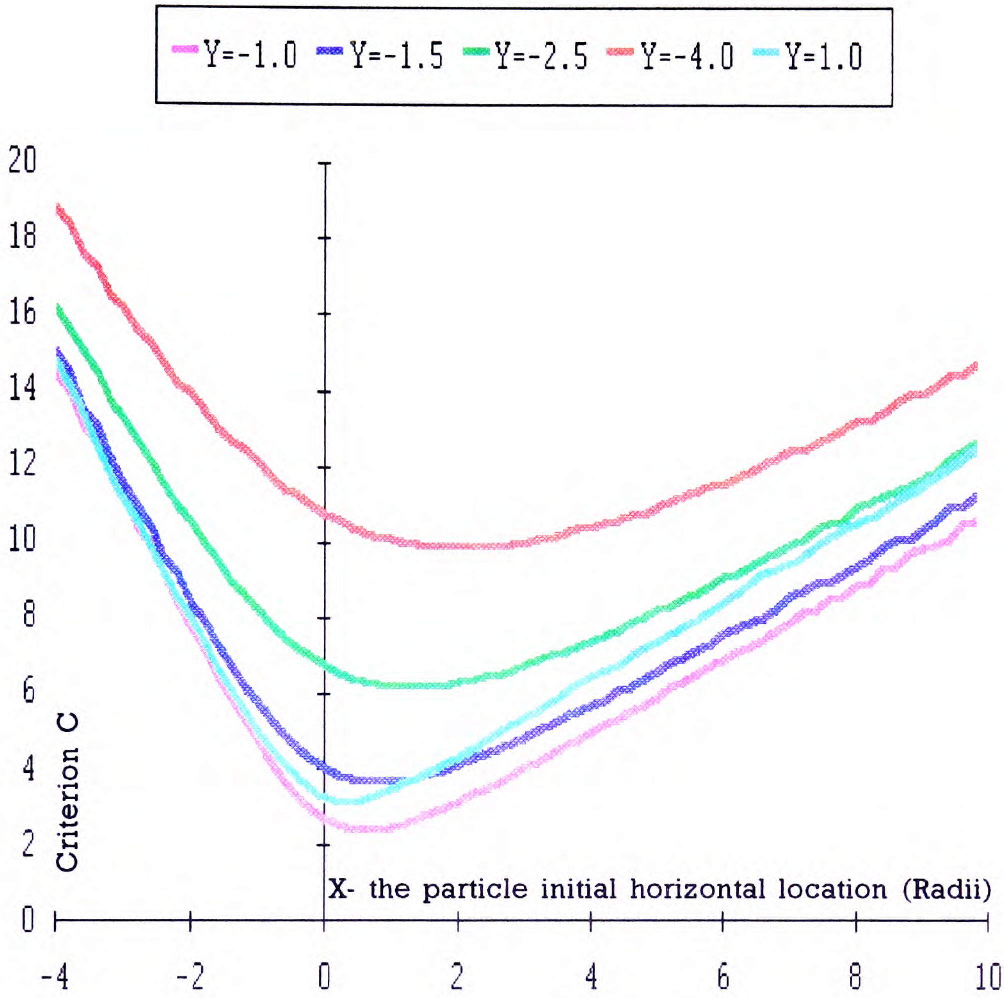

Figure 4. Values of the capture criterion for various values of particle starting position (X,Y) at zero initial particle velocity.

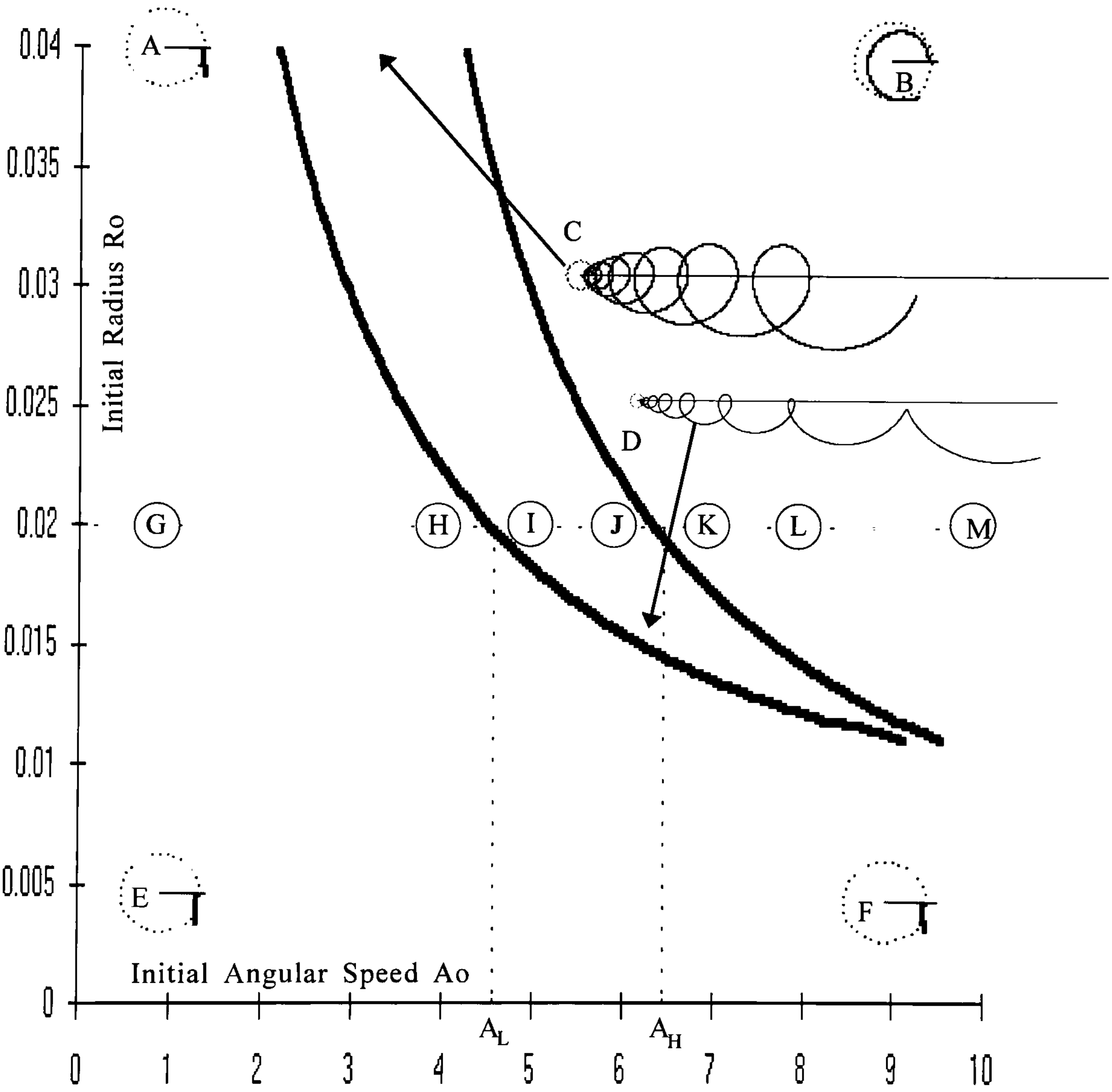

Figure 5. The parameter space diagram for a particle of quiescent fall speed V=0.076m/s at a vortex growth rate G=0.01m/s. The pictures A-F show the particle trajectories, in a frame of reference moving with the vortex, at the point in the parameter space where the centre dotted circle (core radius) lies. The vortices rotate in an anti-clockwise direction. Between the low (L) and high (H) values of A, at one specific radius, the particle trajectory contains a number of loops (the capture trajectories).

CHAPTER 8: REFERENCES

Acarlar MS & Smith CR (1987a). *A study of hairpin vortices in a laminar boundary layer. Part 1. Hairpin vortices generated by a hemispherical protuberance.* J Fluid Mech **175** pp 1-41.

Acarlar MS & Smith CR (1987b). *A study of hairpin vortices in a laminar boundary layer. Part 2. Hairpin vortices generated by fluid injection.* J Fluid Mech **175** pp 43-83.

Allen JRL (1984). *Sedimentary Structures, their Character and Physical Basis.* Elsevier Press.

Anderson CR (1986). *A method of local correction for the velocity field due to a distribution of vortex blobs.* J Comput Phys **62** pp 111-123.

Antonia RA & Bisset DK (1990). *Spanwise structure in the near-wall region of a turbulent boundary layer.* J Fluid Mech **210** pp 437-458.

Atkins R & Soulsby RL (1992). *Measurements of flow and sediment dynamics over an estuarine sandwave - data report.* Report SR249. HR Wallingford, Oxfordshire.

Auton TR (1987). *The lift force on a spherical body in a rotational flow.* J Fluid Mech **183** pp 199-218.

Auton TR (1984). *The dynamics of bubbles, drops and particles in motion in liquids.* PhD Thesis, University of Cambridge.

Batchelor GK (1967). *An Introduction to Fluid Mechanics.* Cambridge University Press.

Berlemont A, Desjonqueres P & Gouesbet G (1990). *Particle Lagrangian simulation in turbulent flows.* Int J Multiphase

Flow **16** (1) pp 19-34.

Bernal LP (1981). *The coherent structure in turbulent mixing layers, II: Secondary streamwise vortex structure.* PhD Thesis, Caltech.

Besnard DC & Harlow FH (1988). *Turbulence in multiphase flow.* Int J Multiphase Flow **14** (6) pp 679-699.

Blevins RD (1984). *Applied Fluid Dynamics Handbook.* Van Norstrand Reinhold Co.

Brown GL & Roshco A (1971). *The effect of density difference on the turbulent mixing layer.* AGARD conference proceedings **93** 23-1-23-11.

Brown GL & Roscho A (1974). *On density effects and large structure in turbulent mixing layers.* J Fluid Mech **64** pp 775-816.

Celik I (1982). *Numerical modelling of sediment transport in open channel flows.* Euromech 156. Mechanics of Sediment Transport. Istanbul, 12-14 July.

Chein R & Chung JN (1988). *Simulation of particle dispersion in a two-dimensional mixing layer.* AIChE Journal **34** (6) pp 946-954.

Clift R, Grace JR & Weber ME (1978). *Bubbles, Drops and Particles.* Academic Press.

Coles D (1956). *The law of the wake in the turbulent boundary layer.* J Fluid Mech **1** p191.

de Ruiter JCC (1982). *The mechanism of sediment transport on bedforms.* Euromech 156. Mechanics of Sediment Transport. Istanbul, 12-14 July.

Dimotakis P & Brown GL (1976). *The mixing layer at high*

Reynolds number: large structure dynamics and entrainment. J Fluid Mech **78** pp 535-554.

Dyer KR (1986). *Coastal and Estuarine Sediment Dynamics.* Wiley Press, Chichester.

Elghobashi SE, Abou-Arab TW, Rizk M & Mostafa A (1984). *Prediction of the particle-laden jet with a two-equation turbulence model.* Int J Multiphase Flow **10** (6) pp 697-710.

Elghobashi SE & Abou-Arab TW (1983). *A two-equation turbulence model for two-phase flows.* Phys Fluids **26** (4) pp 931-938.

Engelund F & Fredsoe J (1982). *Sediment ripples and dunes.* Ann Rev Fluid Mech **14** pp 13-37.

Favre AJ, Gaviglio JJ & Dumas R (1957). *Space time double correlation and spectra in a turbulent boundary layer.* J Fluid Mech **2** pp 313-41.

Fink PI & Soh WK (1974). *Calculation of vortex sheets in unsteady flow and applications in ship hydrodynamics.* Proc of the 10th Symp on Naval Hydro, Cambridge, Mass, pp 463-488.

Fleming CA & Hunt JN (1976). *A mathematical sediment transport model for unidirectional flow.* Proc Inst Civ Engrs **61** (2) pp 297-310.

Freymuth P (1966). *On transition in a separated boundary layer.* J Fluid Mech **25** pp 683-704.

Ghoniem AF, Chen DY & Oppenheim AK (1986). *Formation and inflammation of a turbulent jet.* AIAA J **24** (2) pp 224-229.

Grass AJ (1982). *The influence of boundary layer turbulence on the mechanics of sediment transport.* Euromech 156.

Mechanics of Sediment Transport. Istanbul, 12-14 July.

Grass AJ (1971). *Structural features of turbulent flow over smooth and rough boundaries.* J Fluid Mech **50** pp 233-255.

Grass AJ (1974). *Transport of fine sand on a flat bed: Turbulence and suspension mechanics.* Euromech 48. Tech Univ Denmark, Copenhagen, 12-14 July.

Greengard L & Rochlin V (1987). *A fast algorithm for particle simulations.* J Comput Phys **73** pp 325-348.

Gyr A (1983). *Towards a better definition of the three types of sediment transport.* J Hyd Res **21** (1) pp 1-15.

Hallermeier RJ (1981). *Terminal settling velocity of commonly occurring sand grains.* Sedimentology **28** pp 859-865.

Hansen EA, Fredsoe J & Deigaard R (1991). *Distribution of suspended sediment over wave generated ripples.* Int Symp on the Transport of Suspended Sediments and its Mathematical Modelling. Florence (Italy), September 2-5.

Hernan MA & Jiminez J (1982). *Computer analysis of a high speed film of the plane turbulent mixing layer.* J Fluid Mech **119** pp 323-345.

Hill PS, Nowell ARM & Jumars PA (1988). *Flume evaluation of the relationship between suspended sediment concentration and excess boundary shear stress.* J Geophys Res **93** (C10) pp 12499-12509.

Ho Ching-Ming, Zohar Y, Foss JK & Buell JC (1991). *Phase decorrelation of coherent structures in a free shear layer.* J Fluid Mech **230** pp 319-337.

Ho CM & Huerre P (1984). *Perturbed free shear layers.* Ann Rev Fluid Mech **16** pp 365-424.

Hunt JCR, Auton TR, Sene K, Thomas NH & Kowe R (1988). *Bubble motions in large eddies and turbulent flows.* Transient Phenomena in Multiphase Flow. Ed NH Afghan. Hemisphere.

Ikeda S & Asaeda T (1983). *Sediment suspension with rippled bed.* J Hyd Eng **109** (3) pp 409-423.

Jackson RG (1976). *Sedimentological and fluid dynamic implications of the turbulent bursting phenomenon in geophysical flows.* J Fluid Mech **77** pp 531-560.

Jacobs PA & Pullin DI (1989). *Multiple-contour-dynamic simulation of eddy scales in the plane shear layer.* J Fluid Mech **199** pp 89-124.

Jiminez J (1980). *On the visual growth of a turbulent mixing layer.* J Fluid Mech **96** (3) pp 447-460.

Johns B, Soulsby RL & Chesher TJ (1990). *The modelling of sandwave evolution resulting from suspended and bed load transport of sediment.* J Hyd Res **28** (3) pp 355-374.

Johns B (1991). *The modelling of the free surface flow of water over topography.* Coastal Engineering **15** pp 257-278.

Julien PY (1986). *Concentration of very fine silts in a steady vortex.* J Hyd Res **24** (4) pp 255-264.

Karahan ME & Peterson AW (1980). *Visualisation of separation over sand waves.* J Hyd Div ASCE **106** (HY8) pp 1345-1352.

Kaul UK (1988). *Do large structures control their own growth in a mixing layer? An assessment.* J Fluid Mech **190** pp 427-450.

Kennedy JF (1969). *The formation of sediment ripples, dunes and antidunes.* Ann Rev Fluid Mech **1** pp 147-168.

Kim HT, Kline SJ & Reynolds WC (1971). *The production of* *turbulence near a smooth wall in a turbulent boundary layer.* J Fluid Mech **50** pp 133-160.

Kiya M & Sasaki K (1983). *Structure of a turbulent separation bubble.* J Fluid Mech **137** pp 83-113.

Kline SJ, Reynolds WC, Schraub FA & Runstadler PW (1967). *The structure of turbulent boundary layers.* J Fluid Mech **30** pp 741-773.

Konrad JH (1976). *An experimental investigation of mixing in two-dimensional turbulent shear flows with applications to diffusion limited chemical reactions.* PhD Thesis, Caltech.

Kovasznay LSG, Kibens V & Blackwelder RF (1970). *Large scale motion in the intermittent region of a turbulent boundary layer.* J Fluid Mech **41** pp 283-325.

Lamb H (1932). *Hydrodynamics.* Cambridge University Press, 6th Ed.

Lasheras JC & Choi H (1988). *Three dimensional instability of a plane free shear layer: an experimental study of the formation and evolution of streamwise vortices.* J Fluid Mech **189** pp 53-86.

Lazaro BJ & Lasheras JC (1992a). *Particle dispersion in the developing free shear layer. Part 1. Unforced flow.* J Fluid Mech **235** pp 143-178.

Lazaro BJ & Lasheras JC (1992b). *Particle dispersion in the developing free shear layer. Part 2. Forced flow.* J Fluid Mech **235** pp 179-221.

Lee KB & Chung MK (1987). *Refinement of the mixing length model for prediction of gas particle flow in a pipe.* Int J Multiphase Flow **13** (2) pp 275-282.

Leonard A (1980). *Vortex methods for flow simulation.* J Comput Phys **37** pp 289-335.

Lyn DA (1993). *Turbulence measurements in open-channel flows over artificial bed forms.* J Hyd Eng **119** (3) pp 306-326.

Markatos NC (1986). *The mathematical modelling of turbulent flows.* Appl Math Modelling **10** (June) pp 190-220.

McLean SR (1991). *Depth-integrated suspended-load calculations.* J Hyd Eng **117** pp 1440-1458.

Muller A & Gyr A (1986). *On the vortex formation in the mixing layer behind dunes.* J Hyd Res **24** pp 359-75.

Nakagawa H & Nezu I (1987). *Experimental investigation on turbulent structure of backward-facing step flow in an open channel.* J Hyd Res **25** (1) pp 67-88.

Nezu I & Nakagawa H (1991). *Turbulent structures over dunes and its role on suspended sediments in steady and unsteady open-channel flows.* Int Symp on The Transport of Suspended Sediments and its Mathematical Modelling. Florence, Italy, September 2-5.

Nielsen P (1984). *On the motion of suspended sand particles.* J Geophys Res **89** (C1) pp 616-626.

Offen GR & Kline SJ (1974). *Combined dye-streak and hydrogen bubble visual observations of a turbulent boundary layer.* J Fluid Mech **62** pp 223-239.

Onslow RJ, Thomas NH & Whitehouse RJS (1994). *Vorticity and Sandwaves: The dynamics of ripples and dunes.* In Turbulence: Perspectives on Flow and Sediment Transport. Ed NJ Clifford, JR French & J Hardisty. Wiley.

Panides E & Chevray R (1990). *Vortex dynamics in a plane,* *moderate Reynolds number shear layer.* J Fluid Mech **214** pp 411-435.

Phillips BC & Sutherland AJ (1986). *Diffusion models applied to channel degradation.* J Hyd Res **25** (3) pp 411-435.

Phillips BC & Sutherland AJ (1989). *Spatial lag effects in bed load sediment transport.* J Hyd Res **27** (1) pp 115-133.

Picart A, Berlemont A & Gouesbet G (1986). *Modelling and predicting turbulence fields and the dispersion of discrete particles transported by turbulent flows.* Int J Multiphase Flow **12** (2) pp 237-261.

Rao KN, Narashima R & Badri Narayanan MA (1971). *The 'bursting' phenomenon in a turbulent boundary layer.* J Fluid Mech **48** pp 339-352.

Raudkivi AJ (1967). *Loose Boundary Hydraulics.* Pergamon Press.

van Rijn LC (1985). *Mathematical models for sediment concentration profiles in steady flow.* Euromech 192. Transport of Suspended Solids in Open Channels. Neubiberg, 11-15 June.

van Rijn LC (1984). *Sediment pick-up functions.* J Hyd Eng proc ASCE **110** (10) pp 1494-1504.

Rizk MA & Elghobashi SE (1989). *A two equation turbulence model for dispersed dilute confined two-phase flows.* Int J Multiphase Flow **15** (1) pp 119-133.

Rodi W (1979). *Turbulence Models and their Applications in Hydraulics.* IAHR state-of-the-art paper presented by the section on Fundamentals of Division II: Experimental and Mathematical Fluid Dynamics.

Sarpkaya T (1989). *Computational methods with vortices, the*

1988 Freeman scholar lecture. J Fluids Eng **111** pp 5-52.

Schreider MI & Amsler ML (1992). *Bedforms steepness in alluvial streams.* J Hyd Res **30** pp 725-744.

Sene K, Hunt JCR & Thomas NH (1993). *Role of coherent structures in turbulent shear flows.* J Fluid Mech (In press).

Simons DB & Richardson EV (1961). *Forms of bed roughness in alluvial channels.* J Hyd Div ASCE **87** (HY3) pp 87-105.

Simpson RL (1989). *Turbulent boundary layer separation.* Ann Rev Fluid Mech **21** pp 205-234.

Sleath JFA (1982). *The suspension of sand by waves.* J Hyd Res **20** (5) pp 439-452.

Sommeria J, Staquet C & Robert R (1991). *Final equilibrium state of a two-dimensional shear layer.* J Fluid Mech **233** pp 661-689.

Soulsby RL (1989). *Bedform migration in sandy estuaries.* Report SR208, HR Wallingford.

Soulsby RL (1981). *Measurements of the Reynolds stress components close to a marine sand bank.* Mar Geol **42** pp 35-37.

Soulsby RL & Bettess R (1991). *Field measurements of suspended sediment over sandwaves.* Euromech 262. Sand Transport in Rivers, Estuaries and the Sea. Wallingford, Oxfordshire. 26-29 June 1990. Ed R Soulsby & R Bettess. AA Balkema, Rotterdam/Brookfield, 1991.

Soulsby RL & Bettess R (1990). *Sand transport in rivers, estuaries and the sea.* Euromech 262. Sand Transport in Rivers, Estuaries and the Sea. Wallingford, Oxfordshire, 26-29 June.

Spalding (1961). *A single formula for the law of the wall.* J Appl Mech **28** pp 455-57.

Spreiter JR & Sacks AH (1951). *The rolling up of the trailing vortex and its effect on the downwash behind wings.* J Aeronaut Sci **18** pp 21-32.

Stride AH (1982). *Offshore tidal sands: processes and deposits.* Chapman & Hall, New York.

Thomas NH (1990). *Fluid-particle transport dynamics of sandwaves.* Report FAST9003.HR(RW)/NHT. SERC-CASE project with Hydraulic Research - agreed proposal.

Thomas NH, Auton TR, Sene K & Hunt JCR (1983). *Entrapment and transport of bubbles by transient large eddies in multiphase turbulent shear flows.* BHRA International Conference on Physical Modelling of Multiphase Flow. Coventry, England. April 19-21.

Tiemroth EC (1986). *Simulation of the viscous flow around a cylinder by the random vortex method.* PhD Thesis, Univ of Calif, Berkley.

Townsend AA (1956). *The Structure of Turbulent Shear Flow.* Cambridge University Press.

Tsuji Y, Morikawa Y, Tanaka N, Nakatsukasa N & Nakatani M (1987). *Numerical simulation of gas-solid two-phase flow in a two-dimensional horizontal channel.* Int J Multiphase Flow **13** (5) pp 671-684.

Tunstall EB & Inman DL (1975). *Vortex generation by oscillatory flow over rippled surfaces.* J Geophys Res **80** (24) pp 3475-3484.

Utami T & Ueno T (1987). *Experimental study on the coherent* *structure of turbulent open-channel flow using visualisation and picture processing.* J Fluid Mech **174** pp 399-440.

West JR, Oduyemi KOK, Bale AJ & Morris AW (1990). *The field measurement of sediment transport parameters in estuaries.* Estuarine, Coastal and Shelf Science **30** pp 167-183.

Whitehouse RJS (1992). *Sea bed scour in the offshore environment.* Evening lecture, Offshore Engineering Society. London, 9 December.

Wille R & Fernholz H (1965). *Report on the first European mechanics colloquium, on the Coanda effect.* J Fluid Mech **23** (4) pp 801-819.

Willmarth WW & Lu SS (1972). *Structure of Reynolds stress near the wall.* J Fluid Mech **55** pp 65-92.

Winant CD & Browand FK (1974). *Vortex pairing: the mechanism of turbulent mixing layer growth at moderate Reynolds numbers.* J Fluid Mech **63** pp 237-55.

Yalin MS & Ferreira da Silva AM (1991). *Computer simulation of suspended load transport.* International Symposium on the Transport of Suspended Sediments and its Mathematical Modelling. Florence, Italy, September 2-5, pp 287-292.

Yalin MS (1964). *Geometrical properties of sand waves.* J Hyd Div ASCE **90** (HY5) Sep pp 105-119.

Yalin MS (1972). *Mechanics of Sediment Transport.* Pergamon Press.

Yang X & Thomas NH (1994). *Simulation of particle and bubble dispersion in turbulent free shear flows.* Int Symp on Numerical Methods for Multiphase Flows. Lake Tahoe, NV

USA.

APPENDICES

APPENDIX 1: BOUNDARY LAYER STUDIES

1 HISTORICAL ASPECTS

Boundary layer flows have classically been split into the study of three layers, the viscous sublayer, the buffer layer and the logarithmic and outer layer. In the viscous sublayer $\mathbf{y^+}=\mathbf{u^+}$ for $0<\mathbf{y^+}<7$ (wall units defined below). In the buffer layer where approximately $7<\mathbf{y^+}<30$, several relationships exist such as the one given by Spalding (1961),

$$y^+=u^++e^{-Kc}\left[e^{Ku^+}-1-Ku^+-\frac{1}{2}(Ku^+)^2-\frac{1}{6}(Ku^+)^3\right] \tag{1}$$

In the logarithmic and outer layer where approximately $30<\mathbf{y^+}<\boldsymbol{\delta^+}$, Coles (1956) gave an empirical formula that works well for a variety of pressure gradients

$$u^+=\frac{1}{K}\ln y^++C+\frac{\Pi(x)}{K}2\sin^2\left(\frac{\pi}{2}\frac{y^+}{\delta^+}\right) \tag{2}$$

where

$$y^+=\frac{yu^*}{\nu},\ \delta^+=\frac{\delta u^*}{\nu},\ u^+=\frac{u}{u^*},\ u^*=\sqrt{\frac{\Gamma_w}{\rho}},\ \Gamma_w=\mu\frac{\partial u}{\partial y}\Big|_{y=0} \tag{3}$$

Typical values are K=0.4 and C=5.0 and Π=0.62 for zero pressure gradient. The boundary layer thickness is determined from

$$\delta = \frac{\nu e^{\left(K\frac{u_\infty}{u^*} - KC - 2\Pi\right)}}{u^*} \qquad \textbf{(4)}$$

The first interesting feature is that in the near wall region where approximately $\mathbf{y^+}>30$, $\mathbf{y^+}/\boldsymbol{\delta^+}<<1$, there is a logarithmic dependence of u on y regardless of the pressure gradient, Reynolds number or wall roughness. The second feature is that the turbulent energy production

$$-\langle u'v'\rangle \frac{\partial \overline{u}}{\partial y} \qquad \textbf{(5)}$$

(where < > denotes conditionally sampled averages) shows a sharp peak at the outer edge of the viscous sublayer, and that the first 5% of the boundary layer accounts for over half of the total production of turbulent energy.

2 NEO-CLASSICAL AND MODERN RESEARCH

Studying the coherent structure of the boundary layer was one route to an improved understanding. The technique of flow visualisation was, and still is, used to great effect in the study of this coherent structure.

Favre et al (1957) used spatially separated probes and found that the large scale structure was convected at the mean stream speed and inclined to the wall in the forward direction. Kline et al

(1967) used hydrogen bubble visualisation deep into the layer ($\mathbf{y}^{+}=2.7$) and found that bubbles did not travel along straight trajectories, but accumulated into a series of high and low speed regions called streaks. These streaks were observed to interact with the outer portions of the flow through a sequence of four distinct phases, the first three of which were termed bursting and consisted of a gradual outflow, liftup and sudden oscillation. The intensity and frequency of bursting was found to reduce with a favourable pressure gradient ($dP/dx < 0$) and to increase with an adverse gradient. The spanwise spacing was found (by visual inspection) to be $\lambda^{+}_{z}=\lambda_{z}u^{*}/\upsilon=100$. Kim et al (1971) showed further that virtually all of the net production of turbulent energy in the range $0<\mathbf{y}^{+}<100$ occurred during bursts. Willmarth & Lu (1972) also found large values of u′v′ near the wall with rare values of about 60<u′v′> at $\mathbf{y}^{+}=30.5$. Rao et al (1971) were the first to conjecture that the mean burst period scales with the outer ($\mathbf{u}_{\infty}, \boldsymbol{\delta}$) rather than the inner ($\mathbf{u}^{*}, \upsilon$) variables to give a dimensionless time between bursts of

$$\frac{u_{\infty}T}{\delta} \approx 6 \tag{6}$$

They also found that the mean burst rate did not differ significantly with increasing distance from the wall, suggesting that such events were a general feature of all turbulent flows. This suggests a process where large outer eddies scour the slow moving inner layer releasing bursts of turbulent energy. This energy could be created from intense shear in the inner layer created by local instabilities, making neither the inner layer nor the outer layer solely responsible for turbulent energy production: but rather ascribing this process to their interaction.

Grass (1971) reported on extensive experiments using smooth and rough walls ($\mathbf{u^*k}/\upsilon$=0.0, 20.7, 84.7; k is the roughness height) and found that ejections and inrushes remained unchanged. Offen & Kline (1974) proposed a kinematic description of the link between the inner and outer flow, hypothesising that pairing of vortices associated with two to four bursts led to bulges in the superlayer. Kovasznay et al (1970) were the first to notice the saddle point on the upstream facing (rear) side of the outer flow bulges at a height of $\mathbf{y}/\boldsymbol{\delta}$=0.8 when seen in a reference frame convected with the flow.

Antonia & Bisset (1990), used a spanwise array of hot wires to detect bursts and sweeps, and found that the streamwise length of a sweep was about twice that of a burst, with a value of about 960 wall units at y^+=15. The spanwise extent of a sweep was about 25% larger than that of a burst.

Both the length and width of sweeps and bursts were found to increase with distance from the wall and contours of <u> with ∂<u>/∂x and ∂<u>/∂z showing the presence of a three dimensional shear layer associated with the end of the burst phase and marking the probable interface between a burst and a sweep. They also found that the largest values of instantaneous $\partial u/\partial z$ were comparable with those of the mean velocity gradient at the wall.

The burst-sweep dynamics study of Utami & Ueno (1987), used flow visualisations taken by two still cameras for picture processing of horizontal cross-sections taken just above each other at 0.2s intervals. They proposed a detailed mechanism for the flow structure as shown in figure 1. From their visualisations they concluded that a perturbation in the high shear and vorticity layer very close to the wall (ie the viscous sublayer) produced vortex filaments in this sublayer which were lifted and elongated by the mean shear flow. Such vortices interacted with each other forming a horseshoe vortex as in figure 1a.

Utami and Ueno then proposed that the horseshoe vortices rolled around each other and were stretched further to give the large scale spiral and slightly inclined vortex shown in figures 1b,c. The fluid between the legs of the main spiral would thus be driven in the upstream-upward direction consistent with an ejection and the outer fluid would be driven in the downstream-downward direction, consistent with a sweep.

Whether this work presents an accurate picture is still open to debate, but it is given some credence by the work of Acarlar & Smith (1987a,b), who studied hairpin vortices shed firstly from a hemispherical protuberance and secondly by fluid injection in a developing laminar boundary layer. Their visualisations (shown in figure 2) and hot-film-anemometry studies have shown that such boundary layers develop remarkably similar velocity profiles to those found in a turbulent boundary layer, and that the hairpins interacted in the exact same way as described by Utami and Ueno.

They also noticed that the tangled legs could be identified far downstream but the transverse head had nearly disappeared, presumably due to being stretched in the main stream, which was precisely the picture given by Utami and Ueno.

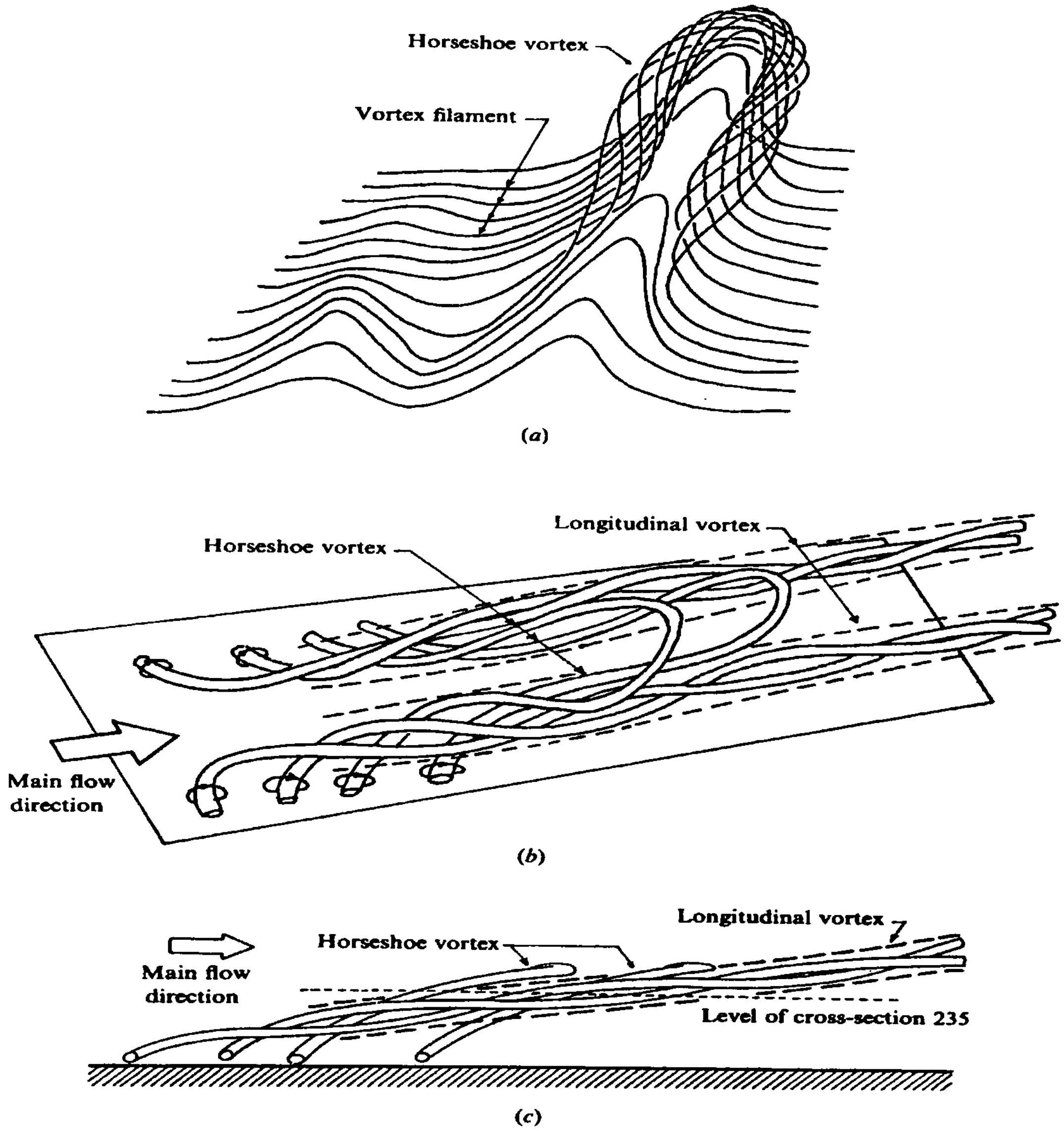

Figure 1. Utami & Ueno (1987). Conceptual model of the horseshoe vortices in the boundary layer. a) The formation and development stages (lines represent vortex filaments). b-c) Fully developed stage (vortex tubes are multiple horseshoe filament structures in a).

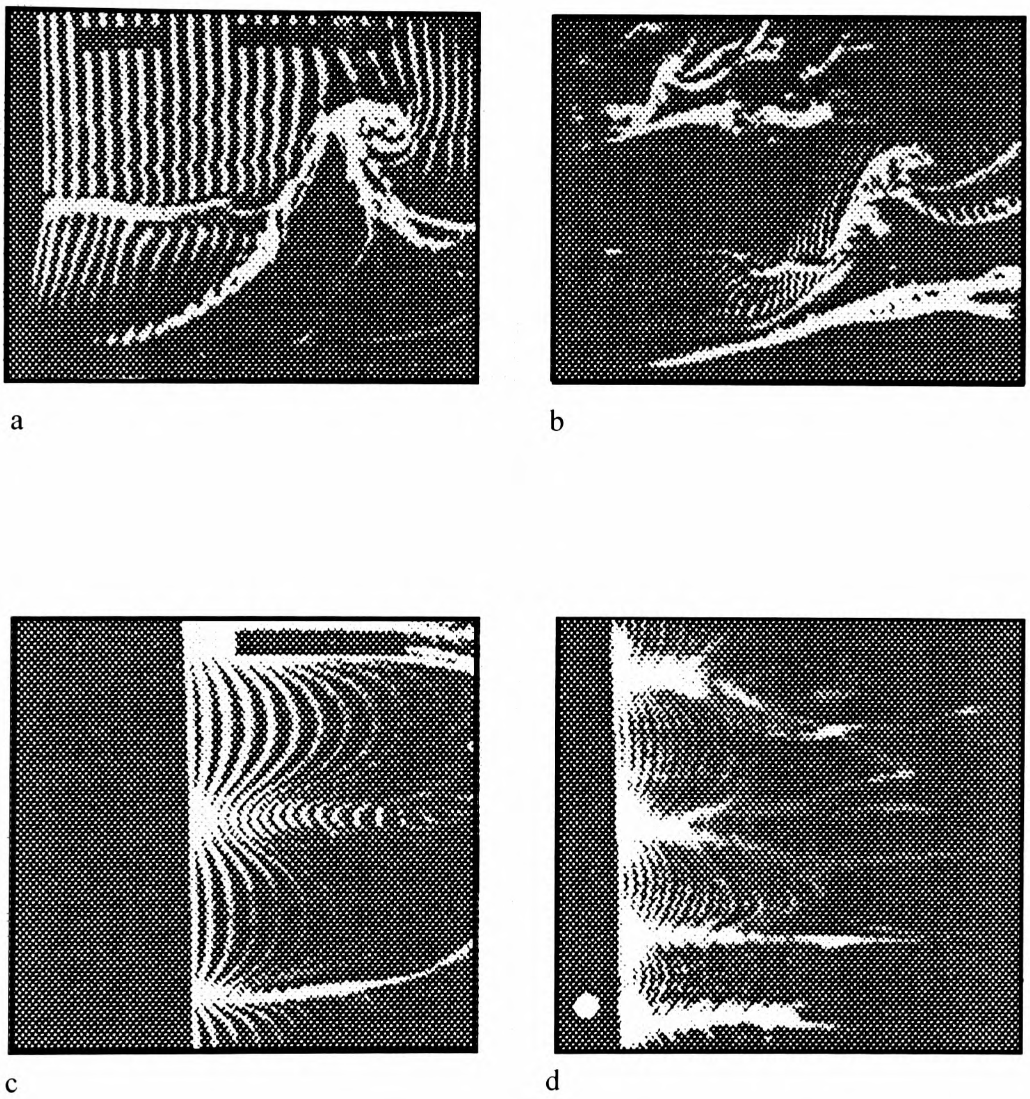

Figure 2. Acarlar & Smith (1987). a-b) Side view comparison between hairpin vortex and turbulent boundary layer patterns visualised by hydrogen bubbles. a) Hairpin vortex x/R=20 b) turbulent boundary layer at Re=2200. c-d) Top view comparison.

APPENDIX 2: FAST9003.HR(RW)/NHT - PROJECT PROPOSAL

FLUID-PARTICLE TRANSPORT DYNAMICS OF SANDWAVES

A three-year PhD project supervised by:
Dr NH Thomas, FAST Team, Birmingham University
and
Dr RJS Whitehouse, HR Wallingford

CONTEXT

The Maritime Engineering Department of Hydraulics Research (MEHR below) undertakes a wide range of basic and applied work on practical problems of bed erosion and deposition in estuaries and surfzones. Their internationally recognised expertise resides mainly in field measurements and large-scale laboratory modelling both for fundamental research and with reference to site-specific problems. In addition, they undertake numerical modelling in support of such work, using large computational codes to represent the shear-turbulent flows due to waves, currents and bedforms. The Fluid and Surface Transport Team (FAST below) undertakes fundamental and applicable research associated with industrial and environmental problems. Currently eight full-time research projects are under way on topics such as two-phase and three-phase transport dynamics of bubbly flows and bubble-driven dispersion of particles and of droplet flows. The collaborative project described below will provide an opportunity for MEHR to benefit from the fundamental generic methodologies in which the FAST team specialise and for FAST to expand the current activities to the special problems involved in bed-particle dynamics.

GOALS

The project will entail experimental and computational investigations of the basic mechanisms involved in particle capture, transport and settling motions in the vicinity of defined bed forms. Three stages to the work are envisaged, as follows.

Firstly, idealised small-scale studies will be executed in Birmingham, initially with particles on beds of fixed, sharp crested, geometries. Trajectory imaging and local flow measurements will be the main objective here, to identify precisely the role of vortex shedding and reattachment in the engagement and escape of individual particles. The aim will be to establish experimental conditions which can be realistically represented in detailed computational simulations of these unsteady events, using methods which have already been successfully used to diagnose previously unexplained phenomena in bubbly vortex flows. When the underlying structure has been properly characterised in this detailed fashion, we plan to develop both aspects of the project as follows.

Secondly, on the experimental side, we shall extend the work using mobile beds to gauge the effects of evolving crest shapes and mass loading by suspended material on the transport capacity of the vorticity shed into the near wake flows. Again, the emphasis in Birmingham will be complemented by the work at Wallingford where large-scale flumes are available for evaluating the fundamental modelling in situations which, though realistic, are still accessible to detailed interpretations and comparisons with the theoretical modelling.

Thirdly, on the numerical side, we shall evaluate the implications of our computational modelling for the effective transport coefficients employed in engineering codes for shear-turbulent bed flows: eg the eddy diffusivities of current closure schemes based on the $k-\epsilon$ equations. Of special interest here will be to view the results in the light of recent field measurements of suspended sand transport over sandwaves made by MEHR (Soulsby, 1989) and, in particular to sensibly accommodate the inertially enhanced capture of particles by concentrated vorticity. In comparison with conventional theory, anomalous results have been reported regarding the distributions of fluid shear and particle concentrations over the bedform. Comparable anomalies have been found in the modelling of bubble transport by flows with concentrated vorticity and we are confident that realistic phenomenology can be incorporated in Reynolds averaged transport modelling of the particle fluxes.

TRAINING

The project will be conducted within securely established environments for flow transport dynamics research, both in the

FAST team managed by Dr Thomas at Birmingham and as part of the MEHR programme managed by Dr Soulsby at Wallingford. Both laboratories possess excellent experimental and computing facilities.

Training experience at MEHR will be available for up to six weeks each year. Hydraulics Research expertise in instrumentation and modelling of coastal, estuarine and river flows is renowned and the student will gain valuable experience from participation in their activities. During these stays the student will be expected to perform experiments in one of their large-scale experimental facilities and to use the results to evaluate and enhance the small-scale studies and computational modelling work. The student will also be encouraged to contribute on a day-to-day basis to the operation and recovery of data from these test facilities commercially valued at £1000 per day. The substantial interest of the company in our project is demonstrated by their generous offer of £1000 pa as a financial contribution to the student, in addition to meeting in full expenses incurred during these stays. Our common interests and excellent contacts will ensure that close monitoring of the student's progress is maintained for the duration of the project.

The student will also benefit from undertaking this research as a 'FAST' team project in Birmingham. The team currently has seven full time workers (four students, one associate and two fellows) with an eighth registered as an external student for a higher degree. All are concerned with aspects of flow and transport dynamics of multiphase fluids, ranging from fundamental studies on bursting bubbles, droplet motions, surface waves and buoyant convection, through applicable algorithms for airlift bioreactors and biokinetics, to systems evaluation for bioprocessing equipment. Our project with MEHR will benefit from overlapping generic interests with most of these other activities.

ACKNOWLEDGEMENT

Enabling work for the preparation of this proposal was done under the auspices of Flow Research Evaluation Diagnostics Ltd (R & D Institute, University of Birmingham). In connection with the application of our findings to the wider interests of Hydraulics Research, FRED will be available to supply technical advisory services on specific practical situations such as the practical implications for prediction of erosion and deposition by wavebreaking in the surfzone, by tidal reversals in estuaries and by longitudinal vorticity in flood channels.

COST

Maintenance supplement for student	£1000pa
Maintenance contribution to school (approx)	£1000pa
Additional contribution for project	£1000pa
Total	£3000pa

Total for 3 years (Oct 90 - Sep 93): £90000

Note. Services to the value of £10000 will be contributed by

Hydraulics Research, representing 20x½ days access to their experimental facilities.

APPENDIX 3: FUNDAMENTAL NAVIER-STOKES EQUATIONS

The three fundamental equations (Rodi, 1979) are mass conservation (ie the continuity equation)

$$\frac{\partial U_i}{\partial x_i}=0 \tag{1}$$

momentum conservation, the Navier Stokes equations

$$\frac{\partial U_i}{\partial t}+U_j\frac{\partial U_i}{\partial x_j}=-\frac{1}{\rho}\frac{\partial P}{\partial x_i}+\nu\frac{\partial^2 U_i}{\partial x_j \partial x_j} \tag{2}$$

and scalar conservation

$$\frac{\partial \phi}{\partial t}+U_i\frac{\partial \phi}{\partial x_i}=\lambda\frac{\partial^2 \phi}{\partial x_i \partial x_i}+S_\phi \tag{3}$$

where U_i is the instantaneous velocity in direction x_i, P is the static pressure minus the hydrostatic pressure, ϕ is a scalar such as temperature or concentration of a solute, S_ϕ is a source term such as heat generated from a reaction and υ and λ are the kinematic viscosity and the diffusivity of the scalar. The velocity, pressure and scalar terms may be split into a time averaged and a fluctuating part such that

$$U_i=\overline{U}_i+u_i, \quad P=\overline{P}+p, \quad \phi=\overline{\Phi}+\varphi \tag{4}$$

where the mean quantities are defined by

$$\overline{U}_i=\frac{1}{t_2-t_1}\int_{t1}^{t2}U_i dt\ ,\ \overline{P}=\frac{1}{t_2-t_1}\int_{t1}^{t2}Pdt\ ,\ \overline{\Phi}=\frac{1}{t_2-t_1}\int_{t1}^{t2}\phi dt \tag{5}$$

and t_2-t_1 is long compared with the velocity fluctuations in the flow but short compared with the scale of the mean flow. The averaged equations are given below.

Mass conservation,

$$\frac{\partial\overline{U}_i}{\partial x_i}=0 \tag{6}$$

Momentum conservation,

$$\frac{\partial\overline{U}_i}{\partial t}+\overline{U}_j\frac{\partial\overline{U}_i}{\partial x_j}=-\frac{1}{\rho}\frac{\partial\overline{P}}{\partial x_i}+\frac{\partial}{\partial x_j}\left(\nu\frac{\partial\overline{U}_i}{\partial x_j}-\overline{u_i u_j}\right) \tag{7}$$

Scalar conservation,

$$\frac{\partial\overline{\Phi}}{\partial t}+\overline{U}_i\frac{\partial\overline{\Phi}}{\partial x_i}=\frac{\partial}{\partial x_i}\left(\lambda\frac{\partial\overline{\Phi}}{\partial x_i}-\overline{u_i\varphi}\right)+S_\Phi \tag{8}$$

The averaged multiples of the fluctuating terms ie,

$$-\rho\overline{u_i u_j}\quad,\quad-\rho\overline{u_i\varphi} \tag{9}$$

represent the turbulent transport of the momentum and scalar quantities respectively.

APPENDIX 4: CLOSURE METHODS

1 ZERO EQUATION MODELS

Zero equation models do not include a transport equation for any of the turbulent quantities. They employ the eddy viscosity concept and obtain an appropriate eddy viscosity from experiments, by trial and error, or by relation to the mean flow quantities. The basic equation relates the turbulent fluctuations after Boussinesq

$$-\overline{u'v'} = \nu_t \frac{\partial U}{\partial y} \qquad \textbf{(1)}$$

where u′ and v′ are the fluctuating components of the horizontal and vertical velocity and y is the vertical distance. υ_t is the eddy viscosity; setting it to a realistic value is the downfall of this method in all but the simplest of systems (such as thin shear layers; Rodi, 1979). This method is also undermined by the fact that it assumes - without physical basis - that the generation and dissipation of turbulent energy is in balance at all points in the flow (ie that transport of turbulence is zero). Fuller reviews are presented by Markatos (1986) and Rodi (1979).

Lee & Chung (1987) modelled a gas-particle disperse flow using a two fluid model with two eddy viscosities, one for each phase. A simple mixing length model was then applied to the k equation at equilibrium. As pointed out by Rizk & Elghobashi (1989), the mixing length model is not suitable when convective and diffusive turbulent transport are important, and is certainly not suitable when the mixing length varies in different areas of the flow as, for example, in shear layers.

2 ONE EQUATION MODELS

This method attempts to account for the transport of turbulent quantities by solving a differential transport equation. It was introduced by Kolmogorov and Prandtl independently and derived exactly from the NS equations (Rodi, 1979). The formulation of this kinetic energy (k) transport equation is

$$\frac{\partial k}{\partial t} + U_i \frac{\partial k}{\partial x_i} = -\frac{\partial}{\partial x_i}\left[\overline{u_i\left(\frac{u_j u_j}{2} + \frac{p}{\rho}\right)}\right] - \overline{u_i u_j}\frac{\partial U_i}{\partial x_j} - \beta g_i \overline{u_i \varphi} - \nu \overline{\frac{\partial u_i}{\partial x_j}\frac{\partial u_i}{\partial x_j}} \quad \textbf{(2)}$$

where the first term LHS is the time rate of change and the second term LHS is the convective transport. The first term RHS is the diffusive transport, the second term RHS is P the production of k by shear, the third term RHS is the buoyant production of k and last term RHS is ϵ the viscous dissipation of turbulent kinetic energy.

This equation is of little use as it stands due to the new correlations of fluctuating quantities in the diffusion and dissipation terms. These are cleared up using model assumptions for the diffusional flux of k and the dissipation ϵ, expressed as

$$\overline{-u_i\left(\frac{u_j u_j}{2}+\frac{p}{\rho}\right)} = \frac{\nu_f}{\sigma_k}\frac{\partial k}{\partial x_i}\ , \quad \epsilon = C_D\frac{k^{3/2}}{L} \tag{3}$$

where σ_k and C_D are empirical constants. It should be noted that this form of the k equation is for high Reynolds number flows and is not applicable to the viscous sublayer near walls.

When the rate of change, diffusive and convective terms are negligible, production and dissipation are equal and the special state of local equilibrium of k is obtained and a mixing length model is retrieved. When the assumption that the mixing length is either constant or is empirically based on the local velocity or its gradient is not valid, the length scale must be found via a dynamic equation. This form is the two equation model as discussed in the main text.

APPENDIX 5: SECOND-PHASE MODELLING

1 DISPERSION TENSOR MODELS

Picart et al (1986) used the k-ϵ model to calculate the fluid motion and a separate transport equation for the dispersed phase that contained a dispersion tensor dependent on the fluid and turbulence characteristics and the particle properties. Their model (called DISCO) quite accurately predicted flows in a Eulerian framework when the continuous phase was unaffected by the dispersed particles. The method relied on an 'effective viscosity' for turbulent closure based on k and ϵ and six empirically determined closure constants. They also included the hypothesis that the mean pressure and kinetic energy dissipation rate were equal when solving the equations for tangential fluctuating components, correctly stating this could only be valid for steady, homogenous flow.

2 TWO-FLUID MODELS

Besnard & Harlow (1988) described a two-fluid-field turbulent flow model using two turbulent fields designed to be expanded to consider the mixing of two turbulent fields. They modelled solid particle dispersion in incompressible flow for the case where the turbulence scale was much larger than both the dispersed phase particle size and the inter-particle distance. They defined a coupling function between the two fields, K, such that

$$K = C_D \epsilon_1 \epsilon_2 \rho_2 |U_2 - U_1| = \epsilon_1 \epsilon_2 C \quad (1)$$

where ϵ was the volume fraction, ρ the density and U the velocity of each phase. The coupling coefficient C was then defined according to whether Stokes drag or high particle Reynolds number flows were being considered. The subsequent time averaging of this expression over the chosen timescale brought in the fluctuating component of C, ie C′.

The key to successful modelling was to ensure that the prescription for C′ was acceptable for the flow situation being considered. Besnard and Harlow neglected this quantity for the sake of simplicity, so no valid comment can be made on the real fluid-particle interactions which should include lift and acceleration terms. They did not present data for comparison with experiment.

Elghobashi & Abou-Arab (1983) developed a two-equation two-phase model in which the averaged momentum equations were closed by modelling the turbulent correlations to third order, thus eliminating the need for *ad hoc* modelling of the dispersed phase contribution to the turbulence. The 38 terms in their exact equation for the kinetic energy and the 67 terms in the turbulent kinetic energy dissipation rate were each modelled independently and ignored above third order. The correlations required setting of three coefficients in addition to the five required for the k-ϵ model, but the applicability of these coefficients to other flows was not discussed. The model naturally predicted the results of the data to which it was fitted but no other data was presented. A later paper, Elghobashi et al (1984), used the model to simulate a similar jet with different sized particles and found agreement with experiment to within 8% for the particle velocity for this similar flow geometry.

3 LAGRANGIAN PARTICLE MODELLING

Berlemont et al (1990) used a second order k-ϵ closure scheme in a two-fluid simulation. The dispersed phase was tracked in a Lagrangian trajectory approach, wherein a number of trajectories were simulated in a given turbulence field and then reassembled statistically to give the particle dispersion rates.

Their main assumption was that the turbulence was homogenous, so when the model was validated by comparison with grid generated turbulence and pipe flow the results compared well with experiment. When particle-laden jet flows were predicted and compared with experiments the errors were of order 200% in some areas of the flow. While fluid RMS velocities agreed well a wide disparity existed between experimental and calculated particle velocities.

APPENDIX 6: K-ϵ MODEL OF JOHNS ET AL (1990)

The horizontal and vertical equations of motion and the continuity equation used by Johns et al (1990) were

$$\frac{\partial u}{\partial t}+u\frac{\partial u}{\partial x}+w\frac{\partial u}{\partial z} = -\frac{1}{\rho}\frac{\partial p}{\partial x} \;,\quad \frac{\partial w}{\partial t}+u\frac{\partial w}{\partial x}+w\frac{\partial w}{\partial z} = -g-\frac{1}{\rho}\frac{\partial p}{\partial z} \;,\quad \frac{\partial u}{\partial x}+\frac{\partial w}{\partial z} = 0 \tag{1}$$

where ρ was the liquid density (viscous stresses were omitted in this equation). Combining the continuity and vertical equations gave

$$\frac{\partial w}{\partial t}+\frac{\partial (uw)}{\partial x}+\frac{\partial (w^2)}{\partial z} = -g-\frac{1}{\rho}\frac{\partial p}{\partial z} \tag{2}$$

which was integrated from an arbitrary depth to the free surface with boundary condition $p=p_a$ (ie constant atmospheric pressure) at $z=\xi$. The kinematic condition at the free surface gave

$$w = \frac{\partial \zeta}{\partial t}+u\frac{\partial \zeta}{\partial x} \;,\quad at\ z=\zeta \tag{3}$$

and then vertical integration gave

$$\frac{p}{\rho} = \frac{p_a}{\rho}+g\zeta-gz+\frac{\partial}{\partial t}\int_z^{\zeta} wdz+\frac{\partial}{\partial x}\int_z^{\zeta} uwdz\ -w^2 \tag{4}$$

Reynolds averaging and substitution, neglecting turbulent departures in ξ gave

$$\frac{\overline{p}}{\rho} = \frac{p_a}{\rho} + g\zeta - gz + \frac{\partial}{\partial t}\int_z^{\zeta} \overline{w} dz + \frac{\partial}{\partial x}\int_z^{\zeta} \overline{u}\,\overline{w} dz - \overline{w}^2 + \frac{\partial}{\partial x}\int_z^{\zeta} \overline{u'w'} dz - \overline{w'^2} \quad (5)$$

and similar averaging of the horizontal equation gave

$$\frac{\partial \overline{u}}{\partial t} + \frac{\partial}{\partial x}(\overline{u}^2) + \frac{\partial}{\partial z}(\overline{u}\,\overline{w}) = -\frac{1}{\rho}\frac{\partial \overline{p}}{\partial x} + \frac{\partial}{\partial x}(\overline{-u'^2}) + \frac{\partial}{\partial z}(\overline{-u'w'}) \quad (6)$$

Defining E to be the turbulence energy density, they set

$$\overline{u'^2} = E\ , \quad \overline{w'^2} = 0.35E \quad (7)$$

after Soulsby (1981) and expressed the horizontal Reynolds stress in terms of a gradient transfer law

$$\tau_{xy} = \overline{-u'w'} = K\frac{\partial \overline{u}}{\partial z} \quad (8)$$

where K was a prescribed variable, the eddy viscosity. Hence, omitting the overbars and substituting into the equations gives

$$\frac{p}{\rho} = \frac{p_a}{\rho} + g\zeta - gz + \frac{\partial}{\partial t}\int_z^{\zeta} w dz + \frac{\partial}{\partial x}\int_z^{\zeta} uw dz - w^2 - \frac{\partial}{\partial x}\int_z^{\zeta} K\frac{\partial u}{\partial z} dz - 0.35E \quad (9)$$

and

$$\frac{\partial u}{\partial t} + \frac{\partial u^2}{\partial x} + \frac{\partial uw}{\partial z} = -\frac{1}{\rho}\frac{\partial p}{\partial x} - \frac{\partial E}{\partial x} + \frac{\partial}{\partial z}\left(K\frac{\partial u}{\partial z}\right) \quad (10)$$

They then defined a hydrodynamic component of the kinematic pressure field, P, as

$$P = \frac{\partial}{\partial t}\int_z^{\zeta} w dz + \frac{\partial}{\partial x}\int_z^{\zeta} uw dz - w^2 - \frac{\partial}{\partial x}\int_z^{\zeta} K\frac{\partial u}{\partial z} dz + 0.65E \qquad \textbf{(11)}$$

which gave

$$\frac{\partial u}{\partial t} + \frac{\partial u^2}{\partial x} + \frac{\partial uw}{\partial z} = -g\frac{\partial \zeta}{\partial x} - \frac{\partial P}{\partial x} + \frac{\partial}{\partial z}\left(K\frac{\partial u}{\partial z}\right) \qquad \textbf{(12)}$$

Turbulence closure was achieved using a turbulence energy equation

$$\frac{\partial E}{\partial t} + u\frac{\partial E}{\partial x} + w\frac{\partial E}{\partial z} = K\left(\frac{\partial u}{\partial z}\right)^2 - \epsilon + \frac{\partial}{\partial z}\left(K\frac{\partial E}{\partial z}\right) + K\frac{\partial u}{\partial z}\frac{\partial w}{\partial x} - E\frac{\partial u}{\partial x} - 0.35E\frac{\partial w}{\partial z}$$

with

$$K = c^{1/4} l E^{1/2} \ , \quad \epsilon = \frac{c^{3/4}E^{3/2}}{l} \qquad \textbf{(14)}$$

where c was an empirical constant taken as 0.08 and l was the characteristic length scale of the vertical mixing process. l was prescribed by

$$l = \frac{\kappa(z+h+z_0)(\zeta - z + z_0)}{H+z_0+z_s} \qquad \textbf{(15)}$$

where κ is the Von Karman constant.

APPENDIX 7: DISCRETE VORTEX MODELLING METHODS

1 THE POINT VORTEX APPROXIMATION PROBLEM

The DVM relies on concentrating vorticity at points and allowing these points to interact with time using the Biot-Savart law (Batchelor, 1967). This law gives the velocity induced by one vortex on another as proportional to the vorticity and inversely proportional to their separation. Close to the vortex these induced velocities are large thus requiring a very small time interval to prevent unrealistic inter-vortex accelerations. This problem has been solved using a variety of methods as detailed below.

1.1 Vortex Amalgamation

The method of vortex amalgamation is often used to stop mutual vortex orbit, to limit high mutually induced velocities, to limit computational time and to simulate a naturally occurring merging process. The process is again ad hoc since there are no rules to govern the amalgamation action, but one common method is to place the new vortex at the centre of the vorticity of the pairing couple and conserve the total circulation.

1.2 Discrete Vortex in Cell Method

Other pseudo amalgamation methods are based on the temporary amalgamation of clusters of vortices that are close to each other with respect to the rest of the vorticity field. The Discrete Vortex In Cell method of Tiemroth (1986) replaced a large collection of vortices by a single vortex, relying on the dominance of the first order term in the interaction between members of the cluster and vortices away from the cluster. In this situation the inter-cluster spacing should be large with respect to the intra-cluster inter-vortex spacing.

1.3 Dipole in Cell Method

Ghoniem et al (1986) used the dipole in cell method. Vortices were combined, if they appeared in the same square on a superimposed grid, by conservation of their first moments into two new vortices dependent upon the sign of their vorticity. The far field was then computed from this dipole whilst the near field was computed directly. Again, this was a time saving device used when many vortices had formed into large scale coherent structures.

Other cut-off methods exist, such as Anderson (1986) and Greengard & Rochlin (1987), where the far field interactions were approximated using Taylor series expansions and finite difference meshes.

1.4 Rediscretisation

The rediscretisation method of Fink & Soh (1974) overcame the problem of vortex proximity by rediscretising the sheet of vortices at every time step. In this way the vorticity density was fairly accurately modelled at the same time as maintaining the vortex separations at a value such that induced velocities were not too large. In general, these rediscretisation methods delayed the onset of numerical instability but reduced resolution in areas of large gradients.

1.5 Cut-off Schemes

These were devised to remove the singularity at the point vortex. The commonly used methods have compact supports which are rigid cores with fixed or variable radius and vorticity distribution. Lamb (1932), used a vortex core with a Gaussian vorticity distribution which is an exact solution to the Navier Stokes equations (though the linear superposition of two Lamb vortices does not satisfy them). Spreiter & Sacks (1951), used the Rankine vortex core, which rotates as a solid body with the outer flow inversely proportional to the radius from the core. A velocity gradient discontinuity exists at the edge of the core and the Rankine vortex does not satisfy the Navies Stokes equations, but this has not prevented its widespread use.

2 THE SIMULATION OF VISCOUS DIFFUSION

The above discussion was confined to inviscid or infinite Reynolds number flows, but in many engineering applications the flows are either viscously dominated or contain a mixture of viscously dominated and inertially dominated regions.

The vorticity equation can be split into a convective term and a diffusive term. At low Reynolds number the convection term is small and the viscous term dominates the equation. When the magnitudes of the two terms are comparable both terms must be used. One method here is to use the operator splitting technique where at one time step the diffusion term is considered to be zero and at the next time step the convective term is considered to be zero. The diffusive term can be solved statistically by recourse to the probability density function of two Gaussian random variables, one for each of the two dimensions.

These methods are riddled with problems as discussed by Sarpkaya (1989). Two key problems are, firstly, the rapidly increasing number of vortices in a viscous region (a problem which generally requires the use of VIC schemes with their own problems) and, secondly, that the random walk process will be used in regions of the flow where viscosity is of no importance.

APPENDIX 8: REPORT - FAST9108.RJO/NHT

SUMMARY

The effect of bedforms on the dynamics of fluid motions and the resulting feedback on the bedforms is critical in determining the rate of sediment transport over topography. In the region of the crest of a sandwave, an adverse pressure gradient generally forces the boundary layer to separate and so form a shear layer. The instabilities in this layer grow and discrete vortices are shed which entrain fluid as they are swept downstream by the flow. These pseudo 2D structures pair at least once in their lifetime and engulf more fluid, constrained only by the available fluid depth (Muller and Gyr, 1986). These vortices provide one possible mechanism for the transport of sediment particles from the crest region, lee slope and from the upstream face of the of next sandwave, akin to the transport of a gaseous second phase by a submerged jet (Thomas et al. 1983). They are certainly responsible for the boils and scour patterns as seen in many rivers and streams (Jackson, 1976). The main goal of this project is to determine the interaction between the vorticity and the sediment in these areas.

The position of the separation point depends upon the local pressure gradient around the crest region, and there is no reason to expect the point at which this causes boundary separation to be steady with time. Our work has shown that this is almost certainly not the case, and that shifting of the separation point

around the crest and the motion of the reattachment zone has a marked effect on the size of the separation zone. This flicking of the separation point, due to turbulence from upstream bedforms and possibly unsteady wave motion at the surface may even cause the sweeping away of the separation zone, as shown in plates 1.

1 EQUIPMENT AND METHODS

The experimental work was performed at Wallingford as part of a CASE study visit and was carried out in a 24.4m long tilting flume, with a width of 0.91m and 0.3m maximum depth. Four sheet-steel unpainted triangular cross-section bedforms with a nominal height of 0.07m and length 1.14 metres were placed in the tail section of the flume as shown in figure 1 with an average water depth of 0.17m. The actual in-situ bedform profiles were measured using a point gauge mounted on a trolley on rails attached to the flume. This trolley was also used to support a micro-propeller meter with a measurement area of 10mm diameter and a pointer to mark the length scale. The working section was from 8.2 to 9.3 metres on this length scale attached to the flume.

Control of the water flow depth was by a sluice at the discharge end of the flume, the flowrate (up to 0.17 cubic metres per second) corresponding to a crest depth integrated velocity of 0.9 m/s being set by a manual control valve on the gravity feed tank which was run at a constant level. A 'V' notch weir gave an indication of the flowrate. The water surface was set parallel to the bed for each flowrate by tilting the flume

Surface waves excited by the entry condition and the unsmooth flume walls were damped using two expanded polystyrene boards floating four metres upstream of the first bedform. These introduced drag on the upper part of the velocity profiles in figure 2. The profiles obtained up to 0.3 m away from the centreline differ little from the centreline value (figure 2). The velocity profiles were obtained from micro-propeller meter readings against calibrations by the HR instrument support unit both before and after a four week period of use. The calibration drift over the period was insignificant.

Flow visualisation was achieved using a slit of light, the width of which varied from 10 to 50 millimetres and illuminated by 2000 Watt lamps shining on a silver painted adjustable plywood slit. The choice of visualisation particle was limited by availability at the time the work began. There are many factors that must be taken into account when selecting the particle and lighting conditions, and scaling from the 0.1 m channel used in the laboratory work at Birmingham to the larger flume at Wallingford in four weeks is difficult. The ideal particle for our work would have been similar to the 400 micrometer white Amberlite resin of which we had only 0.5 kilogrammes at the time; a quantity closer to 10 Kilogrammes would have been more appropriate. This particle would have allowed us to obtain sharp images of the complete flow over the bedform using a video camera. The actual particle used (Rilsan powder) had a size range 20-200 micrometers, with mean of 80 micrometers. The relative area of the particles is thus 25:1 and hence the quantity of reflected light from rilsan powder is proportionately lower per particle, resulting in video imaging of poor quality. As an expedient for the study visit, the imaging was done using 35 millimetre cameras to separately capture 3 overlapping regions of the flow. The three Nikon F3 cameras were fired simultaneously every 0.25 seconds with either 1/60 or 1/30 second shutter speeds. This gave a series of composite photographs showing the evolving flow structure in a qualitative sense, and hence velocity information from streak lengths. For closer inspection of the crest region, say up to a 5 centimetre viewing length, the video camera was adequate for resolving the motions.

2 OPERATING CONDITIONS USED DURING THE WORK

Condition	Water height above crest (m)	Flume Tilt +/- 20	Velocity at crest H=112mm (m/s)
1	0.089	210	0.28
2	0.172	260	0.57
3	0.209	230	0.45
4	0.176	230	0.65
5	0.207	230	0.35
6	0.182	230	0.35
8	0.193	230	0.43
9	0.187	230	0.66

3 INDIVIDUAL RUNS

The velocity profiles collected for individual runs are shown in figure 2. Since lack of adequate flow tracers was a problem, the best and most useful results came from the optical camera rather than the more manageable video camera. Still photography has the major disadvantage in that it is difficult to capture vortex events clearly since the motion data is lost due to slow frame rates. What can be captured are events like that shown in figure 4 where a region of obvious vorticity is swept from one region to another.

Visual observation of the flow shows that at all conditions vortices are responsible for lifting sediment from the crest and lee slope regions. Vortices are clearly seen, and the eye is sensitive enough to follow their progress both from formation at or near the crest or from upstream bedforms. Regularly the flow reverses direction at a fixed point say 0.01m above the lee slope as the size of the separation region changes, sweeping away the vorticity from the crest.

Also visually observed was the effect that these vortices have on sediment at the crest and on the lee slope. At the crest the finer particles (say less than 200 microns diameter) are captured by the vorticity and moved away from the crest to fall out either on the lee slope or on the next bedform. Larger particles are seen to jet out into the flow before being captured by the return flow and brought to rest on the lee slope. Regular lift-up of sand from the lee slope by impinging vortices is also visible, this being confined to the smaller particles depending upon the intensity of the incident vortex.

4 COMPARISON WITH PREVIOUS WORK

Soulsby (1989) performed velocity and suspended sediment concentration measurements over a sandwave in the Taw estuary. The observed velocity profiles at the bedform crests showed similar jetting due to acceleration up the flank of the bedform as our velocity profiles; see figures 1 and 2. The bedforms used for our work were also similar in shape, with comparable height:length ratio of about 1:15. We thus feel confident in saying that the cloud of suspended sediment deduced by Soulsby to move downstream from a sandwave, as shown in figure 3 is the separated flow region being shed, as shown in plate 1.

The reasons for the unsteadiness in the local pressure gradient around the crest may be due to surface waves excited by the bedforms or by wind, the uneven flume walls, pressure fluctuations caused by the passage of large scale structures shed from upstream crests or possibly a combination of effects.

This shedding phenomenon highlights the complex nature of the system. These complications hamper fundamental understanding of particle-vortex interactions, which is surely the method by which the sediment is moved from the bed into the separation cloud. It points to the serious need to pinpoint the mechanism by using single sharp crests in the absence of external forcing from the eddies shed from upstream and by surface waves. When the fundamental system is understood, its extension to the real system may be trivial in the light of our current knowledge concerning separation zone shedding. However, the extent to which current calculation methods, viz k-epsilon closure, could reliably reproduce the oscillatory patterns of separation zone behaviour reported here remains to be established.

Figure 1 : Flume Condition 5 - Velocity profiles

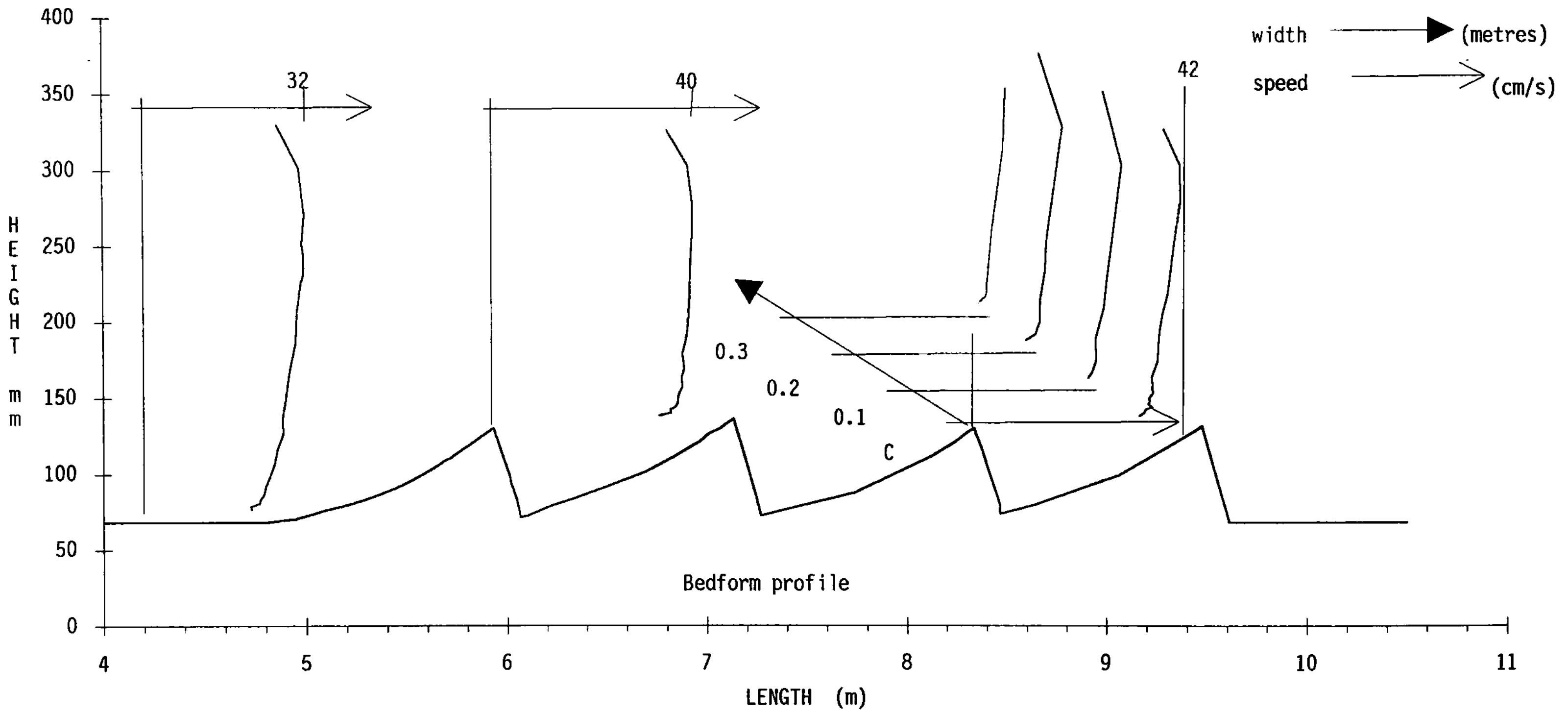

Figure 2 : Flume Condition 6, 8, 4, 9 - Velocity Profiles at Crest 3

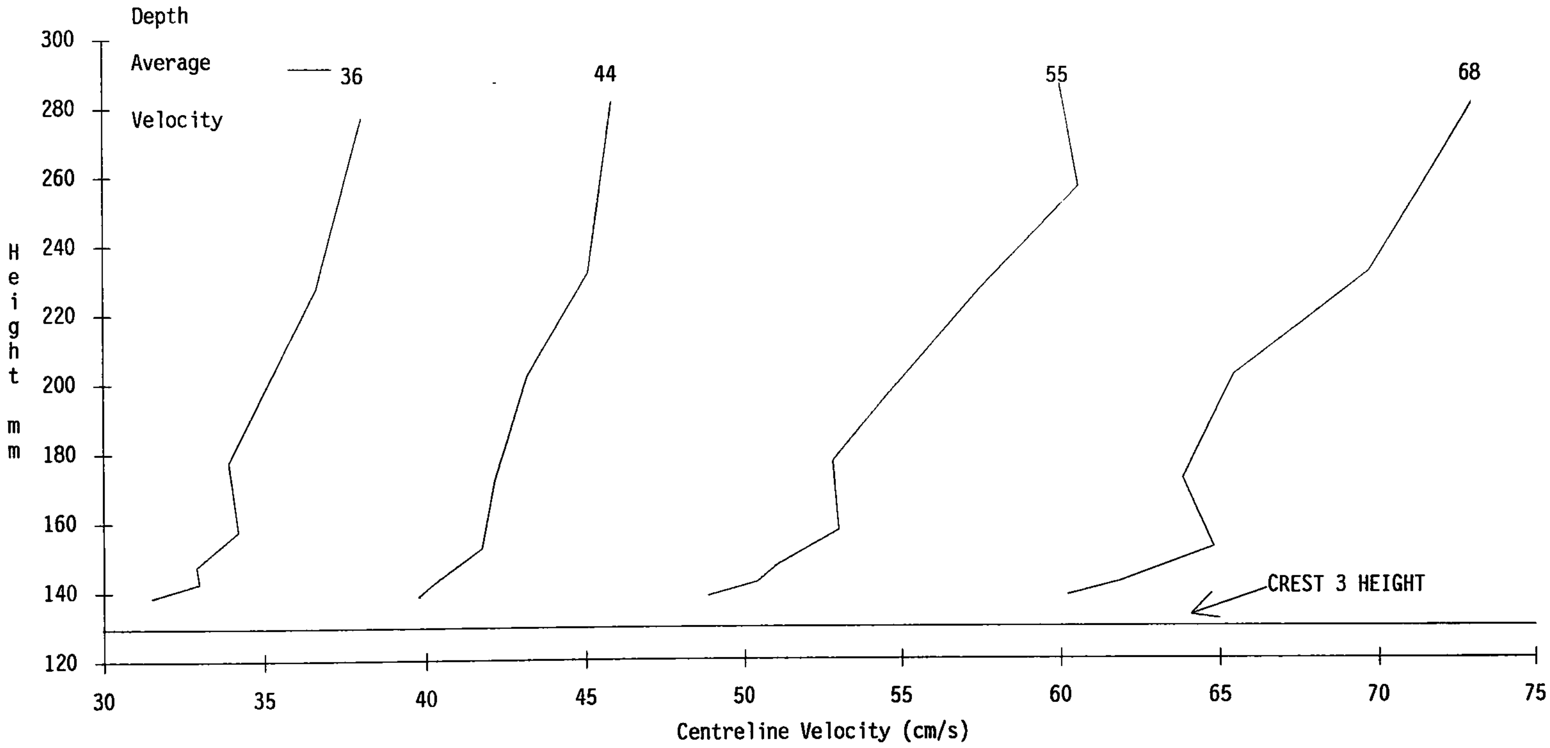

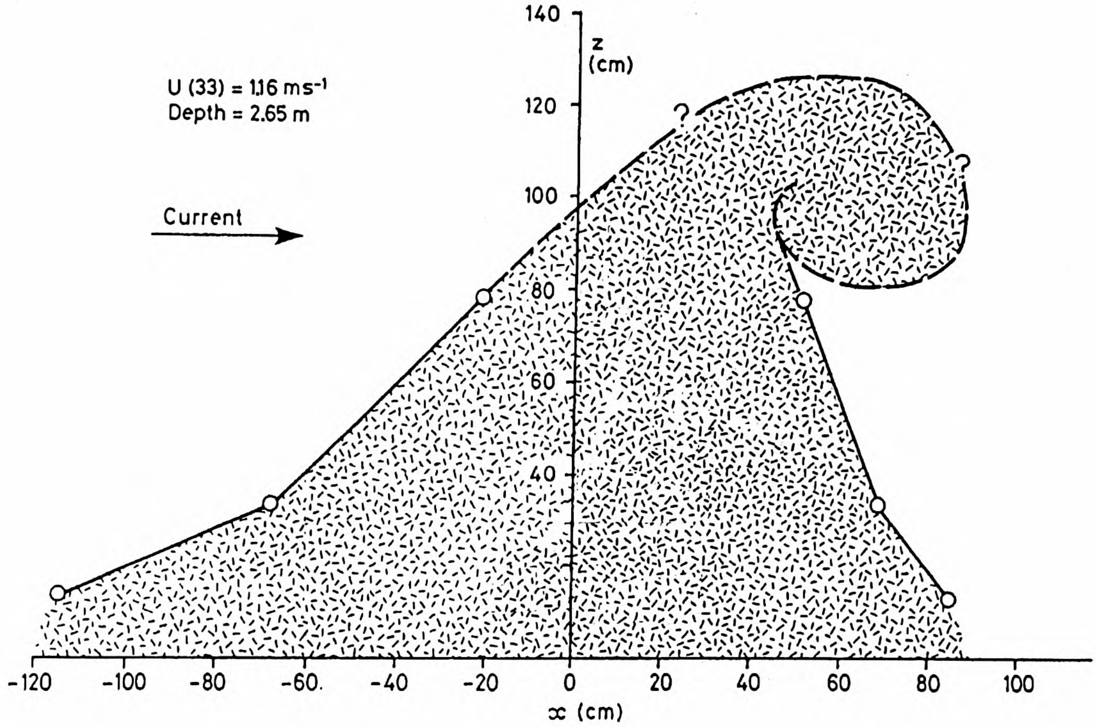

Figure 3. After Soulsby (1989). The shape of a cloud of sediment downstream of a sandwave crest in the estuary of the river Taw, Devon, England. The flow is left to right, z is height, U current velocity and x horizontal length scale.

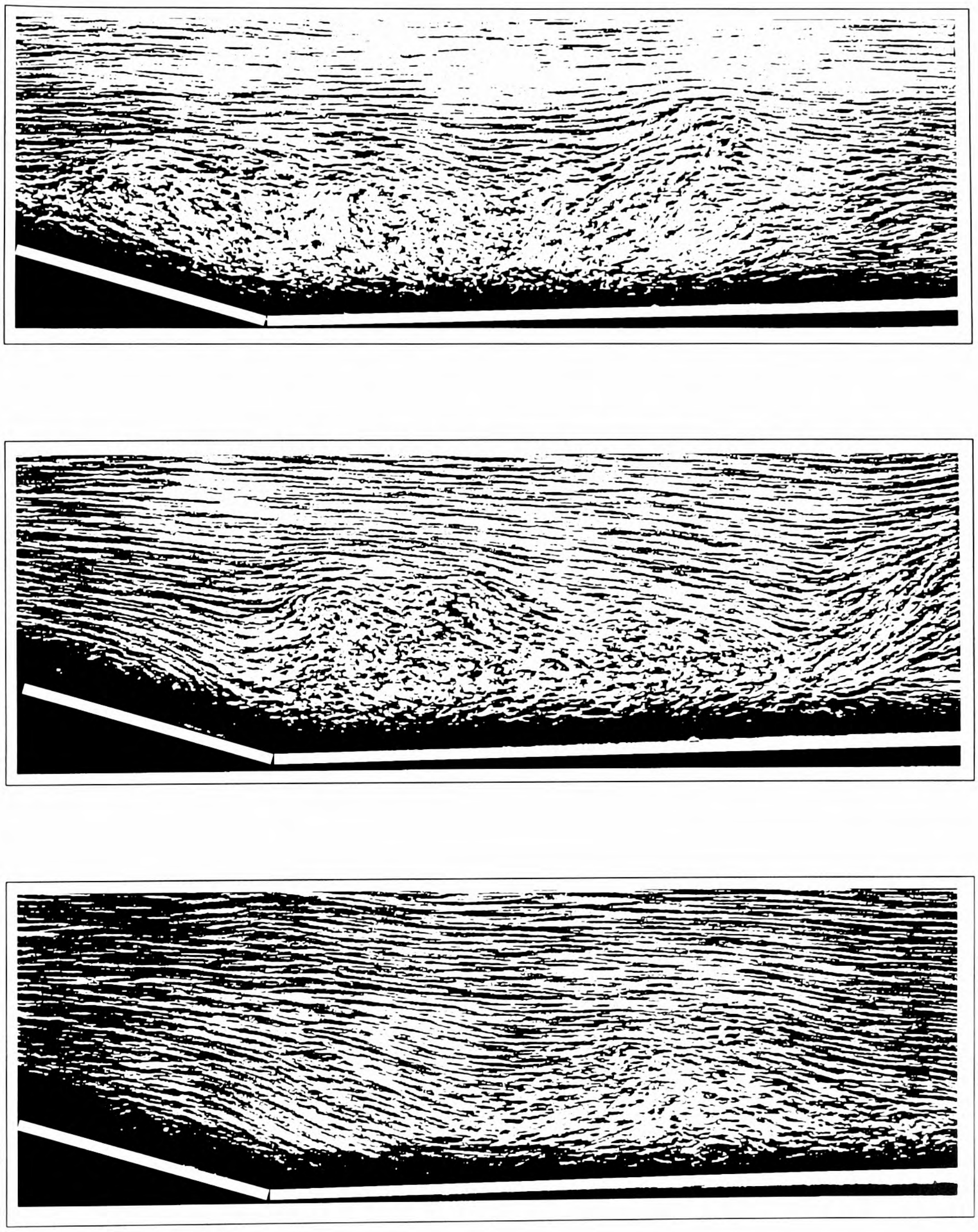

Figure 4. The plates show three views of the recirculation region behind an experimental bedform. The shots are 0.35 secs. apart and clearly visualise the sweeping away of the turbulent region, leading to re-attachment close to the trough.

APPENDIX 9: DERIVATION OF FORCES ON PARTICLE IN A RANKINE VORTEX

The velocity vector U for a Rankine vortex is given by

$$U=\frac{AR^2}{r}, \; r>R \qquad U=Ar, \; r<R \tag{1}$$

where R is the core radius and r is the distance of the particle from the core. The horizontal and vertical components of the fluid velocity, U_X and U_Y are found by multiplying this by Y/r and X/r respectively, where X and Y are the horizontal and vertical distances of the particle from the core centre. The spatial partial derivatives of these velocities are required to calculate the pressure and fluid gradient forces on the particle. These are presented below for the horizontal component. Inside the core the gradients are

$$\frac{\partial U_X}{\partial X}=0 \qquad \frac{\partial U_X}{\partial Y}=A \tag{2}$$

and outside the core they are

$$\frac{\partial U_X}{\partial X}=\frac{2AR^2XY}{(X^2+Y^2)^2} \qquad \frac{\partial U_X}{\partial Y}=\frac{A(Y^2-X^2)}{(X^2+Y^2)^2} \tag{3}$$

hence, the force due to the pressure gradient and fluid inertia (PI), outside the core is

$$PI=-\left(1+\frac{1}{C_{VM}}\right)\left(\frac{R^4}{r^4}\right)A^2X \tag{4}$$

and inside the core is

$$PI=-\left(1+\frac{1}{C_{VM}}\right)A^2X \tag{5}$$

where A is the rotational speed of the core and C_{VM} is the coefficient of virtual or added mass. The force due to fluid drag (D), outside the core is

$$D=B\left(V_X+\frac{AY}{r^2}\right)\left|V_X+\frac{AY}{r^2}\right| \tag{6}$$

and inside the core is

$$D=B(V_X+AY)|V_X+AY| \tag{7}$$

where V_X and V_Y are the particle velocity in the X and Y directions respectively and

$$B=\left(\frac{-1}{C_{VM}}\right)\left(\frac{g(\rho_P-\rho_L)}{\rho_L}\right) \tag{8}$$

where g is the gravitational acceleration and ρ_P and ρ_L are the particle and liquid densities. The vorticity lift force is only used inside the core, and is found from

$$L=\frac{-2C_LA}{C_{VM}}(V_Y-AX) \tag{9}$$

where C_L is the vorticity lift coefficient.

APPENDIX 10: MODEL CODE FOR CALCULATING THE FORCE ON THE PARTICLE

```
*****************************************************************
***Subroutine for calculating the forces on a particle in the***
***             vicinity of a Rankine vortex core            ***
*****************************************************************

      SUBROUTINE RANKINE

***Set the buoyancy parameter

      BOY=(-1.0/CVM)*(GR*(DENP-DENL)/DENL)

***Set R equal to the radial distance between the particle and
***the centre of the vortex core at the last timestep

      R=SQRT(X(T-1)**2+Y(T-1)**2)

***Is the particle inside or outside the vortex core?

      IF (R .GT. 1.0) THEN

     ***
     ***If outside the core:
     ***calculate the forces for a particle outside the core
     ***

     ***Fluid gradient and pressure force in the x and y direction

           AX(T)=-(1+1/CVM)*(1/R**4)*(ANG**2*X(T-1))
           AY(T)=-(1+1/CVM)*(1/R**4)*(ANG**2*Y(T-1))

     ***The lift force is identically zero outside the core

           LX(t)=0.0
           XY(t)=0.0

     ***Drag force in the x and y direction

           DX(T)=BOY*(VX(T-1)+ANG*y(t-1)/r**2)
                *SQRT((VX(T-1)+ANG*Y(T-1)/R**2)**2)
           DY(T)=BOY*(VY(T-1)-ANG*x(t-1)/R**2)
                *SQRT((VY(T-1)-ANG*X(T-1)/R**2)**2)


     ***
     ***If inside the core:
     ***calculate forces for a particle inside the core
     ***

      else

     ***Fluid gradient and pressure force in the x and y direction

           AX(T)=-(1+1/CVM)*(ANG**2*X(T-1))
           AY(T)=-(1+1/CVM)*(ANG**2*Y(T-1))
```

```
    ***Lift force in the x and y directions

          LX(T)=(-2*ANG*CL/CVM)*(VY(T-1)-ANG*X(T-1))
          LY(T)=(2*ANG*CL/CVM)*(VX(T-1)+ANG*Y(T-1))

    ***Drag force in the x and y direction

          DX(T)=BOY*(VX(T-1)+ANG*y(t-1))
                *SQRT((VX(T-1)+ANG*Y(T-1))**2)
          DY(T)=BOY*(VY(T-1)-ANG*x(t-1))
                *SQRT((VY(T-1)-ANG*X(T-1))**2)

     endif


***Calculate the new particle velocity in x and y directions
***from the velocity at the previous time interval plus the
***forces calculated above multiplied by the time interval

     VX(T)  =  (DT/(DENP/(DENL*CVM)+1))*(AX(T)+LX(T)+DX(T))
               +VX(T-1)
     VY(T)  =(DT/(DENP/(DENL*CVM)+1))*(AY(T)+LY(T)+DY(T)+BOY)
               +VY(T-1)

***Calculate the new particle x and y coordinates

     X(T)  =  X(T-1)  +  VX(T)*DT
     Y(T)  =  Y(T-1)  +  VY(T)*DT

***Finish

     RETURN
     END
```

APPENDIX 11: MODEL CODE FOR GROWING RANKINE VORTEX

```
      SUBROUTINE GROWTH
      INCLUDE 'a:COMDATA.FOR'
5     DO 100 T = 1,10
***CHANGE NON-DIMENSIONAL FACTORS TO NEW VALUES DUE TO GROWTH
      VORAD=VORAD*GROWN
      ANG=ANG/GROWN
      RES=RES+DT
***GROW VORTEX AT LINEAR RATE
      if(res .eq. dt) goto 10
      GROWN=(RAD0+GRAD*RES)/(RAD0+GRAD*(RES-DT))
10    R=SQRT(X(T-1)**2+Y(T-1)**2)
      GAM=ATAN2(Y(T-1),X(T-1))

      IF (R .GE. VORAD) THEN
      CALL GOTOXY(1,1)
       WRITE(5,'('' OVERLAP AT TIME'',F10.5)') RES
      goto 1000
       ENDIF
***RESOLVE FOR R<VORAD

***ADDED MASS IN x AND y

       AX(T)=-(1+1/CVM)*(ANG**2*X(T-1))

       AY(T)=-(1+1/CVM)*(ANG**2*Y(T-1))

***LIFT IN x AND y

       LX(T)=(-2*ANG*CL/CVM)*(VY(T-1)-ANG*X(T-1))

       LY(T)=(2*ANG*CL/CVM)*(VX(T-1)+ANG*Y(T-1))

***DRAG TERM IN x AND y

       DX(T)=BOY*(VX(T-1)+ANG*y(t-1))
     &              *SQRT((VX(T-1)+ANG*Y(T-1))**2)/(VTER*VTER)
       DY(T)=BOY*(VY(T-1)-ANG*x(t-1))
     &              *SQRT((VY(T-1)-ANG*X(T-1))**2)/(VTER*VTER)


***CALCULATE NEW VELOCITY AND POSITION
11    VX(T)=(DT/(DENP/(DENL*CVM)+1))
           *(AX(T)+LX(T)+DX(T))+VX(T-1)

      VY(T)=(DT/(DENP/(DENL*CVM)+1))
            *(AY(T)+LY(T)+DY(T)+BOY)+VY(T-1)
***CHANGE DT IF WRONG SIZE

      X(T)  = X(T-1)  + VX(T)*DT

      Y(T)  = Y(T-1)  + VY(T)*DT
      if ((y(t) .ge. 0.0) .and. (y(t-1) .lt. 0.0)) then
      flag1=flag1+1
      endif
```

```
      if((x(t) .gt. 0.0) .and. (y(t) .lt. 0.0) .and.
     &  ((VY(T) .lt. 0.0) .and. (vy(t-1) .gt. 0.0)) .and.
     &  (x(t-1) .lt. x(t))) goto 1000



      IF(SQRT((VX(T)*DT)**2+(VY(T)*DT)**2) .LT. 0.000005) THEN
        RES=RES-DT
        VORAD=VORAD/GROWN
        ANG=ANG*(GROWN**2)
        dt=dt*2
        GOTO 11
      ENDIF
      IF(SQRT((VX(T)*DT)**2+(VY(T)*DT)**2) .GT. 0.0001) THEN
        RES=RES-DT
        VORAD=VORAD/GROWN
        ANG=ANG*(GROWN**2)
        dt=dt/2
        GOTO 11
      ENDIF

100   CONTINUE
      call gotoxy(1,1)

***PLOT PARTICLE AND AXES AND FORCES

      CALL PLOT (NINT(X(10)/RAD0/scalef*151+151)
     &          ,NINT(276-Y(10)/RAD0*151/scalef),0)

      CALL draw(151,276,nint(151+151*VORAD/RAD0/scalef),276,1)

      CALL DRAW(451,200,NINT(451-40*AX(0)/BOY)
     &              ,NINT(200+40*AY(0)/BOY),7)
      CALL DRAW(451,200,NINT(451-40*AX(10)/BOY)
     &              ,NINT(200+40*AY(10)/BOY),0)
      CALL DRAW(451,200,NINT(451-40*DX(0)/BOY)
     &              ,NINT(200+40*DY(0)/BOY),7)
      CALL DRAW(451,200,NINT(451-40*DX(10)/BOY)
     &              ,NINT(200+40*DY(10)/BOY),4)
      CALL DRAW(451,200,NINT(451-40*LX(0)/BOY)
     &              ,NINT(200+40*LY(0)/BOY),7)
      CALL DRAW(451,200,NINT(451-40*LX(10)/BOY)
     &              ,NINT(200+40*LY(10)/BOY),2)
      CALL DRAW(451,200,451,NINT(200+40*BOY/BOY),14)
***PRINT DATA TO SCREEN OR END IF CHOSEN
      if (.not. keypressed()) goto 110
      call getkeyboard(ch,scancode)
      if (scancode .eq. 57) then
      CALL DRAW(451,200,NINT(451-40*AX(10)/BOY)
     &              ,NINT(200+40*AY(10)/BOY),7)
      CALL DRAW(451,200,NINT(451-40*DX(10)/BOY)
     &              ,NINT(200+40*DY(10)/BOY),7)
      CALL DRAW(451,200,NINT(451-40*LX(10)/BOY)
     &              ,NINT(200+40*LY(10)/BOY),7)
      CALL DRAW(451,200,451,NINT(200+40*BOY/BOY),7)
      call getkeyboard(ch,scancode)
```

```
      if (scancode .eq. 57) stop
      GOTO 1000
      else
      call getkeyboard(ch,scancode)
      if (scancode .eq. 78) then
      dt=dt+.001
      else if (scancode .eq. 74) then
      dt=dt-.001
      endif
      endif

      CALL GOTOXY(1,1)
      WRITE(5,'(''  T,DT '',F6.4,''   '',F8.5)') RES,DT
      WRITE(5,'(''  X,Y,R '',F5.3,''   '',F5.3,''   '',F5.3)')
     &X(10),Y(10),R
      WRITE(5,'('' X,Y VELY '',F7.4,''  '',F7.4)') VX(10),VY(10)
      WRITE(5,'('' X,Y LIFT '',F9.5,''  '',F9.5)') LX(10),LY(10)
      WRITE(5,'('' X,Y DRAG '',F9.5,''  '',F9.5)') DX(10),DY(10)
      WRITE(5,'('' X,Y BODY '',F9.5,''  '',F9.5)') AX(10),AY(10)
      WRITE(5,'(''  BUOYANCY '',F15.7)') BOY
      WRITE(5,'(''  ang,rad '',F9.5,''   '',F9.5)') ang,vorad
      WRITE(5,'(''  grad, grown '',F15.7,f15.7)') grad,grown
105   IF (.NOT. KEYPRESSED()) GOTO 105
      call getkeyboard(ch,scancode)
      call gotoxy(50,1)
      write(5,'(''   Yel=buoyancy, Red=drag, Green=lift'')')
      call gotoxy(50,2)
      write(5,'(''         Black=fluid acceleration'')')
***RESET DATA
110   X(0) = X(10)
      Y(0) = Y(10)
      VX(0) = VX(10)
      VY(0) = VY(10)
      AX(0) = AX(10)
      AY(0) = AY(10)
      DX(0) = DX(10)
      DY(0) = DY(10)
      LX(0) = LX(10)
      LY(0) = LY(10)
      T=0
      GOTO 5

1000  return
      end
```